Modeling an oil injector for a FCC reactor

Javier Añez

Normandie Université

THÈSE

Pour obtenir le diplôme de doctorat

Mécanique des fluides

Préparée à l'Université de Rouen Normandie

Modélisation de l'injection de pétrole pour les procédés FCC (Fluid Catalytic Cracking)

Présentée et soutenue par
Javier J. Anez P.

Thèse soutenue publiquement le (16-11-2018) dans la Faculté de Sciences, Amphithéâtre E devant le jury composé de		
M. Dominique LEGENDRE	Professeur, Université de Toulouse	Rapporteur
M. Erwin FRANQUET	Maître de conférences, Ecole d'Ingénieurs	Rapporteur
M. François-xavier DEMOULIN	Professeur, Université de Rouen	Directeur de thèse
M. Julien REVEILLON	Professeur, Université de Rouen	Codirecteur de thèse
M. Amsini SADIKI	Professeur, Technische Universitat Darmstadt	Examinateur
M. José PASTOR	Maître de conférences, Universitat Politècnica de València	Examinateur

Thèse dirigée par François-xavier DEMOULIN et Julien REVEILLON, laboratoire CORIA (UMR 6614)

UNIVERSITÉ DE ROUEN NORMANDIE

ED PSIME

UMR 6614 CORIA COMPLEXE DE RECHERCHE INTERPROFESSIONNEL EN AEROTHERMOCHIMIE

Modeling an oil injector for a FCC Reactor

Thesis submitted for the degree of Doctor of Philosophy of the University of Rouen Normandie

Javier J. Añez P.

javier.anez@coria.fr

Jury:

Professor Dominique Legendre	University of Toulouse
Dr. Erwin Franquet	University of Pau and pays de L'Adour
Professor Amsini Sadiki	Technische Universitat Darmstadt
Dr. Jose Pastor	Universitat Politecnica de Valencia
Professor Francois-Xavier Demoulin	University of Rouen
Professor Julien Reveillon	University of Rouen
Project Manager Abderrahim El Hodhar	VINCI Technologies®

CORIA UMR 6614 - University of Rouen Normandie

University avenue, B.P. 12

76801 Saint-Etienne du Rouvray - France

November 2018

Phd research, University of Rouen Normandie and CORIA - France

This research was done under the supervision of Pr. F.X. Demoulin and J. Reveillon, with the financial support of VINCI Technology®.

Edition date *March 27, 2019*

Résumé

Cette thèse est une entreprise commune de VINCI Technologies et du laboratoire CNRS CORIA. De nombreux injecteurs comportent une zone de mélange interne dans laquelle les phases liquides et gazeuses sont toutes deux présentes dans une proportion significative. Par conséquent, cette zone appartient à la catégorie des écoulements diphasiques denses. Pour simuler la dispersion du liquide et caractériser le spray de ces injecteurs, des modèles appropriés sont nécessaires. Les points clés de cette approche sont la dispersion du liquide qui peut être associé au flux liquide turbulent et la quantité de surface liquide-gaz. En particulier, ce manuscrit rapporte, d'une part le développement théorique des modèles de la famille ELSA et, d'autre part, les approximations industrielles correspondantes. Le solveur proposé bascule dynamiquement du spray ICM au spray de sous- maille, à travers le concept ELSA et grâce à l'indicateur basé sur la résolution (IRQ). D'autre part, une fois la zone diluée se forme, l'approche ELSA est couplée à la méthode d'écoulement multiphase, qui vise à déterminer la distribution du spray à l'aide de l'équation WBE. Cette dernière équation est résolue avec une méthode hybride Euler-Lagrange. Le but est de résoudre l'équation WBE avec une approche stochastique Lagrangienne, tout en préservant la compatibilité avec la description Eulerienne de l'écoulement diphasique, basée sur ELSA, pour tirer parti des deux approches. Finalement, ces approches développées ont été utilisées pour des applications industrielles montrant leur robustesse et leur capacité à aider dans le processus de développement de nouveaux injecteurs.

Mots-clés: Approche multi-échelle dynamique, Couplage hybride Euler-Lagrange.

Abstract

This PhD is a joint venture between $VINCI\ Technologies$ and the CNRS Laboratory CORIA. For its application, $VINCI\ Technologies$, developed mainly oil-related equipments and in particular injection/atomization systems. Some of these injectors are characterized by a very big geometrical dimensions (several meters long), that leads to very high Reynolds and Weber number. In addition, many injectors incorporate an internal mixing zone, in which liquid and gas phases are both present in a significant proportion. Consequently, this zone belongs to the dense two-phase flow category. To simulate the liquid dispersion and to characterize the spray formation special from these injectors, appropriate models are required. On its side, the CORIA team, has developed a suitable approach, so-called $ELSA$, based on the pioneering work of Borghi and Vallet [1, 2]. Key points of this approach are the liquid dispersion that can be associated to the turbulent liquid flux and the amount of liquid-gas surface that can be used to determine eventually the Sauter mean diameter (SMD) of the spray.

During this PhD, the applications proposed by $VINCI\ Technologies$, have promoted a review of a large part of the multiphase flow approaches to find the more appropriate for each case. This has been the opportunity to clarify the range of application of each approach, and therefore stress the necessity to develop coupled approaches, in order to cover the proposed application in the most suitable way. In particular, this manuscript reports, in one hand, the theoretical development of the $ELSA$ family models, and on the other hand, the corresponding industrial approximations. Since $ELSA$ approaches are originally developed for RANS simulation of the dense zone, it has been extended to LES description. The link of this approach to the $DNS-ICM$ approach, has been studied with a special care. The resulting proposed solver, switches dynamically from ICM to subgrid spray, through the $ELSA$ concept, and thanks to resolution based indicator (IRQ). On the opposite side, once the dispersed spray is formed, the $ELSA$ approach is coupled to multiphase flow method, that aims to determine the spray distribution through the WBE equation. This later equation, is solved with an original hybrid Euler-Lagrange method. The purpose is to solve the WBE equation with a *Lagrange stochastic approach*, and at the same time, preserving the compatibility to the Euler description of two-phase flow, based on $ELSA$, to benefit from both approaches. This coupled approach has been tested against academic experimental data coming from ECN research initiative, a combined DNS and experimental measurement of dispersed spray on a Diesel jet, and under an air-blast atomizer numerical test case, for which the mean liquid volume fraction has been measured. Eventually, these developed approaches have been applied to industrial application showing there robustness and their capacity to help in the process of design development of new injectors.

Keywords: Dynamic multi-scale approach, Hybrid coupling Euler-Lagrange.

Table of Contents

List of Tables

Table **Page**

List of Figures

Figure **Page**

Nomenclature

Acronyms

Symbol	Description	Dimensions	Units
DNS	Direct Numerical Simulation	-	–
ECN	Engine Combustion Network	-	–
$ELSA$	Euler-Lagrange Spray Atomization	-	–
ESA	Euler Spray Atomization	-	–
FCC	Fluid Catalytic Cracking	-	–
$HELSA$	Hybrid Euler-Lagrange Spray Atomization	-	–
ICM	Interface Capturing Method	-	–
IRQ	Interface Resolution Quality	-	–
LES	Large Edyy Simulation	-	–
LVF	Liquid Volume Fraction	-	–
PDF	Probability Density Function	-	–
PMD	Projected Mass Density	-	–
SDE	Stochastic Differential Equation	-	–
SMD	Sauter Mean Diameter	-	–
TIM	Transversed Integrated Mass	-	–
WBE	Williams-Boltzmann Equation	-	–

Greek Symbols

Symbol	Description	Dimensions	Units
α	Liquid Volume Fraction	-	–

ϵ	Turbulent energy dissipation	L^2/T^3	m^2/s^3
λ	Taylor length scale	L	m
μ	Dynamic fluid viscosity	M/T.L	Kg/m^1s^1
ν	Kinematic fluid viscosity	L^2/T	m^2/s^1
ρ	Mixture density	M/L^3	Kg/m^3
Σ	Surface Interface Density	1/L	$1/m^1$
σ	Surface Tension	M/T^2	Kg/s^2

Roman Symbols

Symbol	Description	Dimensions	Units
a	Volume cell length scale	L	m
D	Diameter	L	m
g	Gravity	L/T^2	m/s^2
J	Momentum flux ratio	-	–
K	Curvature	-	–
k	Turbulent kinetic energy	L^2/T^2	m^2/s^2
N	Nitrogen	-	–
n	Interface Unit Vector	-	–
p	Pressure	$M/L.T^2$	N/m^2
Re	Reynolds number	-	–
t	Time	T	s
U	Mixture velocity	L/T	m/s^1
We	Weber number	-	–

Subscripts

Symbol	Description	Dimensions	Units
32	Sauter Mean Diameter	-	–
D	Related to Drift term	-	–
g	Gas	-	–
h	Hydrolic	-	–
i	Intensity	-	–
$init$	Initial quantity	-	–
inj	Injection	-	–

l	Liquid	-	–
m	Mixture	-	–
mix	Liquid/Gas mixing for source term	-	–
r	Relative	-	–
rlg	Related to Local relative velocity	-	–
sgs	Subgrid-scale	-	–
slg	Related to Local relative velocity	-	–

Chap. 1 | Introduction

1.1 General context

Nowadays, global demand for transportation fuels will continue to grow and this demand will be met largely by gasoline and diesel fuels. The fluid catalytic cracking (FCC) process continues to play a key role in an integrated refinery, as the primary conversion process of transforming crude oil into lighter products. It converts crude oil to useful and lighter products like LPG, gasoline and cycle oils by catalytic cracking [25]. A schematic view is shown in Fig. 1.1, where FCC Nozzles can be viewed within the highlighted small circle.

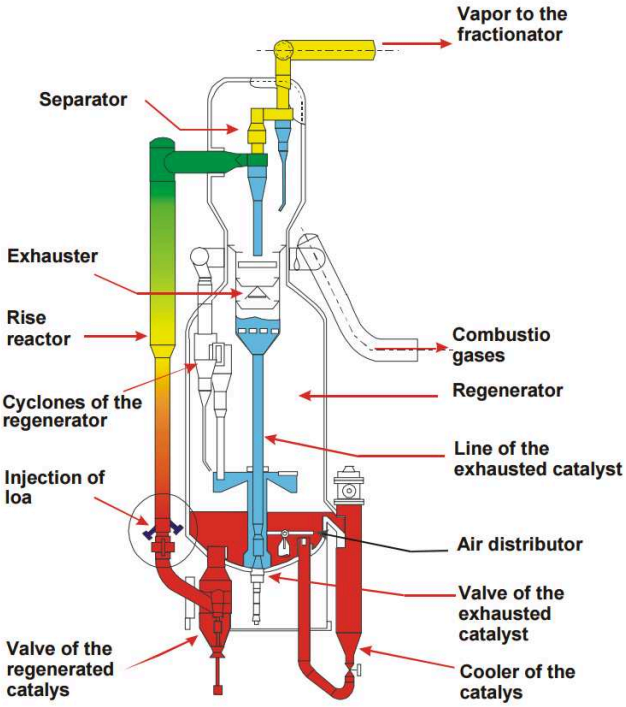

Figure 1.1: Emblematic FCC Reactor [8].

Since the first FCC Reactor unit started in 1942, several design improvements have been made [26]. On one hand single parts were added to enhance the FCC performance over the years, such as the regenerators, separated cyclones, stripper section, among others. On the other hand, special attention was also given to FCC catalysts quality, higher pressure regenerator, nozzle design, and feed atomization zone to named just a few. Besides the developments in FCC technology toward the conversion of heavier feedstock, recent developments have also been implemented to satisfy the increasing propylene demand [27]. The FCC alliance (Axens, Shaw, Total and IFP Energies Nouvelles) funded in 2008, have worked since then on the PetroRiser technology, which is designed for the production of high yields of propylene. This new technology incorporates a separate riser in the FCC process, in which the light

cracked naphtha produced in the first riser is sent to this second riser for further cracking [28]. The French enterprise Vinci Technologies, manufactures and provides a broad range of laboratory equipments and specific field instruments for the Oil and Gas Industry. A portion of them is developed in close collaboration with IFPEN. One of its goals is to design and build durable, reliable, high-efficient and low maintenance FCC Nozzles. To that end, Vinci Technologies and the research institute CORIA (COmplexe de Recherche Interprofessionnel en Aerothermochimie) have begun a project to assist the design of new generation of FCC Nozzles, by using Computational Fluid Dynamics (CFD).

1.2 Fluid Catalytic Cracking

A typical FCC Reactor consists of a three-step process: reaction, product separation, and regeneration, as shown in fig. 1.1. Being the latter, the most important step in the conversion process, namely, the regeneration or commonly known as the Riser. The feed atomization, vaporization and cracking reactions occur inside the riser, while catalyst, hydrocarbon liquid droplets, and hydrocarbon vapors travel upward [27]. In the next two decades, the FCC process will be likely used with biofuels, as a enhanced process for reducing CO_2 emissions [9]. For clarity, the process description has been broken down into the following main sections: Catalyst separation, Stripping, Regenerator, and Feed nozzles/riser.

Separator

After exiting the riser, catalyst enters the reactor vessel which serves as housing for the cyclones and/or a disengaging device for catalyst separation, as shown in fig. 1.1 and on the left of Fig. 1.2. Most FCC units employ either single or two-stage cyclones to separate the remaining catalyst particles from the cracked vapors. The cyclones collect and return the catalyst to the catalyst stripper or exhauster. The product vapors exit the upper cyclones and flow to the main fractionator tower (not shown in the fig. 1.1). It is important to separate catalyst and vapors as soon as they enter the reactor. If not, the extended contact time of the vapors with the catalyst in the reactor housing will allow for non-selective catalytic to recrack some of the desirable products. The extended residence time also promotes undesirable thermal cracking of the intermediate products [9].

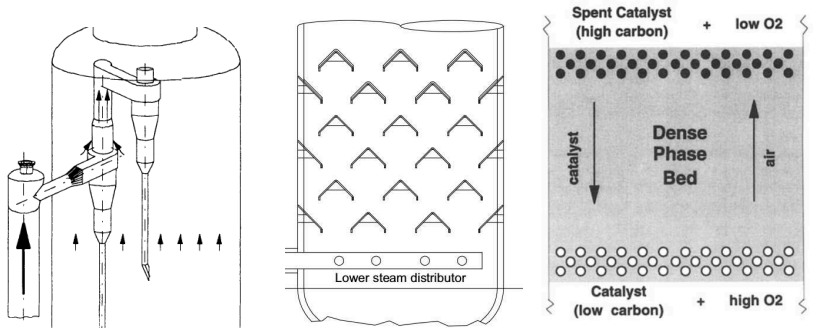

Figure 1.2: An example of a Catalyst separator[9] (left), Stripper[9] (center), and Regenerator[10] (right).

Stripping section

The stripper or exhauster in the fig. 1.2 is a standpipe, which typically has horizontal baffles. Steam is injected in one or more locations in the lower section of the stripper and rises counter-currently to the down-flowing solids. The steam displaces hydrocarbon vapor and strips hydrocarbons adsorbed on the catalyst. There are hydrocarbon vapors that fill the catalyst's pores, and hydrocarbon vapors that are entrained with the catalyst [9]. More

importantly, these hydrocarbons are not combusted in the regenerator, where they deactivate the catalyst and decrease the allowed cracking severity, otherwise the throughput of the FCC unit will be reduced [10].

Regenerator catalyst recovery

The regenerator in FCC units is a combustor where coke deposited on the catalyst and unstripped hydrocarbons are oxidized by air [10]. The regenerator has three main functions. Firstly, it restores catalyst activity. Secondly, it supplies heat for cracking reactions, and finally, it delivers fluidized catalyst to the feed nozzles.

Feed nozzles/riser

The reactor-regenerator is the heart of the FCC process. In today's cat cracking, the riser is the reactor, see Fig. 1.3. Efficient contact of the feed and regenerated catalyst is critical for achieving the desired cracking reactions [9]. Feed nozzle(s) are used to atomize the feed with the help of dispersion or atomizing steam. The cracking reactions ideally occur in the vapor phase. Cracking reactions begin as soon as the feed is vaporized by the hot regenerated catalyst. The expanding volume of the vapors is the main driving force that is used to carry the catalyst up in the riser. The hot regenerated catalyst will not only provide the necessary heat to vaporize the gas oil feed and bring its temperature to the desired cracking temperature, but also compensate for the internal cooling that takes place in the riser due to endothermic heat of reaction.

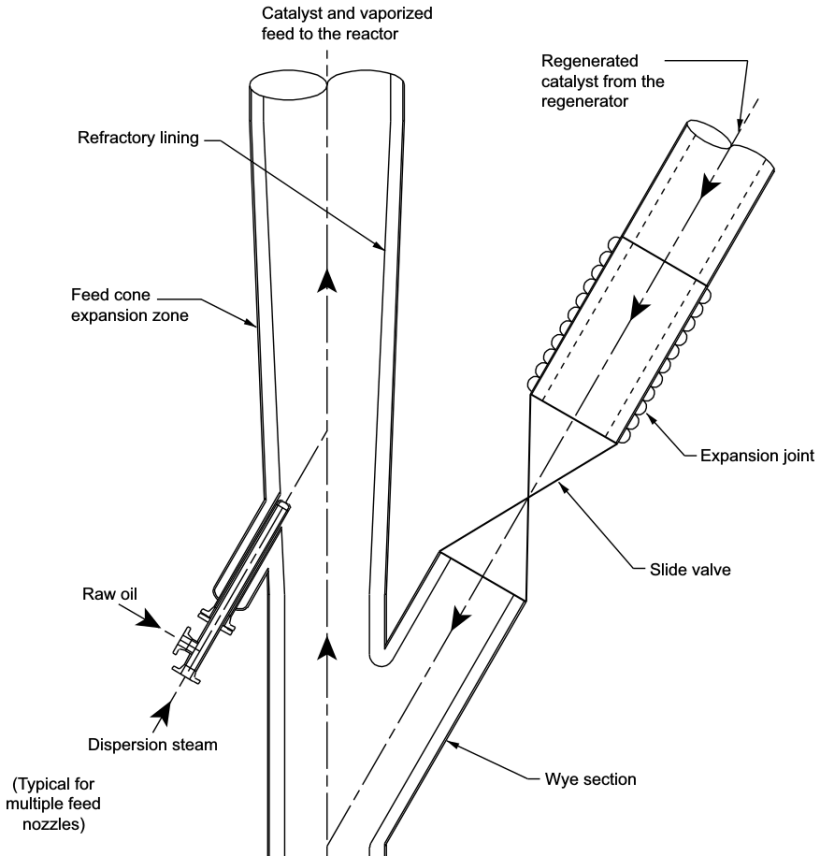

Figure 1.3: Typical riser section [9].

There are some design requirements that any FCC Nozzle must meet, specially within the atomization zone in the Riser, such as:

- Fast and uniform mixing is essential to ensure quick vaporization and intimate contact between the oil and catalyst during their brief residence time in the riser. Therefore, oil needs to be atomized into small droplets with a narrow size distribution since small droplets vaporize more quickly than larger ones.
- The feed injection system (FCC Nozzles) and the design of the riser should produce the most uniform cracking environment possible. Poor feed injection creates localized regions of high and low catalyst-to-oil ratios and induces catalyst back-mixing. This generally reduces conversion and leads to increased coking.
- The feed also needs sufficient momentum to effectively penetrate the flowing catalyst without causing erosion of the riser wall [10].

As shall be explained later in chapter 5, to the best of our knowledge, very few experimental and numerical simulations have been made inside the FCC Injector itself, and even less, coupled with the feed atomization zone, under normal industrial operating conditions. Despite the recent advancement of LES and $RANS$ turbulence models, and above all, CPU available power, the majority of numerical research, have been focused instead on internal combustion (IC) engines, in which the atomization process within and in the near-field zone of the fuel injector, have been extensively studied (see chapter 3 for more details). Another injector type, which is used for completely different application range, is the following water sprayer.

1.3 Water spray systems

Another twin-fluid injector of relevant importance is the water spray injector, that has been recently used in many industries such as, petrochemical, thermo-electrical, automotive, biological, among others. Cooling is achieved by spraying a cooler liquid that absorbs and carries away heat, in which usually, the liquid is sprayed-assisted with steam. Heat energy is transferred to the coolant either by warming it or by evaporating the liquid into a gaseous state. The water latent heat capacity (energy to change water from liquid to gas) and the water specific heat capacity (energy needed to warm the water in its liquid phase) are both high compared to most other fluids. These thermal properties of water make it a useful coolant. A typical arrangement e.g., in turbine applications, a steam-water air-cooling device is shown in the fig. 1.4.

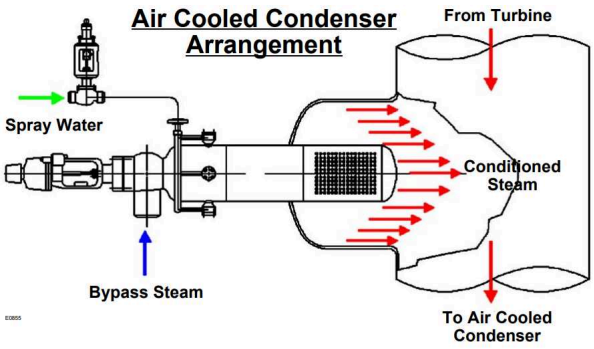

Figure 1.4: Air-cooled-system [11].

On the figure above, the application was designed for steam conditioning, the case corresponds to a typical heat recovery device in a power plant, however, there are other scenarios when waste heat is not utilized thus, cooling of flue gases in special cooling chambers becomes necessary. The two most common methods of gas cooling are by dilution with ambient air, and by evaporation of water in the gas stream [29]. In this research project, we will focus on the latter method. Therefore, flue gas efficiency depends on the location, type and maintenance of the spray nozzles. Correct nozzle selection is then of critical importance, as the properties

of the spray will determine how quickly heat is absorbed and where the spray will reach within a given gas flow. Moreover, the rate of evaporation will depend on the average droplet size of the spray i.e., smaller droplets will evaporate far more rapidly that sprays containing larger droplets. It is also true, whilst sprays consisting of very small droplets will absorb heat faster, they will also become entrained within gas flows more easily. This means that if the spray dispersion is too fine, it may only cool a channel within a gas flow rather than the whole gas volume. So there is often a balancing act to be performed between getting sufficiently small droplets to achieve rapid heat transfer and have the adequate spray dispersion to distribute it evenly, as can be seen in the fig. 1.5. For instance, the temperature distribution within the flue gas line (Grey pipe in the figure), can be greatly disturbed by the location, momentum, and spray characteristics of the water sprayers.

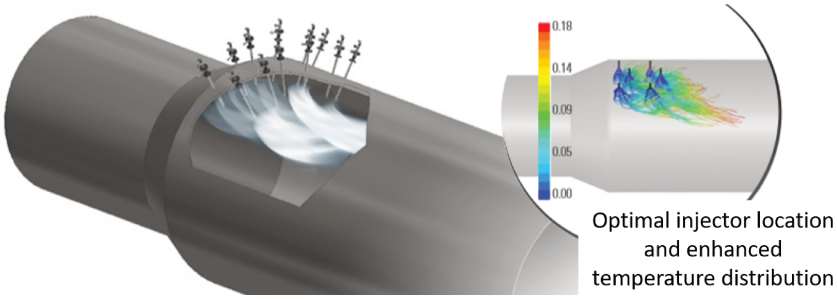

Figure 1.5: Water Spray dispersion effect in Gas cooling [12].

In many applications, the amount of gas that needs to be cooled can vary, depending on operating conditions. Additionally, variable cooling loads, present problems for spray cooling, because lowering the amount of coolant spray will typically mean lowering fluid pressure, which will increase the droplet size and thus increase evaporation time. This means that in lower gas flow scenarios, cooling may not be achieved in time, or may need a deliberately larger chamber. There are a number of ways in which nozzle selection, can help overcome variable gas flow cooling problems. For instance, the air atomizing systems, which can be used with variable air and fluid pressures to maintain smaller droplets at reduced flows. Additionally, multi nozzles arrays can be deployed, to a given variable flow at stable droplet sizes.

1.4 Project objectives

The French enterprise Vinci Technologies®, manufactures and provides a broad range of laboratory equipment, and specific field instrumentation for the Oil and Gas Industry. A portion of them, is developed in close collaboration with *IFP Energies nouvelles*. One of its goals, is to design and build durable, reliable, high-efficient and low maintenance FCC Injectors. To that end Vinci Technologies®, and the research institute CORIA (by its French acronym, Complexe de Recherche Interprofessionnel en Aerothermochimie), have begun a collaboration, by this 3-years project. There are two injection systems to numerically evaluate, namely, the FCC Injector and the Water Spray nozzle. When it comes to the FCC Injector, several studies have shown the paramount influence of the feed injection system on FCC Reactors [30] [31] [25]. Hence, the global FCC Reactor efficiency is improved by optimizing the feed atomization zone [8] [32]. Within the FCC Nozzle, the oil flows co-currently along with the steam, to promote the necessary fluidity and turbulence required for mixing, and possibly vaporization before the mixture gets atomized as soon as it exits the injector. As it can be recognized, just a few investigations have been made on the feed atomization zone and moreover, just a few within the FCC Nozzle. On the contrary, CFD modeling and experimental ground-breaking research in the automotive industry has recently emerged over the last decades. For instance, primary atomization has been extensively studied be several authors [33, 34, 35, 36],

nevertheless, turbulence disturbances within nozzle were missing. Non-evaporating diesel fuel spray measurements were compared with VOF phase-fraction based interface capturing method [37], in which well-resolved Large Eddy Simulation (LES) and subgrid-scale modeling were used for inside and near nozzle flow, respectively. However, first and second order time discretization schemes showed up some numerical issues, that the Volume of Fluid (VOF) model can not overcome due to grid resolution restriction outside of the nozzle. Therefore, passage modeling from segregated and dispersed flow regimes cannot be neglected [38] (more detail about this topic will be given in chapters 2 and 3). Transition from primary to secondary atomization is found even more challenging. Small-scale droplets not captured by direct numerical simulation (DNS) nor Interface Capturing Method (ICM) i.e., mainly due to mesh resolution and CPU time limitations, are numerically modeled as a mass transfer to the gas phase. Thus, the Lagrangian method is used instead, to modelise the small liquid ligaments or structures not captured by subgrid modeling using LES. Several switching criteria from Euler to Lagrange already exist [38, 39, 7] (more detail about this topic will be given in chapter 4).

These atomization scales are found externally i.e., at the exit of both FCC and water spray injector, and some of them are found internally, depending on the operating conditions. It is the purpose of this project to propose a numerical strategy, using CFD, to study the flow within a chosen FCC and water spray injector, in order to know the key parameters that influence its performance on certain variables of interests, for instance, turbulence mixing, droplet diameter, droplet surface interface, among others. To accomplish such tasks, numerical development and validation steps of the discretized Navier-Stoke equations, for liquid turbulent jets, against experimental and DNS data already available, are planned.

1.5 Outline

This research project is systematized in five chapters, organized as follow:

Chapter 2:Atomization: theory and modeling

This chapter, describes the atomization theory, which is a especial case of two-phase flow. Firstly, the two-phase flow is characterized for turbulent liquid jet atomization purpose i.e., primary and secondary atomization, physical scales, turbulence, among others physics, are detailed. Secondly, experimental techniques applicable to two-phase flow are reviewed. These experimental techniques, are the one used on the experimental data available, that will be later employ for comparison and validation purpose in the following chapters 3, and 4. Finally, a state of art modeling approach on turbulent liquid jets, is presented.

Chapter 3: Dynamic multi-scale spray atomization model.

This chapter constitutes the development and validation procedure of the coupling between two interface topological regions in the atomization of turbulent liquid jets i.e., resolved and unresolved interface. To that end, the coupling of an Eulerian-Lagrangian Spray Atomization (ELSA) model and an Interface Capturing Method (ICM), is assessed based on several criteria, such as, mesh-based, and gas-liquid surface interface criteria. Lastly, a validation procedure will be carried out, employing experimental data already available by the Engine Combustion Network (ECN).

Chapter 4: Transition from multi-scale approach to dispersed phase

This chapter gives the details of WBE modeling (solved by a Lagrangian formalism) for the dispersed flow region of turbulent liquid jets. Additionally, a coupling strategy is proposed between the dispersed and multi-scale approach (chapter 3). Two specific aspects are approached: droplet turbulent dispersion and the Lagrange droplet production and characterization from

the Eulerian field i.e., droplet velocity and diameter at the mixing layer of liquid turbulent jets. Firstly, a literature review will be made for existing turbulent dispersion models, followed by an implementation of an enhanced turbulent dispersion model in the numerical software OpenFOAM® , namely a Stochastic Differential Equation ($\boldsymbol{SDE}$). Secondly, several droplet injection methods at the turbulent mixing layer are examined. Finally, the model performance is compared with experiments, DNS, and previous LES data available.

Chapter 5: Industrial liquid jets application

This chapter is about the application of the physical models developed and validated in the previous chapters 3, and 4. As previously mentioned, there will be two injectors, completely different from the physical point of view, namely the FCC Injector and the Water Sprayer. To that end, the previous validated model in chapter 3 will be applied.

Chap. 2 | Atomization: theory and modeling

This chapter, describes the atomization process in general, which is a especial case of two-phase flow. Firstly, the liquid surface instabilities are detailed. Secondly, experimental limitations in spray measurements with high Weber and Reynolds number are highlighted. Thirdly, the two-phase flow is characterized for liquid jet atomization purpose i.e., primary and secondary atomization, physical scales, turbulence liquid jets, among others physics, are detailed. Finally, a state of the art modeling approach on turbulent liquid jets, is presented.

2.1 Multiphase approach

Commonly, the term *multiphase flow* is used to refer any fluid flow consisting of more than one phase or component [40]. One could classify them according to the state of different phases or components (gas/solids flows, or liquid/solids flows or gas/particle flows or bubbly flows and so on). In the context of this thesis, only two-phase flow is considered i.e., a liquid and a gas phase, separated by a well defined liquid-gas interface. Therefore, two topologies can be identified, namely *disperse flows* and *separated flows*.

Disperse flows, consist of well defined particles (disperse phase), distributed in a connected volume of continuous phase. The coupling between the particle and its surroundings can be used to classify and choose the appropriate numerical technique. As shown in the figure 2.1, a multiphase flow can be considered *dispersed*, if the effects of particle-fluid interactions dominates the overall transport of particles. On the contrary, if particle-particle motion dominates, the flow can be considered to be *dense*. *Dispersed* flow, will generally include one-way coupling (where the dispersed-phase motion is affected by the continuous phase), two-way coupling (in which the dispersed-phase also affects the continuous phase), three-way coupling (in which particle wakes, and other continuous phase disturbances, affect the particle motion), and four-way coupling (where particle collisions, and particle-wall interactions dominate the particle motion). *Dense* flow, in this case, can be considered a special case of four-way coupling (e.g., granular flow).

Regarding dispersed flow in sprays, they can be divided into two regions, namely *dilute* and *dense* flow, depending on the relevance of droplets-droplets interactions and the possibility and frequency of droplet-droplet collisions. Therefore, at low droplet concentration (*dilute* flow), droplet motion is influenced by the continuous phase. However, at high droplet concentration (*dense* flow), droplet size distribution and motion are mainly governed by droplet-droplet collisions. In sprays, the are close to the atomizer is typically a *dense* spray, as here the number concentration of droplets is high, while with an increase in distance to the atomizer, due to the spreading of the spray cone, droplet collisional effects decrease and transition to dilute flow is achieved [13].

From the numerical point of view, there are two modeling approaches prevalent in disperse flows, namely *trajectory models* and *two-fluid models* [40]. In the former, the motion of

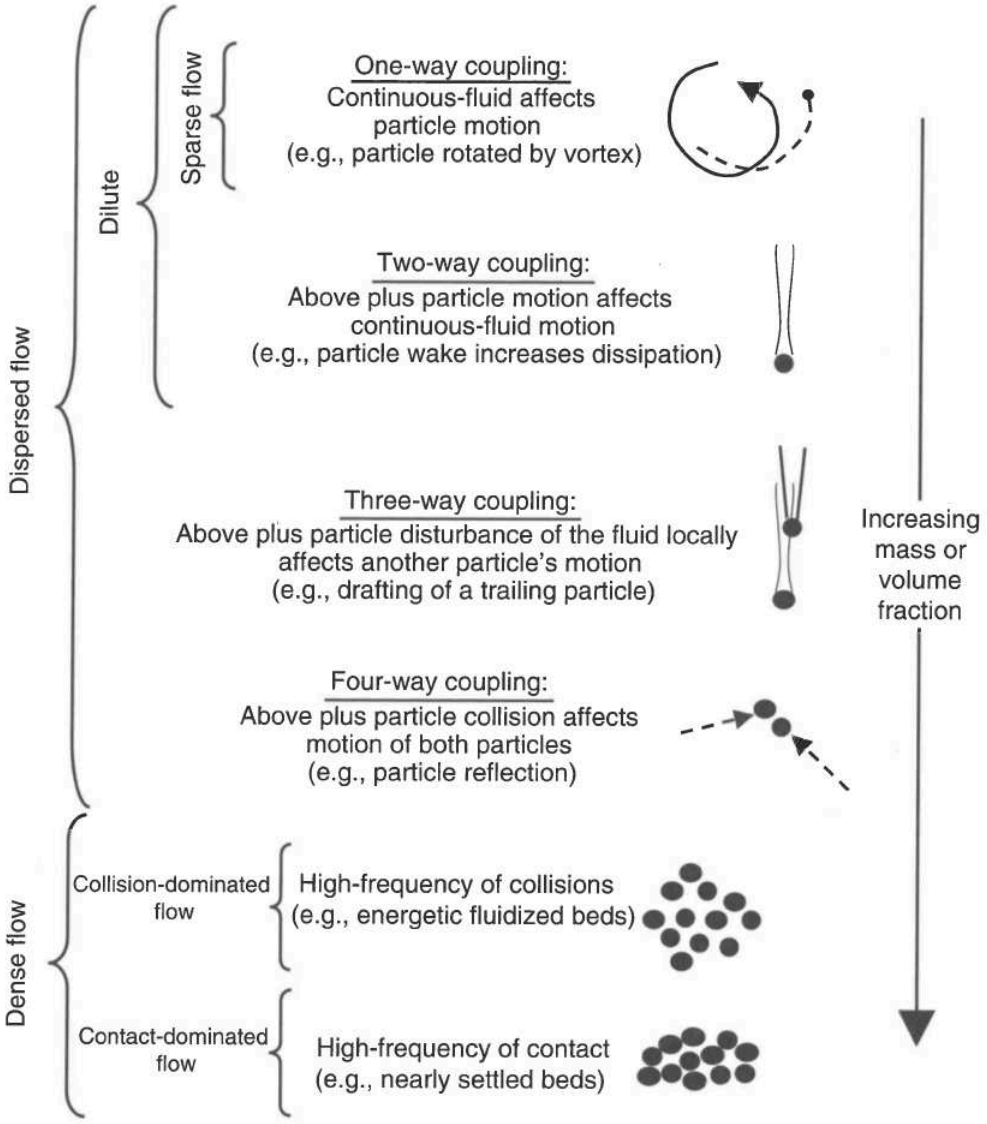

Figure 2.1: Dilute, dispersed, and dense flow conditions based on various interphase coupling [13].

the disperse phase is assessed by following either the motion of actual particles, or larger representative particles. In this case, a discrete method, normally referred to as Lagrange method, is applied on each droplet (or representative droplet), in which droplet properties are update along the path of an individual (or cloud of) droplets. In the latter modeling approach, *two-fluid models*, the discrete phase is treated as a second continuous phase on which conservation equations (of mass, momentum and energy) are developed for the two-fluid flow. This modeling approach, is also referred as multiphase approach, in which an Eulerian treatment describes the droplet concentration through a droplet volume fraction, which is the fraction of computational cell composed of droplets. Treatment selection is highly dependent on the droplet number density, N_p, see figure 2.2. Normally, Lagrangian treatment is preferred for nondeforming droplets, in which high accuracy of the interface discontinuity is desired, however, the Eulerian treatment is more efficient in terms of droplet breakup or coalescence. There is a third approach, which uses particle distribution functions (PDF approach), to describe the particle flow properties in stochastic systems, based on the well-known Maxwell-Boltzmann equation [41, 42]. More information about the Lagrangian, Eulerian, and PDF treatment on droplet field can be found in [13, 40].

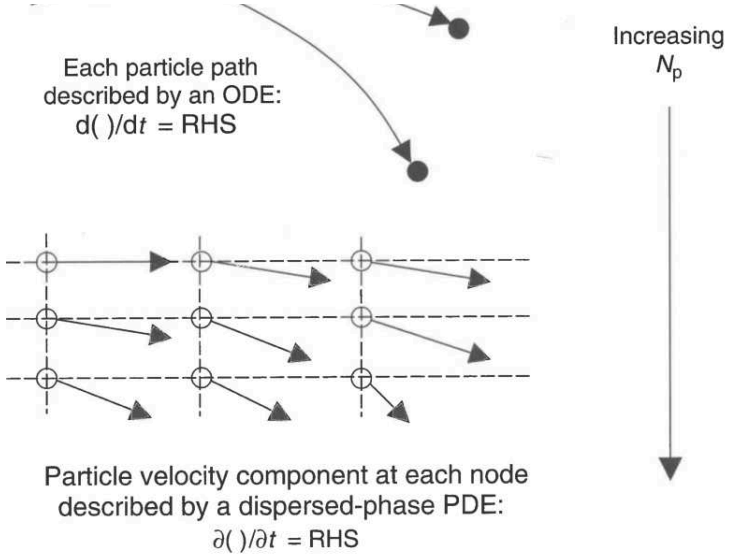

Figure 2.2: Lagrangian approach defined on droplet centroid (Top). Eulerian approach defined on Eulerian computational nodes (Bottom) [13].

On the other hand, *separated flows* consists of two continuous streams of fluids separated by a well-defined interface. In turbulent liquid jets, *separated flows* are found close to the exit of the nozzle. There are several modeling approaches to compute the interface motion. Front Tracking Methods [43], Volume of Fluid Methods [44] and Level Set methods [45], are the most common numerical strategies used to predict interface motion. Front Tracking Methods, are based on the Lagrangian approach of marker particles, that are attached to the interface motion, however, is numerically limited for 3D geometries, especially for the distribution of the marker particles when irregularities occur on the liquid-gas interface. Volume of Fluid Methods (VOF), are based on the description of the volumetric fraction of each phase in grid cells. The main difficulty of the method is that 2D interface reconstruction, is quite difficult, and 3D reconstruction is numerically prohibitive. A consequence of that, is the uncertainties on the interface curvature thus, on the surface tension forces. The basis of the Level Set methods (LS), has been proposed by [46], in which the interface is described with a zero level curve of a continuous function, defined by the signed distance to the interface. Nevertheless, it is well known that, can numerically generate mass losses in some regions. This is the main drawback of level set methods. Finally, to describe the interface discontinuities, two approaches can be used, namely the Continuous Force Formulation (*delta* formulation), which assumes that the interface is $\mathbf{2}$ or $\mathbf{3}$ grid meshes thick, and the Ghost Fluid Method (GFM), which has been derived by [47], to capture jump conditions on the interface. The GFM approach, not only avoids the introduction of fictitious interface thickness, but provides also a more accurate discretization of discontinuous terms hence, improving the resolution on the pressure jump condition [48, 49, 50]. More than a decade ago, improvements have been obtained by combining VOF-LS methods (i.e., the so-called CLSVOF), in which interface tracking is performed by level set method, the ghost fluid method is used to capture accurately sharp discontinuities, and the level set and VOF methods are coupled to ensure mass conservation [51, 34, 34].

Hybrid regimes, namely both *disperse* and *separated* flows, are formed when the interface between liquid and gas becomes highly deformed and droplets might be generated, which normally occurs in turbulent liquid jets. Consequently, it is not straightforward to define a *discrete* phase and a *continuous* phase, as it is normally requested by multiphase flow approaches. Indeed, just at the exit of the injector nozzle, the amount of liquid phase is very high, and cannot be decomposed as set of discrete particles. Moreover, bubbles could

be present in the liquid flow due to penetration of the surrounding gas during the breakup process, and to previous cavitation inside the nozzle injector also. Following, the continuous phase would be the liquid and the discrete phase, the gas bubbles. On the contrary, further downstream, a dispersed spray is created, in which the continuous phase is gas and the discrete phase, corresponds to droplets. Between these two limits, a two-phase flow exists with unclear discrete and continuous phase [52]. Detailed information about this regime is found in chapter 3.

Finally, atomization by definition is the process of converting a liquid form to a free gaseous atom. In other words, it is the transformation of a bulk liquid into a spray of droplets in a surrounding gas or vacuum [53]. Conclusively, three different zones in turbulent liquid jets, can be easily defined in figure 2.3. The first region near the tip of the injector is called primary atomization (explained in detail later). In this area the liquid volume fraction is close to one and the liquid surface topology is very complex. Here the liquid sheets experience longitudinal instabilities based on liquid and gas interactions (Kelvin-Helmholtz instabilities) which disturb the plane sheet in a sinusoidal stream-wise oscillation mode. The second region on top of the figure is called secondary atomization (also explained in detail later), begins downstream of the flow, where instabilities turn into three dimensions, and the sheet breaks into smaller liquid packs, ligaments and bag-like structures. This zone ends with the formation of a spray of droplets, namely *dispersed* zone/region/phase [54]. Detailed information about *dispersed* zone is found in chapter 4.

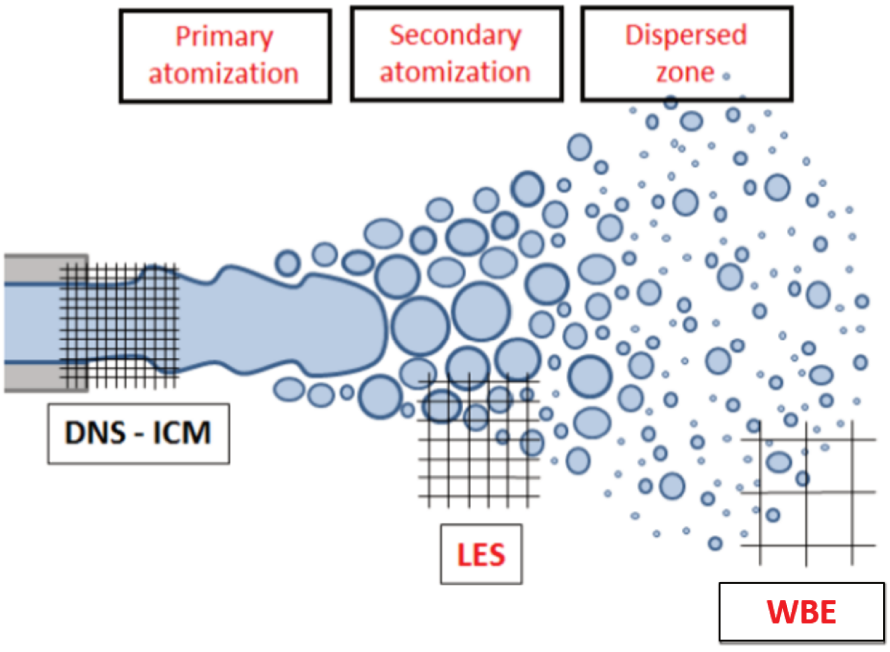

Figure 2.3: Atomization zones.

2.2 Experimental observations

Experimental two-phase flow observations, within the near field injector, are presented. Firstly, surfaces instabilities can be observed using relative low liquid injection velocities. Secondly, recent experimental advancements made it clear the dominant liquid core, at the exit of the injector, as shown in the figure 2.4 for a coaxial liquid jet, in which the liquid is surrounded by a annulus gas flow with higher velocity. On the experimental figure, it is visualized the Kelvin-Helmholtz instabilities [55] due to the initial aerodynamic high shear stress between the liquid and gas, hence the first liquid waves are formed. Later on, irregularities on the interface start to grow based on the density ratio i.e., Rayleigh-Taylor instabilities can be inferred, thus perturbations are expected to increase exponentially and the instabilities are no longer two-dimensional. On the bottom part of the figure, ligaments are broken up into droplets, which is a Rayleigh-Plateau instability. The Rayleigh-Plateau instability is defined by two factors: the growth rate of the perturbations and length scale over which the instability grows [56].

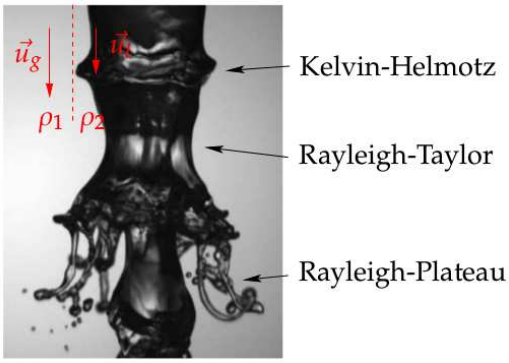

Figure 2.4: Liquid jet instabilities visualization [14].

It is to be remarked, that the experimental conditions used to characterize the liquid/gas interface instabilities shown on the figure, were far from the one used in industrial injectors, in which the liquid Reynolds and gas Weber numbers, defined below, are a lot higher.

$$\begin{cases} Re_l = \dfrac{\rho_l U_l d_l}{\mu} \quad , \\ We_g = \dfrac{\rho_g (U_{rel})^2 d_l}{\sigma} \quad , \\ M = \dfrac{\rho_g (U_g)^2}{\rho_l (U_l)^2} \quad , \end{cases} \tag{2.1}$$

where, M, is the momentum flux ratio per unit volume. This quantity is an important parameter [57], especially in coaxial jets. Considering an hypothetical case, in which gas velocity were higher, thus stronger shear stress exists. The Kelvin-Helmholtz instabilities would grow faster and smaller liquid structures would be developed close to the exit of the nozzle. Therefore, for experimental measurements, become even harder to assess the two-phase flow morphology and measurements uncertainties increase within near flow field. Two decades ago, some interesting experimental findings were made available while varying Reynolds, Weber, and Mass flux ratio [3]. Figure 2.5, displays instantaneous images of the near-field regions of the breakup of a round water jet by a high-speed annular air jet, under different operational conditions (see the table 2.1, below).

Table 2.1: Operational conditions used in figure 2.5 [3].

Cases	U_g $[m/s]$	M	We_g	Re_g
a	15.75	3.8	16	850
b	21.7	7.35	31	1120
c	28	12.2	52	1450
d	40.6	25	110	2100
e	21.7	2.05	31	1120
f	40.6	7	110	2100
g	56	13	210	2900
h	85.4	31	489	4400

Liquid velocity and Reynolds were kept $U_l = 0.33\ m/s$, $Re_l = 1250$, respectively. Surface tension clearly dominates the near-field breakup in figure 2.5 for cases a, b, and c, but qualitatively, seems to play a minor role in figure d. Fiber-type ligaments begin to form in case d, and they are observed to be broken into drops, via a Rayleigh-type capillary breakup mechanism. In figure 2.5 from cases e to h, similar images are displayed, however, with the air velocity going up to $85\ m/s$ ($Re_g = 4400$) and for a water velocity $0.58\ m/s$ ($Re_l = 2230$). These fibers are also seen to decrease in size as the gas Weber number is increased. However, increasing the air velocity for a given water velocity increases not only the gas Weber number but also momentum flux ratio M. Looking at the same gas Weber number We_g, but for different values of M (cases b and e), it was found the following: at lower M, an intact liquid core persists further downstream (case e). On the other hand, when the gas Weber number is large (cases d and f), the momentum flux ratio M is, therefore, the crucial parameter in determining the liquid core length (or liquid intact length).

2.2.1 X-Ray radiography: Industrial nozzle application

Experimentally speaking, there are some drawbacks such as the measures on a dense gaseous atmosphere, surrounding the liquid core, related to engine operating conditions (e.g., high temperature and pressure), which are difficult and expensive to replicate in a laboratory scale. In another example, within the far field of two-phase flow, the Phase Doppler Anenometry (PDA) is a experimental technique normally used for droplet size and velocity measurements, specially for the secondary atomization. One drawback in this technique, is that droplets interaction can not be captured. On the other hand, recently, there have been quite a few advancements in technique measurements, specially within the near flow field, such as: Laser Correlation Velocimetry (LCV) [58], balistique image [59], X-Radiography [60], among others. The latter, X-ray radiography, has been developed as a spray diagnostic tool that specializes in measuring the density in the spray formation region [61]. The results obtained by means of this experimental technique [61], were used for comparison purposes in this work. Since the main interaction between X-rays and fuel spray is absorption, this technique allows for quantitative measurements of fuel density in the dense spray region. Comparisons have also been made with the near-field dense spray structure (spray boundary) between the light-based optical microscopy and X-ray radiography [62].

2.2.2 Image technique: Diesel injector application

Although a number of optical techniques are commonly used for the study of fluid motion on small scales and at high velocity, the most are not suitable for the study of diesel injection that produces a flow optically dense. Indeed, single-point techniques, such as laser Doppler velocimetry and other related methods [58] are based on properties of spherical droplets which make them not usable in the near field of the injector. Laser correlation velocimetry (LCV) is

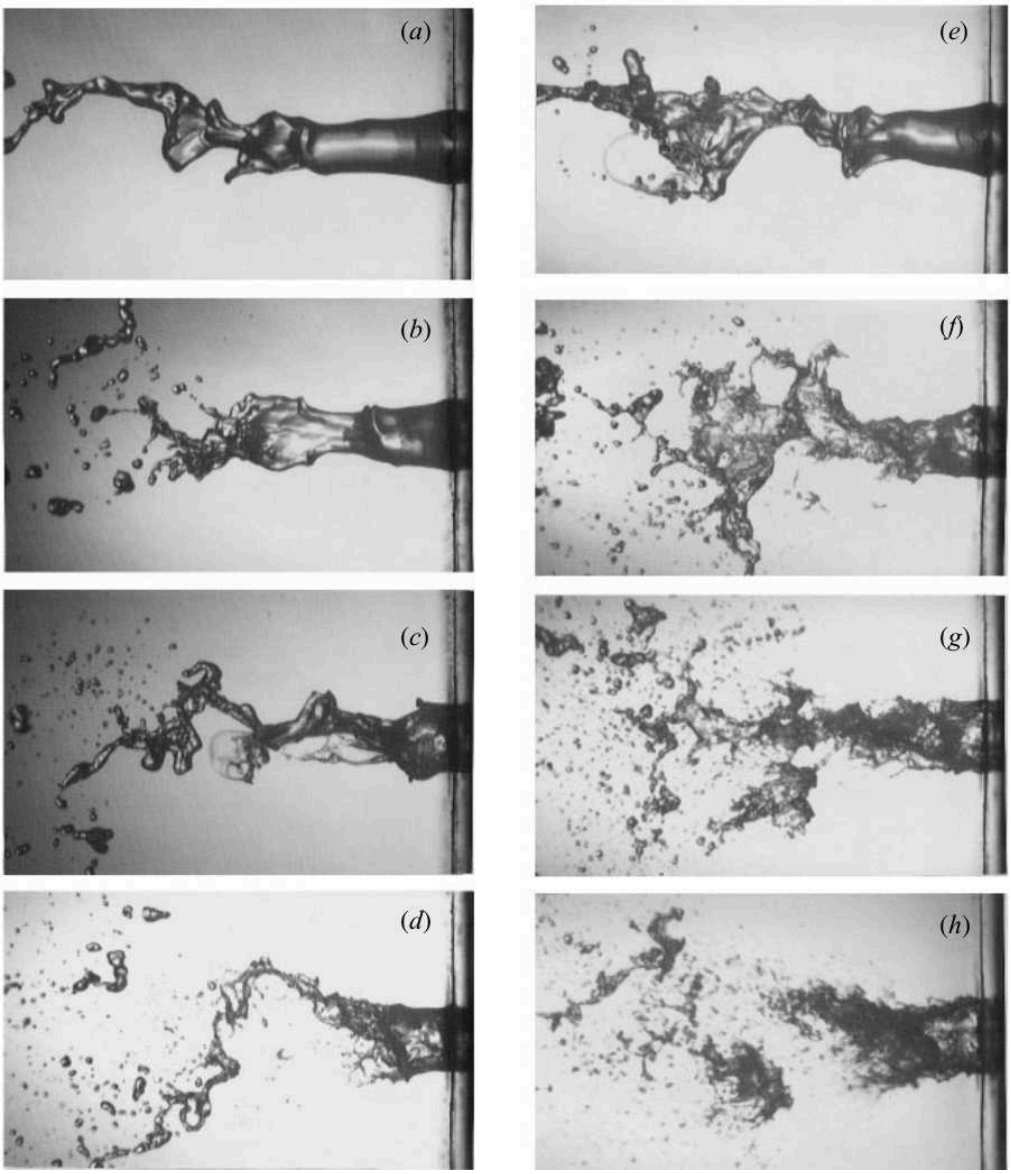

Figure 2.5: Instantaneous flow visualization of the break-up of the liquid jet by annular air jet [3].

a local velocity measuring technique which has proved applicable to flows with high optical thickness [63]. However, the interpretation of the LCV information requires consideration of various parameters (distance, time of flight, time window size, etc.) making the measurement complicated. Particle image velocimetry (PIV), the most used imaging technique for velocity measurement, requires that the region of interest is seeded with particles [64]. This technique has been successfully used to measure the velocity of gas flow around the spray, but it is difficult to use this technique on the jet itself. One useful technique developed for industrial Diesel injectors, in the near-field region of practical fuel-injection sprays (which generally require high injection pressures (>100 MPa) and small nozzle orifice diameters (100 μm)), is the high-resolution imaging technique, as shown in the figure 2.6.

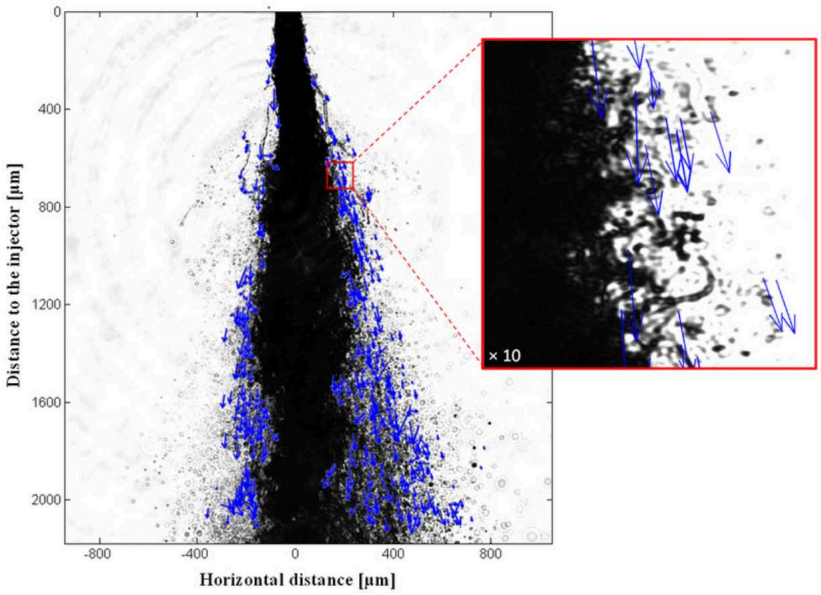

Figure 2.6: Spray image with displacement vectors estimated from the time-correlated image-pair [6].

The idea is to get velocity field information from spatially resolved regions of spray images by identifying and correlating image features in successive time-resolved image-pairs. This procedure is selectively applied over the spatial extent of the image-pair, yielding a map of displacement vectors describing fluid motion [6]. The velocity data and shadow images of the diesel spray used in the analysis were obtained by ultrafast imaging, which provides high-resolution visualization of the spray edges and droplets. The results obtained by means of this experimental technique [6], were also used for validation purposes in this work.

2.3 Liquid jets: theoretical background

Technically, there are many ways to atomize a liquid jet e.g., by means of the liquid kinetic energy, gas kinetic energy, mechanical and acoustical devices, among others. Atomization process is the mechanism that leads to increase the liquid-gas interface area. Liquid atomization has applications in numerous industrial branches, for instance, atomized fuel inside combustion chambers, liquid film atomizers, water spray for gas cooling/scrubbing applications, aerospace, pharmaceuticals, just to name a few. Atomization, by definition, leads to pulverization of the liquid jet into multiple droplets in which, eventually will become smaller and smaller. Within atomization, the pulverization / disintegration process itself is caused either by intrinsic (e.g., potential) or extrinsic (e.g., kinetic) energy, where the liquid, which is typically fed into the process in the form of a liquid jet or sheet, is atomized either due to the kinetic energy contained in the liquid itself, by the interaction of the liquid sheet or jet with a (high-velocity) gas, or by means of mechanical energy delivered externally (e.g., by rotating devices).

2.3.1 Liquid atomizers

For internal combustion engines, the purpose of an liquid injector is to introduce the liquid fuel into a combustion chamber and, at the same time, to favor the mixing of the combustive agent and the combustible, in order to optimize the conditions of combustion. In industry, at least two main configurations of injector can be distinguished [13, 65]:

- **Pressure or single fluid atomizers:** In these devices, high pressure forces the liquid to flow at high velocity through a small opening into a steady ambient atmosphere.

Velocity difference between liquid and gas leads to the disintegration of liquid until droplet clouds are obtained. This type of injectors are widely used in industries, such as agriculture, cosmetics, automotive motors or aeronautic motors. They have the benefit to be simple and cheap to manufacture. Droplet sizes can be controlled by adjusting the injection pressure: the higher the pressure, the smaller the droplets. On the other hand, the necessary energy to atomize the fluid increases very rapidly with the mass flow rate, which in some cases, economical analysis are needed.

- **Air-blast or twin-fluid or pneumatic atomizers:** These devices exploit the shear effect of an accelerated, pressurized air flow parallel to the fuel. Here, the atomizers with external and internal mixture of gas and liquid are distinguished. Within internal mixing atomizers, gas and liquid are mixed in a premixing chamber and the gas-liquid mixture is ejected from the atomizer orifice directly. In twin-fluid atomizer with external mixing, the gas interacts with the liquid outside of the atomizer. In principle, these mechanisms work at low relative speed and high air flow, as it happens for aircraft engines. Air-blast atomizers have the benefit that, for a given mass flow rate, less energy is necessary to atomize the liquid, in comparison with a pressure atomizers. Higher fuel flow rate can thus be obtained. It is nevertheless necessary to have a high velocity gas flow to obtain a satisfying mixing.

2.3.2 Atomization process

The atomization process can be split in three distinctive zones: primary atomization, secondary atomization and dispersed spray, as shown in the figure 2.7 below. For a first classification of liquid fragmentation in various configurations, the disintegration behavior of a liquid jet or sheet is subdivided into different atomization modes depending on the boundary conditions. As results of several investigations [13], the disintegration behavior of a liquid has been globally classified, regimes have been identified, and interfaces between the different regimes have been correlated.

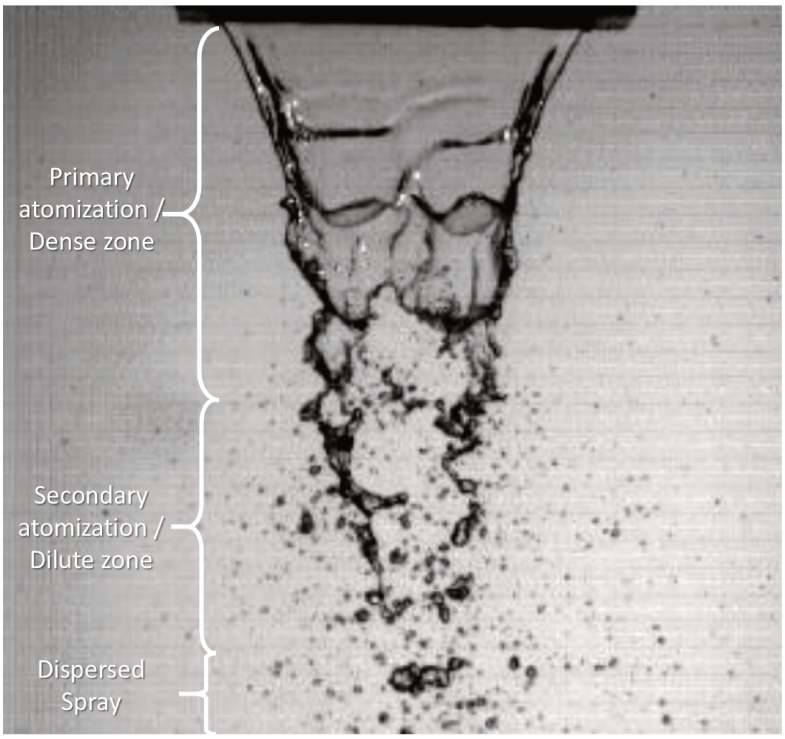

Figure 2.7: Air-blast atomizer of a planar liquid film [15].

Primary Atomization

For the case of a liquid emerging into a quiescent gaseous atmosphere e.g., pressure or single fluid atomizer, the interface regimes have already been detailed [66]. Some examples are illustrated in figure 2.8. It can be seen, at low Reynolds number, on the first image from left to right, the jet disintegrates due to surface tension effects i.e., *Rayleigh regime*, into fairly identical droplets sizes. At intermediate Reynolds numbers, drop formation is influenced by aerodynamic forces, namely the *aerodynamic regime*. Finally, at higher Reynolds numbers, the jet disintegrates almost spontaneously at nozzle exit. This mode is called the *atomization regime*.

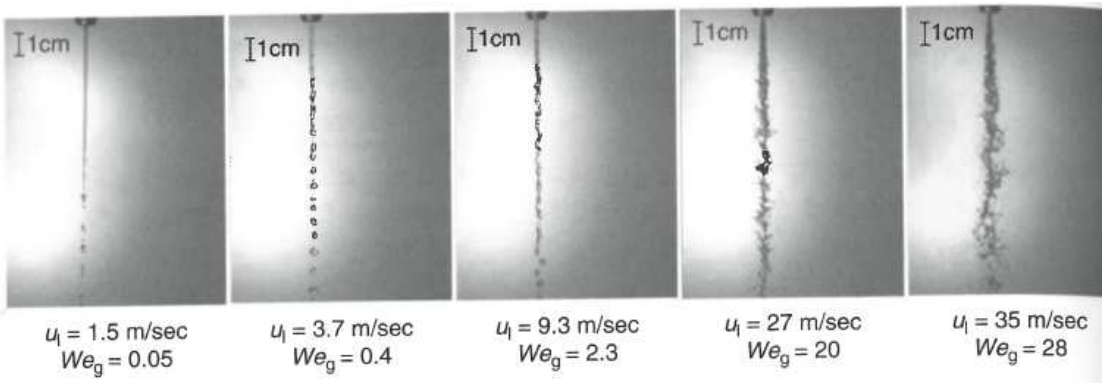

Figure 2.8: Disintegration of a liquid jet in a pressure atomizer [13].

This region where instabilities and first liquid detachments appear, is called primary atomization zone, also dense zone of the spray. In this thesis, there will be two atomizers, one pressure atomizer, in which X-ray radiography has been taken from previous experiments [67], and one air-blast atomizer, where fluorescence induced in the liquid phase by a pulsed laser sheet has been used to derive the near field of liquid volume fraction [17]. These two atomizers will be used for the numerical validation step i.e., along with Large Eddies Simulations (LES), which will be explained in detail and validated in the following chapter 3.

Secondary Atomization

Secondary atomization follows the primary atomization. It is defined as the disintegrations of larger droplets and ligaments into smaller droplets. There are five distinct mechanisms of droplet breakup as determined by the initial Weber number. They are categorized based on the gas Weber number We_g, and displayed in table 2.2.

Table 2.2: Breakup mechanisms based on gas Weber number We_g [4].

Vibrational breakup	$We_g \leq 12$
Bag breakup	$12 < We_g \leq 50$
Bag-and-stamen breakup	$50 < We_g \leq 100$
Sheet stripping	$100 < We_g \leq 350$
Wave crest stripping followed by catastrophic breakup	$We_g > 350$

These breakup mechanisms, are illustrated in the following figure 2.9.

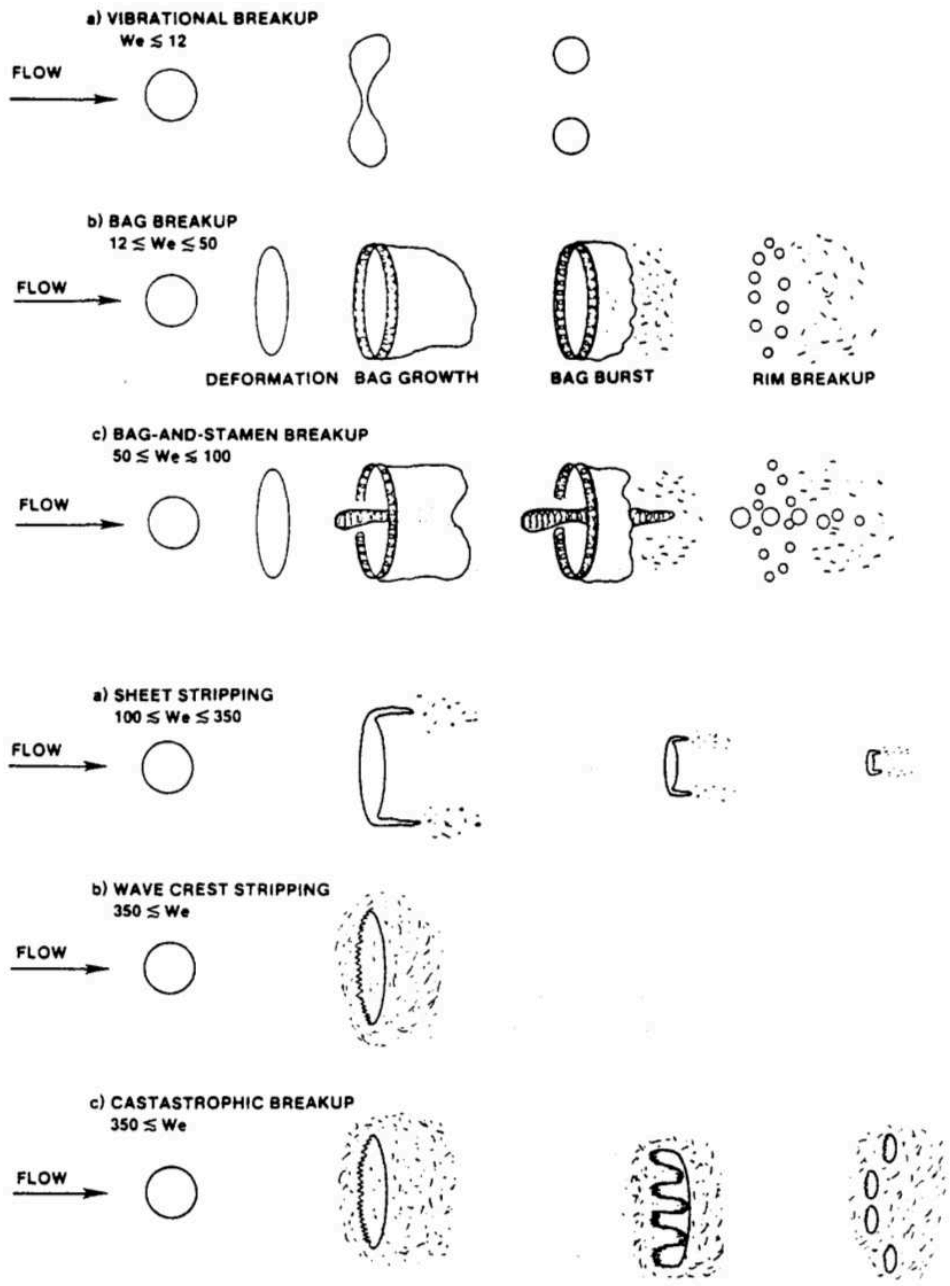

Figure 2.9: Breakup mechanisms [4].

- *Vibrational breakup*, can occur when the gas Weber number is small, oscillations develop at the natural frequency of the drop. Under certain conditions, the flow field interacts with the drop in such a way as to increase the oscillation amplitude, which in turn causes the drop to decompose into a few large fragments. *Vibrational breakup*, does not necessarily occur in every instance. This breakup mechanism, when it does occur, only produces a few large fragments, and the overall breakup time is long compared to the other breakup mechanisms. Consequently, *vibrational breakup* is not usually considered when drop breakup is studied.
- *Bag breakup*, is analogous to the bursting of soap bubbles blown from a soap film attached to a ring. A thin hollow bag is blown downstream, while it is attached to a more massive toroidal rim. The bag eventually bursts, forming a large number of small

fragments. The rim disintegrates a short time later, producing a small number of large fragments.

- *Bag-and-stamen breakup*, is a transition mechanism that has several features in common with *bag breakup*. As in *bag breakup*, a thin bag is blown downstream while being anchored to a massive toroidal rim, however, a column of liquid (stamen) is formed along the drop axis parallel to the approaching flow. The bag bursts first, rim and stamen disintegration follows.
- *Sheet stripping*, is distinctly different from the two breakup mechanisms just discussed. No bags are formed; instead, a thin sheet is continuously drawn from the periphery of the deforming drop. The sheet disintegrates a short distance downstream from the drop. A coherent residual drop exists during the entire breakup process.
- At still higher Weber numbers, large-amplitude, small-wavelength waves are formed on the windward surface of the drop. The wave crests are continuously eroded by the action of the flow field over the surface of the drop. This process is referred to as *wave crest stripping*. Large-amplitude, long-wavelength waves ultimately penetrate the drop creating several large fragments before *wave crest stripping* can significantly reduce the drop mass. Drop penetration by large-amplitude surface waves is referred to as *catastrophic breakup*. *Catastrophic breakup*, leads to a multistage process in which fragments, and fragments of fragments, are subject to further breakup. This cascading process continues until all the fragments have gas Weber numbers below a critical value.

Finally, liquid structures leaving the primary atomization area, may interact between them. Two typical interactions are coalescence and collision. In the coalescence case, two liquid structures encounter each other and are unified to form a single entity. In the collision case, the two structures have different velocities and encounter each other in a more violent way, that could eventually provoke their breakup i.e., the creation of smaller structures [68, 69].

Dispersed Spray

Further from injector, liquid structures do not interact each other any more (or very weakly). At this scale, surface tension prevails. This zone is called dispersed spray. The analysis of spray behavior is divided into two regions, depending on the relevance of droplet-droplet collision and the possibility and frequency of droplet-droplet collision, namely dilute and dense spray region. Therefore, at low droplet concentration (dilute flow) particulate transport is mainly determined by fluid dynamic interactions of individual droplets with the continuous carrier phase (e.g., drag, lift, etc.). At high droplet concentration (dense flow), the influence of particle collision affects the movement of the droplets and the droplet size distribution [13]. In this thesis, a first attempt was made, using a dilute flow assumption, to couple Euler-Lagrange equations to model the spray development, from the exit of the nozzle to the far field flow. Chapter 4 will explain the Lagrangian approach more in depth.

2.3.3 Liquid spray modeling

Several strategies can be found in literature to model fuel injection and to cope with the multi-phase / multi-scale nature of the flow within FCC Nozzles. A full resolution of the interface thanks to direct numerical simulation (DNS), either Interface Capturing Methods (ICM) or/and reconstruction methods [52, 34, 35, 36], becomes unfeasible as far as industrial applications are concerned, due to high computational costs. Moreover, the notion of DNS when an interface is considered must be approached with special care.

In any event, atomization modeling is necessary. Many approaches are based on kinetic theory, where the spray is described through a number density function, that verifies the Williams-Boltzmann Equation (WBE) [70], containing terms for spatial transport, evaporation

and fluid drag. A widely used approach to solve the WBE, is the Lagrangian-Monte-Carlo method [71], where the liquid is tracked with a Lagrangian description and the gas is solved in an Eulerian framework. Its advantage lies in a straightforward implementation of physical processes e.g., evaporation and secondary break-up, even if its computational cost is generally challenging, especially in unsteady configurations. Indeed, a high number of parcels is required in each cell of the numerical domain, to reach statistical convergence. Another approach to solve the WBE, is to consider a Euler-Euler (EE) formulation, where both phases are treated as a continuum. This solution is very attractive to describe the evolution of the spray characteristics. Moreover, reduced computational costs and high capabilities in terms of parallel computing are among the advantages of this formulation. These features are even more prevalent, considering the growing use of resolved scale techniques, such as Large Eddy Simulation (LES), to achieve a physical description of the gas flow field.

However, despite the efficiency of EE methods on actual super-computers, the direct resolution of WBE is generally infeasible, since the dimension of the problem is multiplied by the number of spray characteristics (position, velocity, size, temperature, etc). This feature constrains EE methods, to only address a limited description of these properties. The numerous possible hypotheses, have led to an abundant research in this framework. For instance, in Multi-Fluids models [72, 73] the droplet geometry information is discretized in sections to represent the spray distribution. Another solution [74] is a smooth reconstruction method, based on a sum of kernel of the density functions and a quadrature method of moments, employed for this purpose. Nevertheless, all these methods based on WBE, assume generally that the spray is composed by numerous individual spherical droplets with well-defined features as position or diameter, which is far from being the case with atomizers generally employed in an industrial framework. Indeed, the liquid phase is initially a continuum (i.e. liquid jet or film) and it is not possible to define such well-defined characteristics until the end of primary breakup.

2.3.4 Single-fluid approach

In single-fluid models, only one set of governing equations is used for the whole two-phase flow. Therefore, the two-phase flow can be regarded as a single-fluid flow, with a single velocity and a single pressure, composed of two species. Distinction between carrier and discrete phases is avoided and the topology of the interface between the two phases is determined as part of the solution. Let us describe, the two types of single-fluid models used in this project.

Unresolved interface model: ESA

A more general description of the two-phase flow has been developed by Vallet and Borghi [1]. In this model, the boundary separating pure liquid and pure gas, is considered as a mixing zone so, both liquid and gas phases coexist at the same macroscopic position, with an occupied portion of volume defined by the liquid volume fraction (α_l). In this context, two family of equilibrium models have been developed. A first possibility [75], is to use the liquid volume fraction as the unique variable, allowing the description of the interface when is resolved. On the contrary, another set of approaches are used, which are based on a transport equation for the liquid/gas interface density [52, 1].

In this model, the Eulerian-Lagrangian Spray Atomization (ELSA) models are of major importance [52, 1]. From this work, different models based on Eulerian modeling for atomization have been studied. Later on, Blokkeel et al. [76] working with the same team, completed the original approach by a Lagrangian description of the spray once the primary break-up is achieved. In addition, they proposed to call this approach ELSA, which stands for Eulerian-Lagrangian Spray Atomization model, however, other names are still in use e.g., $\Sigma - Y$, $\Omega - Y$ or ESA, depending on which variable has been retained or whether the Lagrangian phase has been activated or not. An extension to LES, has been carried out by Chesnel et al. [77].

Moreover, a new model has been attached to this approach, namely, Quasi-Multiphase Euler (QME) [78, 50], to account for a slip velocity between phase. Indeed, despite the unique, mixture velocity flow, a phase velocity can still be acquired, by considering phase fluxes with respect to the flow velocity. This idea is also known as the *drift model* in the literature. All in all, they belong to the ELSA family models, that try to consider and to model the two main terms that drive the atomization process for non-fully resolved cases, hence the subgrid/unresolved turbulent liquid flux term $\boldsymbol{R}_{ai}$, and the unresolved liquid/gas interface density, that will be characterized in this work by Σ' (liquid/gas interface area per unit of volume).

Resolved interface model: ICM

The ICM (interface capturing method) model, is VOF (volume of fluid) phase-fraction based, giving an implicit representation of the interface. This model is one of the first interface capturing method to have been developed. It is based on mass conversation principle [79]. Initially, volume fraction of liquid (or gas) is distributed over the whole computational domain, then transported by the velocity field.

VOF methods, are robust regarding topological changes, since they are implicit. Volume conservation is guaranteed by transporting volume fraction, but if mesh is not fine enough, parasite effects may occur in singular zones. This phenomenon, called numerical surface tension [80], seems unavoidable with Eulerian formalism, in which interface structure width is of the same order than cell size. The ICM is thus poorly adapted for dispersed flows unless the mesh is fine enough, but it can lead to prohibitive computational costs. Another drawback in VOF method, is the difficulty to compute geometric characteristics of the interface (normal $\mathbf{n}$ and curvature $\mathbf{K}$). A balance equation for the liquid volume fraction will provide the location of the interface, but any information regarding its geometric characteristics explicitly, will be missing. It is thus necessary to use interface reconstruction methods.

One of the first interface reconstruction method to be proposed, is the SLIC (Simple and Line Interface Calculation) method [81]. In this method, considering a Cartesian mesh, the interface is approximated in each cell, as segments (or planes in three dimensions), aligned with one of the mesh coordinates. This direction depends on flow direction. The PLIC (Piecewise Linear Interface Calculation) [82], is more accurate than the SLIC method. In PLIC, an interface within a cell is approximated by a segment with a slope determined from the interface normal. The resulting fluid polygon, is then used to compute fluxes through any cell face. An alternative to geometric reconstruction algorithms, is to avoid interface reconstruction by using an interface sharpening approach. Its principle lies on correcting the numerical diffusion of liquid volume fraction in the advection equation, with a sharpening term. This sharpening approach, benefits from a high resolution differencing schemes to calculate volume fluxes [83]. Additionally, its numerical implementation on arbitrary unstructured meshes, is quite straightforward. This approach, is used in OpenFOAM® solver [21, 22], namely `interFoam`. Equations of this treatment, will be more detailed in chapter 3. Historically, VOF method has been recently used for simulation of primary atomization in air-blast atomizer [84], and in a high-pressure diesel atomizer by Ghiji et al. [85, 86, 87].

2.3.5 Turbulence in liquid jets

Turbulence flow regimes, in contrast with laminar flow regimes, are characterized by chaotic fluctuations in pressure and velocity, i.e., presence of eddies with different length and time scales. Because of these fluctuations, a turbulent flow is by nature unsteady, meaning it cannot reach a steady state. Turbulence is maintained through a energy transfer process, namely energy cascade, that occurs from the largest scale eddies to the smallest ones. Energy is dissipated through viscosity when reaching the smallest eddy scales. This process is known

as the theory of energy cascade of Kolmogorov [88]. Apparition of turbulence in a flow can be predicted with the dimensionless Reynolds number, Re, that is defined as the ratio between inertial and viscous forces. Intensity of the turbulence also depends on this number, the higher the Reynolds number, the greater the range of scales become. Normally, the largest eddies will remain of the same size, defined by the flow geometry, while the smallest eddies size, will decrease with the Reynolds number. For single-phase flow, the smallest scale of the flow is called Kolomogorov scale. Nevertheless, in two-phase flow e.g., liquid-gas, the smallest scale could be smaller than the Kolmogorov scale, based on surface instabilities in ligaments and in coherent liquid structures [89]. Besides, the Kolomogorov scale for two-phase flow is not well defined, after all, two-phase properties such as viscosity, density ratio, surface tension, are not accounted.

Therefore, to run a Direct Numerical Simulation (DNS), all these scales must be taken into account, in particular the Kolmogorov scale that dissipates energy. The size of the discretization elements of the computational domain must be, at least, in same order than the Kolmogorov scale, defined for an equivalent single-phase flow. Nonetheless, high Reynolds number flows, usually leads to a very large number of numerical cells and as a consequence, a prohibitive computational cost. Considering current computer performances, DNS are limited to academic studies (e.g., for low Reynolds number flows) hence, it is far for being used in industrial applications, such as the one used in this project, specially for high values of Reynolds and Weber number. On the other hand, DNS, can be used to create numerical experiments, for regions where no real experimental data can be obtained.

The cheapest turbulence approach, computational speaking, is the Reynolds Averaged Navier-Stokes (RANS), which consists in averaging out all of the unsteadiness (fluctuations) of the flow. These equations are time-averaged and additional unknowns appear, namely, the Reynolds stresses. To close the system, additional transport equations are solved, from the zero model (e.g., Mixing length model) to a model with several variables (e.g., Reynolds stresses model). One of the most popular model is the k-ϵ model, that solves two additional transport equations. RANS models are computationally cheap, in terms of computing resources, in comparison with Large Eddy Simulations (LES), and they are also preferred in industry, since for most engineering purposes, it is unnecessary to resolve all the details of turbulent fluctuations, as soon as the closure models are sufficiently accurate.

Large Eddy Simulation (LES) approach, is the second big family of turbulent models. It consists in modeling only the smallest scales of the flow, in which viscous dissipation becomes preponderant. The dynamic of large-scale motions (which are affected by the flow geometry and are not universal) are computed explicitly, the influence of smaller scales are represented by simple models (e.g., eddy-viscosity models). Recently, LES is being introduced in industry due to the increase of computational resources, which allows to access additional flow information, such as unsteady effects, that were not available before [90, 91]. Indeed, the more computational power, the less modeling the simulation requires, hence the more accurate the results become.

To perform numerical simulation of primary atomization, which is turbulent flow in many industrial cases, one shall apply one of the three approaches described previously, i.e. DNS, RANS or LES. As in turbulent flow of a single-phase fluid, multiphase flows generally possess a large range of scales, ranging from the sub-millimeter size of a small bubble or droplet to the size of the system under investigation. In primary atomization process, thickness of ligaments and droplets that follow the break-up of the interface can be smaller than the Kolmogorov length scale, as previously explained. DNS-VOF of such flows without any modeling of the two phases aspect, becomes restricted to academic configurations. Two-fluid models, however, may be used for DNS of two-phase flow modeling, for low Reynolds number. On the other hand, for high Reynolds number, Euler-Lagrange DNS approach was used, for understanding the effects

of large-scale structures on the dispersion of particles [92]. Particles with different Stokes numbers were traced by the Lagrangian approach based on one-way coupling between the continuous and the dispersed phases. They found the presence of the streamwise large-scale structures caused the variation of particle concentrations along the spanwise and transverse directions. Indeed, the large structures have a dominant effect on the dispersion of particles over a range of Stokes numbers [93, 94]. Coupling Lagrangian particle tracking of discrete particles with DNS, of forced isotropic turbulence, it was shown that the uncorrelated part of the particle velocities increases with inertia [95]. However, broad applications of the method are still limited by finite computer resources and this limitation restricts the simulations to flows with moderate Reynolds numbers and fairly simple geometries. For instance, Spectral analysis and finite-difference schemes were used to simulate particle dispersion in decaying isotropic and homogeneous turbulence [96]. More recently, Euler-Euler DNS approach has been used by [97], to study the decaying of the dispersed phase in a gas-particle homogeneous isotropic turbulence environment with one-way coupling, for low Reynolds and Stoke number (close to unity). 40 particles were computed per gaseous node. This corresponded to a total of 10.48 million individual particles. This high particle number ensured convergence when grid filtered fields are computed from the discrete particle distribution. Inertial particle simulation results, were found to be very sensitive to the mesh refinement when the particle relaxation time is greater or equal to roughly $1/10$ of the turbulent time macroscale, because the smallest length scales of the predicted dispersed phase velocity field, can become significantly smaller than the smallest length scales of the carrier phase turbulent motion [97].

For low-Reynolds number in turbulent liquid jets, DNS-VOF of primary atomization was performed by Menard et al. [34], with a DNS methodology coupled with VOF (CLSVOF), to study the primary break-up process. In that work, injection speed was deliberately reduced, in order to increase the size of the smallest droplets in the secondary atomization region, hence reducing the mesh resolution and the computational costs. Desjardins et al. [98] ran a DNS of a turbulent atomization of liquid diesel jet. Shinjo and Umemura [35] studied also primary atomization in a pressure atomizer using DNS/CLSVOF. The purpose of these previous works, were to study the physical phenomena in primary atomization and to serve as reference for validating other modeling approaches, such as RANS and LES models. Nevertheless, they involved a quite small area, limited by a few injector diameters in the downstream direction. Whilst simulating the whole atomization process until several hundred of diameters in the downstream direction is hardly feasible with DNS.

Nowadays, some industries have started using RANS with Williams-Boltzman equation (e.g., Euler-Lagrange models), Eulerian approach for the gas phase and Lagrangian approach, "reproducing" the presence of physical particles inside the domain. Normally for full spray modeling, there have been numerous research, that were based on a wrong hypothesis: considering a non-dense flow at the injection, pseudo-correct results can be obtained, thanks to the convective characteristics of the Lagrangian method. Despite the fact that the provided results are rough, this approach has been widely adopted, because of its ability to model the whole spray i.e., from the nozzle exit to the mixing area inside the combustion chamber, even though, if the flow is inaccurate at the nozzle outlet. RANS can be combined also with single-fluid models, as ELSA [99] and two-fluid models.

Application of Large eddy simulations (LES) formalism, to solve primary atomization is relatively recent. Large eddy simulations are an intermediate tool between DNS and RANS, by mitigating the fine mesh constraint. One classical approach, is to combine the single-phase turbulent LES model, with an Interface Capturing Method (ICM) e.g., VOF, Level-Set, among others. Good results have been obtained when applying LES/VOF on primary atomization [100, 84]. Recent developments tend to take into account the issue of liquid structures smaller than the mesh size. We shall refer to this developments as 'two-phase LES' formulation.

Sub-grid methods have been developed and applied for simulating primary atomization in Diesel jets [101, 77] and air-blast atomizer configurations [102, 103]. For which, LES has a great potential in modeling accurately the atomization process, however, computational costs are still too high to be able to treat both primary, secondary atomization region, along with evaporation and combustion zones.

It is the purpose of this project, to validate and to improve an atomization model, capable of dynamically detect sub-grid scales (i.e., in which energy dissipation is modeled by LES), and to switch from primary atomization to dispersed flow, by two ways: (1) when liquid ligaments are broken up until some spherical liquid shape (i.e., at least within certain validity range defined in chapter 4). (2) When certain droplet statistical convergence is achieved within the computational cell. An explicative physical-modeling map is displayed in chapter 3

2.4 Governing equations

2.4.1 Liquid Volume Fraction Equation

VOF methods, track the interface with a specific algorithm. An interface algorithm must then minimize numerical diffusion, by maintaining a compact interface thickness. Different algorithms have been recently developed e.g., Interface Reconstruction methods [81, 82] and Interface Capturing Method (ICM) method from Weller [104], as previously explained. The latter technique, is used in native VOF solvers in `OpenFOAM` . Let's us then, consider a two-fluids flow e.g., liquid and gas. Both fluids are incompressible and non miscible. A volume fraction α_l, is the VOF field, a scalar field representing the volume fraction of liquid:

$$\alpha_l = \begin{cases} 1 & \text{Liquid} \\ 0 & \text{Gas} \\ 0 < \alpha_l < 1 & \text{At the interface} \end{cases} \tag{2.2}$$

Considering turbulent incompressible flows, without mass transfer across the interfaces, the governing equations includes continuity and the momentum balance, given by:

$$\begin{cases} \nabla \cdot \boldsymbol{U} = 0 \quad , \\ \dfrac{\partial \rho \boldsymbol{U}}{\partial t} + \nabla \cdot (\rho \boldsymbol{U}\boldsymbol{U}) = -\nabla p + \nabla \cdot \boldsymbol{\tau}_t + \rho \boldsymbol{g} + \boldsymbol{f}_\sigma \quad , \end{cases} \tag{2.3}$$

where $\boldsymbol{U}$ is the velocity vector, ρ is the density, p is the pressure, $\boldsymbol{\tau}_t$ is the turbulent stress tensor. The latter, $\boldsymbol{\tau}_t$, can be decomposed in the following form:$\boldsymbol{\tau}_t = 2(\mu)\boldsymbol{D}$, in which $\boldsymbol{D}$, is proportional to the rate of deformation tensor $\boldsymbol{D} = 0.5\left[\nabla \boldsymbol{U} + (\nabla \boldsymbol{U})^T\right]$. The *laminar* fluid viscosity μ. The two remaining terms include the gravity acceleration $\boldsymbol{g}$ and surface tension force $\boldsymbol{f}_\sigma$. When a resolved interface between the two fluids is considered, the surface tension force is applied at the interface position. Then it is defined by:

$$\boldsymbol{f}_\sigma = \sigma \kappa \delta(\boldsymbol{x} - \boldsymbol{x}_s)\boldsymbol{n} \quad , \tag{2.4}$$

where σ is the surface tension coefficient, $\boldsymbol{x}_s$ is the interface position, and by defining $\boldsymbol{n}$, as the interface unit normal, then the interface curvature κ, is defined:

$$\kappa = -\nabla \cdot \boldsymbol{n} = -\nabla \cdot \left(\frac{\nabla \alpha_l}{|\nabla \alpha_l|} \right) \quad . \tag{2.5}$$

The mixture density and viscosity are functions of the phase indicator explained above, α_l, with constant gas and liquid viscosity, μ_g and μ_l, respectively. Analogously for the gas and liquid density, it reads:

$$\begin{cases} \rho = \alpha_l \rho_l + (1-\alpha_l)\rho_g \quad , \\ \mu = \alpha_l \mu_l + (1-\alpha_l)\mu_g \quad . \end{cases} \tag{2.6}$$

Besides the mass and momentum equations, the VOF method requires to keep track of the liquid volume fraction (LVF). This is performed by advecting the VOF field with the incompressible velocity field, through the following equation:

$$\frac{\partial \alpha_l}{\partial t} + \nabla \cdot (\alpha_l \boldsymbol{U}) = 0 \quad . \tag{2.7}$$

Equation 2.7 transports mixture properties and position of the interface. In case of a sharp interface, an interface capturing method is necessary to well define geometric characteristics of the interface and correctly compute body force surface tension in momentum equation 2.3. Therefore, a conservative form of equation 2.7 is exploited, with an additional surface compressive term, in order to keep the interface sharp [105]:

$$\begin{cases} \dfrac{\partial \alpha_l}{\partial t} + \nabla \cdot (\boldsymbol{U} \alpha_l) = \underbrace{-\nabla \cdot [\boldsymbol{U}_r \alpha_l (1-\alpha_l)]}_{\text{Sharpening term}} \quad , \\ \boldsymbol{U}_r = |\boldsymbol{U}| \dfrac{\nabla \alpha_l}{|\nabla \alpha_l|} \quad , \end{cases} \tag{2.8}$$

where the $\alpha_l(1-\alpha_l)$ term, enforces the interface compressibility to be concentrated only at the interface region. Thus, it has little or negligible effect on the solution throughout the rest of the domain. $\boldsymbol{U}_r$ is a suitable velocity field, selected to compress the interface region [106], defined as a relative velocity between the two phases. As described by Rusche [105], the artificial compressive term of eq. 2.8 provides interface straightening, without the need to use an interface reconstruction method. The boundedness of α_l, between 0 and 1, is ensured by using a specific procedure called MULES (Multidimensional Universal Limiter with Explicit Solution) [107], already implemented in OpenFOAM® . This method will be referred later on in the following chapters, as Interface Capturing Method (ICM).

2.4.2 Liquid Gas Interface Density Equation

So far the large-scales properties of two-phase flows, have been defined by means of a balance equation of the liquid volume fraction, α_l, eq. 2.8. Now, the small-scale characteristics such as droplet size distribution and mean droplet diameter can be represented by means of the *liquid gas interface density*, namely Σ, which represents the liquid/gas surface interface per unit of volume. The concept of interface density, is more general than droplet diameter or Sauter Mean Diameter (SMD). Indeed, liquid shapes are not always spherical and SMD cannot account for all other shaped of interface. Thus, Σ is a more generalized quantity able to quantify any type of interface. A closed form of Σ equation is not fully established yet. Starting with a phenomenological approach, as also presented by [2] and [33], a general filtered form may be written e.g., Reynolds decomposition:

$$\frac{\partial \Sigma}{\partial t} + \nabla \cdot (\boldsymbol{U}\Sigma) = \nabla \cdot [\Sigma(\boldsymbol{U} - \boldsymbol{U}_\Sigma)] + S_\Sigma \quad . \tag{2.9}$$

The first term of the right-hand side is unclosed, since the interface velocity, $\boldsymbol{U}_\Sigma$, is unknown. This term represents the difference between the interface velocity and the global mixture velocity. It accounts for the dispersion of the interface by turbulence. Thus, namely, a first order closure (or gradient closure), related to the Boussinesq approximation, in which it is modeled as turbulent dispersion [33, 2], and neglecting contribution of slip velocity, leads to the following formulation:

$$\bar{\Sigma}(\boldsymbol{U}-\boldsymbol{U}_\Sigma)=\boldsymbol{R}_\Sigma \approx \frac{\nu_t}{Sc_t}\nabla\Sigma \quad . \tag{2.10}$$

A so-called second order closure, is explained in detail in the following chapter 3, however, the interested reader is referred to [108, 78] for a full description of the method. The equation 2.9 for Σ, takes into account two source terms. The source terms are shown in equation 2.11, which includes firstly, the minimum production of the liquid-gas interface density induced by liquid-gas mixture and secondly, the production/destruction of liquid-gas interface density due to turbulent flow, vaporization, collision, and any coalescence in the dense part of the spray. Vaporization is not considered. Hence, the following equation arises:

$$S_\Sigma = S_{mix} + S_{int} \quad , \tag{2.11}$$

where S_{mix} refers to production of surface density due to liquid/gas mixing, and S_{int} represents production/destruction of surface density by the mean shear, turbulence and liquid structure interactions. Moreover, S_{mix} is the necessary term, that ensures the presence of interface simply because of co-existing phases. Vallet et al. [2] proposed a formulation based on the inverse of the size of the control volume near the injector tip assuming a flat interface at the boundary. Lebas et al. [33] proposed that, liquid characteristic scales are related to turbulent integral scale. In both cases, it is an initialization term that does not have a strong effect on the whole calculation, while producing a minimum surface density immediately after injection, for high turbulent flow. The presence of an interface as long as the liquid comes into contact with the gas, provides a mean to use a formulation based on minimum estimate of the surface density Σ_{min}, thus an additional quantity Σ' is defined, such that:

$$\begin{cases} \Sigma = \Sigma_{min} + \Sigma' \quad , \\ a\Sigma_{min} = 2.4\sqrt{\alpha_l(1-\alpha_l)} \quad , \end{cases} \tag{2.12}$$

where "a" is a length scale related to the control volume. The above equation was based on the assumption that, the surface density is at least equal to Σ_{min}, which is defined as the minimum amount of surface present due to liquid-gas mixing. Note that this definition is coupled with the amount of interface that can be obtained with ICM approach. As a result, it is required only to compute the evolution of Σ', by using equation 2.9. Finally, the transport equation, that represents the additional interface instabilities, is written as:

$$\frac{\partial\Sigma'}{\partial t} + \nabla\cdot(\boldsymbol{U}\Sigma') = \nabla\cdot[\Sigma'(\boldsymbol{U}-\boldsymbol{U}_\Sigma)] + S_{int} \quad . \tag{2.13}$$

Consequently Σ', is solved using Equation 2.13, while Σ, is calculated using eq. 2.12. The closure of S_{int}, comes from the work of Lebas et al. [33], and is given as:

$$S_{int} = C_\Sigma \frac{\Sigma}{\tau_\Sigma}\left(1-\frac{\Sigma}{\Sigma^*}\right) \quad , \tag{2.14}$$

which is based on an equilibrium value of surface density, Σ^*, that should be reached within a characteristic time scale, τ_Σ. C_Σ is a constant that is set equal to 0.4. Σ^* is given by the Weber number at equilibrium, that can be obtained from the work of Duret et al. [89]. Finally the modeled equation for Σ' becomes:

$$\frac{\partial \Sigma'}{\partial t} + \nabla \cdot (\boldsymbol{U}\Sigma') = \nabla \cdot \left[\frac{\nu_t}{Sc_t} \nabla \Sigma' \right] + C_\Sigma \frac{\Sigma}{\tau_\Sigma} \left(1 - \frac{\Sigma}{\Sigma^*} \right) \tag{2.15}$$

Further discussions of these terms are available in works of Lebas et. al [52] and Vallet et al [1], that proposed various forms of modeling terms. Here the purpose is to use first the simplest formulation and introduce more complex models only when necessary. A length scale can be defined from Σ and α_l: $\frac{\alpha_l}{\Sigma}$, which is related to SMD. On the one hand, for mono-dispersed spray of spherical droplets, the $\boldsymbol{SMD}$ will have the following form: $\frac{6\alpha_l}{\Sigma}$. On the other hand, for very small volume fraction leading to bubbly flow: $\boldsymbol{SMD} = \frac{6(1-\alpha_l)}{\Sigma}$. Finally, to account for all structures, a length scale l_{32} is derived in the following equation:

$$l_{32} = \frac{6\alpha_l(1-\alpha_l)}{\Sigma} \tag{2.16}$$

Therefore, by using LES/RANS modeling approach, ELSA has proven to be accurate for the description of the primary atomization, as previously explained by previous research. In addition, high efficient approaches, such as the DNS-ICM, can also be advantageous when interface resolution is affordable, computational speaking. The purpose of the following chapter 3, is to follow the work of Hecht [7] and Chesnel [109, 77], in order to properly build and assess a dynamic multi-scale model, able to take advantage of high resolution and accuracy by using DNS-ICM, in flow regions in which the interface is resolved, and then modelize the unresolved interface by applying LES-ELSA.

Chap. 3 | Dynamic multi-scale spray atomization model.

3.1 Introduction

The purpose of the present chapter is, to present a dynamic multi-scale approach suitable to perform LES for liquid jet atomization, together with the possibility to recover ICM/DNS features for well resolved interface flow. To achieve this goal, the most important unresolved phenomena to address are, the sub-grid turbulent liquid flux and surface density, in which models based on ELSA concept, are developed. The work is organized as follows: section 3.2 is devoted to the description of the Eulerian solver, directly derived from Euler-Lagrange Spray Atomization (ELSA) formulation. Then, an innovative coupling between an Interface Capturing Method (ICM) and a complete $\boldsymbol{ESA}$ approach, is detailed. The acronym $\boldsymbol{ESA}$ comes from the $\boldsymbol{ELSA}$ formalism without Lagrange approach. Section 3.3 accounts for the numerical domain and meshes development. Subsequently, section 3.3.3 reports the validation process of the proposed Eulerian solver, in which different well-established turbulence models, such as $k-\epsilon$ [110, 111], Smagorinksy [112, 113], WALE [114], and modeling strategy, namely ESA, and ICM coupled with ESA, are compared using experimental data. A second numerical case is tested against experiments namely air-blast atomizer test case 3.4, in which the lower liquid Reynolds and gas Weber number are no longer suitable for $\boldsymbol{ESA}$ model, however, the $\boldsymbol{ICM-ESA}$ is found to be quite satisfactory, hence a prove of robustness adaptability based on interface resolution criteria. Finally, in section 3.5 conclusions are sketched, and the best numerical match with the experiments is presented.

3.2 Atomization modeling approach

As previously mentioned, multiphase flow can be classified in discrete and separated flow, however, when it comes to atomizing turbulent liquid jets, a combination of both is rather preferable. Indeed, just at the exit of the injector nozzle, the amount of liquid is very high, and this phase cannot be decomposed as sets of discrete droplets. Moreover, bubbles could be present in the liquid flow due to penetration of the surrounding gas during the breakup process, and previous cavitation inside the nozzle injector. Consequently, the carrier phase would be the liquid and the discrete phase, the gas bubbles. On the contrary, further downstream, a spray is generated, in which the carrier phase is the gas and the discrete phase corresponds to liquid droplets. Between these two limits, a two-phase flow exists with unclear discrete and carrier phases [52].

The key point of the proposed ESA model, is the analogy between atomization, liquid dispersion and turbulent mixing of a jet, with large density difference with the ambient medium [1]. By using single-fluid approach, the choice of both carrier and discrete phases, is avoided [52]. Therefore, the two-phase flow is studied as a single-phase turbulent flow composed of two species with highly variable density.

3.2.1 Basic equations

In this section, starting from this complete approach, for incompressible isothermal fluids, governing equations are presented.

$$\begin{cases} \nabla \cdot \boldsymbol{U} = 0 \quad , \\ \dfrac{\partial \rho \boldsymbol{U}}{\partial t} + \nabla \cdot \left(\rho \boldsymbol{U} \otimes \boldsymbol{U} \right) = -\nabla p + \nabla \cdot (\rho \nu (\nabla \boldsymbol{U} + \nabla \boldsymbol{U}^t)) + \boldsymbol{f}_\sigma + \rho \boldsymbol{f}_b \quad , \\ \dfrac{\partial \alpha_l}{\partial t} + \nabla \cdot (\boldsymbol{U} \alpha_l) = 0 \quad . \end{cases} \tag{3.1}$$

The continuity equation, the mixture velocity $\boldsymbol{U}$, and the liquid volume fraction, follow the classical transport equations in which p is the normal stress in two-phase medium at equilibrium, ν is the kinematic mixture viscosity, $\boldsymbol{f}_\sigma$ is the surface tension force, ρ is the mixture density, all previously explained in chapter 2, and finally $\boldsymbol{f}_b$, is the body forces per unit of mass. Solving these equations 3.1, at all scales, would not require any additional model, hence this case will be refereed as DNS. Nevertheless, these equations use generalized functions, since the surface tension force occurs only at the surface, and thus require a Dirac pick function representative of the interface $\delta(\boldsymbol{x} - \boldsymbol{x}_s)$. In addition, the discontinuity of the liquid volume fraction entrains the discontinuity of density and viscosity, thus their derivatives also require generalized functions. To keep the interface sharp, the profile of the discontinuous variables across the interface, in particular the liquid volume fraction, has to remain a step profile. This expected feature has strong consequences on the numerical method, in which dedicated Interface Capturing Methods (ICM) are required, for instance VOF [115], Level Set [45], Ghost-Fluid [47], among others, as discussed previously in chapter 2. These ICM numerical approaches, share a common feature i.e, they are all incompatible with a smooth profile of the liquid volume fraction.

Whenever it is not possible to solve these equations directly at all scales, some filtering or averaging process is applied, thus necessarily introducing new terms in equations 3.1. It is important to notice, that one of the first feature that is lost, is the accurate position of the interface. Previously, the liquid volume fraction field, or any other phase indicator, was sufficient to determine the position of the interface. For instance, any iso-surface of the liquid volume fraction, within the range [0,1], is identical if the liquid volume fraction profile is a step profile across the interface. Nevertheless, averaging or filtering will smooth the liquid volume fraction profile, and let undetermined the actual position of the interface. Any other VOF method faces the same problem but in different ways. For instance, by forcing a sharp transition between liquid and gas at the interface e.g., Ghost Fluid Method (see chapter 2). This compressive feature, is in contradiction with the averaging/filtering procedure in which, a smooth transition is considered, with the consequence to lose the interface position. Notice that, numerous successful works in the literature ignore these problems, and use averaged/filtered approaches whilst keeping a sharp transition between phases i.e., turbulence models such as RANS or LES, are used and combined with ICM. Normally, it is expected that such effects are negligible, if all scales of the flow are solved.

The purpose of the present chapter, is then to propose a less computationally demanding model than DNS e.g., RANS / LES, dynamically adaptable to turbulent interface fluctuations i.e., interface resolvent dependent. To that end, Interface Resolved Quality (IRQ) sensors are developed, to evaluate when it is necessary to consider either an Interface Capturing Method (ICM) for resolved interface, or subgrid modeling (ELSA) for unresolved interface.

3.2.2 Averaging/Filtering remarks

Before to go any further in the details of RANS and LES approaches, both methods have to deal with density-based correlations. Considering the simple case of constant gas and liquid density, ρ_g and ρ_l , respectively, the filtered density, $\bar{\rho} = \rho_l \bar{\alpha}_l + \rho_g(1 - \bar{\alpha}_l)$, is far for being constant. There are two ways to handle this problem, namely Reynolds or Favre averaging/filtering. Both approaches lead to modeling problems that are not yet completely solved. Using Reynolds averaging/filtering, introduces correlation for which no models have been established yet, for turbulent liquid-gas flow. Thus, these unclosed correlation are generally not considered or consider being part of Reynolds stress and turbulent liquid flux final model [78]. Regarding the Favre approach, it has been widely employed in single phase flow with variable density, hence it can be applied for two-phase flow, by using the ELSA approach philosophy, previously explained [1]. Nonetheless, any Favre-averaged variable is pondered by the density. The particularity of liquid-gas flow with respect to the previously used Favre averaging procedure for single-phase flow, is the magnitude of density fluctuations. Figure 3.1 below, shows the Favre-averaged velocity mixture with respect to the liquid volume fraction $\bar{\alpha}_l$, for constant liquid and gas velocity, $\bar{U}_l$, and $\bar{U}_g$, respectively. The nonlinear relation of the Favre-averaging, namely $\tilde{u} = \frac{\overline{\rho u}}{\bar{\rho}}$, is enhanced as the density ratio ($r = \frac{\rho_l}{\rho_g}$), grows. For instance, when r = 100, and the mixture is composed by 90% of gas ($\bar{\alpha}_l = 0.1$), the Favre-averaged velocity mixture is still mainly related to the liquid velocity.

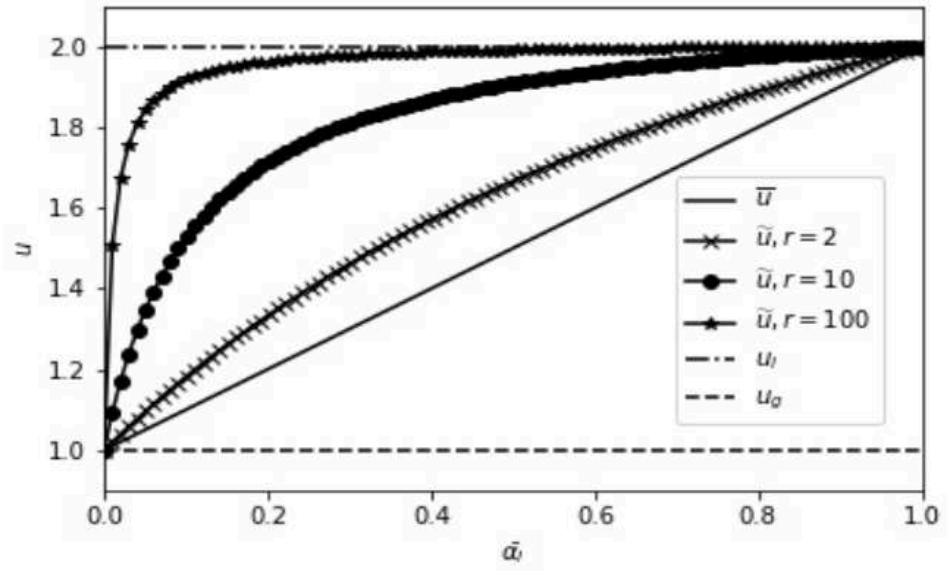

Figure 3.1: Favre-averaged velocity for different density ratio $r = \frac{\rho_l}{\rho_l}$ as a function of the liquid volume fraction [16].

Therefore, as the density ratio increase, in liquid-gas flow, the Favre averaging/filtering tends to link the averaged variable, to the heavier phase [116, 16]. Numerically, it brings many stability problems, because of lack of information about the lighter phase. In addition, through Reynolds averaged/filtered, velocity field is still *divergence free*, which is not the case for the Favre averaged/filtered velocity field. This is in fact, the difficulty of many pressure-based solvers, by coupling the Favre momentum equations to the liquid volume fraction equation.

Despite these problems, both Reynolds and Favre approaches have been applied successfully in RANS context [2, 2, 52, 78, 117]. In this thesis, Reynolds averaging/filtering formulation together with liquid volume fraction (volume formulation) field, instead of liquid mass fraction (mass formulation i.e., Favre-averaged) is considered. This formulation, is considered to be

physically clearer, by letting apparent the unclosed density correlation terms, even if further efforts to define appropriate models still require future work.

3.2.3 Turbulence modeling

The flow considered in the thesis is two-fluid flow, when both characteristic Reynold and Weber numbers of the jet, tend to infinity [1]. In this case, early studies of liquid jets revealed that the turbulence was the primary initiator of break-up [118]. Subsequent studies, for instance [119, 120, 121, 122], have examined how this process works. In the early stages of breakup, the turbulent structures in the jet produce ligaments that project into the gaseous phase, and then fragment to form droplets. Therefore, atomization could be considered as a turbulent mixing process. As a result, the velocity field in a two-phase flow and liquid volume fraction are studied in terms of mean and fluctuating values as for single-phase turbulent flows, based on the Reynolds decomposition [1].

Starting from the least resolved case, RANS approach, in which the two-phase flow considered, is averaged. From this approach, it is expected to recover the large-scales properties (penetration length and angle of dispersion of the liquid core and) small-scales characteristics (mean droplet diameter and their size distribution). Nevertheless, a large part of the flow has to be modeled, and the models are then necessarily dependent on the unresolved small scale features.

The second approach is generally known as Large Eddy Simulation (LES) [77]. In order to separate different length scales in a turbulent flow field, a spatial filter is applied. Large scale structures that can be resolved by the numerical method on a given mesh, are called the super-grid scales. The influence of all other (subgrid) scales to the super-grid behavior is modeled. The rationale behind this principle lies in the fact that, the small scales of turbulence are more homogeneous and isotropic, and therefore, easier to model. As the mesh gets finer, the modeling becomes less significant, thus approaching the DNS [123]. But to recover truly the expected feature of the DNS in liquid-gas flows, ICM has to be activated, since particular numerical models are necessary to represent the sharp interface transition. Applying the Reynolds averaging technique for incompressible flow to equations 3.1:

$$\begin{cases} \nabla\cdot\bar{\boldsymbol{U}} = 0 \quad , \\ \dfrac{\partial\bar{\rho}\bar{\boldsymbol{U}}}{\partial t} + \nabla\cdot\left(\bar{\rho}\bar{\boldsymbol{U}}\otimes\bar{\boldsymbol{U}}\right) = -\nabla\bar{p} + \nabla\cdot\left[\overline{\rho v}(\nabla\bar{\boldsymbol{U}} + \nabla\bar{\boldsymbol{U}}^{t})\right] + \rho\bar{\boldsymbol{f}}_{b} - \nabla\cdot\boldsymbol{R}_{U} + \tau_{\rho} \quad , \\ \dfrac{\partial\bar{\alpha}_{l}}{\partial t} + \nabla\cdot(\bar{\boldsymbol{U}}\bar{\alpha}_{l}) = -\nabla\cdot\boldsymbol{R}_{\alpha_{l}} \quad . \end{cases} \tag{3.2}$$

The first term that arrives from the filtering procedure is the so-called Reynolds stress tensor $\boldsymbol{R}_{U}$. The normal stresses, involve the respective variances of the x-, y- and z-velocity fluctuations. They are always non-zero because they contain squared velocity fluctuations. The shear tresses, contain second moments associated with correlations between different velocity components [110]. The term on the RHS of the liquid volume fraction equation (third equation from top to bottom), is the turbulent liquid flux.

To model these fluctuating terms, namely, Reynolds stress tensor and the turbulent liquid flux, the Reynolds-Averaged Navier-Stokes (RANS) is firstly considered. Regarding the Reynolds stress, single-phase flow model is initially tested. Following Boussinesq's proposal, the turbulent momentum transport is assumed to be proportional to mean gradients of velocity [110]. By analogy, turbulent transport of a scalar is taken to be proportional to the gradient of the mean value of the transported quantity. Thus, the turbulent liquid flux is seen mainly as a dispersion term for the liquid due to the random turbulent motion. The formalism, also shows

that the turbulent liquid flux contains the mean slip velocity of the liquid phase with respect to the mean mixture, thus it is possible to extend the model to account for this effect [78]. Finally, the Reynolds stress tensor and the turbulent liquid flux are presented:

$$\begin{cases} \boldsymbol{R}_U & = (\overline{\boldsymbol{U}\otimes\boldsymbol{U}} - \bar{\boldsymbol{U}}\otimes\bar{\boldsymbol{U}}) \quad , \\ & \approx -\frac{\nu_t}{Sc_t}(\nabla\bar{\boldsymbol{U}} + \nabla\bar{\boldsymbol{U}}^t) \quad . \\ \boldsymbol{R}_{\alpha_l} & = (\overline{\boldsymbol{U}\alpha_l} - \bar{\boldsymbol{U}}\bar{\alpha}_l) \quad , \\ & = \bar{\alpha}_l(\bar{\boldsymbol{U}}|_{\boldsymbol{l}} - \bar{\boldsymbol{U}}) \quad , \\ & \approx -\frac{\nu_t}{Sc_t}\nabla\bar{\alpha}_l \quad . \end{cases} \tag{3.3}$$

where ν_t, is the turbulent viscosity (or sub-grid stress in LES framework) and $\boldsymbol{Sc_t}$, is the turbulent Schmidt number. On RHS of α_l equation 3.3, $\boldsymbol{R}_{\alpha_l}$ is the *turbulent liquid flux*, that represents the transport of the liquid volume fraction induced by velocity fluctuations, and is related to the unresolved part of the velocity that is known to produce additional dispersion. This formulation is only valid in the absence of mean slip velocity between phases. Additionally, it has been proven [33, 78, 50] that even with this single flow approach, it is possible to recover the different mean liquid and gas velocities $\bar{\boldsymbol{U}}|_{\boldsymbol{l}}$, and $\bar{\boldsymbol{U}}|_{\boldsymbol{g}}$, respectively, by means of a drift flux model. Indeed, if both phases are strictly non-miscible, the turbulent liquid flux, can be rewritten in the following form:

$$\boldsymbol{R}_{\alpha_l} = \bar{\alpha}_l(\bar{\boldsymbol{U}}|_{\boldsymbol{l}} - \bar{\boldsymbol{U}}) = \bar{\alpha}_l(1-\bar{\alpha}_l)\bar{\boldsymbol{V}}_{rlg} \quad . \tag{3.4}$$

This shows the strong link between $\boldsymbol{R}_{\alpha_l}$ and the local relative velocity $\boldsymbol{V}_{rlg}$ [124], that can be re-arranged as follows:

$$\bar{\boldsymbol{V}}_{rlg} = \left(\bar{\boldsymbol{U}}_l - \bar{\boldsymbol{U}}_g - \bar{\boldsymbol{V}}_D\right) = \left(\bar{\boldsymbol{U}}_{slg} - \bar{\boldsymbol{V}}_{Dlg}\right) \quad . \tag{3.5}$$

where $\bar{\boldsymbol{U}}_{slg}$, is the average relative velocity between the particle and the surrounding flow, in the vicinity of the interface that is directly related to the drag force acting on the liquid, and $\bar{\boldsymbol{V}}_{Dlg}$, is the conditional average of the fluid turbulent velocity fluctuations with respect to the particle distribution. In the case in which the spray dynamic relaxation time τ_p, and the mean effective slip velocity $\bar{\boldsymbol{U}}_{slg}$, are negligible (i.e., in the case of droplets with small Stokes numbers), the turbulent liquid flux is only due to the drift velocity. The interested reader is then referred to [78] where a so-called QME i.e., second order closure is developed. Meanwhile, we will stick with the first order formulation presented in equation (3.3) in which, based on the actual validation test case [125], was proven to be quite successful.

Additionally, density correlations represented by τ_ρ (equation A.1), appears on this Reynolds formalism. Their effect is still subject of research, e.g. density fluctuations in combustion processes are not necessarily applicable when the density ratio tends to infinity, which is also the present study case. On the other hand, by using the Favre averaging (i.e., the mass formulation) in two-phase flow simulation, there is not an explicit approximation, in modeling liquid-gas turbulent fluctuation stresses, as compared with the Reynolds formalism. However, further development in the Favre formalism for two-phase flow, revealed implicitly an equivalent density correlation issue, especially for high density ratios $\left(\frac{\rho_l}{\rho_g}\right)$. Therefore, since this chapter will treat the conservation equation using a Reynolds formalism (LES/RANS),

based on volumetric variables, the density correlations will be considered as part of the global Reynolds/Residual stress model. Nevertheless, an appendix $\boldsymbol{A}$, is dedicated to the mathematical development for two-phase flow simulation, in which a two-phase decomposition has been made.

3.2.4 Turbulence models

Now the kinematic turbulent viscosity, ν_t, needs to be addressed. The accuracy of different RANS turbulence models, when they are applied to turbulent two-phase flows, was previously studied [124]. It was shown that the **standard $k-\varepsilon$ turbulence model** for atomization process (Launder and Spalding, 1974), is able to reproduce the main characteristics of two-phase flow, if special care is devoted to the modeling of the turbulent mass flux. Nevertheless, the assumption made by RANS models, is that the turbulent viscosity ν_t, is isotropic: in other words, the ratio between Reynolds stress and mean rate of deformation is the same in all directions, which is not the case within the scale spectrum of eddies. For instance, the smallest eddies are nearly isotropic and have a universal behavior. On the other hand, the largest eddies, which interact by extracting energy from the mean flow, are more anisotropic and their behavior is dictated by the geometry of the domain, the boundary conditions and body forces [110].

Large Eddies Simulation filtering

Instead of RANS, LES uses a spatial filtering operation to separate the largest from the smallest eddies. Even though this simple approach permits to deal with flow anisotropy on large scales, which clearly is an advantage over RANS models, there are still some generality issues depending on the rate-controlling process [126]. However, in free shear flows at high Reynolds number, the transport process of interest are affected by the resolved large scales, which makes LES suitable for our case study. The method starts with the selection of a filtering function and a certain cutoff width, with the aim of resolving in an unsteady fashion, all eddies with a length scale greater than the cutoff width. There are three well-known filtering functions, namely, *Top-hat filter*, *Gaussian filter* and *Spectral cutoff*. The first one is widely used in finite volume implementation, and related the mesh size. Further details can be found in [90, 110]. The cutoff width, is intended as an indicative measure of the size of eddies that are retained in the computations, and the eddies that are rejected. In principle, we can choose the cutoff width Δ to be of any size, but in CFD computations, with the finite volume method, it is pointless to select a cutoff width smaller than the grid size. The most common selection, is to take the cutoff width to be of the same order as the grid size, for instance, the cubic root of the grid cell volume:

$$\Delta = \sqrt[3]{\Delta x \Delta y \Delta z} \tag{3.6}$$

As before, the conservation equations governing the filtered velocity $\bar{\boldsymbol{U}}(\boldsymbol{x},t)$, are obtained by applying the *Top-hat* filtering operation to the Navier-Stoke equation and the liquid volume fraction equations, namely equation 3.1, LES-filtered continuity, momentum, and liquid volume fraction equations of the mixture yield the following:

$$\begin{cases} \nabla \cdot \bar{\boldsymbol{U}} = 0 \quad , \\ \dfrac{\partial \bar{\rho} \bar{\boldsymbol{U}}}{\partial t} + \nabla \cdot \left(\bar{\rho} \bar{\boldsymbol{U}} \otimes \bar{\boldsymbol{U}} \right) = -\nabla \bar{p} + \nabla \cdot \left[\overline{\rho \nu} (\nabla \bar{\boldsymbol{U}} + \nabla \bar{\boldsymbol{U}}^t) \right] + \rho \bar{\boldsymbol{f}}_b - \nabla \cdot \boldsymbol{\tau}_r \quad , \\ \dfrac{\partial \bar{\alpha}_l}{\partial t} + \nabla \cdot (\bar{\boldsymbol{U}} \bar{\alpha}_l) = -\nabla \cdot \boldsymbol{\tau}_{\alpha_l} \quad . \end{cases} \tag{3.7}$$

Equations 3.7 should be solved to yield the filtered mixture velocity $\bar{\boldsymbol{U}}$, the filtered mixture pressure field $\bar{p}$, filtered mixture density $\bar{\rho} = \rho_l \bar{\alpha}_l + \rho_g(1 - \bar{\alpha}_l)$, and the filtered liquid volume fraction distribution $\bar{\alpha}_l$. The last term on RHS, $\boldsymbol{\tau}_r$, results from the LES filtering operation, just like the Reynolds Stress, in this case commonly named the *residual-stress tensor* or **LES SGS**, which stands for subgrid-scale. However, unlike the Reynolds stresses in the RANS equations, the LES SGS stresses contain further contributions. Based on the flow variable decomposition $\phi(\mathbf{x},t)$ as the sum of the filtered function $\bar{\phi}(\mathbf{x},t)$ and $\phi'(\mathbf{x},t)$, which contains unresolved spatial variations. Now the residual (or SGS) stresses can be written in the following form:

$$\boldsymbol{\tau}_r = (\bar{\rho}\overline{\bar{\boldsymbol{U}}\bar{\boldsymbol{U}}} - \bar{\rho}\bar{\boldsymbol{U}}\bar{\boldsymbol{U}}) = \underbrace{\bar{\rho}\overline{\bar{\boldsymbol{U}}\bar{\boldsymbol{U}}} - \bar{\rho}\bar{\boldsymbol{U}}\bar{\boldsymbol{U}}}_{Leonard} + \underbrace{\bar{\rho}\overline{\bar{\boldsymbol{U}}\boldsymbol{U}'} + \bar{\rho}\overline{\boldsymbol{U}'\bar{\boldsymbol{U}}}}_{Cross} + \underbrace{\bar{\rho}\overline{\boldsymbol{U}'\boldsymbol{U}'}}_{LES} \quad . \tag{3.8}$$

The Leonard stresses are solely due to effects at resolved scales. The cross-stresses are due to interactions between the SGS eddies and the resolved flow. Finally, LES stresses are caused by convective momentum transfer due to interactions of SGS eddies and are modeled with SGS models explained in the following sections. For a complete definition and mathematical deduction see [110]. Another aspect, in which the filtered equations 3.7 are quite different from the RANS equations, are the three-dimensional, and unsteadiness property of the filtered fields, $\bar{\boldsymbol{U}}(\boldsymbol{x},t)$ and $\bar{p}(\boldsymbol{x},t)$, and $\boldsymbol{\tau}_r(\boldsymbol{x},t)$, even if the flow is statistically stationary or homogeneous [90].

SGS Models

In order to the dynamics of the resolved scales to remain correct, the subgrid terms have to be modeled and some closure of the equations 3.7 needs to be applied, i.e. the subgrid energy interaction with the resolved scales have to be reflected. In gas kinetics theory, molecular agitation draws energy from the flow by way of molecular viscosity. So the energy cascade mechanism [111], will be modeled by a term having a mathematical structure similar to that of molecular diffusion, but in which the molecular viscosity in 3.7 is replaced by a sub-grid (or residual) viscosity ν_{sgs}. Mainly, two approaches were studied depending on the validation test case:

- *Models based on the resolved scales:* The subgrid viscosity, ν_{sgs}, is evaluated using global quantities related to the resolved scales. Within this category is the well-known **Smagorinsky model**. Based on the assumption that the smallest turbulent eddies are almost isotropic, the Boussinesq approach is employed [112]. Thus, local SGS stresses $\boldsymbol{\tau}_r(\boldsymbol{x},t)$, are taken to be proportional to the local rate of strain of the resolved flow [110]. The model is expressed in the following equation:

$$\begin{cases} |\bar{S}| = (2\bar{\boldsymbol{S}}\bar{\boldsymbol{S}})^{1/2} \quad , \\ \boldsymbol{\tau}_r = -2\nu_{sgs}\bar{\boldsymbol{S}} \quad , \\ \nu_{sgs} = (C_s\Delta)^2|\bar{S}| \quad , \end{cases} \tag{3.9}$$

  where C_s is the *Smagorinsky coefficient*, which is proportional to the filter width Δ, $|\bar{S}|$ is the characteristic filtered rate of strain, and $\bar{\boldsymbol{S}}$ is the filtered rate-of-strain tensor based on the filtered velocity $\bar{\boldsymbol{U}}(\boldsymbol{x},t)$. There are many authors that experimentally or numerically have demonstrated different values of the constant C_s, which makes the model flow-dependent. This gave an indication that the behavior of the small eddies is not as universal as was thought, or the model is representative enough. Furthermore, the modeling requires a case-by-case adjustment or a more sophisticated approach. More shortcomings of the Smagorinsky model, have also been reported [90, 126, 111].

- *Wall Adopting Local Eddy Viscosity (WALE) Model:* For reasons connected with the wall behavior of the subgrid-scale model, a new operator based on the traceless symmetric part of the square of the velocity gradient tensor $\bar{\boldsymbol{S}}^d$ is used, then the subgrid-scale viscosity is modeled as [113]:

$$\nu_{sgs} = (C_w \Delta)^2 \frac{\left(\bar{\boldsymbol{S}}^d \bar{\boldsymbol{S}}^d\right)^{3/2}}{\left(\bar{\boldsymbol{S}}\bar{\boldsymbol{S}}\right)^{5/2} + \left(\bar{\boldsymbol{S}}^d \bar{\boldsymbol{S}}^d\right)^{5/4}} \quad , \tag{3.10}$$

  where C_w is a model constant. As reported in [114], WALE model shows better results in predicting near wall turbulence for wall bounded flows. No wall damping is necessary near wall regions in WALE model. Another study in channel separated flow, performed by [127], shows that best match with DNS can be obtained using WALE model along-with power law-wall function, proposed by Werner and Wengle [128].

3.2.5 LES formulation compatible with ICM

An expected feature of LES model, is to retrieve DNS i.e., by using proper mesh resolution e.g., tending to kolmogorov length scales. For single-phase flow, this is true from a theoretical point of view. The residual stress tensor vanishes from the filtered equations. On the contrary, in liquid-gas flow, it means that unresolved interface modeling such as $\boldsymbol{ESA}$, has to be modified for high mesh resolution, in order to recover resolved interface features, by using approaches such as: Interface Capturing Method ($\boldsymbol{ICM}$). Therefore, for highly resolved flow, LES should switch from $\boldsymbol{ESA}$ to $\boldsymbol{ICM}$. In the following part, considering the known shortcomings of unresolved interfaces approaches, in the dense spray region, and in order to develop a model suitable also in the dilute spray region, a coupling technique between $\boldsymbol{ESA}$ and an interface capturing method $\boldsymbol{ICM}$ is proposed and detailed, as displayed in figure 3.2, highlighted in red.

There are some issues that have to be clarified. Firstly, $\boldsymbol{f}_\sigma$, is the additional force in the momentum equation due to the surface tension depending on the local curvature of the interface, and defined in equation 2.4 as $\boldsymbol{f}_\sigma = \sigma\kappa\delta(\boldsymbol{x}-\boldsymbol{x}_s)\boldsymbol{n}$. To compute this force, and to apply the jump of any variable, the most accurate ICM-DNS code applies interface reconstruction, along with dedicated high order numerical schemes. There are many successful examples in the literature of these fully resolved approaches, combining $\boldsymbol{ICM}$ method with DNS using mesh resolution high enough to compute all the flow scales, based on the curvature, VOF-PLIC (piecewise-linear interface construction), VOF/level-set coupling for unstructured and non-uniform meshes, octree meshes, among others [129, 130, 86] (Top-left/center in figure 3.2). For instance, the ARCHER code [34], is based on coupled *VOF-Level set* method for interface reconstruction, together with a *ghost-fluid* approach, to represent accurately the discontinuity of variables such as density, pressure and viscosity at the interface. This reconstruction process generally depends on the mesh geometry, hence are difficult to reproduce for body-fitted methods based on unstructured mesh, which are generally used to address complex geometries. Notice that several proposals exist, for example in the open source software: OpenFOAM® to improve this point, in particular the isoAdvector approach [131], and the so-called `interFoam` [38].

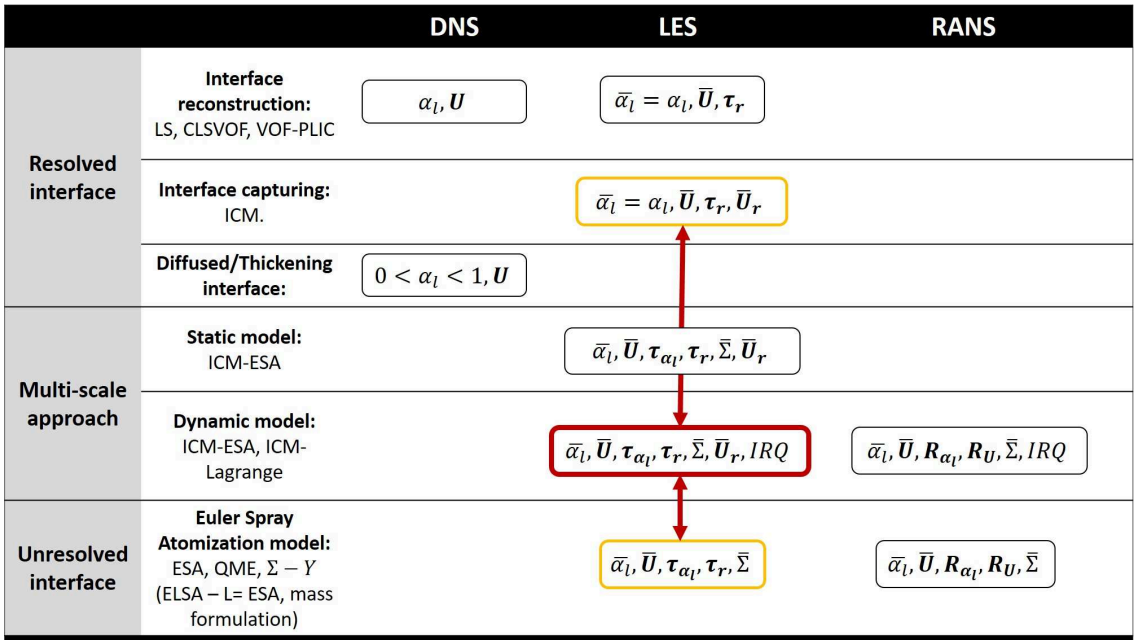

Figure 3.2: Physical-modeling representation of atomization process in turbulent liquid-gas flow. Transition from resolved interface to unresolved interface approach, namely $\boldsymbol{ICM-ESA}$, using LES framework (highlighted in red).

For full-scale resolution, $\boldsymbol{ICM}$ method aims at keeping a sharp interface, thus a discontinuous profile across the phases exits in particular during the convection process. This property is either directly included in the numerical scheme (VOF, Level-Set, ghost-fluid, among others) or obtained by additional correction designed to prevent numerical diffusion that could smear the profile. The `interFoam` solver of OpenFOAM® is based on this last technique, where Weller [104] proposed to use an additional flux of liquid directed toward the interface proportional to the local velocity magnitude ($\boldsymbol{U}_r$) and located only where a mixture of liquid and gas exists (i.e. $\alpha_l \in [0,1]$), in such a way that the local flow steepens the gradient of the volume fraction and thus the interface resolution is improved [132]. This method is often referred as the VOF method, even if there is no real reconstruction of the interface, as detailed in chapter 2 in eq. (2.8), on the right-hand side, thus when Direct Numerical Simulations (DNS) are applied, all fluctuations scales are solved up to the grid level and no filtering is required. On the other hand, following the modeling approach in this study, LES filtering framework is used. As for instance, diffusive methods are designed to smear the interface over several mesh cells, to recover a continuous behavior of any variable. It is important to emphasize that the drift/slip behavior of the residual (unresolved) liquid flux, is not compatible with the $\boldsymbol{ICM}$ method, since the former assumes the profile to be discontinuous, thus both approaches can not coexist at the same place. For unresolved interface approach, the general two-phase flow spray atomization model, originally develop by Vallet and Borghi [1] is used (explained in the preceding chapter 2). In this model, the boundary separating pure liquid and pure gas, is considered as a mixing zone. Mass and volume formulation of the conservative variables (LVF $\bar{\alpha}_l$, and interface surface density $\bar{\Sigma}$), have been already validated against available experimental and DNS data, under LES and RANS formalism, by using to that end, the so-called $\boldsymbol{ESA}$ model [33, 89, 109, 116, 133] (Bottom-right/center in figure 3.2). Hence, starting from the system reported in eq. (3.7), the liquid volume fraction equation is modified, considering $\boldsymbol{C}_\alpha$,

which is a pondering parameter between the ESA and the ICM approach:

$$\frac{\partial \bar{\alpha}_l}{\partial t} + \nabla \cdot (\bar{\boldsymbol{U}} \bar{\alpha}_l) + C_\alpha \underbrace{\nabla \cdot [\boldsymbol{U}_r \bar{\alpha}_l (1-\bar{\alpha}_l)]}_{ICM} = (1-C_\alpha) \underbrace{\nabla \cdot (\boldsymbol{R}_{\alpha_l})}_{ELSA} \quad . \tag{3.11}$$

The advantages of the proposed solver, is to determine a resolution of the interface with ICM in a limited region, whereas it would be disabled when $\boldsymbol{R}_{\alpha_l}$ prevails (i.e. when the interface fluctuations become significant, for instance in LES framework). An additional term is also added to the momentum equations 3.7 to account for the surface tension only when the interface is resolved, $C_\alpha f_\sigma$. The switching strategy is introduced through C_α. Two different criteria have been proposed to determine its value, based on the interface resolution and the curvature of the interface. C_α was set to zero (0), when the interface is poorly-resolved (dilute region) and set to one (1) otherwise (dense region), as shown in the picture below:

Figure 3.3: Ponderation parameter C_α.

- *First criteria:* IRQ_Σ. Given by the ratio of the minimum (resolved) interface area, Σ_{min} (eq. 2.12), over the actual interface area, Σ (eq. 2.15). The interface area is more properly defined as "surface area of the liquid-gas interface per unit of volume", defined here as *liquid gas interface density*. And Σ_{min}, corresponds to the minimum surface density that can be evaluated for a given value of resolved liquid volume fraction, where "a" is a length scale related to the control volume. In the framework of filtering by LES, this length is equal to the LES filter length scale.

$$\begin{cases} a\Sigma_{min} = 2.4\sqrt{\alpha_l(1-\alpha_l)} \quad , \\ IRQ_\Sigma = \dfrac{\Sigma_{min}}{\Sigma} \quad . \end{cases} \tag{3.12}$$

  Here, a simple approach is used to evaluate Σ_{min}, however, if interface reconstruction was available, the actual resolved interface could be used. Thus, the higher the surface interface fluctuates within a cell, the lower IRQ_Σ, which means subgrid effects become important, as shown in the picture below. It is to be noted, that the interface resolution quality IRQ_Σ based on Σ, would then be by definition: $0 \leq IRQ_\Sigma \leq 1$:

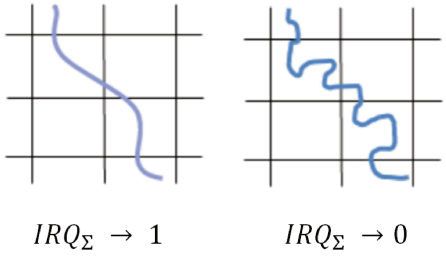

Figure 3.4: Interface Resolution Quality (IRQ) based on Σ.

- *Second criteria:* IRQ_K. A grid-dependent parameter is used to compare the interface curvature, especially if LES turbulence modeling is applied, the LES filter size can be used, defined in equation 3.6. IRQ_K takes into account the curvature of the interface, K, defined below. The higher the interface radius, the better resolved the interface become, thus C_α is then set to one (1).

$$\begin{cases} K = \nabla \cdot \left(\dfrac{\nabla \bar{\alpha}_l}{|\nabla \bar{\alpha}_l|} \right) & , \\ IRQ_K = \dfrac{1}{\Delta . |K|} & . \end{cases} \tag{3.13}$$

  It is to be noticed that for a spherical droplet, the curvature, K, could also be expressed as $K = 2/R$, where R is the droplet radius (see figure 3.5). Assuming then, as an illustrative purpose, a minimal conditioned value of number of cells, within a spherical droplet (e.g., 4 cells) was tested, to consider well-resolved interface. Therefore, IRQ_K higher than 1, would announce more than 4 cells within the droplet (i.e., resolved interface), otherwise, IRQ_K lower than 1 would mean unresolved interface. By experience, for instance, in ARCHER code [34], which is based on coupled *VOF-Level set* method for interface reconstruction. It is considered a minimum of 8 cells within a spherical droplet, in order to warrant the resolution of the interface.

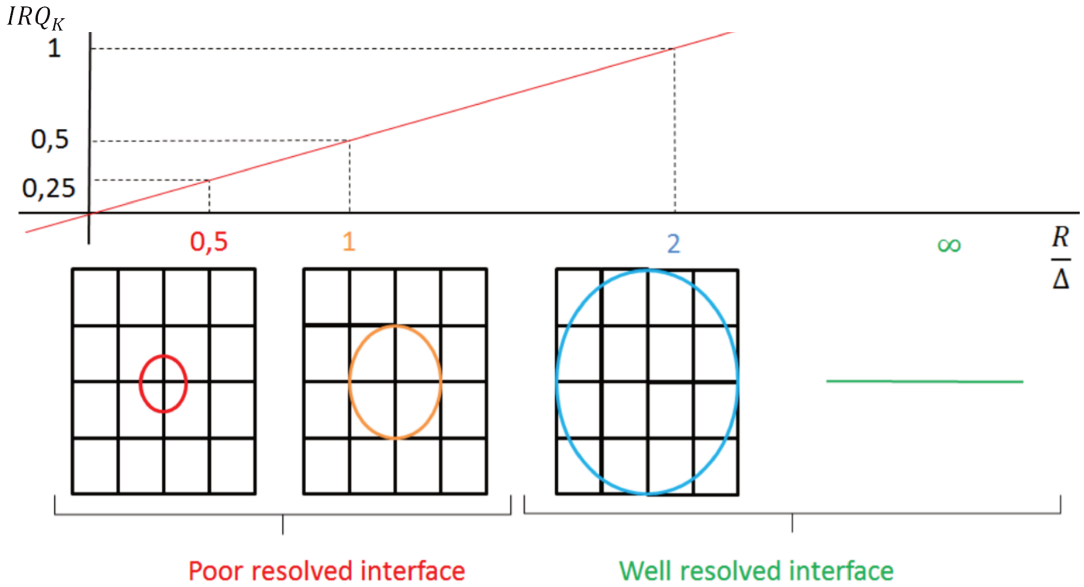

Figure 3.5: Interface Resolution Quality (IRQ) based on K [7].

Therefore, the mesh resolution plays an important role, which symbolizes the effect from the residual structures to the filtered one [134, 135]. On the one hand, as mentioned before, DNS should be capable of resolving all two-phase flow scales, theoretically. Nowadays, however, is unfeasible industrially speaking. On the other hand, the proposed dynamical model in this thesis i.e., eq. 3.11, is thus able to take advantage of a full-interface resolution, to recover a DNS formulation with ICM, and to switch to a diffusive (residual or sub-grid) LES approach, only when necessary. Note that ICM is not compatible with diffusive models, hence C_α will be dynamically adjusted to (1) one or (0) zero, depending on the interface resolution within the cell(s). Furthermore, when the spray is formed and diluted, it is more accurate to use a regular method dedicated to solved the Williams-Boltzmann Equation (WBE) [70], and therefore a Lagrangian formulation should be initiated. This topic will be further explained in the following chapter 4.

3.3 ECN numerical test case

The previous sections have described different available approaches to address the liquid-gas turbulent flow within dense zones (i.e., non-dispersed or primary atomization). The ultimate aim, is to conduct numerical simulation of fuel injection in a industrial scale, for which two comprehensive data base have been set up: (1) by the Engine Combustion Network (ECN) research group [5], and (2) by Stepowski et al. [17]. As a reminder, a full ICM-DNS approach should give the best comparison with experimental data, but it is not affordable for the time being, therefore models are mandatory. A numerical representation based on full ICM-DNS, for the initial destabilization of the complex turbulent liquid jet, going up to the spray formation, for which well established numerical model can be used, is appealing but has not yet been applied. Indeed such an approach requires the ICM-DNS to be applied up to the formation of each individual droplet. Hence, in many situation models have to be applied for the dense turbulent liquid-gas flow, among them the *ELSA* approach, has been successfully applied on an ECN database [5] by several teams [136, 137, 125], mainly in the RANS context, leading to CPU cost compatible with industrial application.

The purpose of the following test cases, is to extend the analysis considering complementary approaches based on Reynolds averaging. In addition, comparisons between RANS and LES for the dynamics of the flow are conducted, a long with an analysis of the numerical model used to represent the interface, in particular for the LES approach. For this latter aspect, the interface can be considered to be captured, at the present mesh resolution, leading to an ICM approach or the interface can be considered at residual (or subgrid) level, leading to a diffused interface approach, for which a turbulent liquid flux driven mainly by liquid dispersion is considered. The diffuse interface approach combined with the dispersion model has already been successfully tested by Chesnel et al [77], in another framework by comparison with DNS results. On the opposite view, a full ICM can be used assuming no liquid dispersion at the subgrid level. Finally, a coupled approach is also tested base on IRQ's sensors to determine locally and dynamically whether or not the interface can be well captured. The following tests, correspond to a validation step, succeeding the previous development phase [7]. Results will be employed for further improvement of the dynamic switching approach of the model i.e., eq. 3.1.

3.3.1 Numerical domain

Regarding the geometry, namely non-evaporative Spray-A, several options may be considered, from simple 2D axisymmetric configurations [136] up to full 3D simulations, with inside-flow injector and needle movement [125]. In both cases it has been possible to show that even with the less resolved modeling (RANS), the essential features of the injection can be captured with *ELSA* approach. An axisymmetric test case was also studied in a previous work [5]. On the other hand, to try to determine the internal flow field as best as possible, the starting point is to get the actual geometry of the injector. A measured 3D geometry is also available from ECN database, which has been obtained using high resolution X-ray tomography [67]. Nevertheless, owning to the measurement uncertainty of the experimental apparatus, combined with the variation in the nozzle diameter/sections of the order of a fraction of microns, a representative average profile cannot be obtained by one such measurement. Instead a smoothing process is required based on detailed measurements of the nozzle exit diameter and specific sections to improve the geometry [67, 138, 139]. In this case, only slight noise suppression was used to smooth the geometry.

It is to be noted that preprocessing of mesh files obtained from tomography takes considerable time. Hence the decision to spend time on this aspect should depend on the expected quality of results and measurement uncertainty of experimental reconstruction algorithms. The most important fact regarding our experience to design such a mesh [16], is the necessity to choose between arbitrary parameters during the mesh construction/smoothing process. Eventually, the proposed mesh would be only one possible representation of the geometry. Other choices during the mesh building process would lead to another approximation of the geometry. The available data, despite the great effort performed by ECN network on this topic, would not permit to discriminate the best solution to this problem. It is also necessary to mention that the moving needle motion is not considered in this thesis either ,which is also an important limitation regarding the internal flow, even if results reported here concern the established flow. Results obtained using such a geometry were reported in [16].

Here, only $3D$ simplified domains are considered, thus better representing the three dimensional nature of turbulent eddies, in particular while using LES formulation. The $1D$ averaged axial profile of the injector (210675) is taken from ECN website (red line on the Figure 3.6). The geometry was extended to include the injector sac and needle. The profile is then rotated to create a $3D$ mesh.

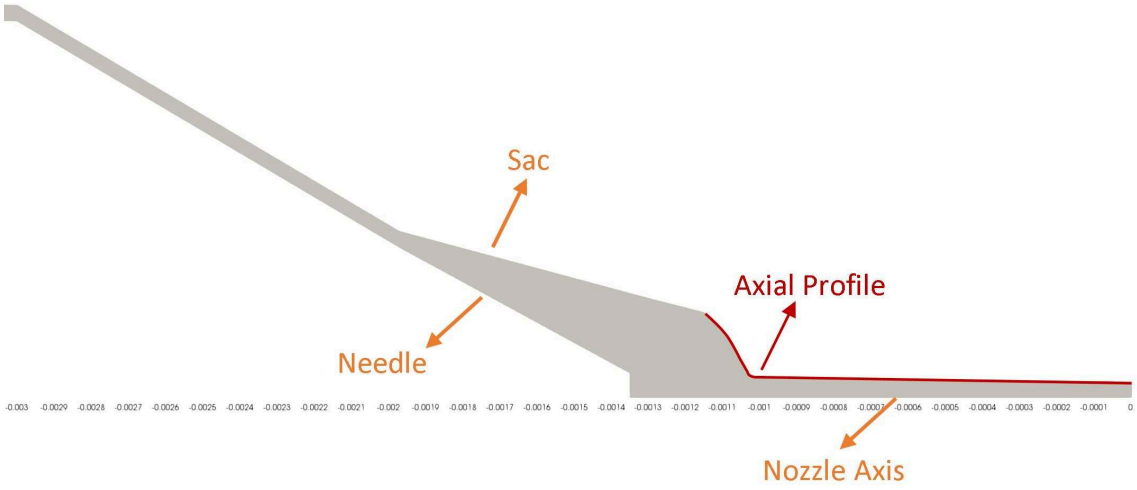

Figure 3.6: Averaged axial profile used, to make a simplified 3D geometry

For the simplified geometry, two numerical meshes have been studied. One *coarse* mesh to get quicker results, and another *fine* mesh to see the fluctuating interactions with the interface. For the latter case, and with initial estimates of velocity profiles from ECN experimental results, the Taylor length scale [90] was used, which can be calculated following the equation below:

$$\lambda_g = D_{inj}\sqrt{10}Re_{D_{inj}}^{-\frac{1}{2}} \quad , \tag{3.14}$$

which gives $\lambda_g \approx 1.26 \times 10^{-6} m$. The *fine* mesh has cell size of about $1\ \mu m$ at the exit of the injector. The cell size was increased gradually to about $12\ \mu m$ at the end of the chamber. The total length of the domain after the injector exit is $10\ mm$. The issued details of mesh parameters are shown in Table 3.1. Indicated number of cells at nozzle exit in the table below, are across the interface.

Table 3.1: 3D Meshes

	Cells at the Nozzle Exit	Total Number of Cells (M)
Coarse mesh	56	4.85
Fine mesh	98	32

The cross-section of meshes for the 3D simplified geometry, transverse section and at the exit of the nozzle, are shown in the figures 3.7 and 3.8, respectively:

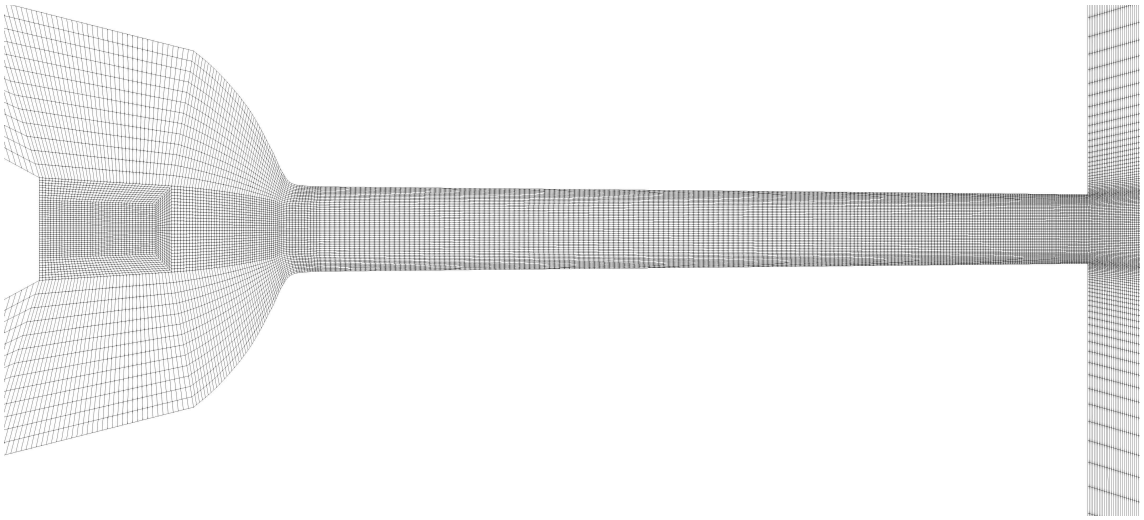

Figure 3.7: A transverse section of the coarse resolution mesh.

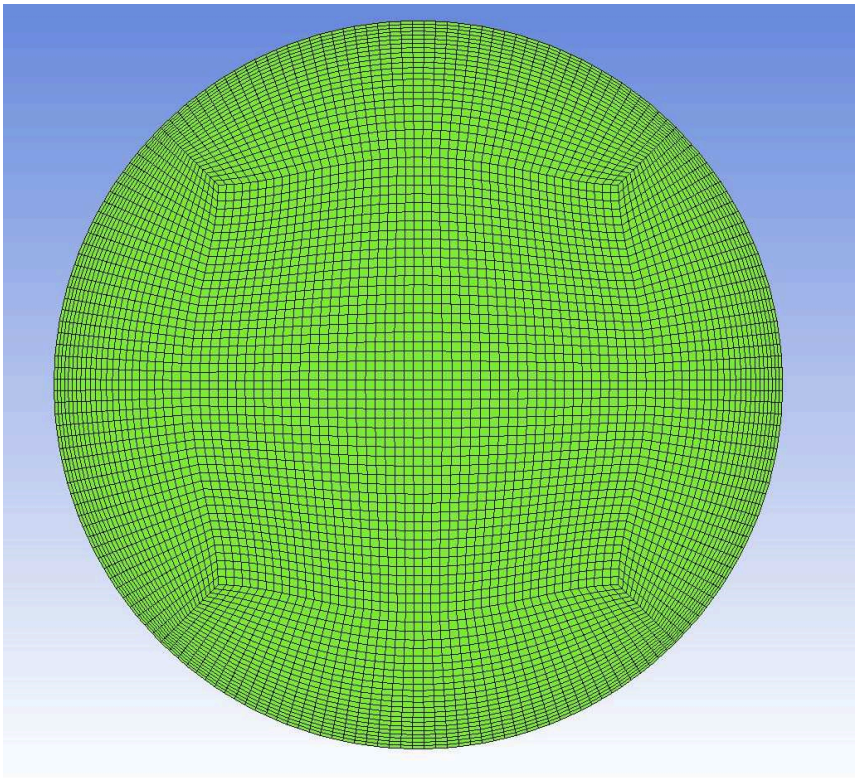

Figure 3.8: Cross sectional view of the mesh, at nozzle exit. Fine resolution mesh

3.3.2 Properties and boundary conditions

In reality, the injector also includes an axial displacement of the needle [125]. Nevertheless, transient mass flow rate inlet boundary condition, allows to reproduce partly the effects of the needle motion [136, 137, 140]. In compressible formulation, one can also use time varying total pressure inlet boundary condition to mimic the actual flow development [141]. Nonetheless, the established jet, which is the main subject of this study, can be obtained directly with a constant mass flow rate inlet [142]. Operating conditions for a typical ECN Spray-A, are reported in Table 3.2:

Table 3.2: Conditions for non-evaporating ECN Spray-A [5]

Fuel	n-Dodecane
Ambient composition	100% N2
Injection pressure [MPa]	150
Ambient pressure [MPa]	2
Ambient temperature [K]	303
Ambient density [kg/m^3]	22.8
Fuel injection temperature [K]	343

Results reported here focus on the established flows, thus simulations were performed with constant mass flow rate inlet boundary condition, until a statistically stationary state is obtained. For the chamber, *outflow* boundary condition is used. While for the chamber tip, i.e. the surface adjacent to the injector exit, is treated as *wall*. A *total pressure* boundary condition is imposed on the outlet and chamber patches. Σ', is modeled with *zero gradient* type boundary condition for all boundaries (outlets), except at the inlet, in which its value is set equal to zero. Second order backward time scheme, is used for all quantities except for α,

in which a special procedure called MULES, is used to preserve boundedness of this quantity. This special treatment is applied for the liquid volume fraction, in order to keep it bounded [104], besides, local sub-cycling of phase fraction equation is possible and in this work, three local sub-cycles are used. The time-step is limited by Courant number Co, and an additional variable defined for two-phase flow, namely Interface Courant number $Co_{interface}$, which is applied on regions near the liquid-gas interface. In the software it is determined as follows:

$$Co_{interface} = pos(\alpha_l - 0.01)pos(0.99 - \alpha_l)\max\left(\frac{|\mathbf{U}|}{\Delta x}\right)\Delta t \quad , \tag{3.15}$$

where $pos(x)$, is a mathematical function specified in OpenFOAM® , which returns 1, if x is greater than or equal to zero, and returns 0, otherwise. Basically, this Interface Courant number $Co_{interface}$, will be only applicable only near the liquid-gas interface. The maximum Co and $Co_{interface}$ are then set to 0.25. The time-step is adjusted automatically to limit the Courant number to be below the imposed constraint, which finally resulted in a time-step between 2×10^{-10} s to 3×10^{-10} s on the fine mesh.

From the previously described models, and depending on the equations solved, there are several possibilities: Initially, ELSA model using RANS, namely `ELSAFoam` solver. Likewise, LES and ELSA using different turbulence models, such as WALE and Smagorinsky. The effect of mesh resolution and type of LES model is also important, thus we have simulated two meshes. Results based on Favre averaging have already been reported previously [136, 137, 125]. As mentioned previously, a Reynolds-based averaging is used in this work. Additionally, LES with ICM, using WALE turbulence model, namely `interFOAM` solver was also examined. In the end, LES coupled with dynamic switching between ICM and ELSA, based on IRQ's, namely `icmElsaFoam` solver was verified. Summary of all the configurations studied are shown in Table 3.3.

Table 3.3: Different cases set-up.

Solver	Equations solved	Coarse Mesh	Fine Mesh
`elsaFoam`	Eqn. 3.11, Static C_α *= 0*		LES (Smag.)
`interFoam`	Eqn. 3.11, Static C_α *= 1*	LES (WALE)	LES (WALE)
`icmElsaFoam`	Eqn. 3.11, Adjustable C_α *(0 or 1)*		LES (WALE)
`icmElsaFoam`	Eqn. 3.11, Adjustable C_α *(0 or 1)*		LES (Smag.)

3.3.3 Results and discussion

A comparison process has been made against experimental and numerical data available from the Engine Combustion Network (ECN) in order to validate the proposed ELSA model. The data available from ECN website, in the form of Liquid Volume Fraction (LVF), Projected Mass Density (PMD) and Transverse Integrated Mass (TIM) are used for validation purpose, and to compare the impacts of different modeling approaches. Note that LVF data were obtained from PMD measurements, with a mathematical transformation [143], that assumed axi-symmetrical flow. The 'Spray-A' non evaporating configuration has been selected, with exact aforementioned fluid properties. The experimental data used for validation include the PMD of the fuel, which was obtained by a line-of-sight integration along the X-ray radiography measurement [138, 62], and the TIM, which was acquired from the integral of the projected density across a transverse position at a particular axial location [61].

In order to visualize the impact of different turbulence models, figure 3.9, shows instantaneous velocity magnitude, scaled to an equal value for all the simulations. Smagorinsky model

(second image from top to bottom) is not able to capture any velocity fluctuations at the exit of the injector, even after the first ten diameters of injector (at 1 [mm]). Indeed, due to the high Reynolds number ($\approx 5.7 \times 10^4$), it is expected a turbulent flow at nozzle exit (right edge of figure 3.6), as also reported in [144]. On the other hand, WALE model (first, third and fourth image from top to bottom) shows some instabilities right at nozzle exit. On the other hand, WALE model is able to capture the internal nozzle flow velocity fluctuations even with *coarse* mesh, (third image from top to bottom), thus giving the opportunity for turbulence inside the jet to be developed. The effect of refining the mesh is not very pronounced here, however, decreasing the mesh size, would certainly help in resolving small-scale vortex structures. To have a clear difference of LES models, visualization of flow field at nozzle exit using fine mesh is shown in the next figure 3.10.

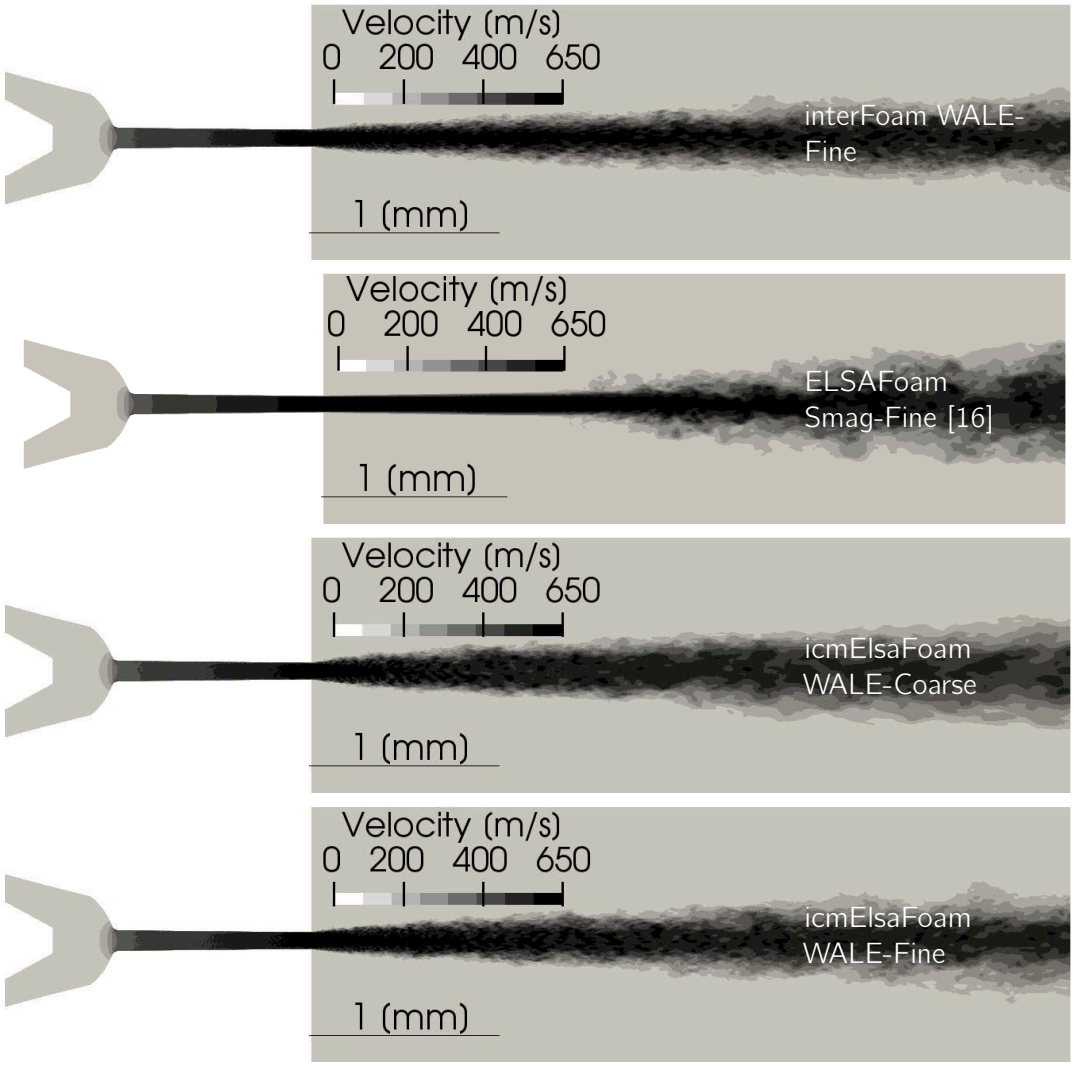

Figure 3.9: Instantaneous velocity magnitude for different cases.

Figure 3.10, the top half image, shows the slice of velocity field at nozzle center plane obtained using Smagorinsky model, while the bottom half, shows the one obtained using WALE model. In-nozzle turbulent flow field fluctuations are captured by WALE model, as expected, in contrast with Smagorinsky model, in which no velocity fluctuations are perceived. By using an even finer mesh with Smagorinsky model tending to a DNS approach, results may be comparable, however such a study is outside the scope of this work. Turbulence field observed by WALE model, also has pronounced effect on interface surface perturbations at the exit of the injector, as shown by the previous velocity field, figure 3.9, within the first few

diameters downstream of the injector. Inlet boundary conditions have always been an issue for atomization process. DNS simulations have shown the strong impact on the flow, based on the inlet conditions, turbulent intensity and velocity profile [34, 34]. The purpose of $\boldsymbol{ESA}$ approach is to be able to represent the flow inside the injector. In this case, it appears that instead of fully developed flow, the flow is driven by of wall boundary layer development i.e., wall-bounded turbulent effects. Consequently, a suitable turbulent model should be used for LES, e.g., WALE turbulence model, has shown better wall-bounded behavior than Smagorinsky in this situation. Thus, in the later part of this paper no results, using Smagorinsky model, are further discussed.

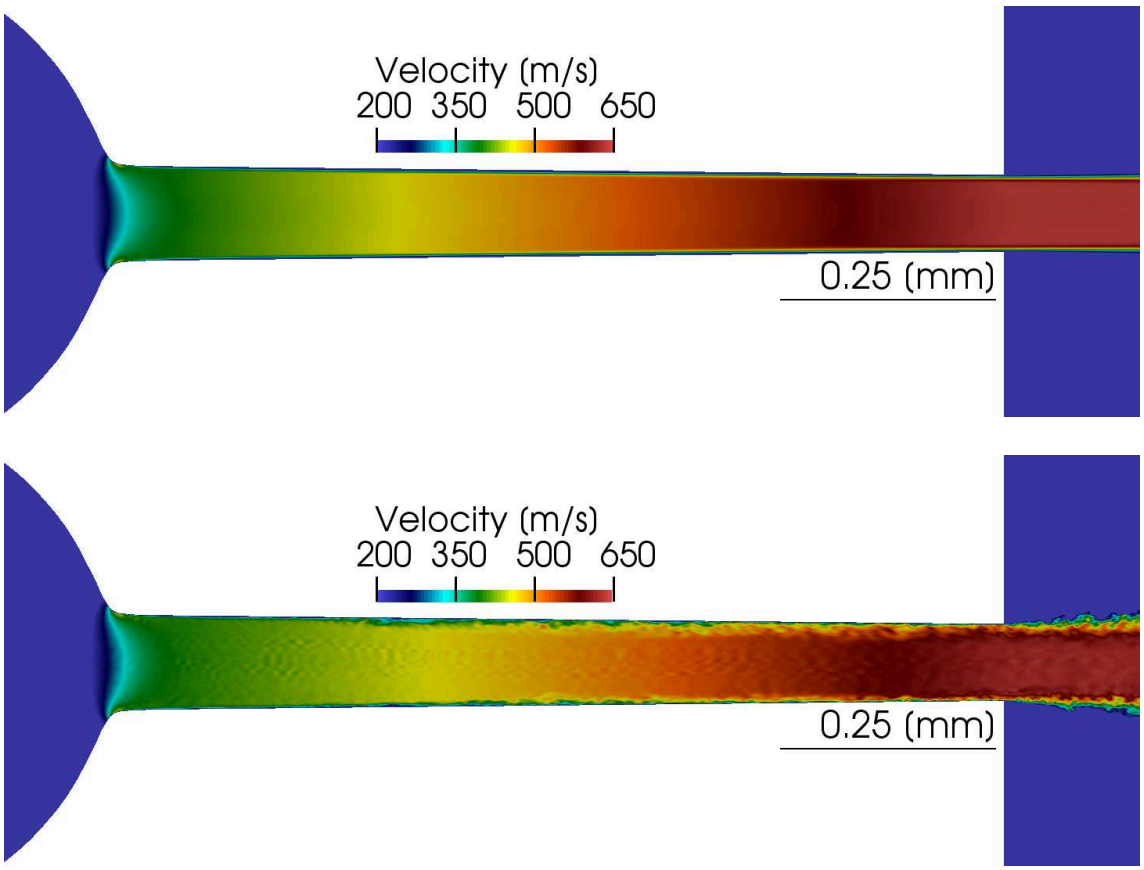

Figure 3.10: Effect of LES model on velocity. Velocity at nozzle center plane. Top figure: Smagorinsky, bottom figure: WALE model with the identical fine mesh. On the right edge of figure, the blue region indicates the start of ambient atmosphere, where nitrogen is initially assumed at rest.

Qualitative analysis of instantaneous LVF of established jet, is shown in figure 3.11. As it is known, the shortcoming of RANS is that, one cannot expect to obtain any further information just by increasing the mesh size implicitly. LES on the other hand, simulates more and more scales, as we keep on refining the mesh, hence decreasing the dependency on the modeling terms (residual or SGS tensor). With LES and the turbulence WALE model, `icmElsaFoam` relies on subgrid modeling, thus by decreasing mesh size, decreases the dependency on subgrid modeling. In-contrast, `interFoam` is developed on the ideology of capturing the interface and keeping it sharp, which is a physically correct approach, but is limited to cases with high mesh resolution. Therefore, if the mesh is not fine enough, the model produces diffused interface, which is basically numerical diffusion. This is clearly visible in figure 3.11, on the first and second row (from top to bottom), it can be seen the effect of mesh refinement,

which changes the liquid volume fraction field significantly. The liquid core appears to be attached for longer axial length, and individual small packets of fluid are captured as well. Even if the numerical diffusion seems to decrease, by increasing the mesh resolution, it only means that the sharpening term is not able to keep the liquid parcel at the present mesh resolution. By doing so, it applies a numerical force, that prevents droplets breakup at smaller scales than the cell size. Indeed, this is another kind of numerical error i.e., an additional surface tension produced by numerical error. This type of numerical behavior has to be prevented and replaced by a physical approach. We have thus, proposed a methodology to identify this mesh-dependent feature, by using the IRQ criteria introduced previously in chapter 2. Consequently, `icmElsaFoam` should give an intermediate result between `interFoam`, within the first millimeter, and `elsaFoam`, in the last part of the domain, which is in fact, the expected behavior of the model. Finally, by using `icmElsaFoam`, the numerical diffusion is replaced by the *residual turbulent liquid flux*, which is a more physical and preferable subgrid approach.

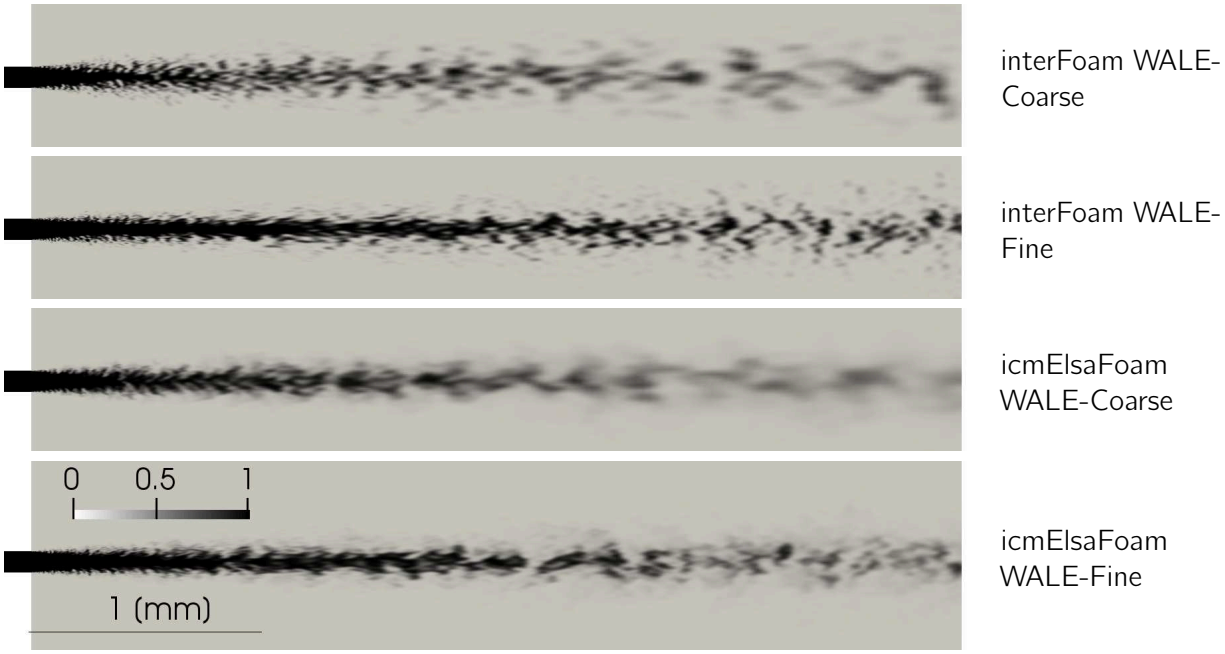

Figure 3.11: Instantaneous liquid volume fraction for different cases

A quantitative analysis for mean LVF is shown in Figure 3.12. The top row in Figure 3.12 shows results obtained using coarse mesh, and those with fine mesh, are shown in the bottom row. At 2 mm with the coarse mesh, figure 3.12(a) on the left, both models, `interFoam` and `icmElsaFoam`, fail to predict the experimental mean LVF profile, underestimating the liquid penetration. These results are expected, since the diffusivity added by the coarse mesh, is playing some role, indicating that a finer mesh is required. This feature is indeed verified in figure 3.12(b) on the left, in which a refined mesh produces comparable results. Therefore, refining the mesh further produces a better experimental match. At 6 mm, on coarse mesh, it seems the numerical diffusion produced by `interFoam` gives the same results as predicted by subgrid modeling, `icmElsaFoam`. This is however, a mere coincidence, since even with fine mesh `interFoam` cannot capture all the flow physics as verified by the unphysical high value peak of LVF, figure 3.12(b) on the right. From this discussion, it is emphasized on the point that, interface capturing methods (`interFoam` and others such as level set [34], ghost-fluid [47], level set coupled with VOF method [51]) are very good as far as the mesh requirements are met. Figure 3.12(a) on the right, proposes a challenge to determine until what extent the numerical diffusion is backing up `interFoam`. Once the mesh is not refined

at satisfactory level, the results obtained, are not very reliable, because there are linked to uncontrolled numerical errors. In the case of `interFoam`, this error appears like a numerical diffusion, which may well disguise the numerical diffusion, into subgrid dispersion. However, this numerical error leads to results that are dependent of the mesh resolution. Other ICM approaches, that always preserve a sharp interface such as based on Level Set Method, limit spray dispersion at the grid resolution and then neglect the subgrid liquid dispersion [77], hence bringing an other kind of numerical error, which also leads to mesh resolution dependency. To address subgrid liquid dispersion, it is better to rely on physical subgrid modeling, and to take advantage of ICM, where the mesh resolution is high enough.

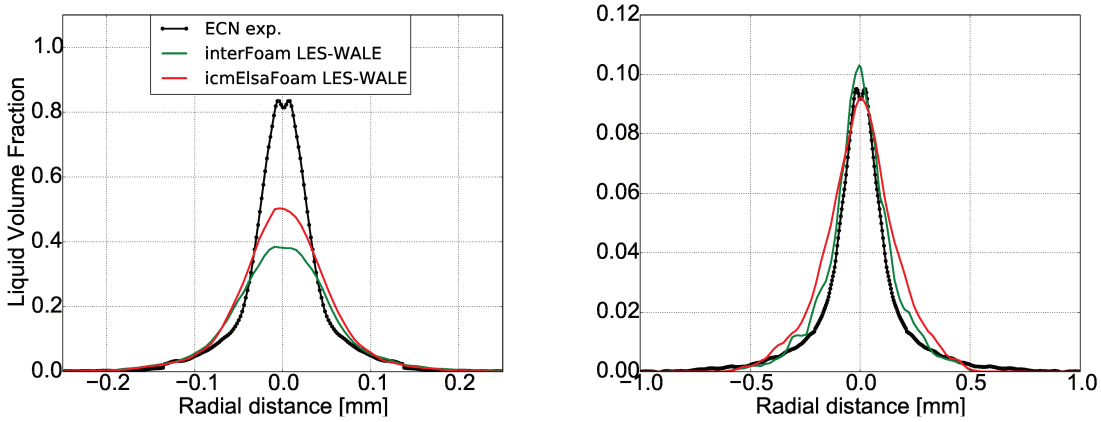

(a) Coarse mesh

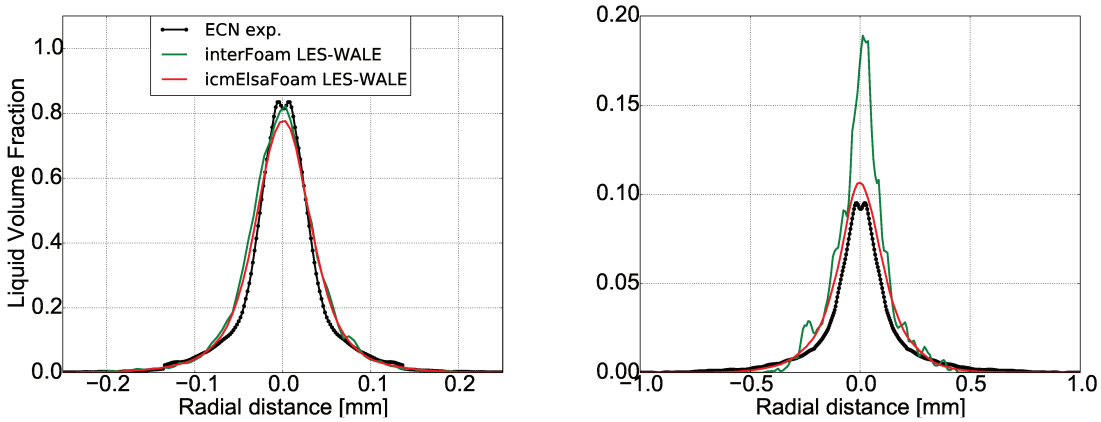

(b) Fine mesh

Figure 3.12: Mean LVF radial profiles at 2 mm (left) and 6 mm (right)

Along the same line of thought, `icmElsaFoam` (see equation 3.11) is introduced to switch off the ICM, when subgrid fluctuations become important, and switch it on, when mesh density supports such implementation. For low mesh resolution, `icmElsaFoam` will rely more on subgrid modeling, however, it seems preferable to recognize the necessity of subgrid modeling and then to close them appropriately. The PMD (from which the LVF has been extracted) is now directly used to compare the numerical results with the experimental ones, from ECN data base. This Projected Mass Density (PMD), was obtained by a line-of-sight integration of fuel density, along the X-ray radiography measurement [138, 62].

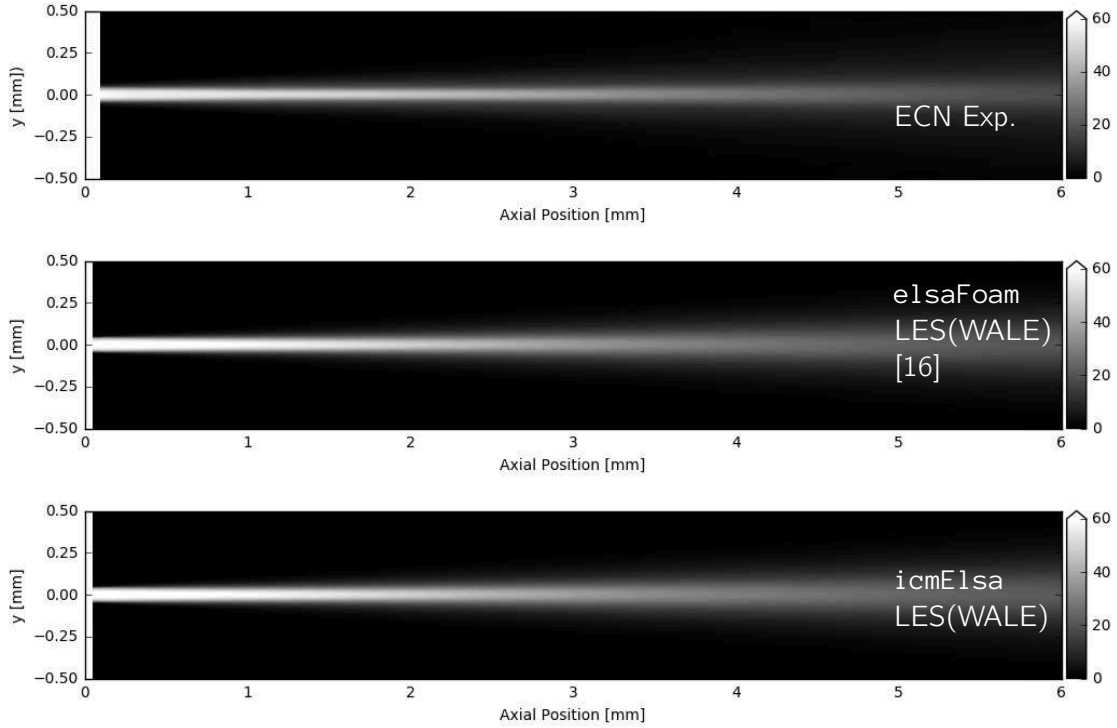

Figure 3.13: PMD results (in $\mu g/mm^2$) for different cases with fine mesh.

Figure 3.13, with regard to previous results, `elsaFoam` and `icmElsaFoam` clearly show much better and comparable results with experiments, for liquid penetration and dispersion. Additionally, there are not observed appreciable differences between both numerical solvers. Hence, a better way to characterize the PMD, is a quantitative radial profile at various axial distance from the exit of the injector. The results for *fine* mesh, and WALE turbulence model for such computations, are shown in figure 3.14. Again LES is able to capture the minute details of flow stretching, at the radial periphery of jet, due to a better capturing of turbulent flow field. Thus, instead of straight line profile at the two tails of the PMD curve, a curved profile is predicted as indicated by experiments as well. Secondly, at 2 mm ($\approx$ 20 times axially, the injector diameter, on the left of the figure) there are no considerable differences between `elsaFoam` and `icmElsaFoam`, which is an indicator of large fluctuations existence in this near-field spray, mainly due to the high turbulence coming from the in-flow nozzle conditions and the high shear stress with the surrounding gas, which is the highest within the near flow field. Thirdly, at 6 mm ($\approx$ 60 diameters from the exit, on the right of the figure), even if differences are small, `elsaFoam` is the one that matches the best compared with experiments. On the other hand, `icmElsaFoam` slightly overestimates liquid penetration, compared to `elsaFoam`, apparently decreasing the additional fluctuations, within this dilute/dispersed zone, more than it should.

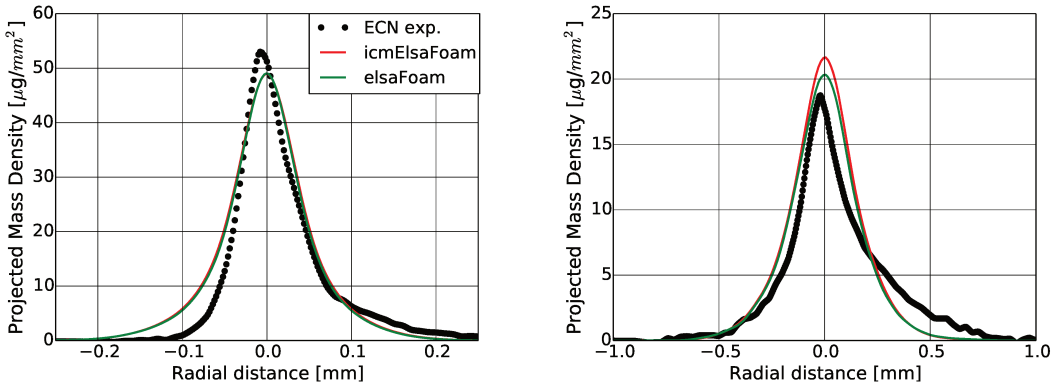

Figure 3.14: PMD radial profiles at 2 mm (left) and 6 mm (right), using fine mesh, and WALE, as the turbulence model.

A useful parameter might help to discern the residual or subgrid dominance within this dilute/dispersed zone, namely C_α, defined in equation 3.11, equals one (1) when the interface is resolved, and equals zero (0) otherwise. It is to be remarked, that this parameter, depends on the interface curvature and surface interface density, in which both variables are only characterize at the interface i.e., there is not sense defining such variables in regions of pure liquid or gas. Figure 3.15 shows just after a few millimeters after injector exit, subgrid scales become a paramount importance and the interface is diffused rapidly, mainly due to two prominent parts: (1) high shear stress with the surroundings i.e., turbulence generated at the liquid-gas interface, that creates small wrinklings on the surface, not captured by the actual *fine* mesh, and (2) quite a few amount of eddies generated within the nozzle, hence increasing velocity fluctuations right at the injector exit. To go further, a better mesh resolution is necessary to keep track of the actual interface position, downstream of the liquid jet. For the present work, the area for which the interface is considered well captured by `icmElsaFoam`, cover a very small range of the atomization process, just at the vicinity of the injector nozzle i.e., *ICM* is rapidly switched off. Nonetheless, this zone may be important to relate the injector in-flow characteristics, especially to the initial destabilization of the liquid jet interface.

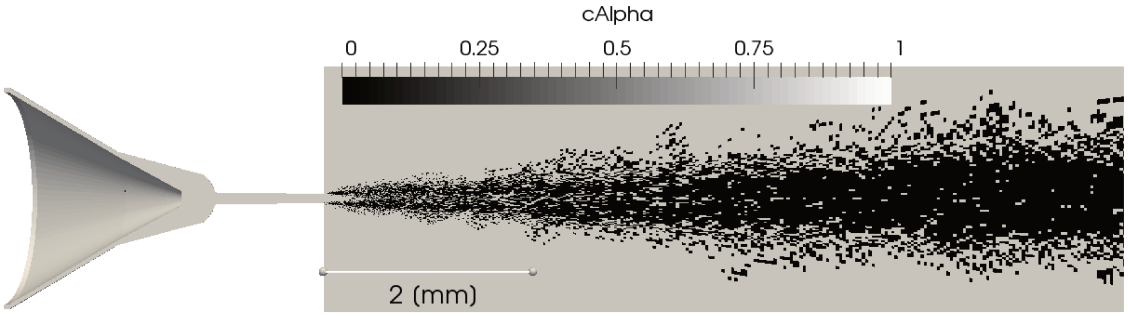

Figure 3.15: C_α colored map.

Transverse Integrated Mass (TIM), which was acquired from the integral of the Projected Mass Density (PMD), across a transverse position, at a particular axial location [61], is another experimental quantity which represents the dispersion of the atomized liquid axially. A higher value, indicates that at certain axial position, the amount of liquid is higher radially. This feature may be due to a high rate of liquid dispersion, that spreads away from the centerline of the jet, or also due to a higher liquid penetration that keeps an important liquid amount on the axis. The results for TIM are shown in figure 3.17. As verified previously, `elsaFoam`,

icmElsaFoam produce comparable results and a noticeable improvement with respect to RANS approach, obtained previously by anez et al.. [16]. Nonetheless, icmElsaFoam displays slightly higher value of TIM than elsaFoam, which does not necessarily mean icmElsaFoam is more diffusive than elsaFoam, but the integral of projected mass density (PMD), across the transverse axis at particular positions is higher, which is in agreement with figure 3.14, owing to greater liquid penetration at 6 [mm] for instance.

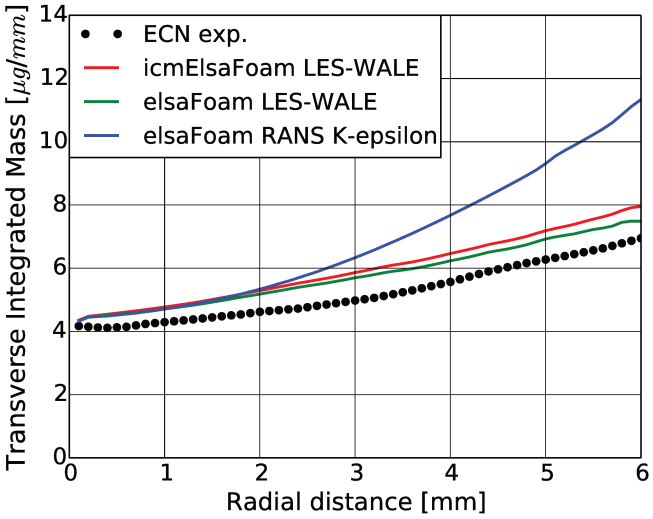

Figure 3.16: TIM for different cases with fine mesh.

The improvement obtain by using LES with respect to RANS simulation, are in line with results presented by Desantes at al. [117]. As for RANS, they have used a mass weighted formulation for LES, however, the results are comparable to those presented in this work. Interestingly, they have used a synthetic turbulent inlet condition, and started the computation from the exit of injector nozzle. One of these inlet model parameters, is the turbulent intensity, that they varied from 3% to 5%. This small change produced differences in terms of PMD and TIM, that are of the same order of magnitude to those obtain in this work between elsaFoam and icmElsaFoam. Since the main difference between these two approaches to the current test case is due to the link with the internal flow, it may be concluded that the model developed are sensible enough to capture the differences within nozzle flow conditions. Accordingly, the internal flow field description, becomes a paramount feature of the whole simulation.

3.4 Air-blast atomizer numerical test case

For this second test case, we apply the solver icmElsaFoam, to predict the primary breakup of a single cylindrical liquid jet in an air-blast atomizer configuration. Numerical results will be compared with experimental results from [17]. The test case has been chosen for three reasons: (i) Experimental data are available, about the mean liquid volume fraction in the primary atomization region; (ii) previous numerical studies [116] showed, on the same test case, that RANS turbulence model requires a strong modification to get appropriate results, hence prompted the use of LES models. And finally (iii), liquid Reynolds and gas Weber numbers are relatively low, compared with the previous ECN test case, hence more flow regions are expected to be resolved (i.e., with $C_\alpha = 1$). Therefore, it seems pertinent to use the solver icmElsaFoam. In the near nozzle field, the ICM will effectively capture the surface instabilities and liquid structure detachments. A fine resolution will thus be necessary in the near flow field. In the far field, however, the *ELSA* method might be able to treat low volume

fractions of the liquid that has been atomized and dispersed. The configuration while being turbulent, a Large Eddy Simulation (LES) turbulent model will be employed, to model until certain extent, the small eddies of the flow.

3.4.1 Numerical domain and flow conditions

The considered configuration, issued from Stepowski et al. [17], consists of injecting a low-speed liquid through a circular pipe, and a high-speed gas through an annular pipe, into a steady atmosphere. Experimentally, to obtain the near field of liquid volume fraction, α_l, the fluorescence emission of an additional specie, incorporated into the water, induced by a pulsed laser sheet, was used [17].The liquid used is pure water, and ambient gas is considered as dry air, leading to a density ratio of approximately 1000. The sketch of the injector is presented in figure below:

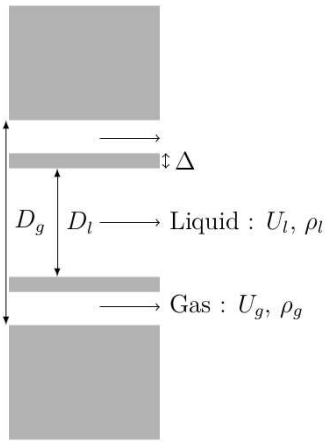

Figure 3.17: Schematic image of air-blast injector used by Stepowski et al. [17].

Geometrical characteristics of the experimental device, are as follows: $D_l = 1.8\ mm$, $D_g = 3.4\ mm$, $\Delta = 0.25\ mm$, $U_g = 115\ m/s$, $\rho_g = 1.2\ kg/m^3$, $U_l = 1.3\ m/s$, $\rho_l = 1000\ kg/m^3$. An additional non-dimensional variable is used for this numerical test case, namely the Momentum flux ratio, J, expressed as:

$$J = \frac{\rho_g (U_g)^2}{\rho_l (U_l)^2} \quad , \tag{3.16}$$

The Momentum flux ratio, plays an important role in destabilization of the liquid jet, and in the liquid core length, especially in this type of injector Values of the known characteristic non-dimensional numbers, are reported in the following table:

Table 3.4: Simulated flow conditions.

$U_g\ (m/s)$	$U_l\ (m/s)$	We_g	Re_g	Re_l	J
115	1.3	500	8000	2600	10

The computational domain is defined as a cylindrical mesh, with height of $16D_l$ and a diameter of $8D_l$, as shown in figure 3.18. A small inner portion of the inlet pipe is modeled, whose length is equal to $0.1D_l$, and allows to account grossly for wall boundary layer, especially with liquid inlet.

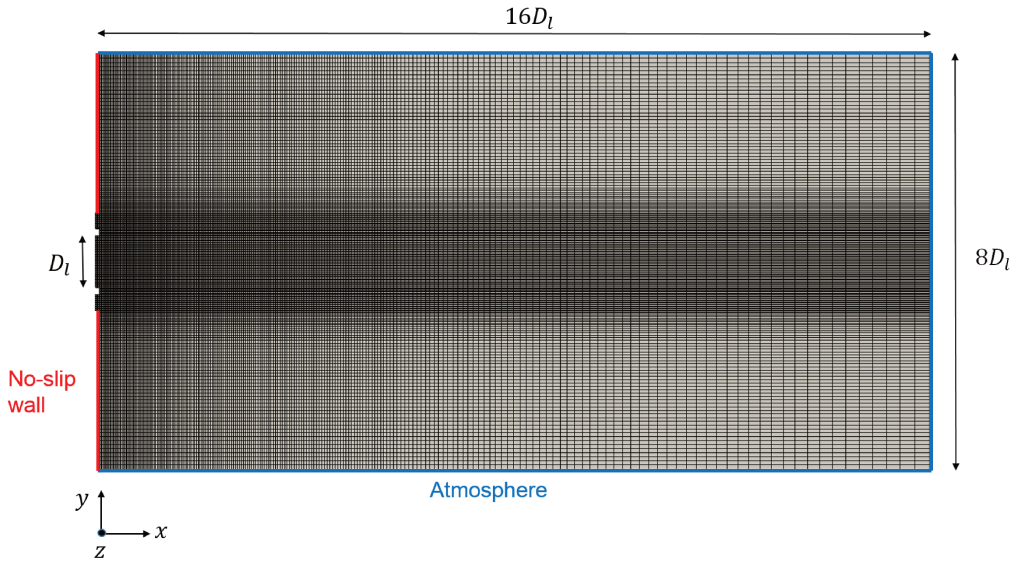

Figure 3.18: Dimensions and boundary conditions of the computational domain. [18].

An expanding mesh is used far from the gas and liquid inlets, to focus refinement efforts close to the inlets, especially in the following region: [$-0.1\ D_l$, $3\ D_l$] x [$-1.1\ D_l$, $1.1\ D_l$] x [$-1.1\ D_l$, $1.1\ D_l$], that covers pretty much primary and secondary atomization. Estimation for the minimal LES mesh resolution, Δ_x, is recommended by Addad et al. [19]:

$$\begin{cases} \Delta_x = max(\Lambda, l/10) & , \\ \Lambda = \sqrt{10} l (Re_l)^{-1/2} & , \\ l = 0.07 D_h & , \\ Re_l = \dfrac{k^{1/2} l}{\nu} & , \end{cases} \tag{3.17}$$

where Λ is the Taylor micro-scale, l is the turbulent length scale at gas nozzle exit, D_h is the hydraulic diameter, and k is the turbulent kinetic energy. Further from the nozzle, the turbulent length scale and the Reynolds number are estimated based on *a posteriori* known spray cone diameter, and mean velocity magnitude. Hence, the above mentioned estimations give the minimum mesh size near the gas nozzle, $\Delta_x = 39\ \mu m$. Finally, the number of cells at liquid nozzle exit, 48, and the cell size both at liquid and gas nozzles, is $37.5\ \mu m$, as shown in the figure 3.19

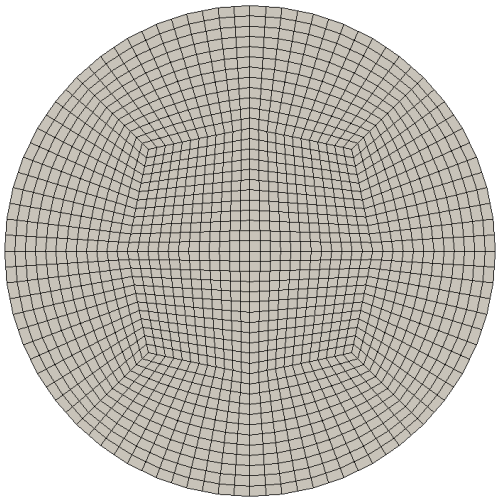

Figure 3.19: Discretized liquid inlet patch. [18].

3.4.2 Boundary conditions

Regarding the boundary conditions, *Dirichlet* boundary condition, for velocity, is imposed at gas and liquid inlets. It is also set to zero (0) value along the walls, and an *inlet-outlet* boundary condition, which is a mixed Dirichlet-Neumann type, is applied on the atmospheric blue patch, highlighted on figure 3.18. For the pressure, *Total pressure*, is specified on atmospheric patch. For the liquid volume fraction, a fixed value equal to one (1) at liquid inlet and to zero (0) at gas inlet. *Zero gradient* is applied along the wall, and an *inlet-outlet* boundary condition is applied on the atmospheric patch. Initial conditions are at rest, for the whole domain, with null velocity and atmospheric pressure. The liquid pipe, is initially filled with water. An adaptive time-step is used, which constraints a maximum $\boldsymbol{CFL}$ condition equal to $\mathbf{0.5}$.

Gas inlet

Gas Reynolds number, $\boldsymbol{Re_g} = 8000$, shows the turbulent character of the flow. It was previously shown, using momentum flux ratio, $\boldsymbol{J}$, varying between $\mathbf{0.17}$ and $\mathbf{2}$, that the initial interface perturbations caused by liquid and gas eddies plays an important role in the resulting surface instability development and primary breakup process [103]. Therefore, when turbulent inflows were specified, it was correctly predicted the experimental core breakup lengths. In the present work, simulated configuration shows a momentum flux ratio with a value of $\mathbf{10}$. One can thus assume that gas eddies, will have an impact on the interface disturbance and that gas unsteady turbulent inlet velocity conditions, should be specified. To do so, the decaying turbulence inflow generator [145, 146] is used. Hence, the velocity field, is represented as the sum of velocities induced by a set of randomly distributed spots. Velocity distribution inside of each spot is found in such a way that, the fluctuations possess prescribed statistical properties. These statistical properties are mean gas velocity $\boldsymbol{U_g}$, turbulent kinetic energy $\boldsymbol{k}$, turbulent length scale $\boldsymbol{l}$, and the known six components of the symmetric Reynolds-stress tensor, expressed for a round jet as [90]. The above expressions are represented as follows:

$$\begin{cases} \overline{\boldsymbol{U'^2}} = \dfrac{2}{3}k \quad , \\ k = \dfrac{2}{3}(\boldsymbol{U_g} T_i)^2 \quad , \\ T_i = 0.14(\boldsymbol{Re_g})^{-0.079} \quad . \end{cases} \tag{3.18}$$

Despite a high mesh refinement, regarding Taylor length-scale, as previously mentioned, it is commonly admitted that the biggest eddies should be modeled with at least $5-8$ cells, to avoid numerical decay of turbulent structures. Consequently, instead of increasing the mesh refinement, hence computational cost and time, we chose to increase the turbulent length scale, see equation 3.17, in order to keep turbulent structures at inlets. The turbulent length scale value, l, used for the turbulence inflow generator, is then set to 20% of D_h.

Liquid inlet

A criterion parameter, K, was defined to assess the relative importance of liquid inlet velocity distributions, on the liquid breakup shape, of a selected atomizer [84].

$$\begin{cases} K = \dfrac{\delta_o}{\Delta} \quad , \\ \delta_o = cD_l(Re_l)^{-1/2} \quad , \end{cases} \tag{3.19}$$

where Δ is the central tube thickness, and δ_o is the liquid initial vorticity thickness, at the nozzle exit. The coefficient c, depends on the nozzle design. Previous work [14], studied the boundary layer in axisymmetric nozzles, and determined that the value of c, is approximately 5.6. From the previous formulations and assumptions, a criteria value of $K = 0.8$, is found appropriate. In [84], small and large K cases, are considered for criterion values of 0.3 and 2.4, respectively. It was shown that an uniform velocity distribution is convenient in the small K case, while an exponential velocity distribution, is suitable in the large ones. In the current configuration, with $K = 0.8$, we consider being closer to a small K case than to a large one. Therefore, a uniform velocity distribution is prescribed to liquid inlet. It also allows to be strictly conservative regarding liquid mass flow rate. Despite this is an approximation, its expected influence should not be very important, because of the high momentum flux ratio, which gives more importance to the gas flow.

3.4.3 Results and discussion

The experimental data available consists of mean liquid volume fraction fields, obtained with 2500 independent samples [17]. In the numerical simulations, mean fields are obtained by averaging within a certain period of time. Consequently, to eliminate the initial transient part, time averaging process was started after 3 liquid advection times, tU_l/D_l, that corresponds to 150 gas advection times, tU_g/D_g. Convergence of each simulation, is monitored with evolution of field averaged and variance volume fraction values. Convergence is obtained after 72 liquid advection times, tU_l/D_l, for both mean and variance values. Fluctuations and variations are though still observable at the end of simulations. Nonetheless, for obtaining complete statistical convergence, simulations should have been run a longer period, which has a non negligible computational cost. It is indeed hardly achievable, numerically speaking, to obtain more than 1000 independent samples, as it can be done experimentally.

Figure 3.20 exhibits the Liquid Volume Fraction (LVF) averaged (top half of each image) and instantaneous (bottom half of each image) of `elsaBase` [19], `interFoam`, and `icmElsaFoam`. Mean LVF values of experiments are also displayed (bottom-right of the figure). Dark blue colors (1) represent the liquid and light yellow colors (0), the gas. Firstly, the mean LVF values on top-left of the figure for `elsaBase`, the diffused interface (LVF values nearly brown), as soon as the liquid is injected into the atmosphere. For `interFoam` (on top-right), the liquid-gas interface is resolved next to nozzle exit, however, after a few diameters axially, some numerical diffusion starts to emerge, due to poor mesh refinement downstream of the flow, as previously explained in the first part of the chapter.

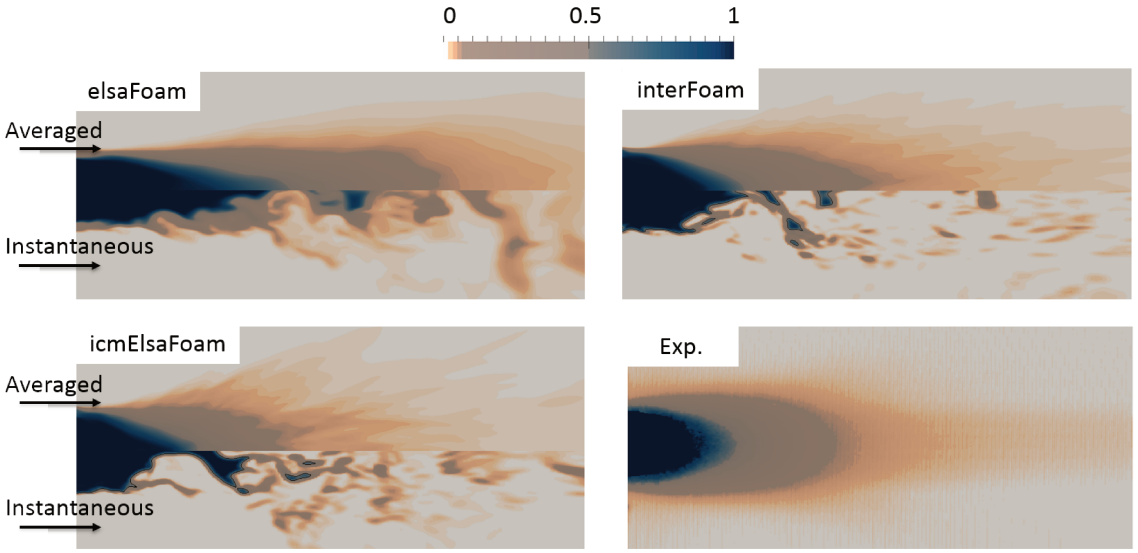

Figure 3.20: Mean (top half of each image) and instantaneous (bottom half of each image) values of Liquid Volume Fraction (LVF) fields of `elsaBase` [19], `interFoam`, `icmElsaFoam`. Mean LVF of experiments (bottom-right of the figure).

Specifically, in the instantaneous field, it is observed that after $3D_l$, approximately, isolated liquid structures, are not correctly captured by the ICM. The iso-contour $\alpha_l = 0.5$ (black continuous line), is a relevant marker of resolved structures. This iso-contour, is absent due to the lack of mesh refinement, that is a source of numerical diffusion. Therefore, `icmElsaFoam`, equation 3.1, should be able to combine the strength of both models, `elsaBase` and `interFoam`, far from the nozzle exit and within the near flow field, respectively, as confirmed in the figure 3.20. Regarding the averaged LVF values, `elsaBase` is over-predicting the liquid penetration compared with experiments, supposedly due to the inadequate interface modeling resolution approach, next to the nozzle exit. Likewise, `icmElsaFoam` performs better compared with experiments. Nonetheless, experimental liquid core shape, is here more spherical, due to repeating flapping in radial directions. This shape is not observed with numerical simulations, in which it tends to a conic shape. Insufficient convergence in time may be an explanation. One can expect to catch this shape with a longer period of simulated time. Another explanation may be the influence of the small inner walls before the nozzle exit. Or the too big eddies injected in the gas flow.

As was demonstrated in the first part of the chapter, turbulence models, are of primordial importance for correctly predicting the detachments of liquid structures. In this second part of the chapter, `elsaBase` model is exposed to be unadapted, for the air-blast atomizer test case, especially for the primary and secondary atomization zone, as verified by the mean axial profiles of Liquid Volume Fraction (LVF) in figure 3.21. Even though a sufficient mesh refinements was employed, see equation 3.17, `elsaBase` axial profiles are far from experimental ones. The turbulence, in this test case, takes time to destabilize and to provoke detachment of liquid structures. This is mainly the liquid-gas shear layer that promote the liquid dispersion. An additional plausible explication, is that the employed LES model, is a single-phase turbulent model, hence is unadapted to modelize small scales of liquid-gas interface. A two-phase LES model combined with `elsaBase` model, might be better to correctly predict the liquid core length. This air-blast atomizer test case, is in fact, quite distinct from the ECN test case previously explained, in which there is a clear resolution of the liquid-gas interface at the exit of the injector, compared with the ECN test case. Therefore, an ICM suitability is then prompted only in the near flow field region, in which the liquid-gas interface can be much

better captured than the ECN test case, and then switch it off, when the residual stresses, due to mesh resolution, arise. This is exactly what the `icmElsaFoam` was designed for.

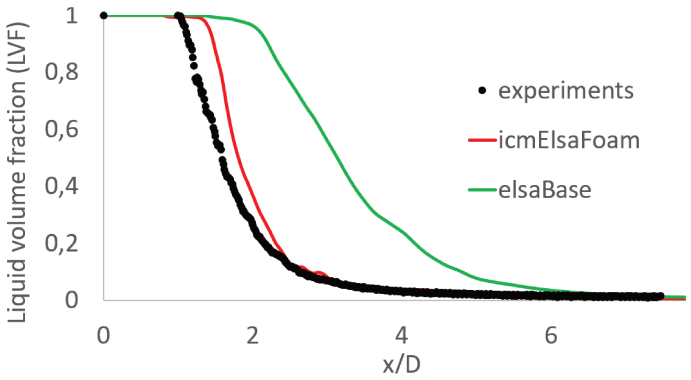

Figure 3.21: Mean axial values of Liquid Volume Fraction (LVF).

Figure 3.22 displays the averaged radial profiles of LVF for `interFoam`, `icmElsaFoam`, and experiments. Firstly, as expected, `interFoam` and `icmElsaFoam` both agree well with experiments at an axial position $X/D = 1$ (figure on the left). Within this near flow field, is where ICM can resolve the small velocity fluctuations i.e., residual stresses would be negligible. However, at $X/D = 1.9$ (figure on the right), `interFoam` deceptively agrees with experimental data, as previously mentioned, with a slight difference on radial profile peak though. Regarding `icmElsaFoam`, in which a physical modeling approach is deployed, in the far field region, the differences with experiments are mainly due to a lack of convergence. Finally, it has been shown by means of a coaxial injector simulation, that the proposed `icmElsaFoam` model, is capable of both improving results. It has been shown that using a resolved interface model, namely `interFoam`, in the whole domain, provides results in good agreement with the experiment in the primary atomization region only. However, in the far field, this model is unadapted upward in the dispersed spray region. It is therefore pertinent in this region to keep a moderate mesh refinement and to switch to a residual or subgrid model, where velocity fluctuations become important.

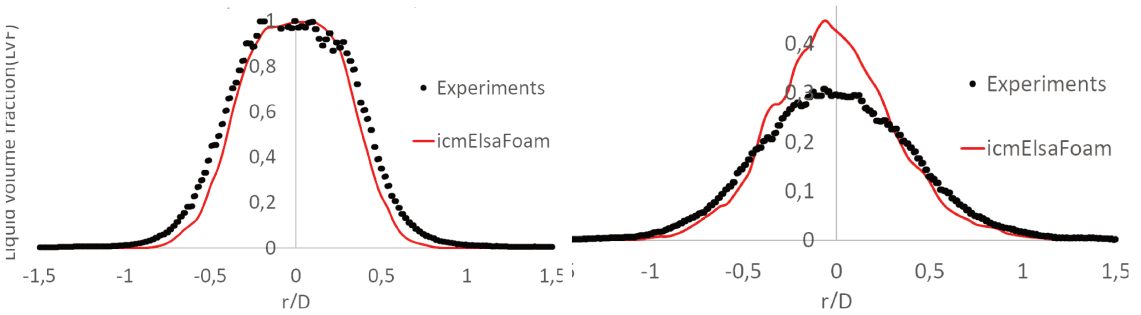

Figure 3.22: Mean radial values of Liquid Volume Fraction (LVF) at axial position $X/D = 1$ (left), and $X/D = 1.9$ (right), respectively.

3.5 Summary and Conclusions

The present work concerns two approaches available to simulate liquid injection system, in flow regimes characterized by high Reynolds and Weber numbers. The focus is on the description of the dense liquid-gas flows, which the spray is not yet formed. Even though, the area covered by this kind of turbulent liquid-gas flow is often less than a few diameters away from injector nozzle, it is mandatory to address it, to link the inside injector flow to the final spray. It is

recognized, that DNS coupled with accurate ICM approaches, are very valuable and accurate tools to describe this flow, as soon as the mesh resolution is sufficient. This requires that the subgrid turbulent liquid flux could be neglected. It is also important to recognize that in many practical applications, such level of mesh refinement is not affordable and physical models, able to represent the subgrid liquid dispersion, are expected. Since the work of Vallet and Borghi [147], the main lines of the so-called ELSA model, have been designed for this purpose. The turbulent liquid-gas flow is the place in which occurs strong density variation. Following the original formulation of Vallet and Borghi, many works have been conducted using Favre mass weighted averaging and filtering. The present work completes these frameworks by considering Reynolds volume averaging and filtering approach. This work has shown that the volume formulation can be used and give comparatively as accurate results as the previous mass formulations, with respect to available experimental data, despite the approximations done in both formulations. A benefit of the volume formulation, is to keep the liquid volume fraction as a primary variable transported by the model, like in many ICM approaches, belonging to the VOF family. Accordingly, a set of models is designed based on ELSA framework, for different levels of refinement. A volume based formulation of ELSA approach, has been implemented using the OpenFOAM® library, leading to the solver namely `elsaFoam`, that can be applied using both RANS and LES turbulence model. This solver considers a subgrid turbulent liquid flux, that depends on the local flow condition. The important point is the incompatibility with ICM, that preserved a sharp interface representation. Thus, even when the interface is well resolved, the turbulent liquid flux vanishes, but the numerical method, not designed to capture the interface, prevent to recover the accuracy of ICM approaches. To solve this problem two criteria for interface resolution quality (IRQ) have been proposed, to determine dynamically if the subgrid turbulent liquid flux has to be considered coupled with a standard numerical method, or if the resolution of the interface is good enough to neglect interface subgrid effect and thus applying ICM. The corresponding solver based on the OpenFOAM® library has been called `icmElsaFoam`. Moreover, the original surface density equation [1] has been extended for all developed formulations.

The second part of the paper is devoted to the analysis of the proposed approach with respect to the experimental data based developed by the ECN [5] research initiative. In particular experimental data from X-ray radiography measurements of non-evaporating Spray A condition have been used. Like previous work based on mass formulation, a global agreement has been obtained with respect to the available data, namely: liquid volume fraction, projected mass density and transverse integrated mass. In particular, even RANS formulation that can be very cheap in term on CPU consumption when using axi-symmetry mesh, is able to reproduce the global behavior of the injection. Nevertheless, to recover the actual dispersion of the liquid, a real improvement can be obtained using LES formulation with both solvers `elsaFoam` and `icmElsaFoam`. Accordingly, a 3D mesh with a high resolution in the injector nozzle is required. In particular, the turbulence inside the nozzle is mainly controlled by the development of a turbulent boundary layer, starting from the internal nozzle cavity, that develops until the end of the injector pipe. To capture this phenomenon, mesh refinement along the injector nozzle wall, combined with an appropriate LES-WALE model has been necessary. This turbulent boundary layer interacts directly with the liquid-gas interface at the exit of the injector, and the it initiates the atomization process. This phenomenon is well captured only with ICM approaches, in particular with the `interFoam` solver. Nevertheless, further downstream as the atomization process continues, the length scale of interface wrinkling decreases continuously, leading to a numerical error in ICM approaches. By changing mesh resolution, it has been shown that this numerical error is driving the liquid dispersion. This mesh dependency can be released by considering subgrid scale effect with the solver: `icmElsaFoam`. Thus, it is better to use a physically-based model, using subgrid turbulent liquid flux, than to rely on numerical errors of ICM (if unresolved), to recover a mesh-dependent result. Finally, the

detailed simulation is sensible enough to relate the liquid dispersion to the internal flow inside the injector, mainly due to geometry uncertainties, meshing process, and numerical model approximations, leading to noticeable modification of the liquid distribution, that finally makes errors of few percents with respect to measured data. For the time being, it is not easy to conclude which of these features are the most important, but the positive conclusion is that the present models are sensible enough to detect these small changes. Main perspectives of this work are twofold: firstly to test `icmElsaFoam` solver on injection with lower Reynolds and Weber number, to recover a bigger region, in which the interface can be better captured; secondly, to test the behavior of the model with respect to the surface density prediction with respect to available data.

Chap. 4 | Transition from multi-scale approach to dispersed phase

4.1 Introduction

The preceding chapter 3 described the modeling of primary atomization process. Accordingly, a deterministic or probabilistic representation of liquid-gas flow is often used, in order to have a good interface representation e.g., DNS-ICM or ICM-ESA, respectively. The former, for instance, allows the representation of complex phenomena and changes in the liquid-gas interface. For both cases, the two-phase flow topology is defined as *separated flows*, as depicted in chapter 2. The other topology specified in turbulent liquid-gas flow, at the bottom of figure 4.1 below, is the well-known *disperse flow*, consisting of well defined particles (disperse phase), distributed in a connected volume of carrier phase. In *disperse flow*, the liquid volume fraction becomes really low hence, the interface cannot be described accurately, even with highly resolved simulations. Within the models previously explained in chapter 3, it was the turbulence, mainly produced in great part inside or in the vicinity of the nozzle, which yielded the first surface instabilities, and later the breakup of the liquid jet, and droplets. Usually, these droplets may undergo several physical mechanisms e.g., breakup and coalescence in smaller, bigger liquid structures, respectively, this is commonly known as *secondary atomization zone*, as explained in chapter 2. Additionally for instance, they can be studied isolated from other droplets i.e., individually, in which aerodynamic forces will act on each droplet, due to the slip velocity between the ambient gas and the droplet.

To put in the context of the work done in this chapter, it is shown in the figure 4.1 (highlighted in red), the coupling between the multi-scale approach (ICM-ESA, developed and validated in chapter 3), and the disperse flow, within the RANS framework. Previous works for example (at the bottom of the figure, for DNS and LES), by using a hybrid Eulerian-Lagrangian method i.e., a particle (stochastic Lagrangian) and a continuum (Eulerian moment method) approach, simulation of the dispersed phase in turbulent gas-solid flows was made [148]. In that work, the domain was split into two regions: a region where the particulate flow is simulate in the Lagrangian framework, and another region, in which the flow is simulated in the Eulerian framework. Flux boundary conditions, were employed at the interface of the two adjacent domains. In another work, coupling a Eulerian interface-tracking method and a Lagrangian particle tracking method to simulate liquid atomization processes has been done [39]. The Eulerian method, was based on the Coupled Level-Set and Volume-of-Fluid (CLSVOF) for interface tracking, and the small-scale droplets were tracked by Lagrangian point-source droplets (droplet dimension were much smaller than the cell size). In that work, once the Eulerian structured was identified as Lagrangian droplet (under certain criteria), the Eulerian structured is replaced by a Lagrangian droplet, with determined droplets mass and velocity. Following a theoretical work [149], a hybrid turbulent spray LES formulation, which included both an Eulerian liquid jet core and Lagrangian (point-particle) droplets, was

proposed [20]. The interactions of unresolved interface and turbulence inside a cell, which finally lead to subgrid droplet generation, were modeled. Mathematical expressions were also derived, that can be directly used to identify LES-grids and determine the resulting atomized droplet characteristics, based on large We and only for a particular turbulent eddy orientation.

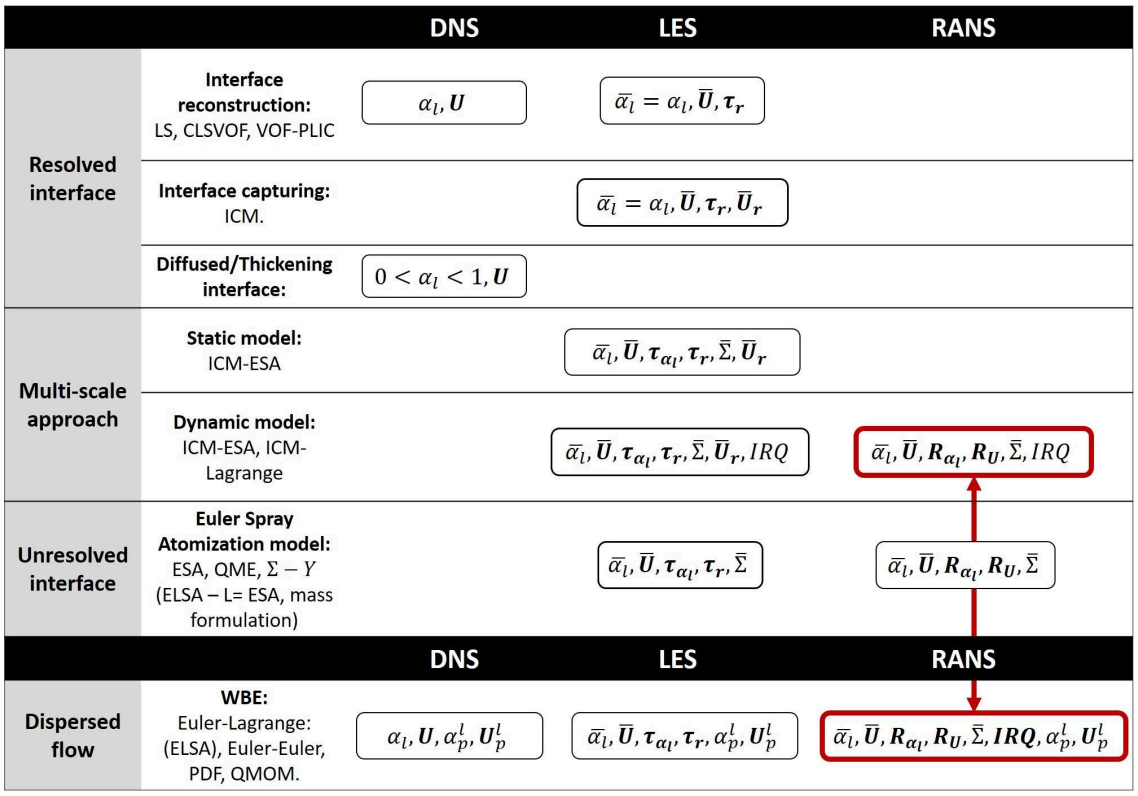

Figure 4.1: Physical-modeling representation of atomization process in turbulent liquid-gas flow. Dispersed flow (bottom part of the figure). Transition from multi-scale approach to dispersed phase flow, using RANS framework (highlighted in red).

Atomization models employed in the dispersed spray zone, are mostly based on Lagrange approach. They are dedicated to solve the statistical evolution equation of spray, made of spherical particles. The well-known Williams-Boltzmann equation (WBE) [70], in which the droplet size distribution, velocity, among other relevant spray variables, are evaluated at each location, at each time. This distribution function, f, more precisely, corresponds to the probability of a droplet to exist within a cell volume $\boldsymbol{x}$, in a certain time t, with velocity $\boldsymbol{U}$, mass m, and temperature $\boldsymbol{T}$. Hence, the number of droplets per unit of volume, in a certain time, can be calculated. The Williams equation, which can be seen as a general population balance equation of particles, is then represented as follows:

$$\frac{\partial f}{\partial t} = -\frac{\partial(\boldsymbol{U}f)}{\partial x} - \frac{\partial(\dot{m}f)}{\partial m} - \frac{\partial(\dot{\boldsymbol{U}}f)}{\partial \boldsymbol{U}} - \frac{\partial(\dot{T}f)}{\partial T} + \boldsymbol{Q} + \Gamma \quad . \tag{4.1}$$

The above equation 4.1, takes into account the droplet size changes $\dot{m}$, aerodynamic forces $\dot{\boldsymbol{U}}$, evaporation, breakup and coalescence trough the source terms Γ, and $\boldsymbol{Q}$, respectively, through appropriate models for each variable. Specifically, numerous source term closures have been developed for dispersed spray [150]. Even though, most closure models were formulated considering the droplet completely spherical i.e., within the dilute zone of the spray, using them in the primary atomization zone could cause some discrepancy, because droplets are

not yet fully formed, as previously explained in detail in chapter 3. Another approach, is to modelize the primary atomization zone, as done in the preceding chapter 3. Thus a realistic fashion should be designed for dispersed particle initialization.

The objective of this chapter 4, is then to analyze the coupling between the multi-scale approach (developed and validated in chapter 3), and the disperse flow, within the $ELSA$ framework. The idea is to take advantage of these WBE developments, in regions in which dilute flow can be applied, in order to improve the Eulerian field solved by the multi-scale approach. Furthermore, the Eulerian turbulent field will be considered for the droplet trajectory model i.e., a stochastic displacement of atomized droplets, will be employed. This chapter is then organized as follows: Firstly, droplet injection criterion transition from multi-scale to disperse approach, is detailed. Secondly, a stochastic differential equation (SDE) derived from the Langevin model for droplets, undergoing turbulent dispersion, is implemented. Thirdly, the newly implemented stochastic differential equation is compared with experimental results. At the end, conclusions are drawn from these results in the last section.

4.2 Dispersed spray modeling for atomization

Firstly, there is a quite large literature on this topic. There are several models, also implemented in the numerical software OpenFOAM® , to approximate the behavior of the primary atomization zone, to cite a few examples: (1) the $Blobs$ modeling [151, 152], by giving directly the velocity and droplet diameter distribution obtained from experiments at a certain distance from the injector. Additionally, mass flow rate of the nozzle and its discharge coefficient as well, spray angle at the injection point, among other variables can be determined. (2) The liquid sheet atomization ($LISA$) model [153, 154], based on the linear instability analysis, takes into account the effects of surface tension, liquid viscosity and the surrounding gas. Supplementary to the atomization models, it exists different breakup models to predict the droplet diameter evolution. One of the most used is the $WAVE$ model, originally developed by Reitz [155]. It is based on the Kelvin-Helmholtz instability applied on the liquid jet. In this model, the diameter of the droplets is the one of the injecting nozzle and it decreases all along the breakup process. The characteristic time of the breakup and the radius of the stable droplet is given by the analysis of the velocity profile. There is also the Taylor-Analogy Breakup (TAB) model [156], which is based on the critical deformation of an oscillating droplet.
All these models fit quite well on the left of figure 4.2, in which the primary atomization zone is not fully simulated, in this case, for a Diesel jet. It is to be noted on both side of the figure, that the red line sets the boundary of the atomization process modeled in this chapter (i.e., spray combustion and phase change are not modeled in this work).

On the other hand the present approach ($ELSA$), is meant to model liquid structures in the vicinity of the injector, but also the full atomization process (from primary to dilute spray zone inclusive), by complementing the multi-scale ($ICM-ESA$) field with a well-established disperse flow approach. This is in fact, the idea behind this chapter (figure 4.2 on the right). Both multi-scale and disperse flow approach, would be computed by the same code at the same time. An schematic representation of their interaction, is displayed in the figure 4.3 below. The transition criterion is based, for instance, on the level of dilution represented by the liquid volume fraction, that is computed everywhere in the computational domain. This transition criteria will determined the transition computational cells, in which disperse flow approach will be applied. Once the transition is set, the part of the computational domain that is described by disperse flow approach (which contains also the multi-scale ($ICM-ESA$) unused equations that are always computed on the whole domain) will be used to correct the velocity field in the multi-scale transport equations 3.1, defined in the previous chapter 3.This point will be further explained in the following sections. Basically, $ELSA$ is used in the dense

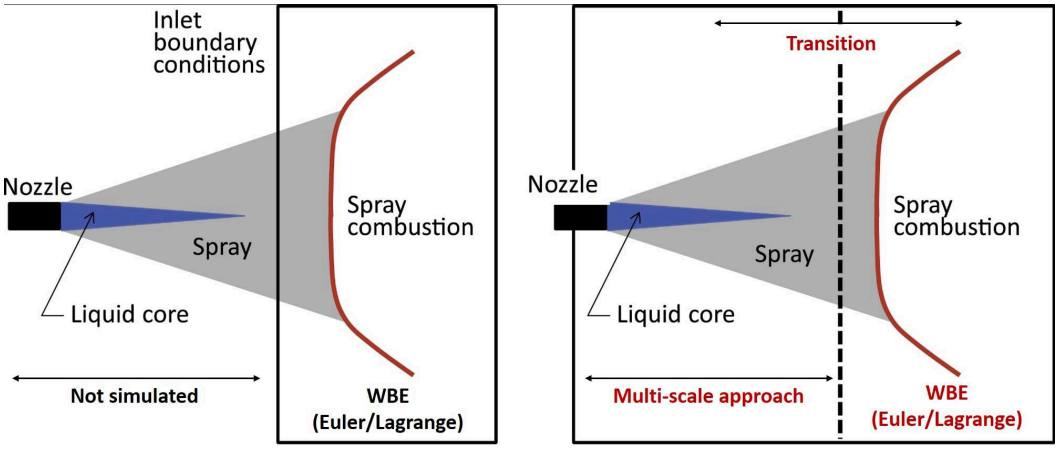

Figure 4.2: Paradigms of spray simulation. On the left, is the conventional one, where the droplet generation (primary atomization) is not directly simulated but given by some input model. On the right, is the proposed paradigm, where the droplet generation is directly considered consistently with the downstream region, typically formulated in a hybrid Eulerian/Eulerian and Eulerian/Lagrangian manner [20].

and dilute part of the flow, and when the main assumptions of dispersed flow are reached, a WBE approach is dynamically initiated i.e., every time-step.

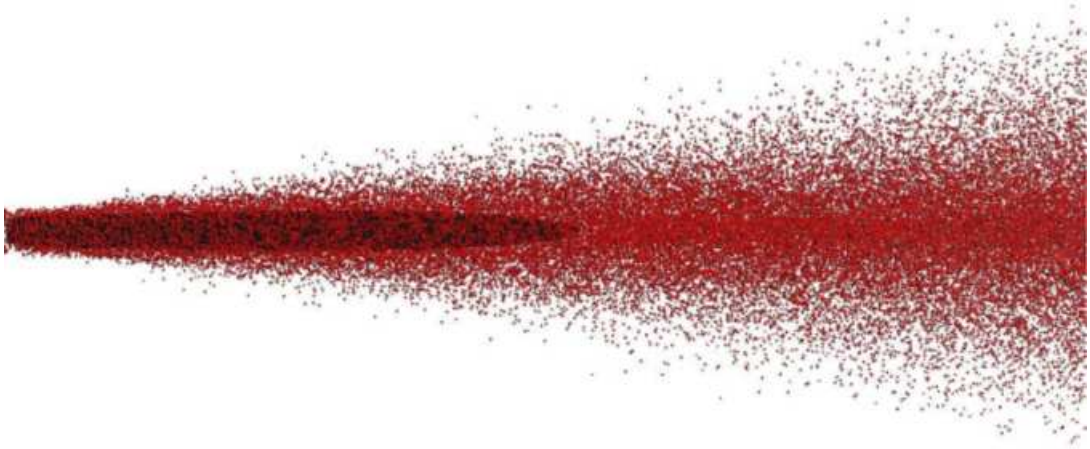

Figure 4.3: Typical picture of an atomizing spray obtained with the $\boldsymbol{ELSA}$ model. The dark part represents the transition zone from the Euler description to the Lagrange description. This transition zone is dynamically computed, hence it evolves during the injection [21].

4.3 Transition to dispersed flow

As previously described, the single-flow approach ($\boldsymbol{ICM-ESA}$), has to be coupled with a $\boldsymbol{WBE}$-related hypothesis formulation, once the spray is considered to be diluted. In order to switch from multi-scale to disperse flow formulation, a criterion must be introduced. Euler formulation of the $\boldsymbol{ESA}$ approach, is applicable to the entire atomization process. Indeed, the averaged mixture velocity $\tilde{\boldsymbol{U}}$, the liquid volume fraction $\tilde{\alpha}_l$, and the interface density $\tilde{\Sigma}$, can be defined even in the disperse zone. However, $\boldsymbol{WBE}$ approach, resolved in this chapter by a Lagrangian method, provide more detailed information. Transition zone, between the dense and the diluted parts, is referred as *transitional cells*. In a previous research [21], one

criterion used, was based on the ratio between the mean distance between droplets l, and the mean droplet diameter l_{32}. In fact, this corresponds to the definition of a dilution factor d_f, displayed in the following equation 4.2:

$$\begin{cases} d_f = \dfrac{l}{l_{32}} = \dfrac{n^{-1/3}}{d} = 0.806(\phi_l)^{-1/3} & , \\ l_{32} \approx \dfrac{6\alpha(1-\alpha_l)}{\Sigma} & , \\ l \approx n^{-1/3} & . \end{cases} \tag{4.2}$$

Once this criteria reaches a threshold, the $\boldsymbol{WBE}$ representation is activated i.e., stochastic particles representing the spray must be created and initial values have to be defined. The stochastic particles are representation of droplets, computed by a stochastic weight, in order to recover the statistical properties of the spray, and in particular the distribution function f in equation 4.1. Those transitional zones, from dense to dilute, has been already identified [76]. Consequently, the criteria conceived agrees with the liquid volume fraction (LVF). In this chapter, the same idea is used i.e., Lagrange field would be initialized, in computational cells, where the liquid volume fraction is less than 1%. According also with DNS results [89], in which it was found that, at low α_l e.g., $\alpha_l \leq 1\%$, small liquid structures with almost spherical shapes are present in the domain, in which can be considered as dilute spray. The values taken in this chapter correspond also to the ones tabulated in [96], in which was established the presence of droplet for liquid volume fraction below 1%.

Additionally to the criteria explained, the transitional cell must also satisfy the Interface Resolution Quality (IRQ) sensors i.e., $\boldsymbol{IRQ_\Sigma}$ and $\boldsymbol{IRQ_K}$, previously defined in equation 3.12, and 3.13 respectively, in chapter 3. For each stochastic particle, velocity, diameter, position, and probability weight is defined. The size of the newly created droplets is chosen equal to the local value of the Sauter Mean Diameter (SMD), as given by l_{32} in equation 4.2, which is based on the liquid volume fraction and interface density, equation 3.11 and 2.15, respectively. Additionally, a method to extract the liquid velocity and the liquid turbulence intensity k_l, from their corresponding variables in the Eulerian formulation based on the *turbulent liquid flux*, has already been developed in [76, 157], using the following hypothesis: $\rho_l k_l = \rho_g k_g$. However, those two hypothesis used at that time, namely the kinetic energy of the liquid and the use of a single value for the droplet diameter within each cell, are probably the two points that need further improvements. Regarding this last point, an up-to-date approach to obtain the lagrangian particle diameter is to inject a Drop Size Distribution (DSD). Yet, it can only be defined if droplets are already formed. Atomization process, as explained, generally starts with a continuous liquid jet, hence a new formulation of the DSD based on the curvature of the interface becomes necessary. A Surface Curvature Distribution, based on Gauss curvature $G = \kappa_1 * \kappa_2$ and mean curvature $H = \frac{\kappa_1 + \kappa_2}{2}$, can be defined everywhere from the liquid jet until the dilute zone, in order to have the curvature evolution during all the atomization process. Information on the Drop Size Distribution can then be deduced. Nevertheless, this procedure is still in development i.e., for the moment, the complete DSD formulation, remains an issue [158].

4.3.1 Stochastic droplet injection

Stochastic droplets should then be initialized based on the multi-scale i.e., Eulerian field of the spray. Accordingly, several stochastic droplet characteristic can be obtained by way of the Eulerian field e.g., droplet velocity, diameter, position, among other variables. Regarding the droplet injection position, it depends of the position of the transitional cell at a time-step Δt_k. Specifically, the geometrical center of the transitional cell, was chosen to be the injection

position. Another droplet position within the transitional cell could also be chosen e.g., by a pseudo-random position within the cell, as proposed by [157]. It is also to be noted that one (1) stochastic particle (or parcel) is injected per transitional cell. Even though, several stochastic droplets could be injected as well (represented by a certain distribution function), to enhance droplet statistical convergence. In the latter case, there exist already a high cell count in the domain, which eventually, would increase the computational memory requirement, and simulation time, becoming the case highly restrictive.

Additionally, in order to quantify the mass transfer (from multi-scale to disperse flow field), momentum and energy, it is then necessary to define the droplet diameter (or DSD) and velocity. In the first place, a spherical droplet assumption, in order to calculate the droplet diameter, seems reasonable to use, since small liquid structures with almost spherical shapes are present in transitional cells. Therefore, the Sauter Mean Diameter (SMD), define previously in equation 2.16 in chapter 2, is recalled here, using from the Eulerian fields (identified by a superindex $\boldsymbol{E}$), mainly liquid volume fraction and interface surface density:

$$\begin{cases} l_{32} = d_k \approx \dfrac{6\bar{\alpha_l}^E(1-\bar{\alpha_l}^E)}{\bar{\Sigma}^E} & , \\ N_k = \dfrac{6\bar{\alpha_l}^E}{\pi {d_k}^3} & . \end{cases} \tag{4.3}$$

where N_k, is the number of particle per parcel, which is directly obtained by considering the liquid mass conservation in the transitional cell. With this definition of droplet diameter d_k, there is one (1) droplet diameter for each transitional cell, however, the diameter will be different in all transitional cells, consequently, there will be a global droplet diameter distribution in the domain. As mentioned previously, another approach to obtain the lagrangian droplet diameter, is to inject a Droplet Size Distribution (DSD) per transitional cell. This is undergoing work [158].

Regarding the droplet injection velocity $\boldsymbol{V}_k$, a method to extract the Eulerian liquid velocity and the Eulerian liquid turbulence intensity, has been developed in [76, 157], however, the hypothesis used to obtain the liquid kinetic energy i.e., $\rho_l k_l = \rho_g k_g$, might be not suitable for this case. Initially, the assumption of different turbulent kinetic energies, one for each phase, would apply only when the flow is separated i.e., there is a clear distinction of the interface. But as soon as liquid-gas fluctuations dominate, the mixing induced by turbulence, will cancel the validity of the turbulent kinetic energy hypothesis, in which should be applied one turbulent kinetic energy equation per phase, with a proper diffusive coefficient between them, which is not the case under the actual single-fluid approach.

In this chapter, two approaches are presented to represent the droplet velocity injection. The *first approach*, is just by using the mixture velocity of the carrier phase. All multi-scale to dispersed flow coupling will use as a basis the mixture velocity, from which the averaged velocity in the liquid part $\vec{U}_l$ can be obtained, defined in chapter 3, and recall here (highlighted in red) in equation 4.4. Using the *turbulent liquid flux* $\boldsymbol{R}_{\alpha_l}$, which has already been explained in chapter 3, it has been proven [33, 78, 50] that even with this single-fluid approach, it is possible to recover the mean liquid velocity $\boldsymbol{U}|_l$, by means of a drift flux model. The interested reader is then referred to [78] where a so-called, second order closure is developed. The formalism shows also, that the *turbulent liquid flux* contains also the mean slip velocity of the liquid phase with respect to the mean mixture, as exposed in the second row from the top, in equation 4.4. In the *second approach*, the initial velocity is given by the mean liquid

velocity $\boldsymbol{U}|_l$, and modulated by a random velocity fluctuation based on the mixture turbulent kinetic energy k, as displayed in the equation 4.4 below.

$$\begin{cases} \boldsymbol{V}_k & = \boldsymbol{U}|_l \quad , \\ & \boldsymbol{R}_{\alpha_l} = (\overline{\boldsymbol{U}\alpha_l} - \bar{\boldsymbol{U}}\bar{\alpha}_l) = \bar{\alpha}_l(\bar{\boldsymbol{U}}|_l - \bar{\boldsymbol{U}}) \approx -\frac{\nu_t}{Sc_t}\nabla\bar{\alpha}_l \quad . \\ \boldsymbol{V}_k & = \boldsymbol{U}|_l + \boldsymbol{U}' \quad , \\ & \boldsymbol{U}' = \boldsymbol{\lambda}\sqrt{\boldsymbol{U}'^2} = \boldsymbol{\lambda}\sqrt{\frac{2k}{3}} \quad . \end{cases} \tag{4.4}$$

In turbulent flows, DNS or LES coupled with Lagrange Particle Tracking (LPT), offer the most rigorous way of treating turbulence-particle interactions in Euler/Lagrange framework [159, 92, 39, 20], however, they are quite time-consuming. Hence, RANS was chosen as a turbulence model for the simulations in this chapter. In consequence, eddies can be estimated isotropic i.e., the fluctuations in all direction are the same. Moreover, in RANS framework, the specific model $k-\epsilon$, yields the mean velocity, and the fluctuating velocity components are based on randomly distributed Gaussian variables, whose root mean square (RMS) values are equal and deduced from the turbulent kinetic energy k, as shown in the last row of equation 4.4. Lastly, λ (fourth row from the top), is a Gaussian random variable with zero (0) mean and unity as standard deviation.

Finally, each stochastic droplet created in the transitional cell, will have a droplet diameter d_k, a droplet velocity injection $\boldsymbol{V}_k$, and will represent the behavior of N_k particles.

4.3.2 Mass conservation

One drawback in the Euler-Lagrange coupling formulation, is the mass conservation in the transition zone. One way to conserve the mass flux at the transition cell, is to compute the incoming flux coming from the Eulerian part and to transfer it to a Lagrangian flux. In practice this simple idea is difficult to achieve everywhere in the computational field. The Eulerian liquid mass flux for instance can be computed as the sum of the convective flux plus the turbulent diffusive flux:

$$\varphi^E = \int_{\Omega_E} \left(\bar{\boldsymbol{U}}\bar{\alpha}_l - \frac{\nu_t}{Sc_t}\nabla\bar{\alpha}_l \right) \cdot n d\Omega \quad , \tag{4.5}$$

where Ω_E is the Eulerian domain. φ^E = $(\varphi_{in})^E$ - $(\varphi_{out})^E$ is the net Eulerian liquid flux to the Lagrangian zone. This flux has to be balanced by the Lagrangian flux, that is φ^L = $(\varphi_{in})^L$ - $(\varphi_{out})^L$. This is simply the difference between the droplet that enters into the Lagrangian domain ($(\varphi_{in})^L$, the unknown variable) minus the droplet that enters into the Eulerian zone $(\varphi_{out})^L$, as exposed in the figure 4.4 below. These last droplets are deleted because Lagrangian droplets are not considered in the Eulerian zone. In fact, for each particle coming from the Lagrangian zone to the Eulerian zone, the huge challenge is to determine what is the transition cell that is affected by this particle, especially when the transition cell evolved during the same time step. Consequently, once the Eulerian formalism evolves in time and space, the interface boundary between the Eulerian and Lagrangian zone, has its own evolution as well, that should be accounted for.

It is to be noted that the Eulerian equations are solved in the whole computational domain. Moreover, $\boldsymbol{WBE}$-related hypothesis formalism is used to improve the Eulerian fields and to add detailed information from the dilute spray zone. Therefore, the first step to mass conservation is to ensure in every computational transitional cell, that the Eulerian and Lagrangian fields transport the same liquid mass quantity and also an equivalent Sauter Mean

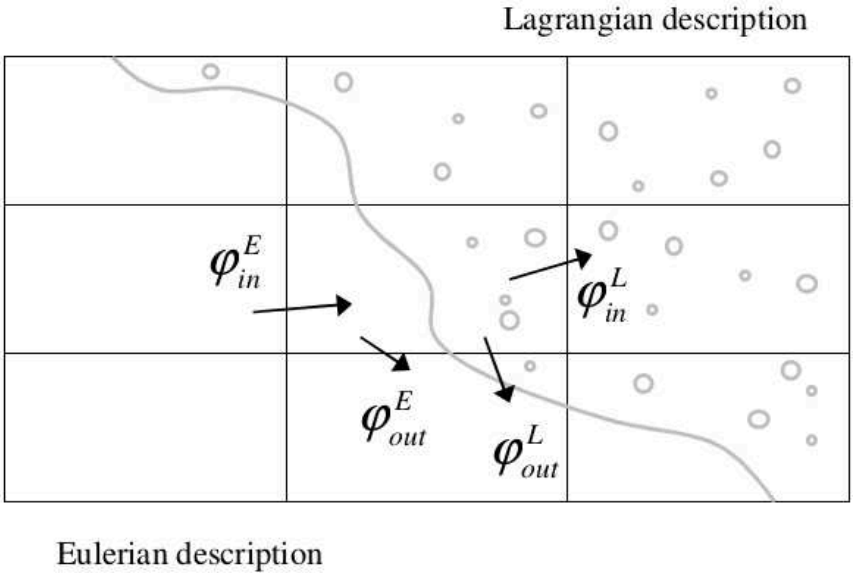

Figure 4.4: Euler-Lagrange transition, schematic view of Eulerian and Lagrangian fluxes [21].

Diameter (SMD). The multi-scale equations of the $ICM-ESA$ model concerned by this point, are the equation for the liquid volume fraction and the liquid surface density, equation 3.11 and 2.15, respectively. With this information, the Eulerian equations are used in the diluted spray zone to correct the Lagrangian variables transported by the stochastic particles. The Lagrangian spray is, as before, described by a set of stochastic particles k, each of them represent N_k droplets of diameter d_k, and with a velocity vector V_k. The density of the liquid ρ_l is supposed to be constant.

The transitional method of this hybrid Euler-Lagrange atomization model, is described below in two steps: Firstly, the coupling Euler-Lagrange is characterized, and secondly, the coupling Lagrange-Euler is also explained.

Hybrid coupling: from Euler to Lagrange

In the mesh cell, a Lagrangian liquid volume fraction ${\alpha_l}^L$ can be defined. Therefore, at every time-step, the properties of the stochastic droplet are determined by summing over all the parcels in a computational cell. For instance, the number density, n, the Lagrange volume fraction ${\alpha_l}^L$, and Lagrange surface interface density Σ^L:

$$\begin{cases} n = \dfrac{\sum_k [N_k]}{V} \quad , \\ {\alpha_l}^L = \dfrac{\sum_k [N_k V_{d,k}]}{V} \quad , \\ \Sigma^L = \dfrac{\sum_k [N_k S_{d,k}]}{V} \quad , \end{cases} \tag{4.6}$$

where $V_{d,k}$, and $S_{d,k}$ is the volume and surface area associated with an individual particle, respectively. Our study considers spherical droplets with high density ratio: $\rho_k >> \rho_g$. In such flows, the droplet response time is much larger than the Kolmogorov time scale τ_K: $\tau_k >> \tau_K$. There are numerous possible ways to correct the Lagrangian variable, in order to warrant mass conservation at the interface boundary between multi-scale and disperse flow approach. If the Eulerian and Lagrangian fields present imbalance of liquid mass quantity, the simplest

method would then consist in changing proportionally (by a mass and diameter corrective factor) either all the N_k or all the d_k. As shown below in equation 4.7:

$$\begin{cases} N_k^* = \epsilon_n N_k & , \\ d_k^* = \epsilon_d d_k & . \end{cases} \tag{4.7}$$

The above equation 4.7, is applied for each stochastic particle k, in the cell considered. It is possible to take into account the fact that the SMD d_{32}, also has to respect the Eulerian phase, arguing that the statistical noise has to be reduced too. The surface density equation, gives the Eulerian value Σ^E, that has to be also compared to the Lagrangian one Σ^L. Thus, to ensure that ${\alpha_l}^L = {\alpha_l}^E$, and $\Sigma^L = \Sigma^E$, ϵ_d and ϵ_n are determined through the following equations 4.8, for further information see [21]:

$$\begin{cases} \epsilon_d = \dfrac{{\alpha_l}^E}{{\alpha_l}^L} \dfrac{\Sigma^L}{\Sigma^E} & , \\ \epsilon_n = \left(\dfrac{\Sigma^L}{\Sigma^E}\right)^3 \left(\dfrac{{\alpha_l}^E}{{\alpha_l}^L}\right)^2 & . \end{cases} \tag{4.8}$$

By using the mass and diameter correction factors proposed in equation 4.8, a new mass and diameter distribution would be obtained at the transitional cells, based on both Eulerian and Lagrangian fields. Until this point, there is no real coupling. Regarding the mean values, they are fully determined from the Euler approach and imposed to the Lagrange one. Next section explains how the Lagrangian approach is used to improve Euler fields.

Hybrid coupling: from Lagrange to Euler

The idea behind the coupling Lagrange-Euler, is to improve the Eulerian fields by the detailed information coming from the Lagrangian field. The Eulerian velocity can then be defined via both Eulerian method (explained in chapter 3) and Lagrangian method, which is detailed in the equation below:

$$\begin{cases} \overline{{\boldsymbol{U}_\alpha}^L} = \dfrac{\sum_k \left[\boldsymbol{U}_k N_k \left(\frac{\pi}{6} {D_k}^3\right)\right]}{V_{l,L}} & , \\ \overline{{\boldsymbol{U}_\Sigma}^L} = \dfrac{\sum_k \left[\boldsymbol{U}_k N_k \left(\pi {D_k}^2\right)\right]}{S_{l,L}} & , \end{cases} \tag{4.9}$$

where $\overline{{\boldsymbol{U}_\alpha}^L}$, and $\overline{{\boldsymbol{U}_\Sigma}^L}$ represent the averaged Lagrangian velocities (in every cell in the domain) for the liquid volume and surface, respectively. $V_{l,L}$, and $S_{l,L}$ represent the total Lagrange liquid volume and total Lagrange liquid surface of the considered cell, respectively. Once these velocities are calculated, the Lagrangian turbulent flux can be determined via the following equation:

$$\begin{cases} {\boldsymbol{R}_\alpha}^L = {\alpha_l}^L \left(\overline{{\boldsymbol{U}_\alpha}^L} - \bar{\boldsymbol{U}}\right) & , \\ {\boldsymbol{R}_\Sigma}^L = \Sigma^L \left(\overline{{\boldsymbol{U}_\Sigma}^L} - \bar{\boldsymbol{U}}\right) & , \end{cases} \tag{4.10}$$

where $\bar{\boldsymbol{U}}$, is the Eulerian filtered mixture velocity explained in chapter 3. It is to be recalled that the Eulerian turbulent fluxes, coming both from the filtering operation, namely ${\boldsymbol{R}_\Sigma}^E$ and ${\boldsymbol{R}_\alpha}^E$ were previously defined in chapter 2 (equation 2.4.2) and in chapter 3 (equation

3.3), respectively. As explained before, $ICM-ESA$ can indeed be still applied for both dense and dilute region of the spray, however, the Lagrangian turbulent fluxes proposed in equation 4.10, can be included in the general conservation equations of liquid volume fraction α_l (chapter 3) and interface surface density Σ (chapter 2), to be integrated in the regions where exist stochastic Lagrange particles (dilute zone). It is clear that big statistical fluctuations of ${\alpha_l}^L$ can be expected if the number of particles in the cell n_p, is not high enough to reach statistical convergence. Considering this key point, it would be advisable to use the less noisy Eulerian variable ${\alpha_l}^E$, instead of the Lagrangian one ${\alpha_l}^L$. Therefore, a proportionality function is proposed to decide between which approach (Euler or Lagrange) should be applied, in dilute flow regions. Consequently, if the considered numerical cell has less than 2 stochastic droplet ($N_k \leq 2$), then the Eulerian formalism will be applied. Likewise, the application between both approaches (Euler or/and Lagrange) will depend on the number of stochastic particles within the cell N_k. The following equation illustrate the principle:

$$\begin{cases} \boldsymbol{R}_\alpha = \dfrac{1}{\sqrt{N_k}} {\boldsymbol{R}_\alpha}^E + \left(1 - \dfrac{1}{\sqrt{N_k}}\right) {\boldsymbol{R}_\alpha}^L \quad , \\ \boldsymbol{R}_\Sigma = \dfrac{1}{\sqrt{N_k}} {\boldsymbol{R}_\Sigma}^E + \left(1 - \dfrac{1}{\sqrt{N_k}}\right) {\boldsymbol{R}_\Sigma}^L \quad . \end{cases} \tag{4.11}$$

This equation 4.11, is based on the statistical convergence error, which in this case is $\approx \frac{1}{\sqrt{N_k}}$. For instance, both approaches would be equally applied (50 % each), if there are within the cell only 4 stochastic droplets. Finally, this new hybrid Euler-Lagrange approach, initiated by [21], is very promising, however, still in its early development during this PhD. One final particle aspect will be studied and adapted: the liquid dispersion. Finally, once mass conservation within the transition zone has been achieved, and Lagrange variable have been corrected by the Eulerian ones, droplet trajectories into a quiescent gaseous atmosphere, carrying liquid turbulent structures, has to be modeled.

4.4 Turbulent dispersed flow modeling: liquid dispersion

To have the evolution of the trajectory of the lagrangian particle, firstly, some Lagrangian approach are review, and the chosen one, is detailed. Secondly, the turbulence influence i.e., vortex in the multi-scale approach, over the disperse flow is addressed. Some authors proposed for example, to solve a stochastic differential equation like the Langevin equation. It corresponds to the fundamental principle of Newton dynamics, with any supplementary force term which corresponds e.g., to the effect of collisions between particles. This force represents a Gaussian noise. This type of equation is already solved in [160], to have the evolution of distributed particles for the composition PDF method.

4.4.1 Lagrange approach

The disperse interface scale is supposed to be composed of spherical droplets with no internal momentum, completely isolated from each other within the gaseous atmosphere. For liquid jet atomizations, this is far from the truth. For instance, previous researchers [161, 162], adopted a Lagrange approach that was not limited to follow fully formed spherical droplets in the dilute zone, but also, to modelize the liquid phase coming out of the nozzle. The liquid jet was also represented as an injection of rather *large* droplet, with initial diameter as big as the nozzle diameter. Therefore, primary atomization was seen as droplet fragmentation i.e., from bigger or *parent droplets* to smaller or *child droplets*. Additionally, stochastic models based on kolmogorov analysis [163], were used for the droplet fragmentation i.e., breakup process, until the child droplet reach a certain critical diameter value, based on the equilibrium

between the turbulence and surface tension. Nevertheless, interface dynamics were usually cast aside [164].

There are mainly three approaches to model the droplet within the dilute spray flow field. One approach is to follow individual particles or sample particles i.e, the Lagrangian approach. Another technique, is to treat the particle as a cloud with continuum-like-equations i.e., Eulerian approach. Another approach is to use particle distribution functions e.g., PDF functions, to describe the particle flow properties [13]. In this chapter, as explained before, an Euler-Lagrange approach is used, hence Euler approach for modeling the primary atomization zone, by using $\boldsymbol{ELSA}$ model already validated in the previous chapter 3, and the Lagrange approach, for the dilute zone of the spray. Moreover, as previously mentioned, different liquid shapes can be formed at the nearly exit of nozzle injector, which later on, will experience primary and secondary breakups depending on the turbulence level [7]. It is to be noted that the Lagrange approach is equally applicable to both dilute and dense flow of dispersed spray. There are two types also of Lagrange approach. If the flow is steady and dilute, then a *trajectory method* is preferable. Likewise, when the flow is unsteady and dense, a discrete element method is used [13]. The latter is the one employed in this chapter (neglecting particle-particle collisions for the time being). For this method, the motion and position of individual droplets or representative droplets i.e., parcels, are tracked with time. It is assumed then that parcels move trough the field with the same velocity as a single physical droplet. If the initial droplet velocity, diameter, and mass are known (from equations 4.4, and 4.7, respectively), the droplet velocity trajectory and position evolution in time, are commonly derived from the known ordinary differential equation (ODE), in which a solid particle drag coefficient is used to calculate the drag force. Therefore, the momentum conservation equation has the form:

$$\begin{cases} \dfrac{d\boldsymbol{V}_k}{dt} = & \sum \boldsymbol{F}_k = \frac{1}{\beta_k}\left(u(\boldsymbol{X}_k,t) - \boldsymbol{V}_k\right) \quad , \\ & \beta_k = \frac{\rho_k (d_k)^2}{18\mu \boldsymbol{C}_k} \quad , \\ & \boldsymbol{C}_k = 1 + \frac{(Re_k)^{2/3}}{6} \quad , \\ & Re_k = \frac{d_k |\boldsymbol{V}_k - u(\boldsymbol{X}_k,t)|}{\nu_g} \quad , \end{cases} \tag{4.12}$$

where $\boldsymbol{F}_k$ is the external applied force to the stochastic droplet k, which can be due to drag, gravity, droplet collision, lift, stress gradient, Basset history, among other variables [13]. In case of liquid transport in spray, only the drag force will be applied, and Magnus force will be neglected (assuming that particle rotation is small, compared to particle translation). $\boldsymbol{V}_k$, is the Lagrange droplet velocity. $\boldsymbol{X}_k$, is the droplet position, $u(\boldsymbol{X}_k, t)$ is the gaseous (carrier phase) velocity seen by the droplet. β_k is the droplet response time, $\boldsymbol{C}_k$, is the drag coefficient, and finally, Re_k is the droplet Reynolds number. In the case of non-settling particles (gravity is neglected), the main force that influence the droplet motion is the the drag force in equation 4.12. Therefore, the motion of each parcel over one time-step, is obtained by integrating the droplet motion equation 4.12.

4.4.2 Turbulent effect on particles

Turbulence in the carrier fluid, implies an unsteady flow field, and in turn unsteady motion of particles, bubbles or drops [13]. Not to mention the significant drag coefficient changes produced by the turbulent motion flow. On the other hand, most of the theory and experiments have been developed for single droplet spheres, a few have worked in droplet size distribution in liquid jet, e.g.[158, 165]. Interactions of droplets and the formation of clusters with correlated motions, play an important role on the value of the hydrodynamic forces exerted by the fluid. Additionally, the motion of droplets within this environment will become more costly,

computationally speaking, as its concentration gets higher. However, on this first part of research, the main focus would be the turbulence influence over droplet motions in liquid jets. Droplet and particle dispersion in turbulence, is important in many engineering applications e.g., the mixing of droplet with liquid-fueled combustion systems, is dependent on turbulent dispersion. Droplet-fluid turbulence interaction is another relevant factor, and depends on the coupling between the phases. Hence, physical coupling between phases will exist. The phase coupling between the dispersed and continuous phase is initially determined by the liquid volume fraction α_l and particle Reynolds number Re_p, which is analogous to Re_k in equation 4.12. A map proposed for coupling interactions projected onto volume fraction-particle Reynolds number, is shown in figure 4.5.

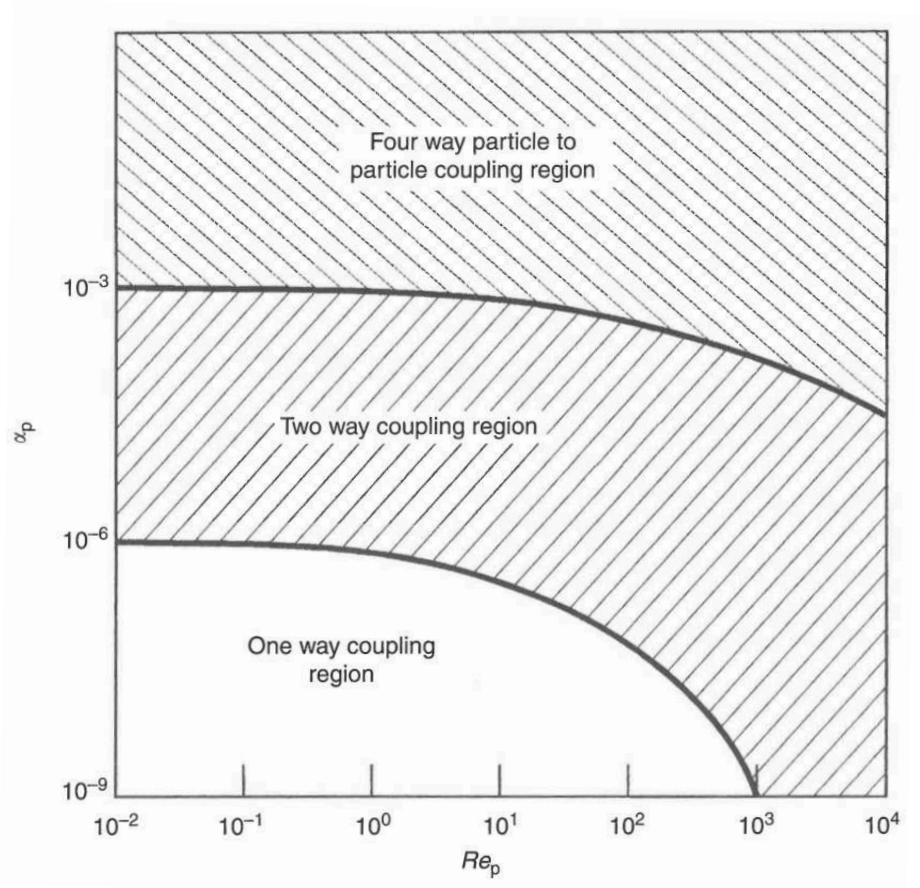

Figure 4.5: Coupling regions for particle-fluid turbulence interaction [13].

The coupling could be divided into three ways, according to [13, 96]. *One-way coupling*, for highly dilute dispersed flow, when $\alpha_l \leq 10^{-6}$, the flow of the carrier fluid influences the particles trajectories, the influence from the particles to the flow is negligible [13]. For low α_l and Re_p, it is expected that one-way coupling dominates. However, as the particle Reynolds number is increased, fluid-droplet turbulence will be produced, requiring two-way coupling. *Two-way coupling*, is then for dilute dispersed flow, when $10^{-6} < \alpha_l \leq 10^{-3}$, it is necessary to account for the influence of the particles on the fluid flow [166]. *Four-way coupling*, for dense dispersed flow, when $10^{-3} < \alpha_l \leq 10^{-2}$, particle spacing is low and the transport of particles is influenced by collisions [166]. Therefore, the particles have influence on both continuum flow and other particles. Consequently, in this chapter, even tough the flow can be considered dense dispersed flow, for the time being, collisions are neglected.

To implement the Lagrangian approach on droplet dispersion in a two-phase flow, a droplet particle motion equation is required, as defined in equation 4.12, plus an additional term that

accounts for the influence of the carrier phase turbulent field. For two-phase flow environment with low particle Reynolds number, it was derived a complex integral-differential equation involving six different forces [167]. During the past decades, physical model development has emphasized the role, that organized vortex structures produced in free shear flows, might have in particle dispersion process [168]. These numerical studies have employed various approaches including discrete vortex method, direct numeric simulation (DNS), and large eddy simulation (LES). Initially, most of these numerical studies concentrated on one-way coupling with two-dimensional flow fields. In recent years, direct numerical simulations of two-phase free shear flow have begun to focus on three-dimensional simulations of particle dispersion [92]. However, DNS requires significant computational resources and its application is limited by a few droplets [159] i.e, for situations involving a large number of droplets, it is not possible to resolve the details of the flow in and around each drop. A remedy to the DNS limitations, would be via LES, however, its application is still at its early stages, and there are several remaining issues regarding the effect of the residual stress tensor fluctuations on the droplets [169, 149, 20]. In RANS, on the other hand, the most practical method has been via stochastic Lagrange models. The simplest stochastic Lagrange model is the Langevin equation [170], which provides a model for the velocity following a fluid particle [90]. These models are derived by using various methods, including those based on time-series analysis [171]. In stochastic simulations, the carrier gas is simulated using Reynolds-Averaged Navier-Stokes (RANS) equations. The RANS models provide mean values, along with second-order moments statistics of the carrier phase properties, such as velocity, and species concentration. The role of the stochastic model, is to provide fluctuating values for carrier-gas properties, for each drop in the domain. These fluctuating quantities, are required in order to capture the effects of turbulence on the drops.

The Lagrangian approach of the fluid velocity along trajectories, was studied in single-phase flows by Pope [41, 172]. This approach was extended to turbulent gas-particle flows by Simonin et al. [42] to account for the inertia of the particles thus, relative velocity. Consequently, in turbulent liquid jets, becomes necessary to take into account the turbulent flow field applied to the particle by the so-called *stochastic lagrangian models*. More than a century ago, Langevin equations were developed as a stochastic model for specific forces on a microscopic droplet undergoing Brownian motion [90, 173]. Therefore, applying the Langevin equation, which is a stochastic differential equation (SDE), the fluid velocity along the droplet path would then follow the paths of Ornstein-Uhlenbeck (OU) processes. This OU process, is a statistically stationary Gaussian process completely characterized by its mean, variance and autocorrelation function based on the integral timescale of the process [90].

A diffusion process is a particular kind of stochastic process. It is a continuous-time Markov process with continuous sample paths. Hence, a diffusion process has two relevant properties defined by the *drift* and *diffusion* coefficient. Let $\boldsymbol{U}_{(t)}$ be a stochastic process, then a non-differentiable diffusion process described by the stochastic differential equation (SDE) is displayed below:

$$\boldsymbol{U}_{(t)} = \underbrace{a\left[\boldsymbol{U}_{(t)}, t\right]}_{drift} dt + \underbrace{b\left[\boldsymbol{U}_{(t)}, t\right]^2}_{diffusion} d\boldsymbol{W}_{(t)} \tag{4.13}$$

The above equation is the basis of different variants for a diffusion process, depending of the coefficients values a, and b. For instance: if the drift and diffusion coefficients a, and b, respectively, are independent of time, the diffusion process becomes statistically stationary. If a, and b are zero and unity, respectively, the diffusion process becomes a vector-valued Wiener process denoted by $\boldsymbol{W}_{(t)}$, which is a Gaussian process with zero mean and variance the time interval. Finally the Ornstein-Uhlenbeck process, is the simplest statistically stationary

diffusion process. It is defined by the linear drift coefficient $a\left[\boldsymbol{U}_{(t)},t\right]=\frac{-\boldsymbol{U}_{(t)}}{T}$, and the constant diffusion coefficient $b\left[\boldsymbol{U}_{(t)},t\right]^2=\frac{2\sigma^2}{T}$, where $\boldsymbol{T}$ is a positive time-scale, and σ a constant. The corresponding SDE equation is the Langevin equation. Moreover, when an extension to inhomogeneous turbulent flows is applied, the SDE based on Langevin equation is then as follows:

$$\begin{cases} \dfrac{d\boldsymbol{X}^*_{(t)}}{dt}=\boldsymbol{U}^*_{(t)} \quad , \\ d\boldsymbol{U}^*_{(t)}=\dfrac{-1}{\rho}\dfrac{\partial\bar{p}}{\partial x_i}dt-G\left(\boldsymbol{U}^*_{(t)}-\bar{\boldsymbol{U}}\right)dt+(C_o\epsilon)^{1/2}d\boldsymbol{W}_{(t)} \quad , \\ G=\left(\dfrac{1}{2}+\dfrac{3C_o}{4}\right)\dfrac{\epsilon}{\kappa} \quad , \end{cases} \tag{4.14}$$

where $\boldsymbol{U}^*_{(t)}$ is the droplet fluctuating velocity with position $\boldsymbol{X}^*_{(t)}$. The term $\bar{p}$, denotes the mean pressure and $\bar{\boldsymbol{U}}$ the mean gaseous velocity, being both obtained from the Eulerian field. The term $\boldsymbol{G}$, is a tensor linked to the fluid turbulence viewed by the droplets [148], which depends on the characteristic timescale of the 'seen' fluid turbulence (eddy-particle interaction time) i.e, *Lagrangian integral timescale* (which is given in terms of Eulerian variables such as dissipation ϵ, and turbulent kinetic energy k). Finally, $\boldsymbol{G}$ stands for the deterministic drift term that causes the velocity to relax toward the mean fluid velocity $\bar{\boldsymbol{U}}$ on the timescale $\boldsymbol{T}$. The third term on RHS of the middle equation, represents the diffusion term that adds a zero-mean random increment of standard deviation $(C_o\epsilon)^{1/2}$, with C_o the Kolmogorov's constant ($Co=6$) [90]. In this work, equation 4.14 forms the *stochastic Lagrange approach* that has been implemented to model turbulent dispersion in the software, OpenFOAM® [174], in absence of collisions. It was numerically solved using a first-order explicit Euler scheme. Even though higher order schemes are also available from the literature [160], the level of statistical errors arising from the finite number of particles is expected to be minimum. This velocity $\boldsymbol{U}^*_{(t)}$, is the added on the RHS of equation 4.12 to close the set of Lagrangian equation, hence each numerical droplet k obeys the following equation:

$$\frac{d\boldsymbol{V}_k}{dt}=\sum\boldsymbol{F}_k=\frac{1}{\beta_k}\left(\bar{\boldsymbol{U}}-\boldsymbol{V}_k-\boldsymbol{U}^*_{(t)}\right) \quad . \tag{4.15}$$

4.5 Bosch injector numerical test case

The previous section has explained the so-called *stochastic Lagrange model* derived from Langevin equation, to account for droplet turbulent dispersion, along with Euler-Lagrange Atomization model ($\boldsymbol{ELSA}$), to account for the Eulerian field variables in the dense part. Additionally, RANS turbulence model is used in this chapter, because in this case $\boldsymbol{ELSA}$ has reached a constant state (in time) that is convenient to test the benefit of Lagrange method. Now, an atomization test case is presented, in order to asses the one-coupling between the multi-scale ($\boldsymbol{ICM-ElSA}$) and the dispersed (WBE: Lagrange) approach, within RANS framework. Finally, the focus is on the drag force on droplet, that leads to turbulent dispersion from the injection point. It is to be noted for a full atomization injection process, there are an amount of experimental techniques applicable to certain regions of the flow. Normally next to nozzle exit (primary atomization), some difficulties arise when it comes to experimental measurements, however, a number of methods have succeeded, such as: LCV [175], image techniques [176], and even X-Ray [177, 178], among others. See chapter 2 for more details. Regarding the dispersed spray, the role that organized vortex structures might play in the particle dispersion process, has been investigated both experimentally and numerically by several research groups. Most of the early efforts in this topic, have concentrated on free

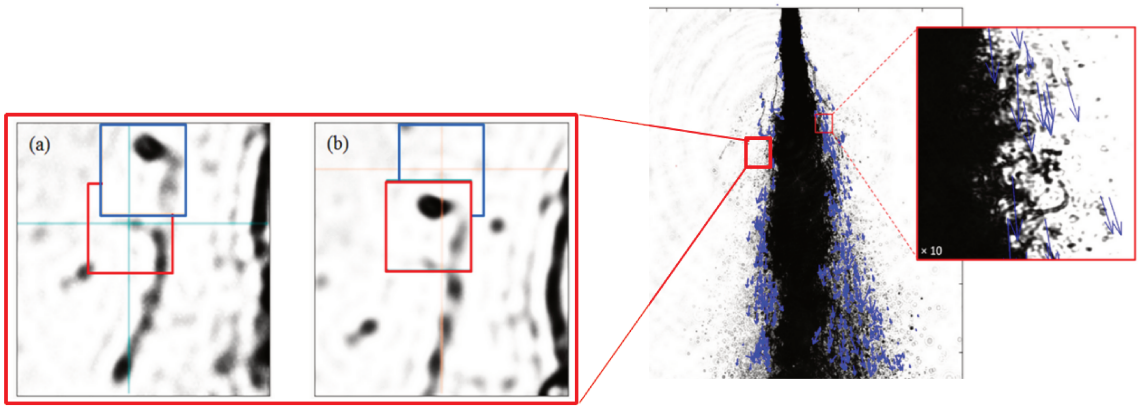

Figure 4.6: Spray image with displacement velocity vectors (blue arrows), estimated from the time-correlated image pairs [6].

shear flow with low particle concentrations and small particle Reynolds number i.e., one-way coupling. Experimental efforts have involved flow image techniques, laser anemometry techniques, and more recently particle image velocimetry (PIV) techniques [179, 180, 93]. In essence, several important findings obtained from these free shear flow experiments, have been reported [13]: (1) Large-scale vortex structures are important controlling mechanisms, for the particle dispersion process. (2) Particle dispersion levels tend to maximize at intermediate values of Stokes numbers, and (3) At intermediate values of Stokes numbers, particles tend to concentrate preferentially near the outer boundaries of large-scale vortex structures. However, these experimental techniques are normally suitable when droplets are already formed. Therefore, in this work, experimental results from an image technique were used [6], in which the spray velocity vectors are obtained from time-correlated image pairs. Therefore, the measured liquid structures are identified, and their velocity is deduced from there motion in between two photos taken at high frequency. The latter experimental data was employed for comparison purpose in this chapter, and it was also included DNS, and LES-ESA results, previously procured in [181, 7], respectively.

Both LES-ESA and DNS are in agreement for the dense part, and tends to match the velocity measurement for most of the dense region, confirming the correct behavior of $\boldsymbol{ELSA}$ in the dense part (see chapter 3). Further downstream, the DNS is limited by numerical cost, and LES-ESA failed to reproduce the velocity in the dispersed spray, as shown in the figure 4.7. The possible reason for that, is the velocity of the liquid structure measured, on the very dispersed flow, which are related to liquid structures detached from the main liquid jet, that have been able to reach certain radial position, away from the liquid centerline. Most probably, the initial transverse velocity has been sufficient to fly away from the main liquid jet. In addition, their inertia have been high enough to keep this velocity. In other words, from the spray distribution, these measurement have selected liquid structures that have been formed as rare events i.e., big droplet diameter and high transverse velocity. These rare events cannot be represented with the Euler version of LES-ESA, that focus mainly on the averaged behavior of the liquid-gas mixture. Therefore, exhibiting some limitations to represent low probability events. This is the reason why these experiments are very challenging tests of special interest for the Lagrange part of the LES-ESA approach, since this is through the Lagrange Stochastic resolution of the WBE equation, that it should be possible to catch less probable events. In particular we guess, that it is the turbulent dispersion model, that is the key point to represent this phenomena.

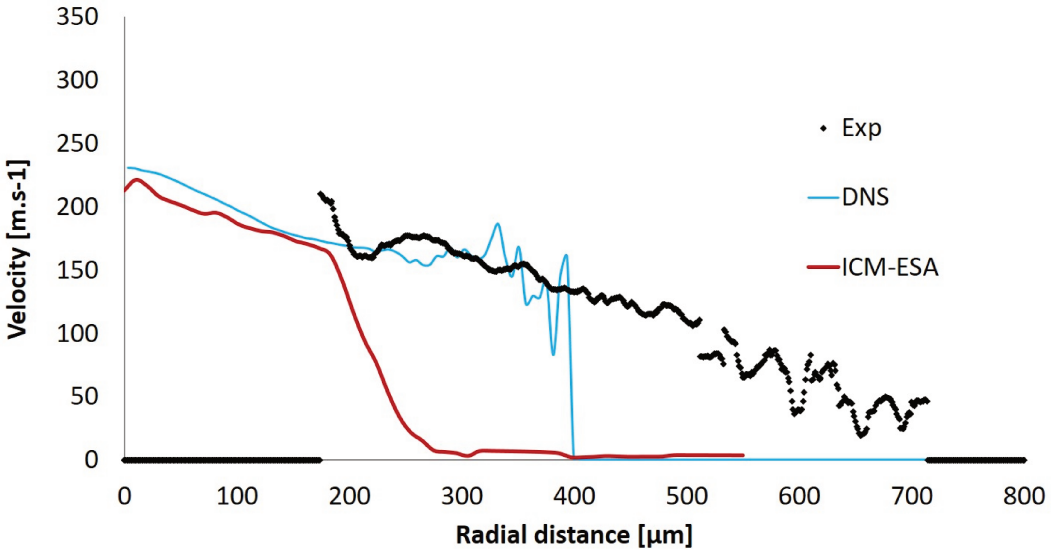

Figure 4.7: Experimental (image technique), DNS, and LES (multi-scale approach) comparison results.

4.5.1 Numerical domain and flow conditions

The injector used in the experimental study [6], is shown in the figure 4.8. This injector geometry is rather simple, and can be considered axisymmetric. Nozzle diameter $D_{in} = 195\ \mu m$. The nozzle geometry used in this case is on figure 4.8, and was selected based on available experimental, DNS results in the near field of the spray (within 20 diameters axially) [6, 181, 7].

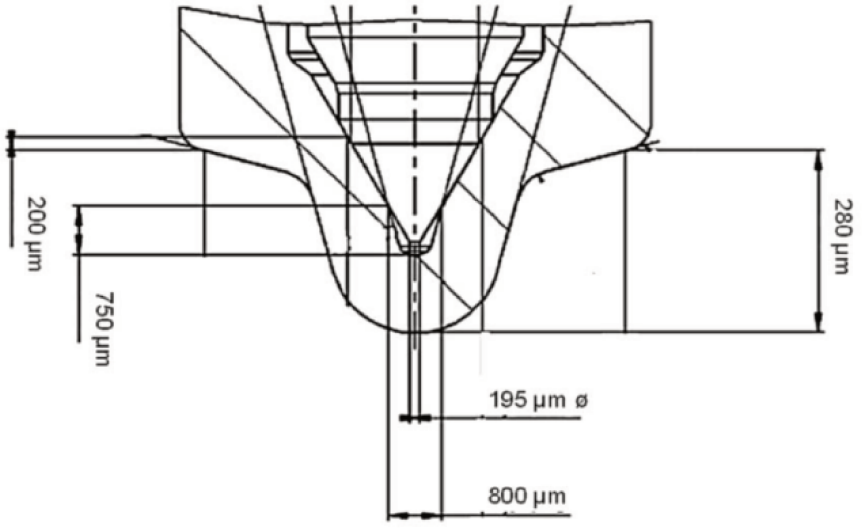

Figure 4.8: Schematic view of the diesel injector nozzle [6].

Finally, the chamber, can be classified as a rectangular parallelepiped, with width and height $L_2 = L_3 = 0.55\ mm$, and the axial distance $L = 2.2\ mm$. With regard to the discretized domain, in the DNS test case [181], a cartesian mesh of $128^2\ x\ 1024$ was used. In this thesis, however, $64^2\ x\ 512$ was employed. As exhibited in figure 4.9 below. Two visible remark are the rectangular and regular cells disposition, and the gradual expanding cell size behavior. The latter starts from the center of the chamber to the outer gray region radially.

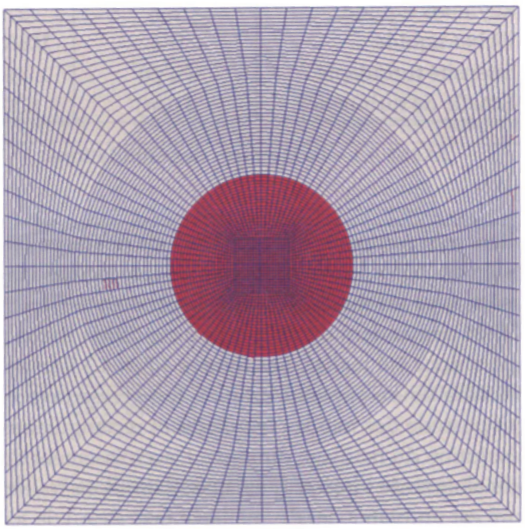

Figure 4.9: Plant view of chamber inlet, highlighted in red [7].

This idea was based on the computational adaptability for demanding industrial test cases. Using this same cell size, a previous research [7] demonstrated the numerical diffusion existence, once the smallest structures are not well captured i.e., some liquid volume fraction diffusion starts while applying Interface Capturing Method (ICM). Even tough the employment of a sharpening term in the liquid volume fraction equation, the small flow scales were not captured. Hence, prompted the use of physical models such as $ICM-ESA$, explained in the previous chapter 3, coupled with the dispersed approach explained in this chapter, namely $HELSA$ (Hybrid Euler-Lagrange Spray Atomization model). A list of relevant fluid an flow physical properties, is gathered in the table 4.1.

Table 4.1: Physical fluid properties of Shell NormalFluid ISO 4113 [6, 7], and flow conditions.

	Symbols	Value
Gas density	ρ_g $[kg.m^{-3}]$	1.226
Liquid density	ρ_l $[kg.m^{-3}]$	821
Gas viscocity	μ_g $[kg.m^{-1}.s^{-1}]$	1.78x10^{-5}
Liquid viscocity	μ_l $[kg.m^{-1}.s^{-1}]$	3.2x10^{-3}
Liquid Reynolds	Re_l	$\approx$ 12500
Gas Weber	We_g	$\approx$ 249
Turbulent intensity	$\frac{\overline{U'U'}}{U^2}$	0.05
Turbulent length scale	L_t $[m]$	0.1 D_{in}

In order to reproduce as faithfully as possible the experimental results, the chosen surface tension is $\sigma = 0.06\ N/m$, and liquid inlet velocity is $V_{in} = 250\ m/s$. Moreover, having a low Reynolds and high Weber number, droplet formation is ensured.

4.5.2 Boundary conditions

Previous simulations of the flow inside the injector were already made [6]. Using a commercial solver (Fluent [182]) and RANS ($k-\epsilon$) as the turbulence model, a velocity profile at the nozzle

exit was obtained. In this thesis, the Klein method [183] was used to modelize approximately the same liquid velocity profile at the chamber inlet, in order to reproduce the velocity profile captured by the simulations inside the nozzle. To that end, a turbulent length scale and intensity of $10\ \%$, and $5\ \%$, respectively, was also employed, with atmospheric conditions for the ambient gas pressure. Finally, experimental interface velocities will be compared against the proposed model radially, on the plane highlighted in red as shown in figure 4.10 on the left, at $1.5\ [mm]$ from nozzle exit.

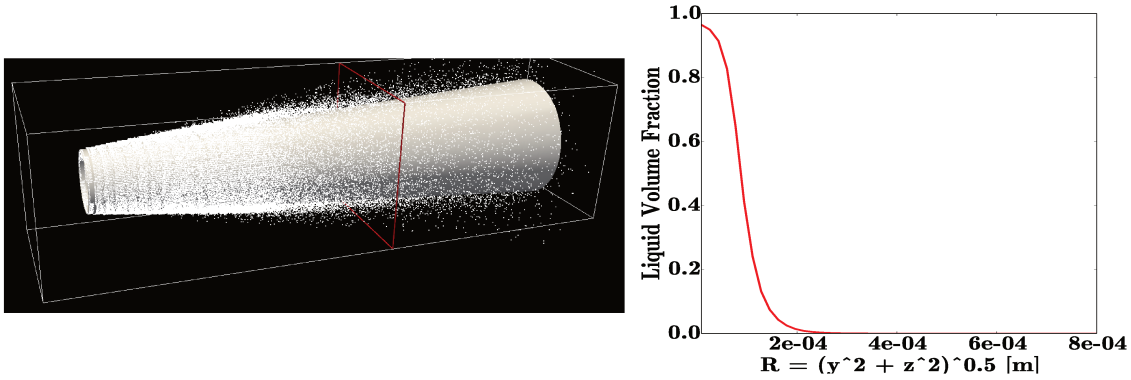

Figure 4.10: Measurement plane located at 5 diameters from the nozzle, represented by 4 red edges, along with droplets colored as white dots (On the left). Euler liquid volume fraction averaged in time and radially, at the red plane shown in the figure on the left (On the right).

On the same plane, some droplet variables will be numerically measured such as, droplet diameter, velocity and position for comparison purpose. As a illustrative purpose, it is shown on the same figure, a representative set of droplets colored in white, surrounding a grey liquid iso-surface equal to $\alpha = 0.01$. This iso-surface represents in fact, the averaged droplet injection surface. Figure 4.10 on the right, liquid volume fraction is displayed averaged in time and radially in space, at the mentioned plane. This liquid volume fraction radial profile will set the minimum radial distance from jet centerline, approximately $200\ \mu m$, to which droplets are injected.

4.5.3 Results and discussion

Results are brought in terms of *Probability Density Functions* (PDF) and its joint PDF for a pair of variables analysis, namely droplet velocity and radial position. These PDF completely characterize the random process of the two-phase flow, based on the *Stochastic Lagrange approach* previously explained. Results are presented by comparing two cases:

- Case a): Stochastic Differential Equation (SDE) for particle trajectory, with droplet injection velocity taken equal to Euler averaged mixture velocity.This case will be later called simply as: **SDE**.
- Case b): SDE with droplet injection velocity taken equal to Euler mixture velocity plus an additional fluctuating velocity (to represent the initial turbulent dispersion), undergoing a Wiener process with zero-mean random increment of standard deviation based on the local turbulent kinetic energy (equation 4.4). This case will be later called simply as: **SDE + PDF velocity injection**.

Probability density functions (PDF) for cases a) and b), are shown in figure 4.11. PDF of droplet velocity for both cases is displayed. At the top row of the figure, there is no appreciable difference, quantitatively speaking, between PDF velocity for case a) and b), which gives an indication of the non-existent influence of adding an initial fluctuating velocity term, for the droplet velocity at the injection. It is necessary to recalled that the fluctuating velocity term, has been is based on variance and Gaussian mean initial velocity, on homogeneous turbulence field.

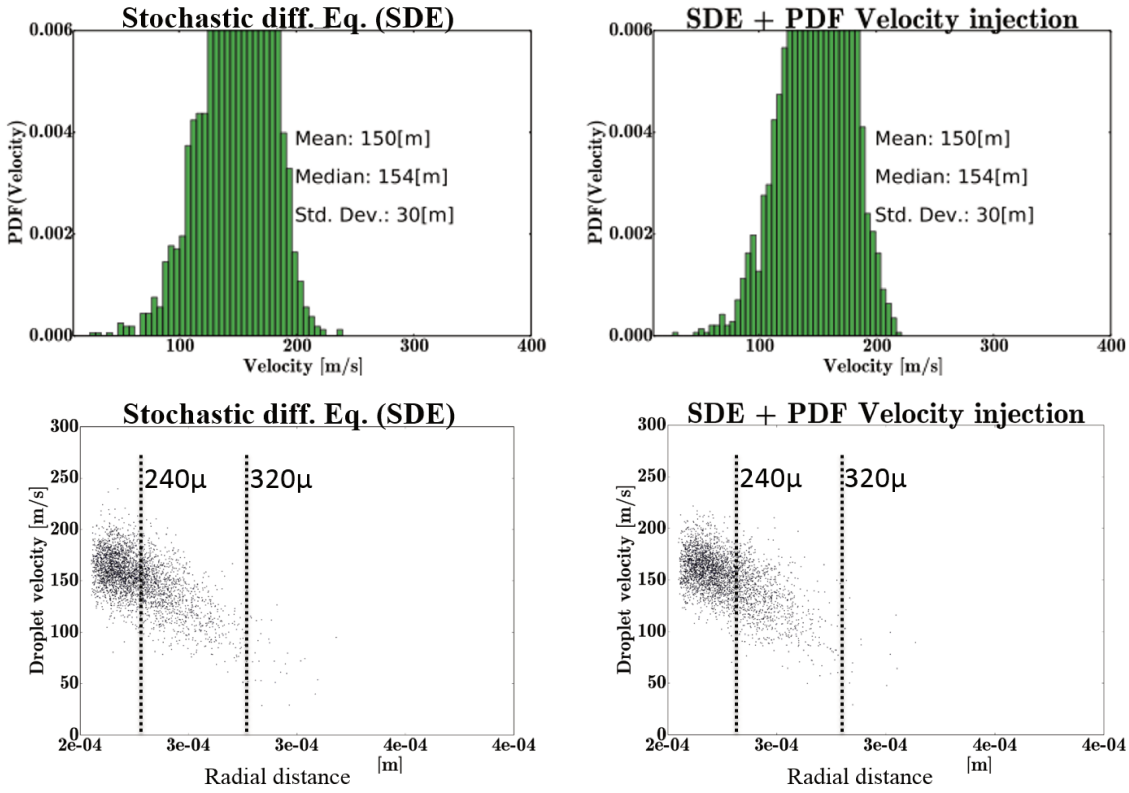

Figure 4.11: PDF of droplet velocity and velocity-distance scatter plots at the measured plane, given by **SDE** (column on the left), and given by **SDE with PDF velocity injection** (column on the right).

Both cases display the same statistics i.e., mean, median, and standard deviation values. Even tough a slightly difference can be qualitatively observed, both of them tend to a Gaussian-shaped PDF droplet velocity behavior. This behavior is actually expected, since the Stochastic Differential Equation (SDE) based on the Langevin model, is deducted from the Ornstein-Uhlenbeck (OU) process, which is a Gaussian process. Looking at the second row on the same figure 4.11, some interesting findings can be drawn, specially to the experiments comparison. It was found experimentally that droplets velocity as high as $150\ m/s$ about a radial distance of $400\ \mu m$ [6] from the liquid jet centerline, as shall be displayed in the following results. Such values, were in fact never obtainable using the SDE model (both with and without PDF droplet velocity injection), as also exhibited at the top row in figure 4.11, with approximately zero probability of finding droplets beyond this point radially. Even though some droplets may appear in a radial position beyond $400\ \mu m$, these are believed to be proves of outliers existence. It is expected in the near future some data screening to decide whether or not take into consideration theses outliers. Moreover, looking at the visible window in the scatter plots, between 240 and $320\ \mu m$ (black vertical dash-lines), there is a qualitative

droplet behavior that might be compared with experiments i.e., cloud of droplets with kinetic energy decaying process, that occur from droplet injection zone to the outer region of the spray radially.

Droplet conditioned-velocity PDF for cases a) and b) are shown in figure 4.12. Those results were obtained via the velocity-position joint PDF, to see how droplet velocity PDF behaves at the certain radial positions e.g., 240 and 270 μm, away from the liquid jet centerline. The blue and red dots, are both distributed samples of droplet velocity and radial position, in which the red dots stands in for samples at radial position equal to 270 μm, and the blue dots equal to 240 μm. Firstly, regarding the impact of droplet velocity PDF at the injection point ($case\ b$), as the previous figures showed, little or not differences between, $case\ a$, is verified here as well. Secondly, some features can be deducted. 1) At 270 μm radially from the liquid jet centerline (red dots), the expected velocity, for the **SDE** case, is ≈ 100 m/s, whereas for the **SDE + PDF vel.** case, there are two peaks with high probability droplet velocity for ≈ 80 m/s, and ≈ 150 m/s. Analogously, at 240 μm radially from the liquid jet centerline (blue dots), a slightly probability appears for ≈ 200 m/s for $case\ b$, that is not apparent in $case\ a$. This behavior might indicate some influence, after all, of the droplet velocity PDF at the injection, however, the outliers hypothesis cannot be discarded nor validated for the time being. Nevertheless, the applicability of either case (a or b), will be tested by comparing with previous experimental and numerical data, in the following pages.

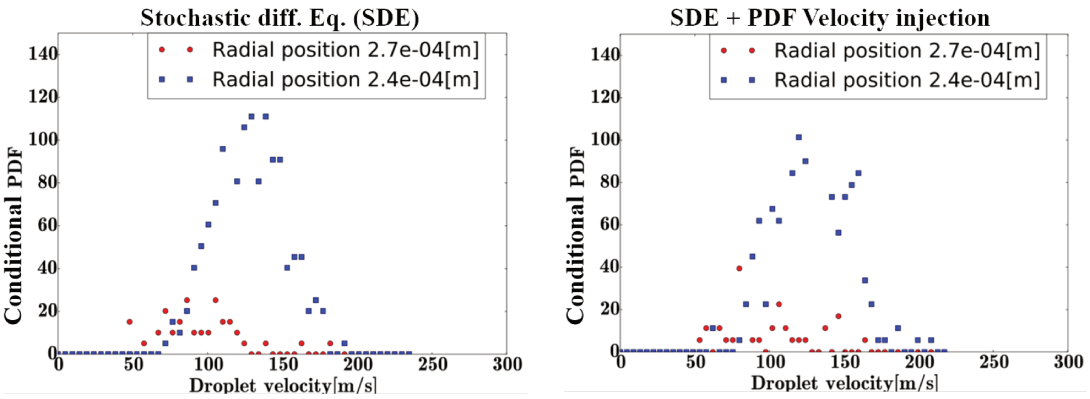

Figure 4.12: Droplet conditioned-velocity PDF based on radial position, at the measured axial plane, for two positions, 240 (blue dots) and 270 (red dots) μm, from the jet centerline, given by **SDE** (on the left), and given by **SDE with PDF velocity injection** (on the right).

Figure 4.13 exhibits the experimental and numerical comparison in terms of the averaged surface liquid velocity, $\boldsymbol{U}|_{\Sigma}$. Results are plotted at the radial plane highlighted as red segmented-line on the left of the figure. This plane was axially positioned at 7.7 diameters away from nozzle exit. Previous experiments [6] (black diamonds), DNS [181] (blue line), LES [7] (read line), are compared with three versions of $\boldsymbol{ELSA}$: (1) ELSA + Turbulent dispersion by SDE (brown line), previously called simply as **SDE**. (2) ELSA + SDE + droplet velocity PDF at injection position (green line), previously called simply as **SDE with PDF velocity injection**. Finally, (3) ELSA with Lagrange approach but without turbulent dispersion nor droplet velocity PDF at injection position (purple line). Experimental results were taken using kind of PTV measurements, based on the structure detected techniques [6]. The experimental technique exerted here was previously explained in chapter 2. Those surface liquid velocities, $\boldsymbol{U}|_{\Sigma}$, cannot be captured by the PTV instrument within the liquid jet core, as shown in the figure on the right (black diamonds). Consequently, in the absence of experimental dataset from the centerline of the liquid jet until ≈ 200 μm, DNS results were employed (blue line), in order to have a continuous validation range. Regarding the DNS, additional features were added to the

convective terms, in the liquid volume fraction and momentum equations. The momentum equation was recast, so the exact convective term could also appear, plus additional terms [181]. Concerning DNS and experimental results, figure 4.13 on the right, displays good agreement between both, from $200\ \mu m$ to $400\ \mu m$, which expands the available validation range. With respect to DNS results further from $400\ \mu m$, DNS (blue line) fails to predict dispersed zone flow field mainly due to insufficient mesh refinement. Therefore, the available validation range is taken to be from the liquid jet centerline up to $\approx 700\ \mu m$, by combining both experimental and DNS results.

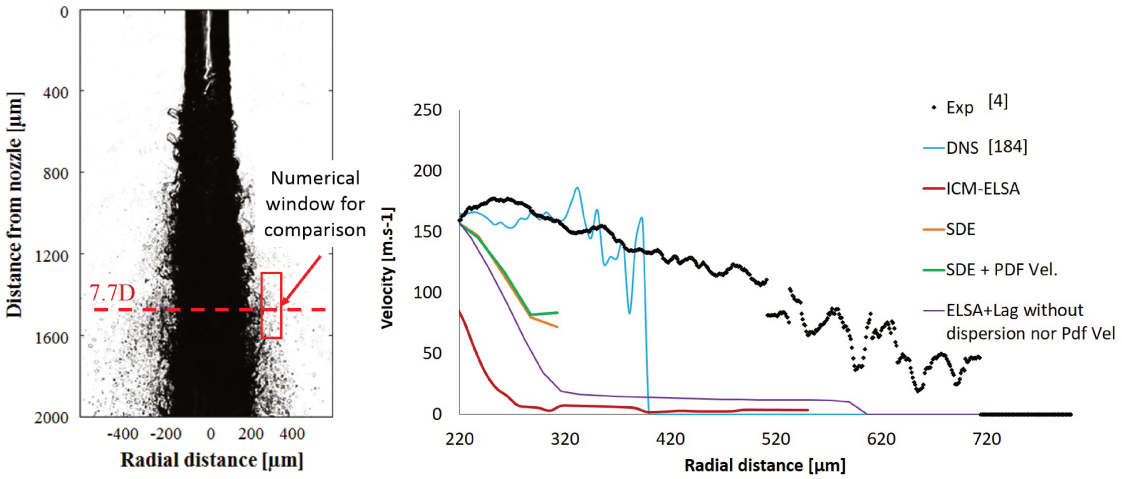

Figure 4.13: Radiography spray image of the Bosch injector [6] (on the left). Red segmented-line represents the measure plane at 7.7 diameters from nozzle exit. Experimental and numerical comparison, at the measure plane (on the right).

With regard to LES results (red line), the explained `icmElsa` model, that follows the equation 3.11, described in the previous chapter 3, was applied [7]. The results developed in this thesis were, namely cases a (brown line), b (green line), and ELSA + Lagrange without turbulent dispersion (purple line). Quantitatively speaking on one hand, figure 4.13 on the right, clearly exhibits some differences, from the centerline of the liquid jet up to $200\ \mu m$, between all ELSA results and DNS/LES. Regarding DNS and LES results, both approximately share the same decreasing velocity tendency, whereas ELSA results (purple line), are nearly constant close to the jet centerline and stable, mainly due to the averaging procedure inherited by RANS turbulence model. On the other hand, beyond $200\ \mu m$, all ELSA and LES results, tend both to underestimate the surface liquid velocity, as compared to DNS and Experimental results. With reference to LES, such logical results arrive from the formation of tiny droplets beyond $200\ \mu m$, thus residual or subgrid scales become relevant as we move outward radially. As also verified in the radiography spray image of the Bosch injector. It is believed when droplets are created, there is a relative velocity between the phases at the interface, instead of an independent flow field for each phase i.e., Lagrange approach is prompted. With respect to ELSA-RANS + Lagrange model, all three versions in this thesis, account properly for the droplets formation in the dispersed spray zone until certain extent. Firstly, as previously checked, there is not an observable substantial difference between brown and green lines, namely case a, and b, respectively, by adding and additional term to account for the droplet velocity PDF at injection point. They differ only at nearly $\approx 350\ \mu m$, away from the liquid jet centerline, maybe resulting from the lowest probability PDF distribution tail values (from the droplet velocity PDF at injection), that push at higher velocity, a few droplets away the of the jet. Secondly, the turbulent dispersion added by cases a, and b, do not decrease too much the gap between experiments and DNS. There are several possible reasons: (1) RANS turbulence

values are not really capturing all details of the two-phase flow field, (2) droplet velocity drift coefficient (the one implemented in Langevin equation, to relax the droplet velocity to the gas ambient field), is too strong i.e., over-relaxing droplet trajectories radially away of the jet, (3) the *turbulent liquid flux* undercover the real direction and magnitude of the liquid velocity at injection point, an additional value would be attained if it were coupled with the droplet velocity PDF injection equation.

Previous results were implemented based on droplet velocity injection defined in equation 4.16. It is true that the simulations were made within RANS framework i.e., (1) the interface boundary from which droplet are injected, is averaged (fixed) during the simulation time. (2) the turbulence anisotropy is not captured at all, among some other modeling assumptions. Therefore, another way to handle droplet velocity injection is presented, to account for non-homogeneous injection properties in two-phase flow. Equation 4.16 shows the new proposal:

$$\begin{cases} \boldsymbol{V}_k = (\boldsymbol{U}|_l)_{(x_{i-1})} + (\boldsymbol{U}')_{(x_{i-1})} \quad , \\ (\boldsymbol{U}|_l)_{(x_{i-1})} = (\boldsymbol{U}|_l)_{(x_i)} + \mathbf{x_{i-1}x_i}[\nabla(\boldsymbol{U}|_l)] \quad , \\ (\boldsymbol{U}')_{(x_{i-1})} = \boldsymbol{\lambda}\sqrt{\frac{2k_{(x_{i-1})}}{3}} \quad , \\ k_{(x_{i-1})} = k_{(x_i)} + \mathbf{x_{i-1}x_i}[\nabla k] \quad . \end{cases} \tag{4.16}$$

This *third approach*, is described for the initial droplet velocity injection $\boldsymbol{V}_k$, in which the turbulence memory feature is adopted, adjacent to the interface boundary between the multi-scale and disperse approach. In reality, the idea is based to hold the predominant momentum inertia from the neighboring eddies (positioned at x_{i-1}), that might have some influence on the near by droplets (positioned at x_i). The position vector $\mathbf{x_{i-1}x_i}$, describes simply a particle moving along the trajectory from its initial position $\mathbf{x_{i-1}}$, to a position $\mathbf{x_i}$. The position vector can be defined based on the *Lagrangian integral timescale* $T_l = \int[\rho(t)dt]$. This timescale is obtained from the Lagrangian velocity autocorrelation function $\rho(t)$ [90]. Consequently, The position vector $\mathbf{x_{i-1}x_i}$ is calculated by means of Lagrangian integral scale $L_L = \mathbf{x_{i-1}x_i} = (\boldsymbol{U}|_l)\boldsymbol{T}_l$. Figure 4.14 displays the results of the proposed droplet velocity injection (gray line):

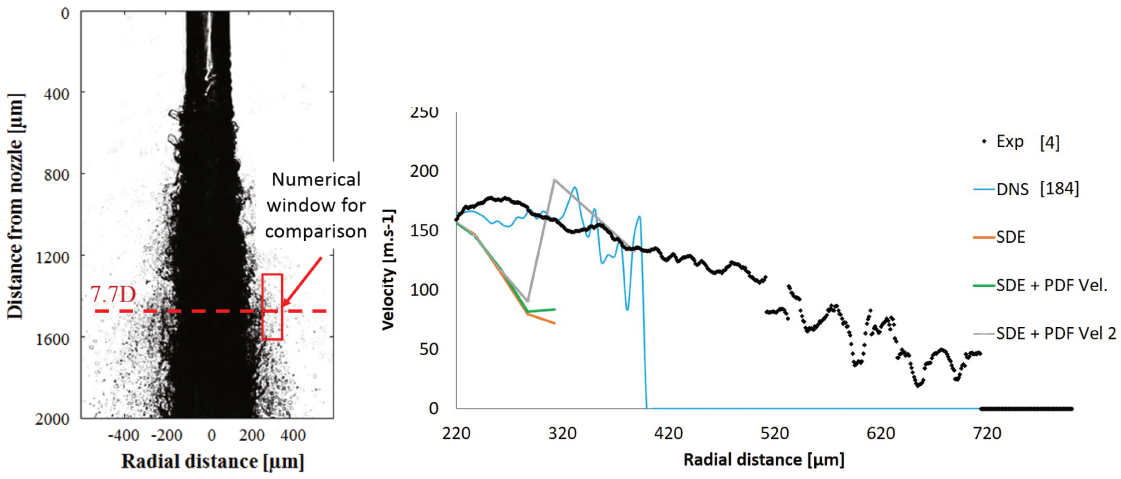

Figure 4.14: Radiography spray image of the Bosch injector [6] (on the left). Red segmented-line represents the measure plane at 7.7 diameters from nozzle exit. Experimental and numerical comparison, at the measure plane (on the right).

The gray line, which represents the new proposed non-homogeneous droplet velocity injection approach, is shown in the figure 4.14. It can be noted that little improvement can be seen from the two previous droplet injection approaches (equation 4.3) (at least, near the liquid jet centerline radially). It is further radially in the dispersed zone (between $350-400\ \mu$), that some droplets get enough radial momentum to achieve certain match with experimental and DNS measurements. This behavior can be explained in the sense that some droplets created indeed exist within the rare event droplet family, which is statistically speaking, belong to the near tail region in the distribution probability function of high droplet velocity injection. These rare droplets, are initiated way before (near nozzle exit) from the axial plane zone, in which they are quantified ($7.7\boldsymbol{D}$, from nozzle exit).

4.6 Summary and Conclusions

Previous chapter 3, verified the need of a dispersed approach, in order to improve the Eulerian formalism of the multi-scale model ($\boldsymbol{ICM-ESA}$) especially within the dilute spray region. Indeed, the objective of this chapter 4 is to take advantage of the large development formalism previously made in the dilute region of the spray i.e., WBE equations, within RANS framework. The resulting novel approach, namely Hybrid Euler-Lagrange Spray Atomization ($\boldsymbol{HELSA}$) model, is based on the paradigm of simulating the full atomization process, beginning with the modeling of liquid structures in the vicinity of the injector (dense flow region), until stochastic droplets are fully formed (dilute flow region), by using the dispersed modeling approach (WBE, solved in this chapter by a Lagrangian approach). A transition zone between the two flow regions, was identified and described. Based on the Eulerian liquid volume fraction field, a threshold was established as $\alpha_l \leq 1\%$, in which small liquid structured can be considered spherical droplets. Regarding droplet velocity and diameter injection. Three cases were set to model the droplet velocity injection: (1) based on the averaged velocity in the liquid part $\boldsymbol{U}_l$, (2) the same velocity in the index before, $\boldsymbol{U}_l$, plus an additional term that accounts for the modulation of a random velocity fluctuation based on the mixture turbulent kinetic energy. Finally (3) includes a new approach , in which non-homogeneous injection property in two-phase flow is presented. With regard to the droplet diameter injection, a Dirac delta function was used for the moment i.e., the averaged Sauter Mean Diameter (SMD) within the transition cell. The evolution of stochastic droplet trajectory undergoing Eulerian turbulent field in two-phase flow, was described and implemented in OpenFOAM® software, based on the *stochastic Lagrangian model*. Stochastic differential equation (SDE), based on Langevin equation, were added to model the fluid velocity along the droplet path. This SDE, was shown to improve from the physical point of view the robustness of the turbulent dispersion for the droplet velocity undergoing Brownian motion. The one-way coupling between $\boldsymbol{ICM-ESA}$ and $\boldsymbol{WBE}$ (Lagrange approach) has been presented and tested. Experimental, DNS, and LES data were available for comparison purpose. Firstly, even though the case $\boldsymbol{a}$, the droplet velocity injection was taken to be the averaged velocity in the liquid part only ($\boldsymbol{U}_l$), it was still possible to recover a PDF droplet velocity distribution at the measured plane, which means that even though there is no fluctuating velocity component added to this velocity injection ($\boldsymbol{U}_l$), the global PDF droplet velocity injection might be playing some role a major role than we thought. Secondly, the droplet velocity injection distribution, based on an additional diffusive term undergoing a Wiener process with zero-mean random increment of standard deviation based on the local turbulent kinetic energy, brought non-existent statistical influence, compared to cases without velocity distribution injection. Even though the outer radial trend was captured by all droplet velocity injection approaches, only the last approach (based on non-homogeneous turbulent injection properties) was able to capture the rare droplets i.e., droplet with high radial velocity and inertia. This droplet behavior is an indication of the turbulence memory feature, which is somehow lost using RANS averaged equations.

Chap. 5 | Industrial applications

5.1 Introduction

As a reminder, the main goal of this thesis is to come up with an accurate two-phase flow liquid atomization model, able to be industrially applied in a computational affordable way. Previous chapters 3 and 4, have addressed multi-scale and multi-physic issues within the liquid jet atomization process. Both chapters have, until some extent, validated the proposed $\boldsymbol{ELSA}$ model for the full liquid spray atomization process i.e., from primary atomization (chapter 3) to dispersed flow (chapter 4).

The test cases exploited for comparison and validation purpose, namely *ECN Spray-A*, *air-blast atomizer* and *Bosch Injector*, have experienced plenty of experimental and numerical measurements, and above all, are well-accepted reference cases. Nonetheless, these test cases still represent a *modeled* version of their industrial counterpart, in which in some cases, experimental conditions were adapted to fulfill the available laboratory equipments, for instance the gas-fuel density corrections [184], to adjust the temperature upper limits in the facility.

The objective of this chapter is then to directly apply the validated $\boldsymbol{ELSA}$ atomization model, to two industrial liquid injectors, namely *FCC Injector* and *Spray water injector*. The particularity regarding these liquid injectors, is the absence of experimental measurements. The reasons are twofold: their operating conditions and dimensional size (explained in detail later on), which make unmanageable to carry out any experimental technique utilized, at least within the scope of previous chapters.

These two liquid injectors have been provided, for numerical study purposes, by VINCI Technologies. The French enterprise Vinci Technologies, manufactures and provides a broad range of laboratory equipments and specific field instruments for the Oil and Gas Industry. A portion of them is developed in close collaboration with IFPEN. One of its goals, is to design and build durable, reliable, high-efficient and low maintenance FCC and Spray water Nozzles.

This chapter is constituted in two parts, one part for each injector, namely *FCC Injector* and *Spray water injector*. It is then organized as follows: Firstly, a recent bibliography review is presented for the FCC Injector, regarding the previous experimental and numerical research. Secondly, from the physical mechanism point of view, the FCC Injector is broken down in two main parts namely, *venturi* and *premixing*. These two parts are numerically studied separately. Several geometrical configurations are tested to evaluate the FCC Injector performance, on both main parts. The Sauter Mean Diamater ($\boldsymbol{SMD}$) and the interface surface density (Σ), were the variables of interest utilized, to compare the mixing performance. Thirdly, with respect to the Spray Water injector, a thermodynamic analysis is first made, to ensure the proper fluid flow mixing properties inside the spray water injector, according to the dimensioned size. Finally, two design geometrical conditions were examined via CFD, using $\boldsymbol{ELSA}$ atomization model inside the spray water injector.

5.2 FCC Injector numerical test case

5.2.1 Previous and related studies

As a refresher from concepts developed in chapter 1, Fluid Catalytic Cracking (FCC), is a process where the crude oil is transformed into Gasoline, olefins and distillates. In this process, the liquid oil feed, is atomized through a set of injectors connected circumferentially to a riser. Moreover, the oil droplets are vaporized and cracked within the riser upon contacting hot gases and catalyst, respectively [9]. The main goal in an FCC Injector design, is to produce small size droplets in order to ensure quick vaporization and intimate contact with the catalyst [185]. To that end, feed vaporization and the cracking reactions occur inside the riser, while catalyst, hydrocarbon liquid droplets, and hydrocarbon vapors travel upward. Therefore, there are several chemical and physical complex phenomena occurring simultaneously at the nozzle exit namely, the feed atomization zone. A summary of relevant features used in FCC Risers modeling is highlighted on figures 5.1 and 5.2:

	A. Gupta 2001	S. V. Nayak 2005	C. Zhu 2006	P. Zhao[1] 2009	M.T Shah 2011
Numerical scheme	Constitutive equations	Euler-Lagrange	Euler-Lagrange (gas-solid, droplets)	Euler-Lagrange (Cluster)	Euler-Euler
Heat Transfer	- Sensible heat - Boiling model (convective)	- Sensible heat - Vaporization model (direct contact) - Boiling model	Energy transfer between gas and droplets and droplets	Isothermal	Not considered
Cracking	4-lump kinetic model	4 and 10-lump kinetic model	Not considered	Not considered	Not considered
Species	Considered	a) Multi-component drops b) Species equation	Not considered	Yes, but not reported	Not considered
Turbulence	Laminar	Laminar	Prandtl mixing length	Yes, but not reported	K-Omega
Collisions	Not considered	Hot solid particles and evaporating liquid drops	Momentum transfer between gas/solid and droplets	Multiphase particle-in-cell + collision term based on Boltzmann equation + momentum transfer	Momentum transfer between gas/solid.
Molar expansion	Considered	Considered	Not considered	Not considered	Not considered
Axial catalyst holdup	Local force balance. Cluster approach	Local force balance	Considered	Yes, but not reported	EMMS based drag model.
Mass transfer	Gas-liquid mass transfer due to vaporization	Gas-liquid mass transfer due to collisions of particles	Gas-liquid mass transfer due to vaporization	Not considered	Not considered
Catalyst deactivation	Non-selective. Based on coke concentration on the catalyst	Non-selective. Based on coke concentration on the catalyst	Not considered	Not considered	Not considered
Backmixing	Not considered	Not considered	Not considered	Not considered	Not considered
Spray penetration	Not considered	Not considered	Effect of nozzle aspect ratio, solid loadings on evaporation length and spray deflection	Penetration parameter for horizontal liquid injection	Not considered

Figure 5.1: Comparative summary of main features for FCC Riser simulations (Part 1).

	A. Dutta 2012	J. Chang 2012	G. Q. Chen 2014	M. Ahsan 2015	S. Chen 2016
Numerical scheme	Euler-Euler + PBM (DQMOM)	Euler-Euler	Euler-Euler + PBM + Single-particle model	Euler-Euler	Euler-Euler
Heat Transfer	Instantaneous vaporization	- Sensible heat - Vaporization rate based on volume fraction and density of droplets	- Instantaneous vaporization - Energy transfer between gas-solid particles	Instantaneous vaporization	Isothermal
Cracking	12-lump kinetic model	12-lump kinetic model	4-lump kinetic model	4-lump kinetic model	Not considered
Species	Species equation in the continuous phase	Considered	Considered	Species equation in the continuous phase	Considered
Turbulence	K-Epsilon. Dilute concentration of secondary phase	K-Epsilon	Yes, but not reported	K-Epsilon.	Laminar
Collisions	Momentum transfer.	Not considered	-Single particle model which considers intraparticle transfer	Momentum transfer.	- Momentum transfer.
Molar expansion	Considered	Considered	Considered	Considered by ideal gas law	Not considered
Axial catalyst holdup	Drag model for polydispersed flows	Considered. Syamlal-O'Brien drag model	Considered	Not considered	Improved EMMS based drag model.
Mass transfer	Catalyst deactivation	Considered	Considered	Not considered	Not considered
Catalyst deactivation	Non-selective. Based on coke concentration on the catalyst	Non-selective. Based on coke concentration on the catalyst	Non-selective. Based on coke concentration on the catalyst	Non-selective. Based on coke concentration on the catalyst	Not considered
Backmixing	Not considered	Not considered	Not considered	Not considered	Back-mixing in the feed injection zone
Spray penetration	Not considered	Not considered	Not Considered	Not considered	Appearance of secondary flow in the feed injection zone

Figure 5.2: Comparative summary of main features for FCC Riser simulations (Part 2).

The figures 5.1 and 5.2, are organized historically, in which main research topics (column on the left) have been selected such as: numerical scheme, turbulence, particle collisions, species equations, catalyst deactivation, spray penetration, among others. Several key points can be extracted from the historical review. For instance, feed vaporization is rarely modeled. Normally, feed vaporization takes place in the first $1.5-3\ m$, of the FCC Riser, which corresponds to $5-10\ \%$, of the riser total length ($30-40\ m$) [186]. On the other hand, the feed needs only approximately $3\ \%$, of the mixture residence time to completely vaporize, which corresponds to $0.3-30\ ms$, depending also on the drop size distribution [187]. Likewise, the cracking reactions occur only when the feed is already vaporized [188], [189], [9], which justifies the assumption of instantaneous vaporization in previous research. With regard to the numerical modeling part, although various modeling approaches for the riser can be found in the literature, mostly one and two-dimensional models can be found [190], [187], [191]. For 3-D models, two kinds of approaches are applied, Eulerian-Eulerian and Eulerian-Lagrangian approaches, both implemented by computational fluid dynamics (CFD). Most aforementioned studies have then assumed instant vaporization and uniform catalyst/oil ratio at the bottom

of riser cross-sectional area, based on the assumption that the cracking time scale, is much longer than the time scale of interface transport in the feed injection zone [192, 193]. Some other studies considered the vaporization rate of the liquid oil, using two approaches, namely homogeneous and heterogeneous approach, in which both methods set the limits for the actual vaporization time [194]. When it comes to FCC riser modeling, many researchers have focused on the upper and middle zone of the riser, and just a few researchers on nozzles and feed atomization zone [195], mainly due to the high constraints using multidimensional models with chemical reactions, vaporization, and atomization within an industrial scale. Theologos [196] studied atomization effects on reactor performance, and found that smaller droplets produce higher vaporization rates. Therefore, the need for a deeper understanding of the physics and atomization mechanisms involved within a FCC injector, coupled with the feed injection zone urged to be tackled. This Ph.D., the aim was to numerically model the oil-steam mixing inside the FCC injector.

As it can be also seen on the above figures, just a few investigations have been made on the feed atomization zone and moreover, just a few within the injector. It is the purpose of this chapter to accurately evaluate, using CFD, the flow within a FCC Injector.

5.2.2 FCC Modeling approach

Several studies have shown the paramount influence of the feed injection system on FCC Reactors [30] [31] [25]. Hence, the global FCC Reactor efficiency is improved by optimizing the feed atomization zone [8] [32]. As previously stated, fast and uniform mixing is essential to ensure quick vaporization and intimate contact between the oil and catalyst, specially during the aforementioned residence time within the feed atomization zone. To accomplish such task, special care should be taken in designing the FCC Injector.

Within the FCC Injector, the oil flows co-currently along with the steam, to promote the necessary fluidity and turbulence required for mixing, and possibly vaporization, before the mixture gets atomized as soon as it exits the injector. Since both volumetric fractions (oil, and steam) are above $\mathbf{10}$ %, the dilute model approach cannot be used. Accordingly, the previously validated Eulerian/Lagrangian Spray Atomization ($\boldsymbol{ELSA}$) model (see chapters 3 and 4 for more details), will be able to characterize the liquid volume fraction that might have been atomized and dispersed. The proposed model has then been proven to be suitable for any interface liquid-gas topology, and it is based on the local liquid volumetric fraction and local interface surface [147] [2]. Moreover, this model has been implemented in a numerical framework, i.e. CFD (Computational Fluid Dynamic) using OpenFOAM® software [174], which solves the equations of fluid mechanics with a finite volume approach [123]. This code, can be easily parallelized to run HPC resources such as French computer centers: CINES, TGCC, IDRIS, CRIHAN [197] [198] [199] [200]. Finally, OpenFOAM® software is distributed by the OpenFOAM® Foundation [201], and is freely available and above all, open source, licensed under the GNU General Public License [202].

This study consists in three parts clearly identified in the figure 5.3, as the main zones within a schematic FCC Injector. These parts are namely *premixing*, *venturi* and *nozzle*. The first zone, *premixing*, is dedicated for phase mixing. Ideally, it is believed, primary atomization takes place and some droplets might be formed. Some features can be highlighted in this zone, based on the oil/steam fluid flow properties, such as non-Newtonian behavior, gas compressibility effects, oil-wall sticking, among others. The second zone, namely *Venturi*, represents the contraction area where the two fluids flow. On one hand, compressibility effects may take part if flow velocity is highly increased, and on the other hand, the contraction may serve as an oil-walls contact inhibitor. Numerical analysis would allow a better understanding of the physics involved in order to optimize the FCC Injector performance. Lastly, the *nozzle* zone, is regarded as the key parameter for several reasons: a) proper radial distribution of the feed

within the riser, b) enough linear momentum of the feed to penetrate the steam/catalyst flow within the riser, and c) adequate droplet size distribution of the spray, for fast vaporization rate.

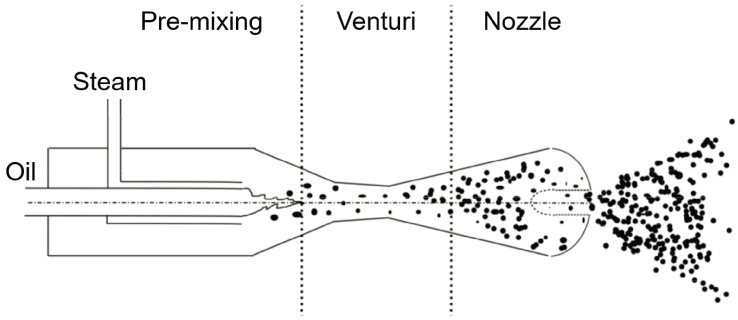

Figure 5.3: Schematic FCC Injector. Primary zones: *Premixing*, *venturi* and *nozzle*.

Initially, the feed atomization zone coupled with *nozzle* zone, seemed an attractive idea to be numerically assessed, specially the spray development inside the riser, interacting also with particle-laden upward flow. What is more, based on spray characteristics, further improvements on $\boldsymbol{ELSA}$ algorithm could be prompted, in order to predict as accurately as possible the physics of the feed atomization zone. However, due to large computational domain (which considers injector-riser assembly), the computational time consumed, and any additional physical model complexity, the numerical simulation would then become largely demanding. Therefore, a decoupling approach was considered instead. Thus, internal and external flow calculations were conducted separately. Meaning firstly, simulation of a full FCC Injector was made. Which later on, would permit to feed the inlet boundary condition of an external flow simulation (i.e., within the Riser), with the fields obtained at the nozzle exit. The full simulation of FCC Injector, taking into account the *venturi* and *premixing* zone, are in fact, the simulations in this chapter.

This $\boldsymbol{ELSA}$ model, which is the model used to numerically appraise FCC injector performance, is thus able to take advantage of a full interface resolution (near nozzle exit) to recover a DNS formulation with ICM, and to switch to a sub-grid approach when necessary (far field flow). Furthermore, when the spray is formed and diluted (dispersed flow), it is more accurate to use a regular method dedicated to solved WBE, and therefore a Lagrangian formulation is initiated in the $\boldsymbol{ELSA}$ model. The capabilities of the whole approach ($\boldsymbol{ICM}$, $\boldsymbol{ELSA}$ for sub-grid scales and $\boldsymbol{Lagrangian}$ tracking) have been previously tested and validated in chapters 3, and 4. Furthermore, this internal flow simulation represents in great part the work done during the first year of Ph.D.

5.2.3 Numerical domain and flow conditions

As stated above, simulations within a FCC Riser, involve complex physics, specially within the feed atomization zone, such as liquid atomization, vaporization, chemical reactions, among others. In this work, the atomization/mixing process is first studied within the FCC injector itself. This advised FCC Injector treated in this chapter, was provided by $\boldsymbol{VINCI\ TECHNOLOGIES}$, as displayed on the figure 5.4. The mechanical part of the FCC Injector, was properly handled using SALOME, which is an open-source, free software, that provides a generic platform for Pre/Post-Processing for numerical simulations, by using Computer-Aided Drawing (CAD) tools [203]. Within the mechanical part of the FCC Injector, a fluid wettable side was extracted and a 3D modeled geometry was built, as shown on the figure 5.4, colored in red. The modeled geometry, is a simplification of its actual counterpart, that *models* the flow passage without unnecessary complexity coming from the mechanical parts e.g., bolts,

joints, nuts, screws, welds, among others. Additionally, the steam pipe, where the steam flows prior entering the injector (mid-way positioned pipe), has been subtracted for simplicity purpose.

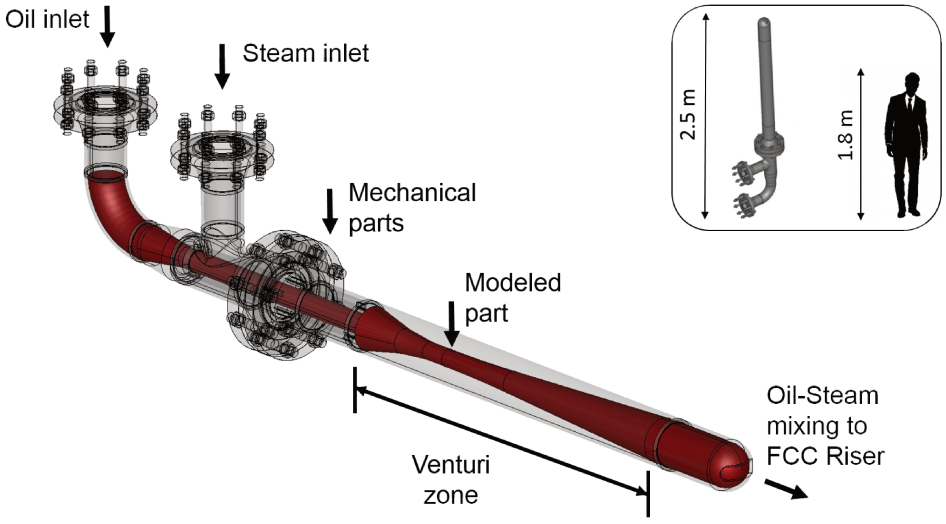

Figure 5.4: Mechanical geometry of VINCI's FCC Injector. Modeled geometry (red).

It is to be noted also on the figure, the industrial nature of the FCC Injector, which is a lot much larger than the numerical test cases studied so far e.g., in the previous chapters 3, and 4. Approximately, $\mathbf{250}$ times the size of both *ECN Spray-A* and *Bosch Injector*'s chamber. This dimensional feature is indeed, an economical limitation when it comes to experimental measurement facilities. Moreover, the fluid and flow operating conditions, are shown in the table 5.1 below, which displays the high pressure of both fluids oil and steam ($\approx \mathbf{10}\ \boldsymbol{Bar}$), making even more challenging the test rig installation setup. For more details on high pressure and high temperature test rig facilities, see [204]. Therefore, for the time being, to the best of our knowledge, there is no experimental data concerning the FCC Injector of $\boldsymbol{VINCI\ TECHNOLOGIES}$. On the other hand, from the numerical point of view, it can also be seen, highlighted in red, the non-dimensional numbers $\boldsymbol{Re_l}$ and $\boldsymbol{We_g}$, equal to $\approx \mathbf{154000}$, and $\approx \mathbf{5000}$, respectively. Which makes suitable the use of the already validated $\boldsymbol{ELSA}$ model on this FCC Injector.

Table 5.1: Fluid and flow Properties.

	Oil	**Steam**
$\boldsymbol{U_{inlet}}$	6.4 m/s	18.01 m/s
ρ	750.1 kg/m^3	3.885 kg/m^3
ν	7e-07 m^2/s	4.7e-06 m^2/s
$\boldsymbol{T}$	280 $\boldsymbol{C}$	280 $\boldsymbol{C}$
$\boldsymbol{P}$	10 $\boldsymbol{Bar}$	10 $\boldsymbol{Bar}$
$\boldsymbol{Re}$	$\approx$ 154000	$\approx$ 47000
$\boldsymbol{We_g}$	–	$\approx$ 5000

Once the modeled geometry is created, a discretization process is carried out. The unstructured hexahedral mesh, with inflation layers adjacent to the wall, with a total of $\approx \mathbf{5}$ million cells,

is shown on the figure 5.5. On the left of the figure, the oil inlet is exhibited with nearly ≈ 50 cells in the transverse direction. On the right of the figure, the initial part of the *venturi* zone, in which the steam is put in contact with the oil is represented, with polyhedral type cells to adjust the circumferential shape of the *venturi* zone. This process is usually refered also as *meshing* process. The idea behind the discretization process, consists in dividing the modeled geometry by a number of small volumes called *numerical cells*. The resulting mesh was done with an open-source library for mesh generation, by this time implemented within OpenFOAM® framework, named `cfMesh` [205]. The library supports generation of meshes of arbitrary cell types, and the currently implemented work-flow generates cartesian type cells, in both 2D and 3D space, tetrahedral, hexahedral and arbitrary polyhedral as exhibited on the right of figure 5.5. Moreover, discretized equations are applied to each numerical cell, based on Finite Volume Method (FVM) [206] [110].

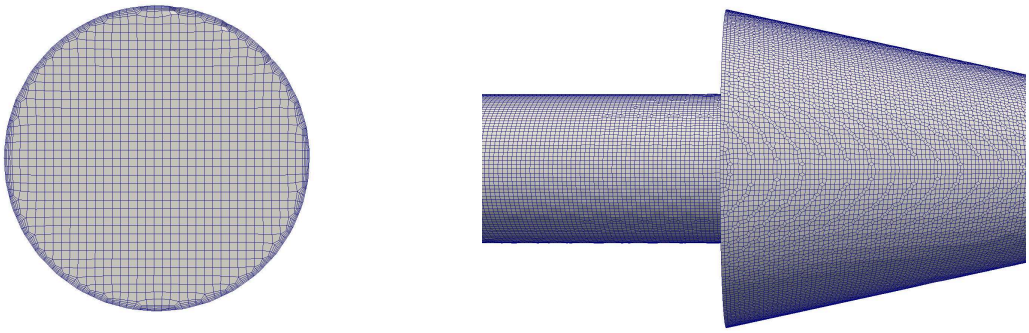

Figure 5.5: 3D Model of VINCI's FCC Injector. Inner cells at liquid inlet (left). Sliced part of *venturi* zone, showing the gas inlet (right)

Estimation for the minimal $\boldsymbol{LES}$ mesh resolution, Δ_x, is recommended by Addad et al. [19], and it is based on the Taylor micro-scale Λ [90], see equation 3.17 in chapter 3 for more details. Finally, the number of cells at liquid inlet, ≈ 50, and the cell size both at liquid and gas nozzles, is $640\ \mu m$, as shown in the figure 5.5. Consequently, to evaluate the above mesh process and get quickly robust and computationally less expensive results e.g., than using Large Eddies Simulation ($\boldsymbol{LES}$), a time-averaging of the governing equations 3.11, of the previously explained Eulerian solver $\boldsymbol{ELSA}$, is used. Figure 5.6, displays the gradients in the span-wise direction of axial velocity, which reveals wall-bounded effects in the apparently phase mixing zone (*venturi*), due to existence of high gradients near the wall colored by red/blue.

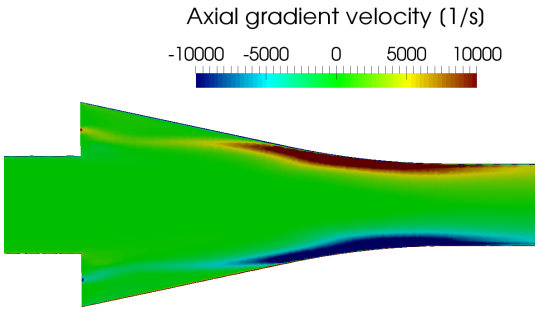

Figure 5.6: Span-wise gradients of axial velocity, in a zoomed region within the *venturi* zone.

This phenomena has never been encountered e.g., in ECN Spray-A injectors [207]. Based on that fact, the model was meshed using the same height for all first cells adjacent to the wall. The first cell height, was then calculated based on the $Y+ > 30$ values at the wall, that fulfill

the turbulent log-wall functions available in OpenFOAM® . It is apparent, by using the same first cell height everywhere, that the highest velocities would give an indication of the highest $Y+$ values in the domain, in which in this case, there are also found in the *venturi* zone. It is clear for the time being, that a full-scale resolution, for this two-phase flow highly turbulent case, using LES (i.e., $Y+ = 1$), is out of the reach of the computational resource available.

5.2.4 Boundary conditions

Regarding the boundary conditions, *Dirichlet* boundary condition, for velocity, is imposed at gas and liquid inlets. It is also set to zero (0) value along the walls, and an *outflow* boundary condition, which is a zero gradient Neumann type, is applied on the nozzle exit. For the pressure, *Total pressure*, is specified on the nozzle exit. For the liquid volume fraction, *Dirichlet* boundary condition equal to one (1) at liquid inlet and to zero (0) at gas inlet. *Zero gradient* is applied along the wall, and an *outflow* boundary condition is applied as well on the nozzle exit. Initial conditions are at rest, for the whole domain, i.e., null velocity and atmospheric pressure. The liquid pipe, is initially filled completely by liquid. An adaptive time-step is used, which constraints a maximum CFL condition equal to 0.5.

Gas Reynolds number $Re_g \approx 47000$, that shows the turbulent character of the flow. It is shown in the work of Xiao et al. [103], in which LES of similar atomization configurations were performed, that the initial interface perturbations caused by liquid and gas eddies plays an important role in the resulting surface instability development and primary atomization process. When turbulent inflows were specified, for instance, they correctly predicted experimental core breakup lengths. Their flow conditions showed momentum flux ratio J (equation 3.16), varying between 0.17 and 2. In the present chapter, simulated configurations own a momentum flux ratio with a value of $J = 0.04$. It can be assumed that gas eddies might have some impact on the interface disturbance, hence gas unsteady turbulent inlet velocity conditions could be specified, as previously expressed in equation 3.18:

$$\begin{cases} \overline{U'^2} = \dfrac{2}{3}k \quad , \\ k = \dfrac{2}{3}(U_g T_i)^2 \quad , \\ T_i = 0.14(Re_g)^{-0.079} \quad . \end{cases} \tag{5.1}$$

No specifications for turbulent liquid inlet conditions were employed, in this case, a full length liquid pipe was employed instead, to let turbulent develop naturally, as displayed in red in the figure 5.4.

5.2.5 Venturi zone modeling

Results have been separated in two parts. Firstly, results including oil volume fraction, mixing velocity, droplet diameter distribution, are obtained using the actual FCC Injector dimensions provided by VINCI's. Secondly, a sensitive parameter was proposed, i.e., the *venturi* position has been tested using different axial positions and diameters, thus allowing estimate their effects, on the performance of the FCC Injector, by means of the Sauter Mean Diameter (SMD). Additionally, in order to reach convergence and hence, get time-independent results, the liquid oil was allowed to cross ten (10) times the FCC Injector completely in the axial direction.

Actual geometry

Figure 5.7 on the left, illustrates the oil volume fraction colored map, using $ELSA-LES$ model without the Interface Capturing Method (ICM) i.e., equation 3.11 with $C_\alpha = 0$. The

two-phase flow within the FCC injector, demonstrates that there is a liquid core flow (colored in red) and annulus gas flow (colored in blue) compressed by the latter inside the injector. This liquid core is then broken up eventually in a certain axial distance from the inlets i.e., approximately at the middle of the *venturi* zone, commonly namely the constricted area or the *throat*.

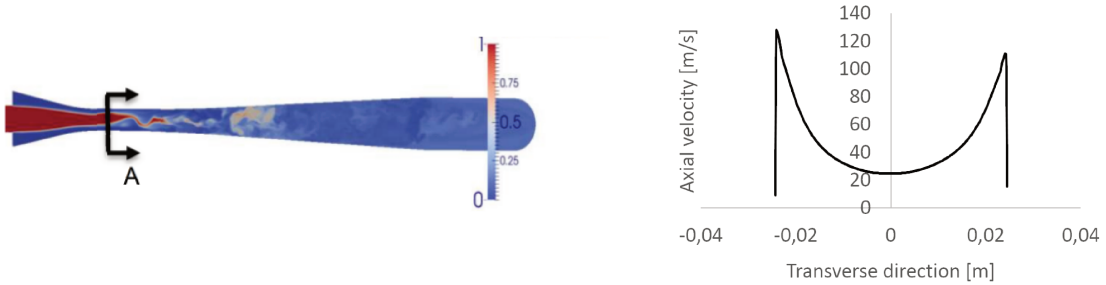

Figure 5.7: Oil volume fraction (left). Axial velocity profile on **A** transverse cross-section (right).

This concentric behavior, compresses the gas to the wall, thus increasing its stream-wise velocity near the wall, specifically at the *venturi zone*. Figure 5.7 on the right, displays the axial velocity profile in the transverse cross-section, **A**, which verifies the aforementioned high velocities near the wall. Consequently, the initial relative velocity verified between the phase at their inlets, is increased considerably at the *venturi zone*, specially near the *throat*. These high velocities are the mechanism from which mixing between phases takes place. The venturi by definition takes advantage of the incoming pressure energy of the flow, to transform it into kinetic energy. It is to be also noted, that gas compressibility effects were not considered in this numerical test case. The *throat*, which is the part within the *venturi-shaped* section with the smallest diameter, is where the highest velocities occur i.e., the turbulent mixing, see figure 5.8 for clarification. It can also be seen in figure 5.7 on the left, a before and after the *throat*, different behaviors of the flow. Before the *throat*, there is a clear distinction of the phases, however after it, the phases begin to mix in a sub-grid scale as soon as they move downstream within its diverging section. Therefore, it is believed that this *venturi-shaped* section of the FCC Injector, plays a paramount role in phase mixing, by increasing the shear rate exerted on the liquid and promoting turbulent mixing, up to the end of its diverging section.

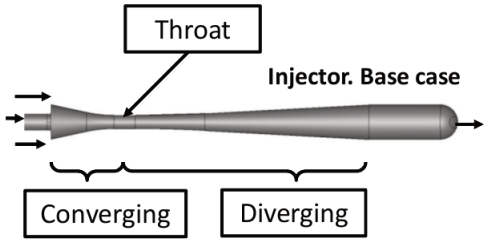

Figure 5.8: Main parts of the *venturi-shaped* section of the FCC Injector.

Different geometrical configurations

Once the *venturi-shaped* section is highlighted, series of modifications are proposed to better understand their effects. Therefore, three alterations have been made to the principal part of the *venturi-shaped* section, the *throat*. Firstly, two different axial positions have been tested to study the repercussions of decreasing/increasing the converging/diverging length of the

venturi, namely $Injector\ 1$ and $Injector\ 2$, displayed both in the figure 5.9 (second and third row from top to bottom). The *throat* for $Injector\ 1$, has been placed at mid-way axially of the *venturi* section, hence the diverging/converging length become exactly the same. In $Injector\ 2$, The *throat* has been moved upstream one-throat length, so the converging zone length is decreased, making the shear stress rate more aggressive within this part. Finally, a 20% diameter reduction of the *throat* is considered, namely $Injector\ 3$ (last row on the figure 5.9). This diameter reduction will certainly increase even more the velocity of both phases, hence the turbulence mixing .

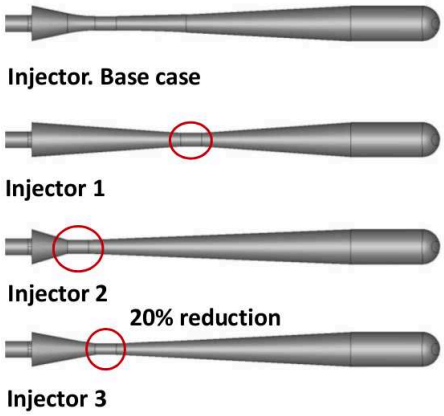

Figure 5.9: Alterations proposed, $Injector\ 1$, 2, and 3, (second, third and last row, respectively) compared to the original FCC Injector geometry, namely $base\ case$ (first row).

Simulations are done using the same validated $ELSA$ model, explained in chapter 3 (equation 3.11). Boundary conditions, and fluid properties are taken from the $Injector\ base\ case$, and will be the same for all the numerical cases. Results are displayed by the oil volume fraction in a transverse plane, left part of figure 5.10, and at plane-view of injector exit, on the right of figure 5.10, for $base\ case$ and the three proposed modifications, namely $Injector\ 1$, $Injector\ 2$, and $Injector\ 3$.

Firstly, $Injector\ 1$ (second row from top to bottom in figure 5.10), displays a similar well-defined oil liquid penetration length to the $base\ case$, with coarser liquid core before the throat. As a reminder, the *throat* for $Injector\ 1$, has been placed at mid-way axially of the *venturi* section, hence the diverging/converging length become exactly the same. Likewise, the *throat* has been axially moved downstream compared to the $base\ case$. It can be seen that the liquid core is still broken up, exactly at the *throat* of $Injector\ 1$, due to the turbulence generated, and after the *throat*, the phases are mixed in a sub-grid scale all the way to nozzle exit. It is indeed at the nozzle exit, which can be verified the flow uniformity. $Injector\ 1$ exhibits higher and lower values of oil volume fraction compared to $base\ case$, at the nozzle exit (from blue to red color transition, in the figure 5.10), supposedly due to diverging section reduction. Therefore, it can be claimed, less time and space exist for the mixing to accommodate and to reach the uniformity obtained in $base\ case$.

Secondly in $Injector\ 2$ (third row from top to bottom in figure 5.10), the *throat* has been axially moved closer to oil and gas inlets. Accordingly, based on previous simulations from $Injector\ 1$, the purpose of approaching the *throat* to both inlets, is to enhance flow accommodation, after the *throat*, by increasing the diverging section length. Nevertheless, the oil volume fraction values observed in the transverse plane are higher than its counterparts (light green instead of blue), which might be a little unphysical while using constant flow rate on both fluids at their inlets. The fact is that unphysical additional liquid mass in the diverging section, is mainly based on the possibly over compression of the gas at its inlet, due to the *throat* newly upward position. This compressible effect, is not being accounted in the

model used. Therefore, this limiting position of the *throat*, sets the boundary at which the incompressible $\boldsymbol{ELSA}$ model, is physically suitable. Further axial movements of the *throat* upstream in the *venturi zone*, will therefore require additional features to be added to the $\boldsymbol{ELSA}$ model, to accurately predict the mixing of the phases.

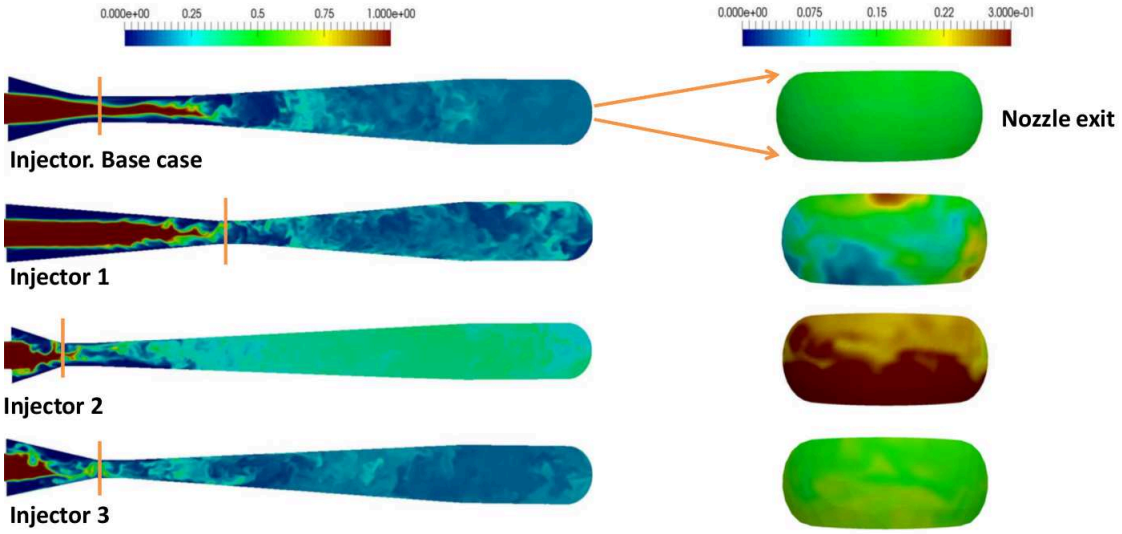

Figure 5.10: Oil volume fraction field. Transverse plane (left). Injector exit (right)

Finally, $\boldsymbol{Injector\ 3}$ (last row from top to bottom in figure 5.10), experiences higher shear rates before the *throat* due to the *throat* diameter reduction. In this case, the span-wise axial velocity gradient is stronger, which is unfavorable from the numerical point of view, since the mesh resolution requirement is increased compared to the $\boldsymbol{base\ case}$. This modification in turn, makes the turbulent mixing more aggressive as can be seen in the figure 5.10 i.e., the phases are mixed well before reaching the *throat*. Likewise, the liquid core is broken up faster compared to the $\boldsymbol{base\ case}$. Nevertheless, at the nozzle exit, the flow uniformity acquired is approximately on the same magnitude, qualitatively speaking, as the $\boldsymbol{base\ case}$. Except maybe for slightly upper values, colored in yellow at the bottom part of the nozzle exit.

Moreover, quantitative results have been reproduced using the sauter mean diameter (SMD). A volume weighted particle size distributions is also used [208], thus it is convenient to report parameters based upon the maximum droplet size, for a given volume percentage of the sample. Percentiles are defined as **DvB**, which: **D** stands for diameter, **v** for volume, and **B** = percentage of sample below a particle size e.g., $\mathbf{50}$ %, or sometimes written as a decimal fraction i.e., $\mathbf{0.5}$. For instance, the $\boldsymbol{Dv50}$, would be the maximum droplet diameter that exists below the $\mathbf{50}$ % of the sample volume. Figure 5.11, illustrates the cumulative volume percentage based on droplet diameter, for $\boldsymbol{Injector\ base\ case}$, $\boldsymbol{Injector\ 1}$ and $\boldsymbol{Injector\ 3}$, colored by black, blue, and red line, respectively. For comparison purpose, $\mathbf{90}$ % of the total volume sample is used. It can be seen the maximum droplet size picked up for each configuration, hence the smallest droplet size among the three geometrical configurations, corresponds to the $\boldsymbol{base\ case}$ with $\mathbf{2}\ \boldsymbol{mm}$, followed by $\boldsymbol{Injector\ 1}$ with $\mathbf{3}\ \boldsymbol{mm}$, and lastly $\boldsymbol{Injector\ 3}$, with a maximum droplet size of $\mathbf{6}\ \boldsymbol{mm}$. Which certifies the $\boldsymbol{base\ case}$ as the best choice among the proposed geometrical modifications. In addition, results show an independent correlations between the diverging section length and droplet size. It is believed that is more important how the liquid core is broken up than the diverging section length. However, a sensitivity analysis of these variables and others such as, nozzle exit diameter, nozzle exit length, *venturi zone* length, among others, should be addressed in a further research.

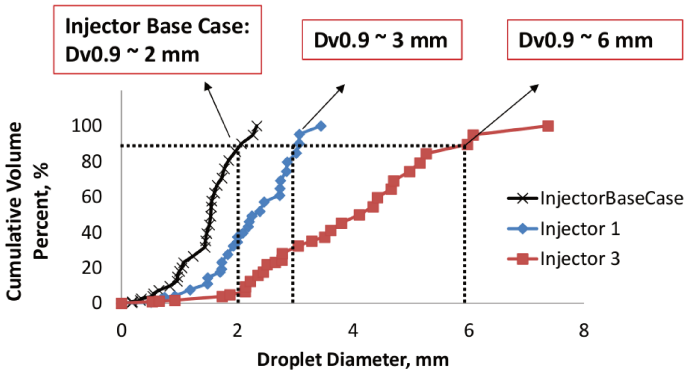

Figure 5.11: SMD cumulative volume percentage for $Injector\ base\ case$, $Injector\ 1$ and $Injector\ 3$.

5.2.6 Premixing zone modeling

The *premixing* zone, refers to the part before the *venturi*, as described in figure 5.3. Much have been said and done with the *venturi* zone. On the contrary, this section is dedicated to this former part, usually disregarded nowadays by the majority of injector designers. In the actual FCC Injector geometry, already described in the previous section 5.2.5, within the *premixing* zone, there is not physical contact between the two phases. Instead, the two phases flow concentrically without any physical transfer mechanism, until they both converge at the entrance of the *venturi* zone. The idea is simple: take advantage of this geometrical available zone, to enhance the turbulent mixing in the *venturi* zone (i.e., the droplet size distribution at the nozzle exit), by *premixing* the phases before the *venturi* zone. Therefore, the available space for mixing would be increased thus, a prior inactive part of the FCC Injector for the atomization process, would then be activated. There are several other researches focusing on the same principle e.g., in gas turbines engines applications [209, 210, 211, 212], in which the mix of liquid-fuel/air is done outside of the combustor of a gas turbine, by means of a so-called *premixing injector*. Outcomes are diverse such as, air pollution emissions, fuel-air non-uniformities efficiency, fuel utilization efficiency, among others. Figure 5.12, clearly shows the parts involved. Highlighted in red, and black, the *premixing*, and *venturi* zone, respectively:

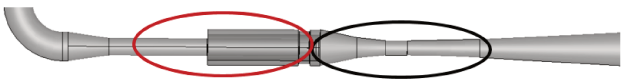

Figure 5.12: Highlight of geometrical parts to be modified.

As summing-up from the previous section 5.2.5, it was found that the FCC Injector heavily depends on the turbulence mixing generated by the shear stress, to actually mix/disperse the phases. Thus, the higher the turbulence level, the better for the resulting phase mixing. The modifications proposal in this section 5.2.6, are based on this statement. Likewise, simulations were done using the previous validated $ELSA$ model, explained in chapter 3 (equation 3.11). Boundary conditions, and fluid properties are taken from the $Injector\ base\ case$ described in table 5.1, and will be the same for all the numerical cases. Furthermore, two propositions are suggested and shown in the below figure 5.13. **Case zero**, is the actual $base\ case$. **Case one** (1), which is positioned within the *premixing* zone before the *venturi*, includes a secondary amount of mass (less than $50\ \%$) for both phases to be deviated from its stream line, and later on mixed together. Doing so, four symmetrical pipes, with 45 degrees angle between each other, connecting the two flow passages have been constructed. **Case two** (2), a lowered flow area available for both phases is proposed, in order to increase the velocity and hence downstream enhance the turbulence mixing, before entering the *venturi* zone. A diameter

reduction for both oil and steam pipes, were made from the outer part. The read line describes the reductions made on both pipes for the 2^{nd} case. These modifications are clearly a first numerical attempt to improve the *premixing* zone, however, structural and economical analysis are strongly recommended to ensure the feasibility of such proposals.

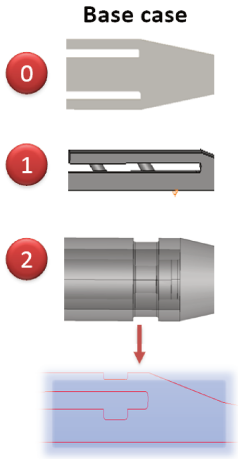

Figure 5.13: Proposal modifications within the *premixing* zone.

The numerical $\boldsymbol{ELSA}$ model previously validated, see equation 3.11, was used to compare the different approaches. Figure 5.14 exposes on the left, the oil volume fraction with no appreciable meaningful differences, specially on the right side of an orange line (placed to separate the injector before and after the modifications), for all the three cases. On the other hand on the right of the figure, velocity contours are displayed, in which differences are noticeable. For instance, for **Case one** (middle figure on the right), some liquid makes its way to the steam side trough the connecting pipes, increasing the velocity of the gas by compressing it to the walls. This expected fluid flow behavior, is mainly due to pipe structural shape and density differences. Nevertheless, after the orange line no significance evidence can be found with respect to **Case one** ($base\ case$). For the **Case two** (last row from top to bottom, on the right of figure), based on the contraction made, the liquid is accelerated as well as the steam, before entering the *venturi* zone, thus a major turbulence mixing potential can be expected after the orange line in the *venturi* zone.

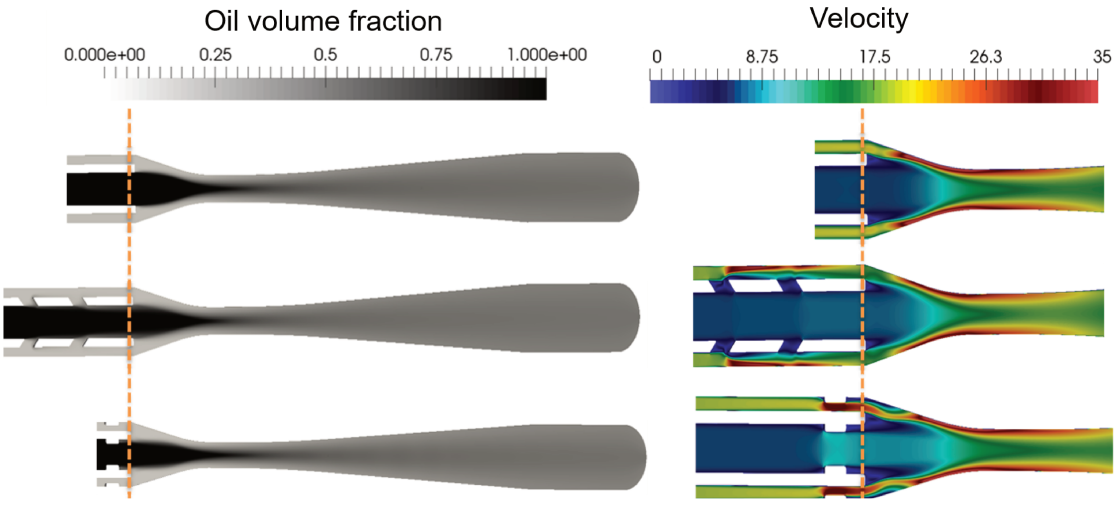

Figure 5.14: Liquid volume fraction color-map (left). Velocity magnitude color-map [m/s](right).

Quantitative results such as droplet diameter, expressed in this case by means of the Sauter Mean Diameter (SMD), and surface interface density Σ, are equally important, specially within the FCC Riser, in which the more surface interface density is, the faster vaporization rate crops up. Figure 5.15 on the top, reveals the variable surface interface density Σ, which represents the amount of surface interface between the phases. And on the bottom the Sauter Mean Diameter (SMD), which is the droplet diameter. For more details, see chapter 3. As the legend shows on the right of both pictures, the green line is for the original $base\ case$ (**case zero**), the blue line for the interconnecting pipes case (**Case one**), and the red line for the restricting flow area case (**Case two**).

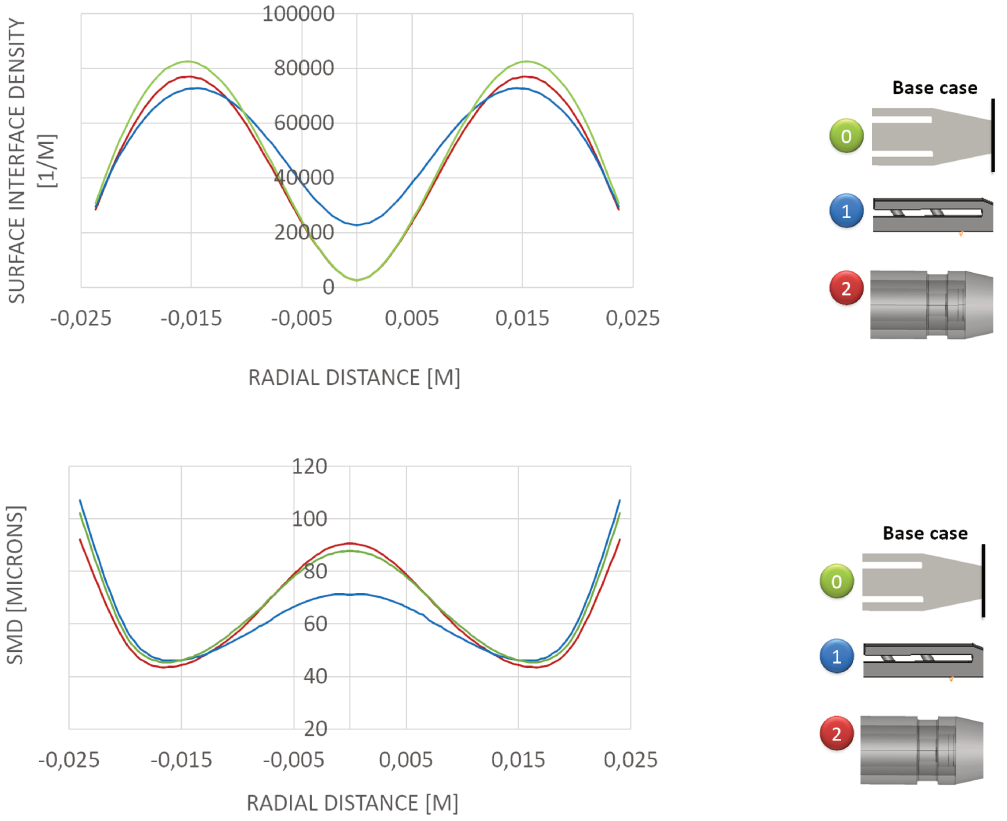

Figure 5.15: Surface interface density Σ $[1/m]$ (top). Sauter Mean Diameter SMD $[\mu m]$ (bottom).

On top of figure 5.15, the surface interface for the contracting flow area case (**Case two**), does not differ much from the original $base\ case$ (**case zero**), however, the connecting pipes case (**case one**), gets the most uniform surface profile of all three cases at the venturi entrance, which is the vertical black line drawn in the legend. The connecting pipes case (**case one**), even manages to get better mixing quality based on the droplet diameter, figure 5.15 on the bottom. Looking at the blue line, droplet diameter is the lowest, if an averaged value is taken, and along with the highest surface interface density, the connecting pipes case (**case one**), exhibits the best performance, making it suitable candidate to improve vaporization rate within the riser. These results however, are the first modifications proposed from the numerical point of view, without any structural nor economical analysis. It is then verified, that the oil-steam premixing zone would be advantageous, specially as highlighted in (**case one**), by premixing both fluids before the *venturi* zone.

5.3 Water sprayer numerical test case

As a memo, the main goal of this thesis is to come up with an accurate two-phase flow liquid atomization model, able to be industrially applied in a computational affordable way. Two test cases have been proposed to be exploited for comparison and validation purpose, namely *ECN Spray-A*, *air-blast atomizer* and *Bosch Injector*. The objective of this chapter is then to directly apply the validated $\boldsymbol{HELSA}$ atomization model, to two industrial liquid injectors, namely *FCC Injector* and *Spray water injector*. The particularity regarding these liquid injectors, is the absence of experimental measurements. This part of chapter, will be dedicated to the *Spray water injector*.

From the $\boldsymbol{VINCI\ Technologies}$ company, it has been expected to study a spray cooling system, and in particular to develop a numerical strategy that could help to the design of those injectors. This injection system belonging to the water spray system, is detailed and some previous design development is conducted. Latter, the design guidelines of such apparatus is studied from the literature review. Eventually numerical study related to this application are sharply review. It appears that the injector design belongs to steam/water system with a premixing inside the injector. Such configuration can only be studied numerically by Direct Numerical Simulation (DNS) or by the multi-scale $\boldsymbol{ICM-ESA}$ approach. Accordingly, the last part of this chapter is dedicated to an application of the previously developed approach (chapter 3, and 4), to study the injector design in the context of this new $\boldsymbol{VINCI}$ application.

5.3.1 Water spray applications

The applications where spray nozzles are utilized can be severe. For instance, primarily spray nozzles are used for exposure protection of bulk storage flammable and combustible liquid tanks to cool the shell, prevent explosion or collapse of the tank and extension of the fire. In addition, when designed properly and correctly installed, water spray systems can be successfully utilized for extinguishment and control of some flammable liquids fires, some combustible liquid fires, Class $\boldsymbol{A}$ combustibles, and electrical transformer applications. Extinguishment of a fire using water spray, is achieved by cooling, smothering, emulsifying or diluting of flammable liquids or by a combination of these factors [213]. Controlling of a fire can be achieved with the same mechanisms that achieve extinguishment, however, due to different characteristics of the fuel, suppression may not be possible [214]. Historically, the term velocity and distribution of the size of water droplets, has been understood to describe the reach or area of coverage of the water spray nozzle pattern [215]. However, it is the velocity and dispersion of the water droplets themselves, which will determine a spray nozzle performance [216].

Another application of spray water system is the *spray cooling*, in which employs a spray of small droplets impinging on a heated surface to increase the effectiveness of heat transfer, as a cooling mechanism with phase change [217]. Spray cooling is widely used in various fields: cooling of hot gases, dermatological operation and cooling of hot surfaces including hot strip mill and high performance electronic devices. For example, in the metal production and processing industry, spray cooling also plays an important role for the high temperature (up to $1800\ \boldsymbol{K}$) steel strip casting and the final micro-structure optimization after hot rolling. Typically, a jet of gas carrying water drops is sprayed towards the hot surface to be cooled [218]. In the electronic packaging industry, spray cooling has drawn great attention due to its high heat flux removal ability ($1200\ \boldsymbol{W/cm^2}$), while maintaining device temperature below $100\ \boldsymbol{C}$, with spatial and temporal variations below $10\ \boldsymbol{C}$ [219, 220]. Finally, spray cooling, is an appropriate technique for high power and high heat flux applications. By taking advantage of the liquid relatively high latent heat, liquid impingement spray cooling, has demonstrated to be an effective way of removing high heat power from surfaces, requiring only a small surface superheat as well as low mass flow rate, which are essential requirements for a compact cooling system designs [218].

The spray cooling, is the application from which the spray water injector, is to be designed in this second part of the chapter. In another example of spray cooling, a power plant cooling tower exhausts heat to the ambient. Improvements of cooling tower performance lead to increases of a power plant thermal efficiency. To enhance the performance of a natural draft dry cooling tower, hybrid cooling methods are suggested [221, 222]. The two most common methods include water deluge and evaporative cooling; the latter is more efficient due to a higher heat and mass transfer contact area. Moreover, hybrid cooling uses less water compared to water deluge. In evaporative cooling, water spray cools down the inlet air, which leads to drop of minimum temperature of the thermodynamic cycle and consequently increase of a power plant thermal (power conversion) efficiency. Conclusively, the evaporating cooling is the specific application of the spray water injector in this chapter, which will be detailed later.

Spray nozzles, are used to help distribute water into the inlet airflow in order to provide a large contact surface area between air-water, and to enhance mixing by producing very fine droplets. This offers higher evaporation rate and greater air cooling. An effective water spray design, needs to avoid local cooling distribution and incomplete evaporation of droplets while providing high cooling efficiency [223]. Generally, there are two kinds of sprays implemented for spray cooling: pressurized spray and gas-assisted spray. Pressurized sprays, are widely utilized in spray cooling researches and applications, which are generated by high pressure drop across the nozzle or with the aid of a swirl structure inside in some cases. Gas-assisted spray, is rarely used in spray cooling due to its complex system structure for introducing the secondary gas into the nozzle to provide fine liquid droplets [218]. However, it is found that gas-assisted spray can provide faster liquid droplet speed, smaller droplet size and more even droplet distribution on the heated surface compared with pressurized spray at similar working conditions [219, 224]. The latter, Gas-assisted spray, is the one developed in this chapter.

There are three basic spray patterns used for two-fluid atomizers: *full cone*, *hollow cone* and *flat fan* (Fig. 5.23). Each of these has specific characteristics and applications. The *full cone* nozzle, can produce large, evenly distributed drops and high flow rates, and it maintains its spray pattern over a range of pressures and flow rates. It is a low-drift nozzle. The *hollow cone* nozzle, shows a spray pattern with more of the liquid concentrated at the outer edge of the pattern, and less in the center. This type of *hollow cone* nozzle, will not provide uniform droplet distribution when directed straight down at the sprayed surface [225]. However, since *hollow cone* nozzles excel themselves by easily atomization of fine drops which move enough to compensate for the non-uniformity of the pattern, they are often used for atomization of fuels, spray-drying and in scrubbing towers for dust and gas [226]. The *flat fan* nozzle is effective in a line of spray. The impact of this spray is high when compared to *full* or *hollow cone* spray patterns. The droplet sizes produced by this type of nozzle are larger than *cone* nozzles, although very fine droplets can be produced by some air atomizing flat fan nozzles [227]. The *full cone* nozzle, is the one studied in this chapter.

Figure 5.16: Basic spray patterns. *Flat fan* (left), *full cone* (middle), and *hollow cone* nozzle (right) [22].

5.3.2 Water sprayer design guidelines

The selection of a specific atomizer, is made based on the feedstock, the required powder (droplets) properties, the dryer type and capacity and the atomizer capacity. Normally there are three types of spray water atomizers i.e., *rotary*, *pressure*, and *two-fluid* atomizers. *Rotary atomizers*, use the energy of a high speed rotating wheel, to divide bulk liquid into droplets. Feedstock is introduced at the center of the wheel, in which it flows over the surface to the periphery and disintegrates into droplets when it leaves the wheel. One advantage is that droplet size can be easily changed by modifying the wheel speed. *Pressure atomizers*, are the most commonly used atomizers. Nozzles generally produce coarser, freer flowing powders than rotary atomizers. Generally, this type of injector also uses a kind of swirl water motion in the breakup process. Some nozzle designs, use slotted vanes to generate the vortex. The disadvantages of slotted designs, are that they are prone to clogging and premature wear. The rotating fluid then allows the nozzle to convert the potential energy of liquid under pressure, into kinetic energy at the orifice by forming a thin, high-speed film at the exit of the nozzle. As the unstable film leaves the nozzle, it disintegrates, forming the first ligaments and then eventually droplets. Pressure nozzles can be used over a large range of flow rates, and can be combined in multiple-nozzle installations to give them a great amount of flow rate and particle size flexibility. *Two-fluid atomizers* or *twin-fluid atomizers*, are the type of injector that combine compressed air (or steam) with liquid feedstock. The design utilizes the energy of compressed air (or steam) to atomize the liquid. Two-fluid nozzles are able to atomize highly viscous feeds, but they are expensive to operate because of the high cost of compressed air. Two advantages of the two-fluid nozzle are its ability to produce very fine droplets and to atomize high viscosity fluids [22]. The spray water injector is based on this type of injector. Some design guidelines of the two-fluid atomizer, are presented below:

- Confirm that the correct nozzle flow rate, spray pattern, and operating pressures have bee selected and supplied for the application, that the correct mounting and accessory hardware such as thick wall adapters and clean out needles are installed on the nozzle and that the correct number of nozzles is available.

- Be sure to account for the air pressure according to the instructions on the chart when sizing the air piping.

- The header (for a multiple nozzle installation) and supply lines, should be sized generously to prevent imbalance between liquid and air pressures for each nozzle and excessive pressure loses along the header that could cause erratic nozzle operation.

- Correct size of the supply piping, to ensure that adequate air and water are supplied to the nozzle This is specially important in multi-nozzle system, in which differences in air and water pressures from one nozzle to the next, can cause erratic operation [22].

There are two type of twin-fluid atomizers namely, internal and external mixing type. Internally mixed atomizers, are the one in which liquid and air streams meet within the nozzle and are mixed together and expelled through the same orifice(s). This internal mixing means the streams are not independent; a change in air flow will affect the liquid flow. This makes precise metering of the liquid more difficult than with an externally mixed atomizers set-up. Externally mixed atomizers, the air and liquid streams exit the nozzle independently and are combined and mixed outside of the nozzle. Because there is no connection between the air and liquid lines within the nozzle, the air and liquid flow rates can be controlled independently, allowing precise metering of the liquid. The atomization can be controlled by adjusting the air flow rate e.g., more air produces finer atomization.

5.3.3 Water sprayer modeling

Research on spray cooling performance, was mainly carried out by single point injection, on the basis of experimentally measured spray characteristics at the breakup length or hypothetically assumed. However, this approach prevents representing real nozzle behavior [223]. Experimental studies inside a twin-fluid atomizer has already been made. Heavy fuels droplet $\boldsymbol{SMD}$ variations, were related to certain geometrical configurations of the nozzle, under sonic (choked) conditions [228]. In a subsequent study, venturi-vortex twin-fluid swirl nozzle, atomizing pure glycerin at room temperature was examined [229]. In this nozzle, air was tangentially injected in a central convergent section, and discharged suctioning the liquid fed to a coaxial chamber. Droplet size distributions were measured with a Spraytec laser diffractometer [230]. The Sauter mean diameter ($\boldsymbol{SMD}$), was used to characterize the atomizer performance. The observed spray, had a *hollow cone* structure, with the biggest droplets in the outer boundary. Additionally, Mean droplet diameter were found to increase with liquid flow rate, and strongly decreases when increasing the gas flow rate [229].

In recent years, Computational Fluid Dynamics (CFD) models are increasingly used to investigate the growth and suppression of fires, including the dynamics of sprays. Among the available CFD based tools, Fire Dynamic Simulator (FDS), developed by National Institute of Standards and Technology (NIST), in USA, is a widely used open-source software, for simulating the spread and suppression of fires in buildings [231, 232, 233, 234, 235, 236]. Moreover, a CFD model was developed to simulate a single cone spray using saline water [237], in a vertical cooling tower representative arrangement. By comparing the results obtained for 3% $\boldsymbol{NaCl}$ concentration (by mass) with pure water, they showed that using saline water shortens the length from the nozzle, covered by the wet stream. In a subsequent study, the previous CFD model was verified against experimental results obtained from a Phase Doppler Interferometry (PDI) study. They showed that in a spray, large droplets push the smaller ones to the middle of the flow [238, 239]. Following this work, the performance of different nozzle arrangements within a cooling tower was tested by using the $\boldsymbol{SIMPLE}$ algorithm [206] with staggered grids for velocity and pressure couplings, and the Discrete Phase Model (DPM) [240], in ANSYS FLUENT [182] to simulate multicomponent droplets in spray. Optimization of spray nozzles design for evaporative cooling applications, using a validated Eulerian-Lagrangian water spray CFD model, has also been made [223]. To the best of our knowledge, no study attempted to relate nozzle design optimization, to spray cooling performance, by investigating the impact of physical spray characteristics, in a numerical point of view. In this second part of the chapter, a nozzle design will be carried out, followed by Euler simulation ($\boldsymbol{ELSA}$ model) inside the nozzle, in order to obtain later on full spray characteristics outside of the water spray nozzle.

5.3.4 Geometrical model and flow conditions

The considered spray nozzle geometrical configuration is designed based on its application. Therefore, is the result of a thermodynamical analysis performed on the sprayed water, in order to correctly satisfy certain heat removal requirement. More specifically, the cooling down process of a by-passed flue gas coming from a power plant regenerator. Water sprayers are located on top half section of the flue gas line on a radial pattern, as displayed in the figure 5.17, in which is also shown a typical mechanical arrangement of a water sprayer.

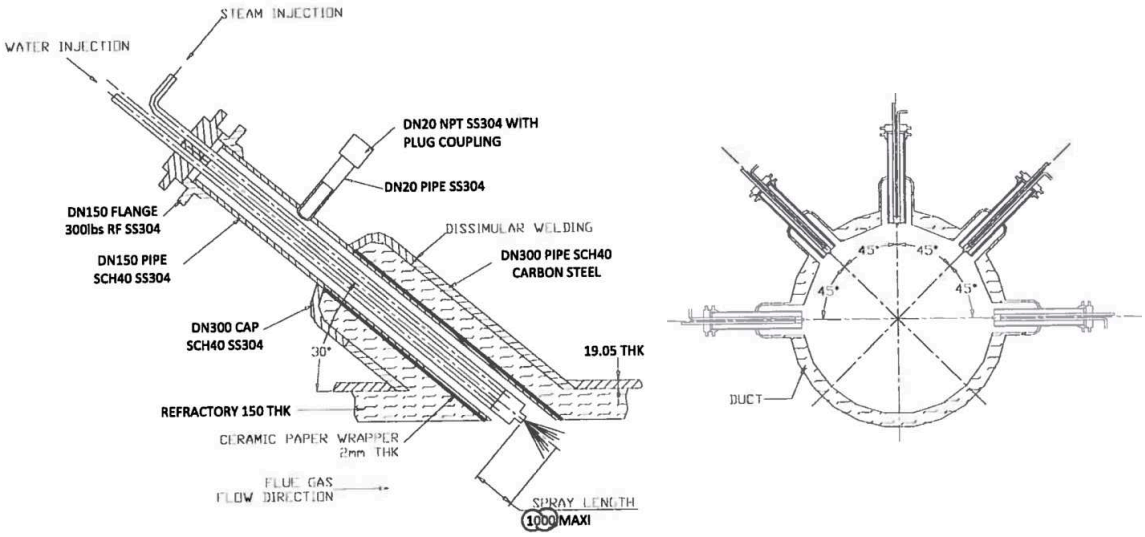

Figure 5.17: Typical mechanical arrangement of water sprayers.

Fluid and flow properties were fixed based on the flue gas line operating conditions. These operating conditions are usually encountered in power plants. Table 5.2 lists the main flow conditions per water sprayer. It is to be noted, that both water and steam volumetric flow rates ($\dot{Q}_{inlet}$), are adapted to already manufacturable water sprayer flow conditions at $P = 7\ Bar$, for instance by BETE®[22].

Table 5.2: Water sprayer fluid and flow Properties.

	Water	**Steam**
$\dot{Q}_{inlet}$	75 l/min	141 Nm^3/h
ρ	947 kg/m^3	3.077 kg/m^3
ν	2.5e-07 m^2/s	5.4e-06 m^2/s
T	115 C	225 C
P	7 Bar	7 Bar
Re	≈ 556000	≈ 77000
We_g	–	≈ 133

The resulting water sprayer that fits the gas heat requirement removal, would be a *high flow air-atomizing*, with a spiral spray set-up. For instance, the commercial (manufacturable available) name for this type of water sprayer is the `SpiralAir` nozzle, from BETE®company. The outside structural shape of water sprayer is shown on the left of figure 5.18, along with some available spray pattern on the right. In this case, the *wide round* 90^o spray pattern, is the one chosen for the heat removal application.

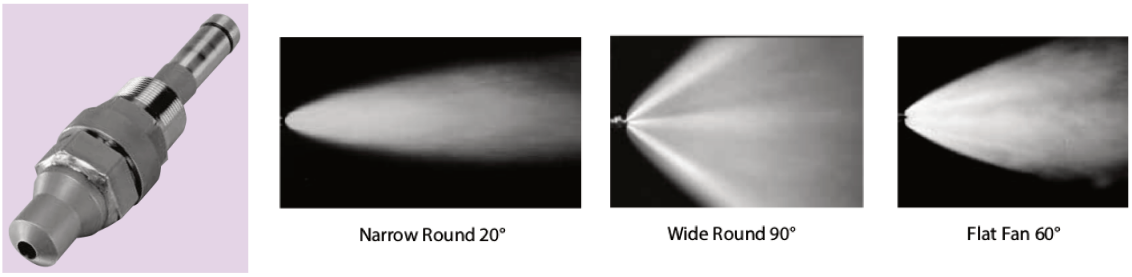

Figure 5.18: Exterior twin-fluid atomizer geometry, by BETE®Company (first on the left) [22]. Different Spray patterns, manufacturable available for the above nozzle (last three from right to left).

The `SpiralAir` nozzle, has a helical element to produce the swirl motion of the steam-water flow, as exposed in the figure 5.19. On top of figure, there is a transversal internal view of the water sprayer, in which the steam flows through the hollow passages forming an annulus gas flow, and the water for the central conduit. Highlighted in red, is the helical element, which is zoomed up at bottom of the figure. This particular design, was made by BETE®, following the US patent design guidelines # $US5240183A$, titled as: Atomizing spray nozzle for mixing a liquid with a gas [23].

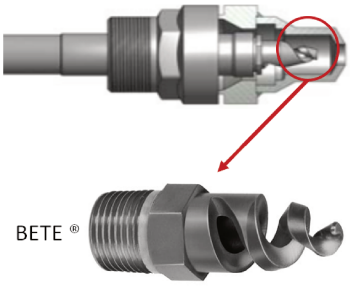

Figure 5.19: Dimensioned twin-fluid atomizer geometry (top). Patented design by Robert E. Bedaw [23] (middle). Spiral design by BETE®[22] (bottom).

The US patent # $US5240183A$ (see [23] for more details), ensures a nozzle which is capable of producing an atomized spray, in which the average droplet size will be within the $10\mu - 500\mu$ range. The design specifics can be viewed in the figure 5.20. Red arrows represent the annular gas passage, the blue arrow acts for the central liquid passage, and the orange square stands in for the *spray head*. The latter, is a key piece in the atomization process i.e., the *spray head* provides a chamber for the mixing of the gas and liquid, and for the discharge of the resulting mixture through the orifice of the head, to finally form an atomized spray [23]. Moreover, the figure also shows the disclosed distance d, and a, which act for the *spray head* length and diameter, respectively. The mixing chamber includes an *open* inner end, having stepped diameters, a generally cylindrical medial portion and conically tapered or spherically shaped outer end portion, namely the outlet orifice (figure 5.20, on the right side of the orange square). The *spray head*, includes two cylindrical tubular portions at the inner ends, of which form shoulders, which disrupt the incoming gas flow as it enters the chamber from the gas passages. Whereby, the high velocity gas, becomes turbulent for enhanced mixing for the atomization of the liquid phase (figure 5.20, on the left side of the orange square).

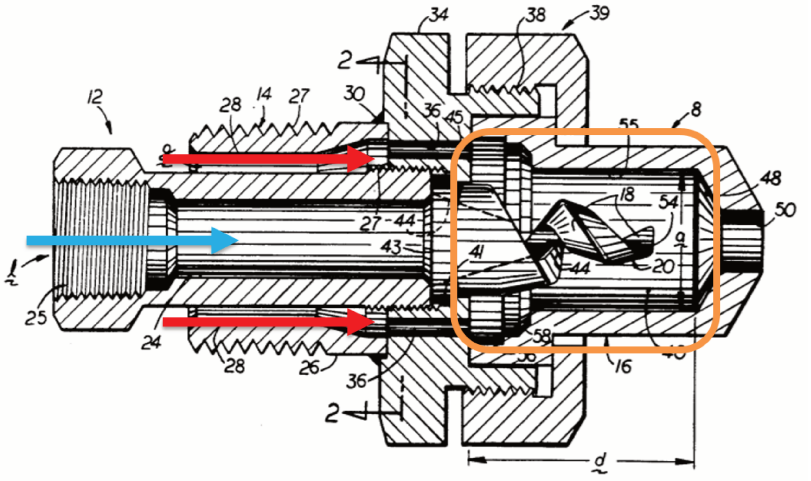

Figure 5.20: Original patent of an atomizing spray nozzle for mixing a liquid with a gas [23].

Some design guidelines are described [23], before constructing the final geometrical model displayed in figure 5.21.

- The inner diameter a, of the cylindrical portion of the *spray head*, be substantially greater than the maximum outer diameter of the helical elements.
- The helical member terminates at a distance from the orifice approximately equal to the radius of the cylindrical portion of the *spray head* $(d/2)$.
- It has also been found that the ratio of the length of the *spray head* d, as shown in fig. 5.20, to inner diameter a, of the *spray head* (i.e., d/a), should be approximately 1.5 to 1.7.
- Further, the ratio of the diameter of the outer tip of the spray head, to the diameter a, of the mixing chamber, should be approximately 0.4. Thus, the cross-sectional area of the spray outlet orifice, is approximately $\approx 20\%$ of the cross-sectional area of the mixing chamber.
- The helical member, includes at least one helical turns, up to as many as two and one-half turns from its inner to its outer end, and the pitch of the helix is about 3 turns per inch.

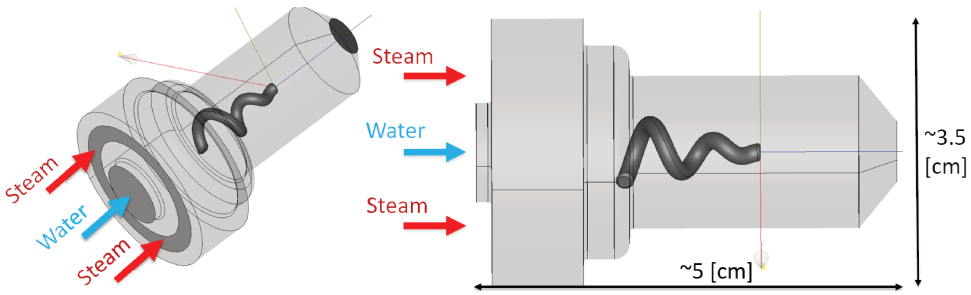

Figure 5.21: Geometrical model of the twin-fluid atomizer..

It is to be noted on the figure 5.21, that the helical elements are not exactly the same as proposed before in figure 5.19 (at the bottom), by BETE®. For legal reasons, this slight modification, was made to produce a geometrical model quite different from the one used in the US patent # $US5240183A$.

5.3.5 Numerical domain and boundary conditions

The computational discretized domain is defined in figure 5.22, in which the liquid inlet is highlighted on the left, and the proposed helical element on the right. Unlike the patented spiral element, the proposed spiral element is a simplified cylindrically extruded shape (i.e., without sharp edges). The turbulent nature of the flow was previously verified with listed flow conditions in table 5.2 (i.e., $Re_l \approx 556000$, and $Re_g \approx 77000$) hence, in this industrial numerical test case, a time-averaged Navier-Stokes equations (RANS) are used e.g., with $k-\epsilon$ as the turbulence model. Using this much simpler and economic turbulence model (compared with LES, computational speaking), some geometrical modifications could then be more easily proposed and constructed. Finally, the cell size is about $12\ mm$, based on the $Yplus > 30$ requirements, according to the wall functions available in OpenFOAM® .

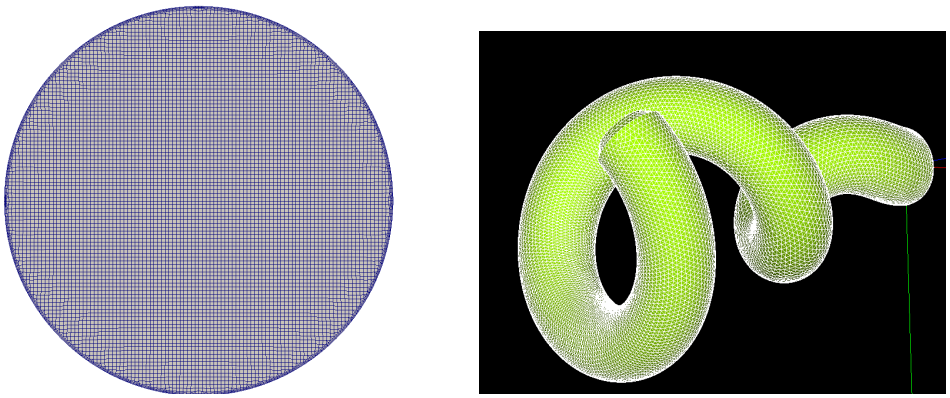

Figure 5.22: Liquid inlet patch faces (left). Discretized view of helical element within the spray head (right).

Velocity is imposed with *Dirichlet* boundary conditions at steam and water inlets. It is set to zero value along the walls (no-slip condition) and an *outflow* boundary condition at the outlet orifice of the spray head, which is a *Neumann* type zero-gradient. Total pressure is specified on *outflow* boundary with a value of 0, with respect to the reference pressure. Other boundary patched (such as walls and inlets) are *Neumann* conditions with zero-gradient specified for the pressure. Volume fraction value is fixed to 1, in water inlet and to 0, in steam inlet. Zero-gradient is applied along the walls (i.e., spray head, and spiral element) and an *outflow* boundary condition is applied at the outlet orifice. Regarding the usual specified turbulent conditions at the inlets, it is not mandatory anymore to use coherent turbulent structure (as the one normally use in LES) instead, a more or less educated guess of the incoming turbulence is sufficient for $RANS$ cases. To that end, a turbulent length scale and intensity of $7\ \%$, and $5\ \%$, respectively, were employed for both water and steam, considering fully developed pipe flow way before inlets.

5.3.6 Results and discussion

First results are shown in figure 5.23. Inlet boundary conditions are colored in blue and orange arrows, for water and steam, respectively. A transverse colored plane (brown and blue-green) has been placed to illustrate the water volume fraction. The phase interface (dark red) is clearly defined from both steam and water inlets up to the orifice exit, at the far right side of the spray head. Moreover, no disturbance is observable in the water side (liquid core). They are mainly two reasons: (1) inherently by RANS turbulence model, which does not account for fluctuating variables field, only mean values are plotted. (2) Even though, the helical element are meant to promote the necessary turbulent mixing between the phases, there is not such tangible behavior. Therefore, a geometrical modification was proposed to the water

inlet i.e., a convergent-shaped inlet, in which the water gets accelerated hence, contributing to turbulent mixing. This modification can be appreciated in the figure 5.24 on the right.

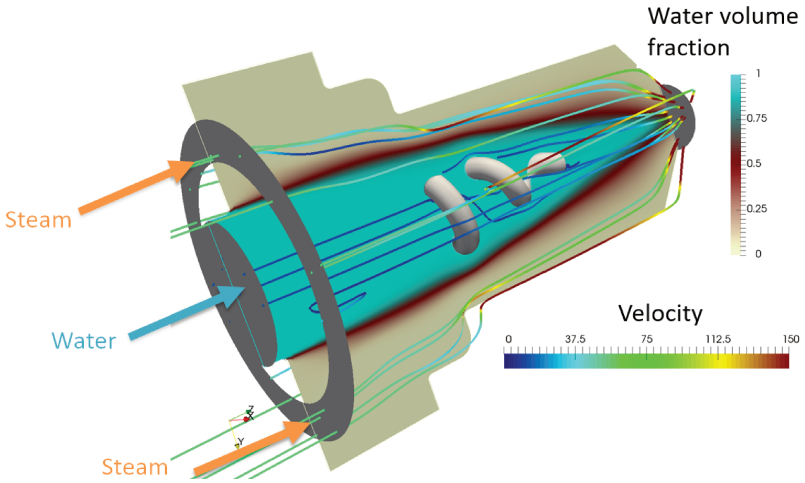

Figure 5.23: Velocity stream lines along with water volume fraction colored map.

In this case, to numerically evaluate the proposed modification, certain body part was extracted from the water sprayer i.e., a cylindrically convergent-shaped, in which only the exit, is used as the new water inlet. More specifically, a small piece of this convergent-shaped, was left with the same convergent angle, to ensure in some way the change in velocity vectors. Additionally, the ancient water mass flow rate was kept the same on both cases. It can be seen in figure 5.24 on the right, that with the proposed water flow inlet condition, both water and steam begin to mix after the helical element, even though there in not evidence of any supplementary turbulence generated near the water inlet. It is to be noted, that the phase interface (colored in the figure for both cases in dark red), is thinner with the new water inlet condition, however, the interface thickness depends heavily on the mesh resolution, as previously verified in preceding chapters. The mesh resolution far from the spiral element are twice as big as the cell size near the spiral elements.

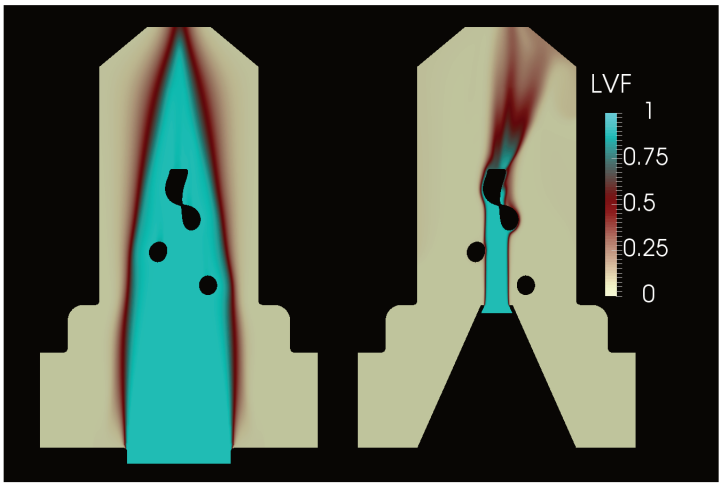

Figure 5.24: Volume fraction colored map comparison. Original case (left). Proposed water inlet modification (right).

Figure 5.25 reveals the velocity vectors on both cases namely, original case (on the left), and the proposed case with the modified water inlet (on the right). Firstly, looking the main

direction and magnitude of steam, specially at the inlet (bottom outer part on both pictures), there is an increased in the steam velocity (highest values colored mainly in dark red) as it gets close to the water inlet. This behavior is mainly due to the reduced steam flow area passage. The two geometrical shoulders, recommended by the US patent, initially to redirect the steam, are here verified on both configurations. Nevertheless, after the steam has passed the geometrical shoulders, another steam condition is recognized compared with the original case. On the case on right (with the reduced steam are flow passage) there is an increased water core velocity in the middle of the spray head (colored in blue-green), in which the steam velocity tends to approach closer to the water core velocity. In the case on the left, the water core was somehow compressing the steam passage, as noticed by its high velocities close to walls (colored in dark red). On the contrary on the right, the water middle core is less thick with higher velocity, hence the velocity distribution near the zone of the spiral head, is more appropriate, in the way to generate the necessary turbulent mixing inside the water sprayer.

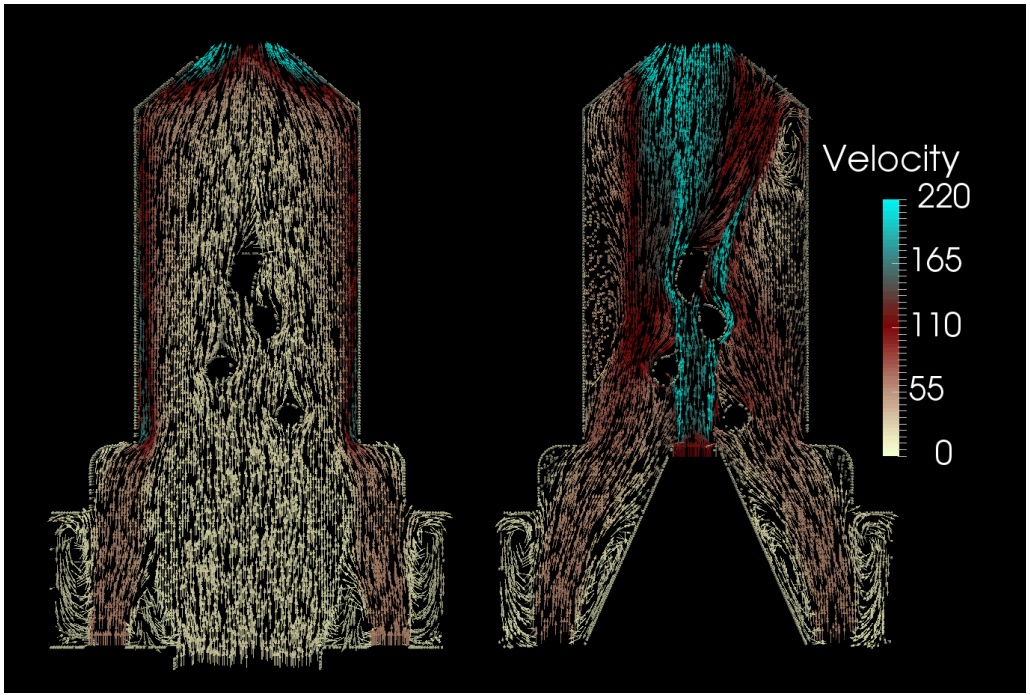

Figure 5.25: Velocity vectors colored velocity. Original case (left). Proposed water inlet modification (right).

5.4 Summary and Conclusions

After the validation procedure of the $\boldsymbol{HELSA}$ approach. The maturity has been tested in such industrial applications, in order to help in the designing of these injectors. Tow cases are studied. The most advanced, numerically speaking, is the originally proposed by $\boldsymbol{VINCI}$, namely the FCC Injector. The actual FCC Injector has been modeled using $\boldsymbol{LES-ESA}$ algorithm implemented in OpenFOAM® . $\boldsymbol{LES-ESA}$ algorithm was validated against experimental available data and DNS analysis. It has been demonstrated the wall-bounded turbulent effects on the two-phase flow within a FCC Injector. Moreover, there is a liquid core flow and annulus gas flow compressed by the latter inside the injector. This concentric behavior pushes the gas to the wall, thus increasing its stream-wise velocity near the wall. A mixing mechanism has been identified within the venturi section of the FCC Injector, *the throat*, which is the part of the venturi with he smallest diameter and where the highest velocities occur, thus promoting turbulent mixing. A series of modifications were made to *the throat*, its

axial position and diameter were changed to evaluate its effects on the Sauter Mean Diameter. On one hand qualitatively results confirmed the balanced performance of the Injector Base Case between the converging and diverging zone. On the other hand, quantitative results revealed the best performance for injector base case, with the smallest SMD taken from a sample of 90% of the total oil volume at its exit. Additionally, the diverging section length was discarded as a mixing mechanism, and the throat diameter heavily regulates droplet size distribution at the exit of the FCC Injector. It is believed that is more important how the liquid core is broken up than the converging section length. However, a sensitivity analysis of these variables and others such as exit diameter, exit length, venturi length, among others, should be equally addressed in a further research.

Two modifications have been made before the throat to create like a premixing section: (1) by taking advantages of individual fluids trajectory before throat to come the two fluids in direct contact, and (2) reducing the flow area just before the throat to increase the velocity, thus the momentum, to enhance the turbulent mixing at the throat. Mixing the fluids before the throat turned out to be much more successful than increasing the momentum. More uniform surface interface (Σ) was obtained and even the droplet diameter (SMD) was reduced compared with the original FCC Injector case. Further research in this area is suggested. Nevertheless, the best modifications might be accomplished based on the liquid jet behavior within the FCC Riser. A first attempted has been made by simulating the Riser gas-solid particle flow, and high solid concentration might have a strong effect on the atomization process. Simulations coupling liquid jet coming from the FCC Injector to gas-solid flow within the Riser are scheduled and underway for next year of the project.

With regard to the water sprayer injector, an spray cooling numerical review and three basis spray pattern were identified, in order to fit the heat balance requirements. The full cone spray pattern was chosen, based on company requirements. Both injectors, namely the FCC Injector and Water sprayer, can be classified as a two-fluid atomizer, in which design guidelines were presented. The validated $\boldsymbol{HELSA}$ model was successfully applied to the simulation of the water sprayer. The idea was to help in the nozzle design for future geometrical optimization. The `SpiralAir` nozzle was selected for the application heat balance requirements. A simplified $3\boldsymbol{D}$ numerical model was made based on two geometrical configurations regarding the internal two-phase flow mixing. Turbulent mixing was found to be a paramount factor in the internal mixing of the water sprayer. Additionally, this internal mixing was found to be sensitive enough to the geometrical liquid and gas inlets, which indicate a prospective focus on optimization in this part of the water spray injector.

Chap. 6 | Conclusions and perspectives

6.1 Conclusions

The focus of this PhD thesis is to develop a numerical strategy that could help in the design process of liquid jet injectors, specially industry-oriented. The aim is to come up with a numerical liquid-gas atomization model applicable to industrial scenarios i.e., high Reynolds number, in which DNS is strictly unaffordable, computational speaking. Accordingly, $\boldsymbol{VINCI\ Technologies}$ and the research institute $\boldsymbol{CORIA}$ (Complexe de Recherche Interprofessionnel en Aerothermochimie) began a 3-years PhD project, to assist the design of new generation FCC (Fluid Catalytic Cracking) nozzle and water sprayer for gas cooling applications. To that end, a Hybrid Euler-Lagrange Spray Atomization ($\boldsymbol{HELSA}$) model, has been proposed, assessed, and validated covering the full atomization process spectrum (from dense to dilute flow formalism). It is the purpose of this project, to validate and to improve an existing atomization model, capable of dynamically detect residuals or subgrid scales (i.e., in which energy dissipation is modeled by $\boldsymbol{LES}$), and to switch from primary atomization to dispersed flow.

Two modeling approaches available have been proposed to simulate liquid injection system, in flow regimes characterized by high Reynolds and Weber numbers. The focus is on the description of the dense liquid-gas flows, in which the spray is not yet formed. Even though, the area covered by this kind of turbulent liquid-gas flow is often less than a few diameters away from injector nozzle, it is mandatory to address it, to link the inside injector flow to the final spray. It is recognized, that DNS coupled with accurate ICM approaches, are very valuable and accurate tools to describe this dense flow, as soon as the mesh resolution is sufficient. This requires that the subgrid turbulent liquid flux could be neglected. It is also important to recognize that in many practical applications, such level of mesh refinement is not affordable and physical models, able to represent the subgrid liquid dispersion, are expected. Since the work of Vallet and Borghi [147], the main lines of the so-called $\boldsymbol{ELSA}$ model, have been designed for this purpose. The turbulent liquid-gas flow is the place in which occurs strong density variation. The main hypothesis of the work of Vallet and Borghi, are liquid dispersion, which is kind of turbulence plus spray size motion in the dense part by the interface surface density ($\bar{\Sigma}$).

Following the original formulation of Vallet and Borghi, many works have been conducted using Favre mass weighted averaging and filtering (see figure 6.1). The surface tension force occurs only at the surface, and thus require a Dirac pick function representative of the interface $\delta(\boldsymbol{x}-\boldsymbol{x}_s)$. In addition, the discontinuity of the liquid volume fraction entrains the discontinuity of density and viscosity, thus their derivatives also require generalized functions. To keep the interface sharp, the profile of the discontinuous variables across the interface, in particular the liquid volume fraction, has to remain a step profile. To compute this force, and to apply the jump of any variable, the most accurate ICM-DNS code applies interface reconstruction, along with dedicated high order numerical schemes. There are many successful examples in the literature of these fully resolved approaches, combining $\boldsymbol{ICM}$ method with DNS using mesh resolution high enough to compute all the flow scales, based on the curvature, VOF-PLIC (piecewise-linear interface construction), VOF/level-set coupling for unstructured and non-uniform meshes, octree meshes, among others [129, 130, 86] (Top-left/center in figure 6.1). For instance, the ARCHER code [34], is based on coupled *VOF-Level set* method for interface reconstruction, together with a *ghost-fluid* approach, to represent accurately the discontinuity of variables such as density, pressure and viscosity at the interface. This reconstruction process generally depends on the mesh geometry, hence difficult to reproduce for body-fitted methods based on unstructured mesh, which are generally used to address complex geometries. Notice that several proposals exist, for example in the open source software: OpenFOAM® to improve this point, in particular the isoAdvector approach [131], and the so-called `interFoam` [38].

On the other hand, following the modeling approach in this thesis, LES filtering framework is used. As for instance, diffusive methods are designed to smear the interface over several mesh cells, to recover a continuous behavior of any variable. It is important to emphasize that the drift/slip behavior of the residual (unresolved) liquid flux, is not compatible with the $\boldsymbol{ICM}$ method, since the former assumes the profile to be discontinuous, thus both approaches can not coexist at the same place. For unresolved interface approach, the general two-phase flow spray atomization model, originally develop by Vallet and Borghi [1] is used in this thesis (explained in chapter 2). In this model, the boundary separating pure liquid and pure gas, is considered as a mixing zone. Mass and volume formulation of the conservative variables (LVF $\tilde{\alpha}_l$, and interface surface density $\bar{\Sigma}$), have been already validated against available experimental and DNS data, under LES and RANS formalism, by using to that end, the so-called $\boldsymbol{ESA}$ model [33, 89, 109, 116, 133] (Bottom-right/center in figure 3.2).

The present work completes these frameworks by considering Reynolds volume averaging and filtering approach. This work has shown that the volume formulation can be used and give comparatively as accurate results as the previous mass formulations, with respect to available experimental data, despite the approximations done in both formulations. Indeed, a mathematical formulation have been made, in which a two-phase flow decomposition is used for unclosed density correlation terms (see appendix A). A benefit of the volume formulation, is to keep the liquid volume fraction as a primary variable transported by the model, like in many Interface Capturing Method (ICM) approaches, belonging to the VOF family. Accordingly, a set of models is designed based on ELSA framework, for different levels of refinement. A volume based formulation of ELSA approach, has been implemented using the OpenFOAM® library, leading to the solver namely `elsaFoam`, that can be applied using both RANS and LES turbulence model.

This solver considers a subgrid turbulent liquid flux, that depends on the local flow condition. The important point is the incompatibility with ICM, that preserved a sharp interface representation. Thus, even when the interface is well resolved, the turbulent liquid flux vanishes, but the numerical method, not designed to capture the interface, prevent to recover the accuracy of ICM approaches. To solve this problem, two criteria for interface resolution quality (IRQ)

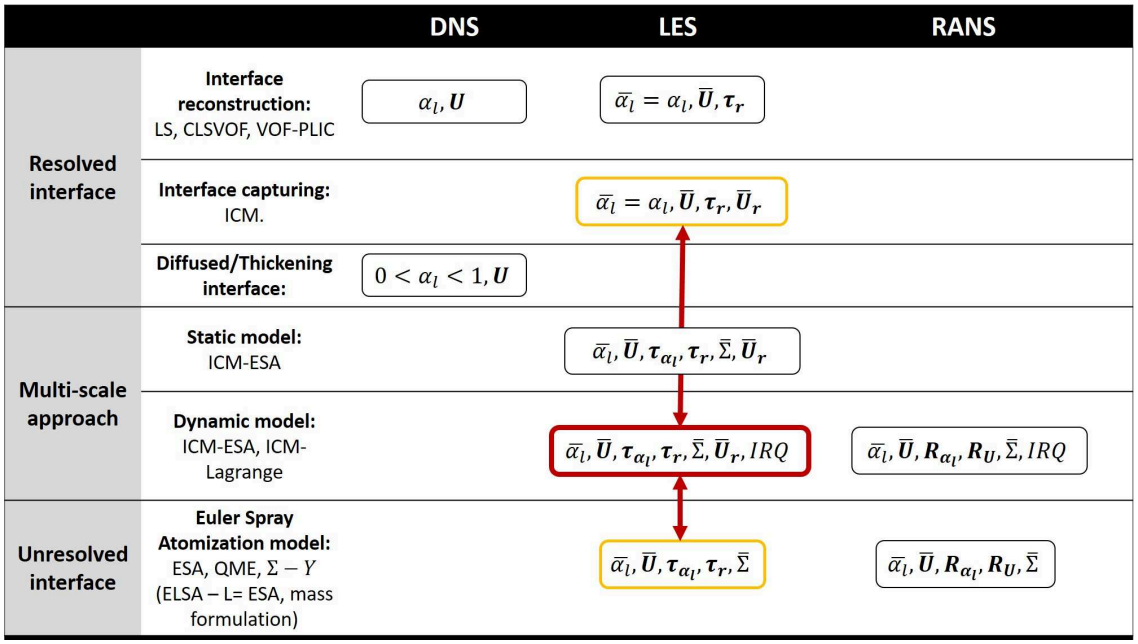

Figure 6.1: Physical-modeling representation of atomization process in turbulent liquid-gas flow. Transition from resolved interface to unresolved interface approach, namely $\boldsymbol{ICM-ESA}$, using LES framework (highlighted in red).

have been proposed, to determine dynamically if the subgrid turbulent liquid flux has to be considered by switching off the ICM, or if the resolution of the interface is good enough to neglect interface subgrid effect and then ICM is applied. The corresponding solver based on the OpenFOAM® library has been called `icmElsaFoam`. Moreover, the original surface density equation [1] has been extended for all developed formulations.

Furthermore, this approach has been compared to experimental data developed by the ECN [5] research initiative, and related numerical simulations published in its workshops. In particular experimental data from X-ray radiography measurements of non-evaporating Spray-A condition, have been used. Like previous works based on mass filtering, a global agreement has been obtained with respect to the available data, namely: liquid volume fraction, projected mass density (PMD) and transverse integrated mass (TIM). In particular, even RANS formulation, that can be very cheap in term on CPU consumption, while using axi-symmetry mesh, is able to reproduce the global behavior of the injection. Nevertheless, to recover the actual dispersion of the liquid, a real improvement can be obtained using LES formulation with both solvers `elsaFoam` and `icmElsaFoam`. Accordingly, a 3D mesh with a high resolution in the injector nozzle is required. It has been found, the turbulence inside the nozzle is mainly controlled by the development of a turbulent boundary layer, starting from the internal nozzle cavity, that develops until the end of the injector pipe. To capture this phenomenon, mesh refinement along the injector nozzle wall, combined with an appropriate LES-WALE turbulence model has been necessary. This turbulent boundary layer, interacts directly with the liquid-gas interface at the exit of the injector, and then it initiates the atomization process. This phenomenon is well captured only with ICM approaches. Nevertheless, further downstream as the atomization process continues, the length scale of interface wrinkling decreases continuously, leading to a numerical error in ICM approaches. By changing mesh resolution, it has been shown that this numerical error is driving the liquid dispersion. This mesh dependency can be released by considering residual or subgrid scale effects, thanks to the solver: `icmElsaFoam`. Thus, it is better to use a physically-based model, using subgrid turbulent liquid flux, than to rely on

numerical errors of ICM (if unresolved), to recover a mesh-independent results.

Finally, the detailed simulation is sensible enough to relate the liquid dispersion to the internal flow inside the injector, mainly due to geometry uncertainties, meshing process, and numerical model approximations, leading to noticeable modification of the liquid distribution, that finally makes errors of few percents with respect to measured data. For the time being, it is not easy to conclude which of these features are the most important, but the positive conclusion is that the present models are sensible enough to detect these small changes.

Thus to go further, a particular numerical test was assessed, namely Air-blast atomizer test case. For this second test case, the above solver `icmElsaFoam` was applied, to predict the primary breakup of a single cylindrical liquid jet. The test case has been chosen for three main reasons: (i) Experimental data are available, about the mean liquid volume fraction in the primary atomization region; (ii) previous numerical studies [116] showed, on the same test case, that RANS turbulence models were unsuitable, which required a strong modification in the turbulence model to get appropriate results, hence prompted the use of LES models. And finally (iii), liquid Reynolds and gas Weber numbers are less, compared with the previous ECN Spray-A test case, hence more flow regions are expected to be resolved. It has been found, in the near nozzle field, the ICM effectively captured the surface instabilities and liquid structure detachments. A fine resolution was necessary in the near flow field. Nevertheless, in the far field, the *ELSA* model was able to treat low volume fractions of the liquid that has been atomized and dispersed. This particular test case showed the importance or resolved interface approaches such as (ICM), when dealing with moderate liquid Reynolds and gas Weber numbers. On the contrary, the ECN Spray-A test case, displayed highly turbulence flow inside the nozzle that atomized rapidly the liquid. Therefore, the unresolved interface approach such $\boldsymbol{ESA}$ was more suitable for this case. More importantly, the proposed multi-scale solver $\boldsymbol{ICM-ESA}$ was able to dynamically adapt to those interface-subgrid based changes on both test cases.

Another flow region that is characterized in liquid-gas flow is the dispersed flow approach, to which extensive literature have been developed. The last part of this thesis is dedicated to the coupling between the developed and validated multi-scale approach ($\boldsymbol{ICM-ESA}$) (see chapter 3), and the dispersed flow approach. The idea is to take advantage of the well-established statistical description of the dispersed spray by Williams-Boltzmann equation (WBE) developments, in regions in which dilute flow can be applied, in order to improve the Eulerian field solved by the multi-scale approach. The present approach ($\boldsymbol{ICM-ESA}$), is meant to model liquid structures in the vicinity of the injector, but also the full atomization process (from primary to dilute spray zone inclusive), by complementing the multi-scale ($\boldsymbol{ICM-ESA}$) field with a well-established disperse flow approach. Therefore, both multi-scale and disperse flow approach, are computed by the same code at the same time.

The resulting novel approach, namely Hybrid Euler-Lagrange Spray Atomization ($\boldsymbol{HELSA}$) model, is based on the paradigm of simulating the full atomization process, beginning with the modeling of liquid structures in the vicinity of the injector (dense flow region), until stochastic droplets are fully formed (dilute flow region), thus the dispersed approach can be modeled by WBE, solved in this thesis by a Lagrangian approach. A transition zone between the two flow regions, was identified and described. The transition criterion is based, for instance, on the level of dilution represented by the liquid volume fraction, that is computed everywhere in the computational domain. This transition criteria determines the transition computational cells, in which disperse flow approach will be applied. Even though the interface boundary is fixed, it is to be recalled that this is not a property of the model, but just a specified condition while using RANS formalism. Once the transition is set, the part of the computational domain that is described by disperse flow approach (which contains also the multi-scale ($\boldsymbol{ICM-ESA}$) unused equations that are always computed on the whole domain) will be used to correct the

Eulerian field in the multi-scale transport equations 3.1, defined in the previous chapter 3. Finally, based on the Eulerian liquid volume fraction field, a threshold was established as $\alpha_l \leq 1\%$, in which small liquid structured can be considered spherical droplets. Regarding droplet velocity and diameter injection. Furthermore, thanks to the findings in chapter 4, in which is demonstrated that the $\boldsymbol{ELSA}$ model without a dispersed approach, is unable to represent the liquid dispersion in the dilute flow regime.

Three cases were set to model the droplet velocity injection at the transition: (1) based on the averaged velocity in the liquid part $\boldsymbol{U}_l$, (2) the same velocity, $\boldsymbol{U}_l$, plus an additional term that accounts for the modulation of a random velocity fluctuation based on the mixture turbulent kinetic energy. Finally (3) includes a new approach , in which non-homogeneous injection property in two-phase flow is presented. With regard to the droplet diameter injection, a Dirac delta function was used for the moment i.e., the averaged Sauter Mean Diameter (SMD) within the transition cell. Stochastic differential equation (SDE), based on Langevin equation, were added to model the fluid velocity along the droplet path. This SDE, was shown to improve, from the physical point of view, the robustness of the turbulent dispersion for the droplet velocity undergoing Brownian motion. The one-way coupling between $\boldsymbol{ICM-ESA}$ and $\boldsymbol{WBE}$ (Lagrange approach) has been presented and tested. Experimental, DNS data were available for comparison purpose.

Firstly, the droplet velocity injection distribution, based on an additional fluctuating velocity term (case $\mathbf{2}$), brought non-existent statistical influence, compared to cases without fluctuating term (case $\mathbf{1}$). Even though the outer radial trend was captured by all droplet velocity injection approaches, only the last approach (based on non-homogeneous turbulent injection properties) was able to capture the rare droplets i.e., droplet with high radial velocity and inertia. This droplet behavior is an indication of the turbulence memory feature, which is somehow lost using RANS averaged equations.

From the theoretical development, in order to fulfill the requirement of $\boldsymbol{VINCI\ Technologies}$. Numerical simulations have been conducted to help to the design of real industrial injector. Several test cases have been set up, however, only $\mathbf{2}$ are described in chapter 5 , because they illustrate the new application suitability issued from $\boldsymbol{ELSA}$ development. The other $\mathbf{2}$ test cases are in the appendix B.1, and B.2. With regard to numerical simulation outside of the FCC Injector, it is a complete different approach to the one developed in this thesis, namely a full multiphase Euler-Euler approach. Additionally, even solid particles trajectory were evaluated. The second test case, namely the water sprayer, this type of injector is more in line to which was made in chapter 3. Indeed, due to the low Reynolds and Weber number, it was solved by using $\mathbf{100}$ % Interface Capturing Approach (ICM). The reason is based on the high viscosity flow inside the injector, which makes low Reynolds and Weber number. With the application of $\boldsymbol{ELSA}$, it has been possible to setup $\boldsymbol{LES}$ simulations that brought new insight, especially with the FCC Injector design concept, and somehow confirm the choice to be applicable to industry. Finally $\boldsymbol{ESLA}$ allows to address the liquid-gas premixing stage inside the injectors, which corresponds to the dense part of the flow. Even if there is not actual measurement to verify the validity of the model in this case. The robustness of the model have been demonstrated through chapters 3 and 4.

6.2 Perspectives

Perspectives of developments and applications for this dynamic methodology are presented.

- From the X-ray measurements previously reported in ECN Spray-A test case, liquid volume fraction (LVF) profiles, and projected mass density (PMD), along with integrated mas density (TIM) profiles were made available for comparison and validation purpose for the aforementioned multi-scale approach, namely $\boldsymbol{ICM-ESA}$. However, very recent experimental data of X-ray diagnostics to the ECN Spray-D standard [241], using cold conditions, enabled also the quantification of distributions of mass, phase interface area, and droplet size in the near-nozzle region from $\mathbf{0.1}$ to $\mathbf{14}$ $\boldsymbol{mm}$ from the nozzle exit. It is also true that the interface surface density $\boldsymbol{\Sigma}$ has not yet been assessed, using the proposed multi-scale model ($\boldsymbol{ICM-ESA}$) in this thesis. Very interesting findings could be drawn for this comparison, especially in the dispersed flow region, in which according to the experimental measurements [241], spray predictions suggests that peaks in the interface area distribution may coincide with regions of finely atomized droplets. Some possible $\boldsymbol{HELSA}$ application could be beneficial to compare as well, in which the coupling approach of dispersed flow with the multi-scale method proposed in this thesis, could be further assessed and improved.

- With regard to the Interface Resolution Quality sensor (IRQ), based on the curvature, it was based on the curvature definition. The issue is based on the fact that the interface capturing method (ICM), does not possess an explicit reconstruction of the interface. Several alternatives can be evaluated. Firstly, a more accurate model to represent the dense flow region in two-phase flow such as the coupling Level set (LS) with Volume of fluid (VOF) approach, namely CLSVOF. In which interface tracking is performed by LS, and mass conservation is ensured by VOF methods. Indeed, adding this feature to the multi-scale $\boldsymbol{ICM-ESA}$ approach could bring a certain improvement regarding the transition from resolved to unresolved interface approach.

- Secondly, a homogeneous isotropic turbulence DNS-based simulation, in which the real interface curvature can be computed (by using an advantageous condition i.e., low liquid Reynolds and gas Weber number outside of the nozzle [34]), could be used to tuned the IRQ threshold value, and determine where interface fluctuations become important. Consequently, the multi-scale approach (ICM-ESA) could benefit from those DNS results for tunning purpose.

- Thirdly, Regarding the nozzle inflow of the ECN Spray-A, there are still some open questions from experimental and numerical sides. Experimentally speaking, some issues to measure the real nozzle geometry are still far from zero tolerance measure, based on the actual measure scale used in the experimental equipments, for more information regarding this limitations see [61, 67, 144]. Numerically speaking, inside nozzle conditions, there is the needle motion, which has been previously evaluated [242], along with phase change phenomena. Nevertheless, its effect on turbulence boundary layer development inside the nozzle has not yet been investigated. Maybe a first attempt would be finding favorable Reynolds numbers in which the turbulence boundary layer development would be completely characterized, in order to have a properly liquid dispersion representation outside of the nozzle.

- Unclosed density correlation terms in two-phase flow modeling, is always an issue specially with high density ratios, whether Favre or Reynolds averaging is applied. Using the Reynolds/Favre averaging/filtering for instance, there is no factual evidence of turbulent liquid flux assumption based on the viscosity Boussinesq approximation, to be valid in turbulent liquid-gas flow. On the other hand, by using Favre averaging, the turbulent liquid flux contribution will be hidden [116, 33]. A new approach is proposed,

in which a liquid-gas decomposition based on the liquid volume fraction is made, using the Reynolds averaging formalism. Mathematical development is shown in appendix A. Further modeling and numerical implementation in DNS of those mathematical equations, would bring a better representation of turbulent liquid-gas interactions.

- To recall, $\boldsymbol{ELSA}$ approach is based on a homogeneous approach, meaning shortly that the averaged mixture velocity can be modeled also by a single-fluid turbulence. Creation of the two-phase flow turbulence i.e., one equation for the liquid and other for the gas, has not yet been done. Liquid-gas interface wrinklings come mainly from the turbulence either by (1) the incoming turbulence-generated field of wall-bounded flow due to inside flow nozzle, or (2) the shear stresses between the phase at the interface. Therefore, how the liquid and gas turbulent kinetic energy play their role in the interface wrinkling, is still an open question. Firstly, a mathematical development of this two-phase flow turbulence, in which exist one turbulence equation for each phase, would be encouraging. Secondly, after developed how each turbulent kinetic energy behave on each phase respectively, specially near the liquid-gas interface, it is therefore necessary to see also how the interaction is to each other, from the liquid turbulent kinetic energy to gas turbulent kinetic energy and vice-versa.

- In the Bosch injector test case, actually we are focusing in trying to capture the rare events, to take advantages on the dispersed flow approach, but finally is not very suitable case to test the dispersed flow, because one need to extend the domain to see really the behavior of dilute flow approach in droplets, and that would be costly (computational speaking), so a better test case would be the air-blast atomizer (chapter 3). This test case presents high momentum and mass flux ratio, which generates dispersed flow in a shorter distance from the nozzle than the Bosch injector test case. But the initial selection of the Bosch injector was due to the available experimental data regarding the droplets velocity ligaments. Experimental speaking, there are the high-speed X-ray imaging flow visualization and Phase Doppler Particle Analysis, in which both are equally applicable to the air-blast atomizer test case. Using these techniques, droplet diameter and velocity can be extracted [243]. They found that at really high momentum flux ratio is $\approx \mathbf{200}$ there is a liquid crow-shaped at the nozzle exit, droplet breakup process occur in the vicinity of nozzle exit, and that even some bubbles were able to enter into the liquid nozzle. Indeed, this numerical test case, would be a challenging approach for $\boldsymbol{ELSA}$. Consequently, dispersed flow regime might be better suitable studied in gas-assisted atomizer, as the one already studied in the second part of chapter 3.

- With regard to the dispersed flow analyzed in chapter 4, the liquid-gas transition boundary, between the multi-scale and dispersed flow approach, was fixed in time and space, due to averaged procedure by using the RANS framework. A LES simulation, would be better suitable to represent the actual displacement in time of the liquid-gas transition boundary. More importantly, the large-scale vortex motion will directly influence droplet motion properly [244]. Additionally, research in the area of droplet breakup, effect of droplet motion on Eulerian turbulence field, are also quite extensive in the literature. Coupling those approaches to the hybrid Euler-Lagrange Spray Atomization ($\boldsymbol{HELSA}$) model, interesting findings can then be drawn for such assessments. Finally, little is known about droplet size distribution at the transition boundary when simulating the full atomization spray process. Recent work [158] however, deduced a surface curvature distribution, based on Gauss and mean curvature, which both being defined everywhere from the liquid jet until the dilute zone, in order to have a curvature evolution. Nevertheless, this procedure is still in its early development stage.
- Regarding the two numerical test cases for industrial application, firstly, the actual oil properties were not accurately represented in this thesis, in special the possible

oil-sticky behavior at the internal FCC Injector walls. High viscosity flow and possible non-Newtonian behavior observed in atomized liquid [245], would certainly draw some new findings on the oil-steam thermal-fluid-dynamic behavior inside the injector. More importantly, how the atomization process is affected by this fluid flow properties, specially within the feed atomization zone inside the FCC Riser (in which another approach has to be used, for instance the Euler-Euler approach or the so-called Granular flow), would be appraised.

Appendices

Chap. A | Two-phase decomposition: Density correlation issue

Either averaging/filtering the equations by RANS and LES approaches, both methods have to deal with density-based correlations. There are two ways to handle this problem, namely Reynolds or Favre averaging/filtering. Both approaches lead to modeling problems that are not yet completely solved. Using Reynolds averaging/filtering, introduces correlation for which no models have been established yet, for turbulent liquid-gas flow. Thus, these unclosed correlation are generally not considered or consider being part of Reynolds stress and turbulent liquid flux final model [78]. Regarding the Favre approach, it has been widely employed in single phase flow with variable density, hence it can be applied for two-phase flow, by using the ELSA approach philosophy, previously explained [1]. Nonetheless, any Favre-averaged variable is pondered by the density. This mathematical development tries to handle this density correlation issues by means of two-phase flow decomposition.

A.1 Two-phase flow filtering

Here, Reynolds averaging/filtering formulation together with liquid volume fraction (volume formulation) field, instead of liquid mass fraction (mass formulation) is considered. This formulation is consider to be clearer by letting apparent the unclosed density correlation terms even if further efforts to define appropriate models still require future work. Applying the Reynolds averaging technique for incompressible flow to equations 3.1, and 2.7:

$$\begin{cases} \nabla\cdot\bar{\boldsymbol{U}} = 0 \quad , \\ \dfrac{\partial\overline{\boldsymbol{\rho U}}}{\partial t} + \nabla\cdot\left(\overline{\rho\boldsymbol{U}\boldsymbol{U}}\right) = -\overline{\nabla p} + \nabla\cdot(\overline{\rho\nu(\nabla\boldsymbol{U}+\nabla\boldsymbol{U}^T)}) + \bar{\boldsymbol{f}}_b + \overline{\tau_\rho} \quad , \\ \dfrac{\partial\bar{\alpha}_l}{\partial t} + \nabla\cdot(\overline{\boldsymbol{U}\alpha_l}) = 0 \quad . \end{cases} \tag{A.1}$$

To evaluate properly these averaged terms, it is necessary first to examine the consequences of turbulent fluctuations for the mean flow equations for constant phase density. By summarizing the rules which govern time averages of fluctuating properties, e.g. $a = \bar{a} + a'$ and $b = \bar{b} + b'$, and their derivatives and integrals, the following expression is obtained [110]:

$$\overline{\nabla\cdot(ab)} = \nabla\cdot(\overline{ab}) = \nabla\cdot(\bar{a}\bar{b}) + \nabla\cdot(\overline{a'b'}) \quad . \tag{A.2}$$

where a and b can represent any fluctuating vector or scalar quantity. Now applying equation A.2 to the averaged LVF equation A.1, and similarly to the gas volume fraction:

$$\begin{cases} \dfrac{\partial \bar{\alpha_l}}{\partial t} + \nabla \cdot (\bar{\boldsymbol{U}} \bar{\alpha_l}) = -\nabla \cdot \boldsymbol{R}_{\alpha_l} = -\nabla \cdot (\overline{\boldsymbol{U}\alpha_l} - \bar{\boldsymbol{U}} \bar{\alpha_l}) = -\nabla \cdot [\bar{\alpha_l}(\bar{\boldsymbol{U}}|_{\boldsymbol{l}} - \bar{\boldsymbol{U}})] \quad , \\ \dfrac{\partial \bar{\alpha_g}}{\partial t} + \nabla \cdot (\bar{\boldsymbol{U}} \bar{\alpha_g}) = -\nabla \cdot \boldsymbol{R}_{\alpha_g} = -\nabla \cdot (\overline{\boldsymbol{U}\alpha_g} - \bar{\boldsymbol{U}} \bar{\alpha_g}) = \nabla \cdot [\bar{\alpha_l}(\bar{\boldsymbol{U}}|_{\boldsymbol{l}} - \bar{\boldsymbol{U}})] \quad . \end{cases} \tag{A.3}$$

On RHS of α_l equation A.3, $\boldsymbol{R}_{\alpha_l}$ is the *turbulent liquid flux* that represents the transport of the liquid volume fraction induced by velocity fluctuations, and is related to the unresolved part of the velocity that is known to produce additional diffusion. This formulation is only valid in the absence of slip velocity between phases. Additionally, it has been proven [33, 78, 50] that even with this single flow approach it is possible to recover the different mean liquid and gas velocities $\bar{\boldsymbol{U}}|_{\boldsymbol{l}}$, and $\bar{\boldsymbol{U}}|_{\boldsymbol{g}}$, respectively by means of a drift flux model. The interested reader is then referred to [78] where a so-called, second order closure is developed. Thus, a relation between liquid and gas turbulent flux can be made:

$$\boldsymbol{R}_{\alpha_l} = -\boldsymbol{R}_{\alpha_g} \quad . \tag{A.4}$$

A.2 Liquid-gas decomposition: First approach

Thereupon, if the previous expression A.2 is used for the momentum equation in A.1, unclosed correlation terms will arise with the density, therefore, the Favre average becomes appealing, however, this approach somehow would hide the contribution of the key term in two-phase flow, namely the turbulent liquid flux. Instead, a liquid-gas decomposition based on the liquid volume fraction is applied. Leading to the following formulation of the Reynolds-averaged transient term in the momentum equation in A.1:

$$\begin{cases} \dfrac{\partial \overline{\boldsymbol{\rho U}}}{\partial t} &= \dfrac{\partial (\rho_l \bar{\alpha_l} \bar{\boldsymbol{U}}|_{\boldsymbol{l}} + \rho_g \bar{\alpha_g} \bar{\boldsymbol{U}}|_{\boldsymbol{g}})}{\partial t} \quad , \\ &= \dfrac{\partial (\rho_l \bar{\alpha_l} \bar{\boldsymbol{U}} + \rho_l \bar{\alpha_l} (\bar{\boldsymbol{U}}|_{\boldsymbol{l}} - \bar{\boldsymbol{U}}))}{\partial t} + \dfrac{\partial (\rho_g \bar{\alpha_g} \bar{\boldsymbol{U}} - \rho_g \bar{\alpha_l} (\bar{\boldsymbol{U}}|_{\boldsymbol{l}} - \bar{\boldsymbol{U}}))}{\partial t} \quad , \\ &= \dfrac{\partial \bar{\boldsymbol{\rho}} \bar{\boldsymbol{U}}}{\partial t} + \dfrac{\partial [\boldsymbol{R}_{\alpha_l} (\rho_l - \rho_g)]}{\partial t} \quad . \end{cases} \tag{A.5}$$

where the mixture density follows also a liquid-gas decomposition: $\bar{\rho} = \rho_l \bar{\alpha_l} + \rho_g \bar{\alpha_g}$, with constant gas and liquid density, ρ_g and ρ_l, respectively. Moreover, the above approach can be also applied to the Reynolds-averaged convective term in momentum equation in A.1:

$$\begin{cases} \nabla \cdot (\overline{\rho \boldsymbol{U}\boldsymbol{U}}) &= \nabla \cdot (\rho_l \bar{\alpha_l} \overline{\boldsymbol{U}\boldsymbol{U}}|_l + \rho_g \bar{\alpha_g} \overline{\boldsymbol{U}\boldsymbol{U}}|_g) \\ &= \nabla \cdot [\rho_l \bar{\alpha_l} (\bar{\boldsymbol{U}}|_l \bar{\boldsymbol{U}}|_l + \boldsymbol{R}_u|_l) + \rho_g \bar{\alpha_g} (\bar{\boldsymbol{U}}|_g \bar{\boldsymbol{U}}|_g + \boldsymbol{R}_u|_g)] \\ &= \nabla \cdot (\rho_l \bar{\alpha_l} \bar{\boldsymbol{U}}|_l \bar{\boldsymbol{U}}|_l + \rho_g \bar{\alpha_g} \bar{\boldsymbol{U}}|_g \bar{\boldsymbol{U}}|_g) + \nabla \cdot \underbrace{(\rho_l \bar{\alpha_l} \boldsymbol{R}_u|_l + \rho_g \bar{\alpha_g} \boldsymbol{R}_u|_g)}_{\text{Reynolds Stress}} \quad . \end{cases} \tag{A.6}$$

The term $\boldsymbol{R}_u|_l$, and $\boldsymbol{R}_u|_g$ are the so-called liquid and gas Reynolds stress tensor, respectively. The normal stresses involve the respective variances of the x-, y- and z-velocity fluctuations. They are always non-zero because they contain squared velocity fluctuations. The shear stresses contain second moments associated with correlations between different velocity

components [110].The Reynolds stress highlighted in equation A.6 can be studied assuming a first order closure [33]:

$$\begin{cases} \nabla\cdot\underbrace{(\rho_l\bar{\alpha_l}\boldsymbol{R}_u|_l+\rho_g\bar{\alpha_g}\boldsymbol{R}_u|_g)}_{\text{Reynolds Stress}} & =\nabla\cdot[\rho_l\bar{\alpha_l}\bar{\nu_t}|_l(\nabla\bar{\boldsymbol{U}}|_l+\nabla(\bar{\boldsymbol{U}}|_{\boldsymbol{l}})^T)]+ \\ & \\ & +\nabla\cdot[\rho_g\bar{\alpha_g}\bar{\nu_t}|_g(\nabla\bar{\boldsymbol{U}}|_g+\nabla(\bar{\boldsymbol{U}}|_{\boldsymbol{g}})^T)] \quad . \end{cases} \tag{A.7}$$

Nevertheless, if the liquid and gas turbulent viscosity are assumed to be the same: $\bar{\nu_t}|_g \approx \bar{\nu_t}|_l \approx \nu_t$, then:

$$\nabla\cdot\underbrace{(\rho_l\bar{\alpha_l}\boldsymbol{R}_u|_l+\rho_g\bar{\alpha_g}\boldsymbol{R}_u|_g)}_{\text{Reynolds Stress}}=-\nabla\cdot[\bar{\rho}\nu_t(\nabla\bar{\boldsymbol{U}}+\nabla(\bar{\boldsymbol{U}})^T)] \tag{A.8}$$

Now, applying some mathematics to the term on the left of the Reynolds stress in equation A.6:

$$\begin{cases} \nabla\cdot(\rho_l\bar{\alpha_l}\bar{\boldsymbol{U}}|_l\bar{\boldsymbol{U}}|_l+\rho_g\bar{\alpha_g}\bar{\boldsymbol{U}}|_g\bar{\boldsymbol{U}}|_g) & =\nabla\cdot(\rho_l\bar{\alpha_l}\bar{\boldsymbol{U}}|_l\bar{\boldsymbol{U}}|_l+\rho_l\bar{\alpha_l}\bar{\boldsymbol{U}}\bar{\boldsymbol{U}}-\rho_l\bar{\alpha_l}\bar{\boldsymbol{U}}\bar{\boldsymbol{U}})+ \\ & +\nabla\cdot(\rho_g\bar{\alpha_g}\bar{\boldsymbol{U}}|_g\bar{\boldsymbol{U}}|_g+\rho_g\bar{\alpha_g}\bar{\boldsymbol{U}}\bar{\boldsymbol{U}}-\rho_g\bar{\alpha_g}\bar{\boldsymbol{U}}\bar{\boldsymbol{U}}) \\ & =\nabla\cdot[\rho_l\bar{\alpha_l}(\bar{\boldsymbol{U}}|_l\bar{\boldsymbol{U}}|_l-\bar{\boldsymbol{U}}\bar{\boldsymbol{U}})+\rho_l\bar{\alpha_l}\bar{\boldsymbol{U}}\bar{\boldsymbol{U}}]+ \\ & +\nabla\cdot[\rho_g\bar{\alpha_g}(\bar{\boldsymbol{U}}|_g\bar{\boldsymbol{U}}|_g-\bar{\boldsymbol{U}}\bar{\boldsymbol{U}})+\rho_g\bar{\alpha_g}\bar{\boldsymbol{U}}\bar{\boldsymbol{U}}] \quad . \end{cases} \tag{A.9}$$

Now replacing $\bar{\boldsymbol{U}}|_l$, and $\bar{\boldsymbol{U}}|_g$ for their respective liquid and gas turbulent flux defined in equations A.3, and A.4, and reordering the terms, it reads:

$$\begin{cases} \nabla\cdot(\rho_l\bar{\alpha_l}\bar{\boldsymbol{U}}|_l\bar{\boldsymbol{U}}|_l+\rho_g\bar{\alpha_g}\bar{\boldsymbol{U}}|_g\bar{\boldsymbol{U}}|_g) & =\nabla\cdot(\bar{\rho}\bar{\boldsymbol{U}}\bar{\boldsymbol{U}})+\nabla\cdot\left[\boldsymbol{R}_{\alpha_l}\boldsymbol{R}_{\alpha_l}\left(\frac{\rho_l}{\bar{\alpha_l}}+\frac{\bar{\rho_g}}{\alpha_g}\right)\right]+ \\ & +\nabla\cdot[(\rho_l-\rho_g)(\boldsymbol{R}_{\alpha_l}\bar{\boldsymbol{U}}+\bar{\boldsymbol{U}}\boldsymbol{R}_{\alpha_l})] \quad . \end{cases} \tag{A.10}$$

Finally, the Reynolds-averaged convective term in equation A.6, is reconstructed based on the equations A.8, and A.10. Thus, the convective term in the momentum equation reads:

$$\begin{cases} \nabla\cdot(\overline{\rho\boldsymbol{U}\boldsymbol{U}}) & =\nabla\cdot(\bar{\rho}\bar{\boldsymbol{U}}\bar{\boldsymbol{U}})-\nabla\cdot[\bar{\rho}\nu_t(\nabla\bar{\boldsymbol{U}}+\nabla(\bar{\boldsymbol{U}})^T)]+ \\ & \underbrace{+\nabla\cdot\left[\boldsymbol{R}_{\alpha_l}\boldsymbol{R}_{\alpha_l}\left(\frac{\rho_l}{\bar{\alpha_l}}+\frac{\bar{\rho_g}}{\alpha_g}\right)\right]+\nabla\cdot[(\rho_l-\rho_g)(\boldsymbol{R}_{\alpha_l}\bar{\boldsymbol{U}}+\bar{\boldsymbol{U}}\boldsymbol{R}_{\alpha_l})]}_{\text{Additional terms}} \quad . \end{cases} \tag{A.11}$$

A.3 Liquid-gas decomposition: Second approach

The additional terms highlighted in equation A.11 come from the liquid-gas decomposition. Nonetheless, a second approach of the convective term in the momentum equation A.1 using the same phase decomposition can be applied after a simple mathematical passage:

$$\nabla\cdot(\overline{\rho\boldsymbol{U}\boldsymbol{U}})=\nabla\cdot(\overline{\rho\boldsymbol{U}}\bar{\boldsymbol{U}})+\nabla\cdot(\overline{\rho\boldsymbol{U}\boldsymbol{U}}-\overline{\rho\boldsymbol{U}}\bar{\boldsymbol{U}}) \quad . \tag{A.12}$$

The second term in equation A.12 is replaced by the proposed formulations A.11, and A.5, respectively. Afterwards, some reordering of the terms was made to finally show the second and preferred form of the convective term in the momentum equation A.1:

$$\begin{cases} \nabla\cdot(\overline{\rho\boldsymbol{U}\boldsymbol{U}}) & = \nabla\cdot(\overline{\rho\boldsymbol{U}}\bar{\boldsymbol{U}}) - \nabla\cdot[\bar{\rho}\nu_t(\nabla\bar{\boldsymbol{U}} + \nabla(\bar{\boldsymbol{U}})^T)] + \\ & \quad + \nabla\cdot\left[\boldsymbol{R}_{\alpha_l}\boldsymbol{R}_{\alpha_l}\left(\frac{\rho_l}{\bar{\alpha_l}} + \frac{\bar{\rho_g}}{\alpha_g}\right)\right] + \nabla\cdot[(\rho_l - \rho_g)\bar{\boldsymbol{U}}\boldsymbol{R}_{\alpha_l}] \quad . \end{cases} \tag{A.13}$$

There are left two terms in the momentum equation in A.1, namely, the pressure gradient and the stress tensor. The former, is directly obtained from Reynolds averaging, i.e. Favre averaging is not required:

$$\overline{\nabla p} = \nabla\bar{p} \quad . \tag{A.14}$$

On the other hand, a liquid-gas decomposition to the stress tensor in equation A.1 leads to the following formulation:

$$\begin{cases} \nabla\cdot(\overline{\rho\nu(\nabla\boldsymbol{U} + \nabla\boldsymbol{U}^t)}) & = \nabla\cdot[\rho_l\bar{\alpha_l}\nu_l(\nabla\bar{\boldsymbol{U}}|_l + \nabla(\bar{\boldsymbol{U}}|_{\boldsymbol{l}})^T)] + \\ & \quad + \nabla\cdot[\rho_g\bar{\alpha_g}\nu_g(\nabla\bar{\boldsymbol{U}}|_g + \nabla(\bar{\boldsymbol{U}}|_{\boldsymbol{g}})^T)] \quad . \end{cases} \tag{A.15}$$

Once again, replacing $\bar{\boldsymbol{U}}|_l$, and $\bar{\boldsymbol{U}}|_g$ for their respective liquid and gas turbulent flux defined in equations A.3, and A.4, and reordering the terms, the laminar stress tensor in equation A.15 reads:

$$\begin{cases} \nabla\cdot(\overline{\rho\nu(\nabla\boldsymbol{U} + \nabla\boldsymbol{U}^T)}) & = \nabla\cdot[\overline{\rho\nu}(\nabla\bar{\boldsymbol{U}} + \nabla\bar{\boldsymbol{U}}^T)] + \\ & \quad + \nabla\cdot[(\rho_l\nu_l - \rho_g\nu_g)(\nabla\boldsymbol{R}_{\alpha_l} + \nabla\boldsymbol{R}_{\alpha_l}^T)] - \\ & \quad - \nabla\cdot\left[(2\boldsymbol{R}_{\alpha_l}\nabla\bar{\alpha_l})\left(\frac{\rho_l\nu_l}{\bar{\alpha_l}} + \frac{\rho_g\nu_g}{\bar{\alpha_g}}\right)\right] \quad . \end{cases} \tag{A.16}$$

Ultimately, the liquid-gas decomposition allows to write the momentum equation using Reynolds averaging with all density related correlations expressed in term of the Reynolds stress and the turbulent liquid flux. After some rearrangement to point out the inner turbulent liquid flux equation, the following expression of the momentum equation is displayed:

$$\begin{cases} \dfrac{\partial\bar{\boldsymbol{\rho}}\bar{\boldsymbol{U}}}{\partial t} + \nabla\cdot(\overline{\rho\boldsymbol{U}}\bar{\boldsymbol{U}}) & = \nabla\cdot[\overline{\rho\nu_{eff}}(\nabla\bar{\boldsymbol{U}} + \nabla(\bar{\boldsymbol{U}})^T)] - \nabla\cdot\left[\boldsymbol{R}_{\alpha_l}\boldsymbol{R}_{\alpha_l}\left(\dfrac{\rho_l}{\bar{\alpha_l}} + \dfrac{\rho_g}{\bar{\alpha_g}}\right)\right] \\ & \quad - (\rho_l - \rho_g)\underbrace{\left[\dfrac{\partial\boldsymbol{R}_{\alpha_l}}{\partial t} + \nabla\cdot(\bar{\boldsymbol{U}}\boldsymbol{R}_{\alpha_l})\right]}_{\text{Turb. Liq. Flux. Eqn}} - \nabla\bar{p} + \\ & \quad + \nabla\cdot[(\rho_l\nu_l - \rho_g\nu_g)(\nabla\boldsymbol{R}_{\alpha_l} + \nabla\boldsymbol{R}_{\alpha_l}^T)] - \\ & \quad - 2\nabla\cdot\left[\left(\dfrac{\rho_l\nu_l}{\bar{\alpha_l}} + \dfrac{\rho_g\nu_g}{\bar{\alpha_g}}\right)(\boldsymbol{R}_{\alpha_l}\nabla\bar{\alpha_l})\right] \quad . \end{cases} \tag{A.17}$$

Chap. B | Other numerical simulations

It is true that no simulations were performed outside of the FCC injector. Indeed, at the beginning of this thesis it was planned to develop such applications, however, by the third and final year of PhD, it was decided to study instead another industrial application of interest. This application is actually the water sprayer, which corresponds to the second part of chapter 5. What it nice about the FCC Riser simulation, is that it is a complete different approach to the one developed in this thesis, namely a full multiphase Euler-Euler approach. The below equations and results represent the first attempts in this direction. It is to be remark, that these results are not yet conclusive and more research in this topic has to be made.

B.1 FCC Injector modeling:"Outlet-Riser" part

On this part of the injector called the *outlet*, see figure 5.3 in chapter 5, is basically the third and final part of the FCC Injector study, and the objectives previously stated that the feed injection system and the design of the riser should produce the most uniform cracking environment possible. Therefore, oil needs to be atomized into small droplets with a narrow size distribution since small droplets vaporize more quickly than larger ones. And the feed also needs sufficient momentum to effectively penetrate the flowing catalyst without causing erosion of the riser wall. [10]. Nevertheless, a deeper understanding of what is going on inside FCC Risers would be advantageous to design FCC Injectors accordingly. For instance, investigations of concurrent injected water into high-density riser demonstrated the spray cone opening angle dependency on the axial feed extent, and a limited feed radial development [246]. Moreover, FCC Riser can be usually considered as dense gas-solid flow device at the feed injection level with 20-30% of solid volume fraction [247]. Therefore, questions such as how the liquid penetrate and distribute inside the dense fluidized bed reactor have been experimentally answered. Liquid atomization is suppressed by the high solid volume concentration, and the jet come in contact with the solids just at the nozzle exit, and no droplets are formed [247].

B.1.1 General conservation equations

Based on the statements above, a 25% solid volume fraction FCC Riser validation test case has been used to validate the model specially at the feedstock injection zone [248]. This type of simulation requires an Euler-Euler approach, meaning a completely set of equations needs to be formulated. The Euler-Euler approach consists of one continuity and momentum equation for each phase and one (1) species equation.

$$\begin{cases} \dfrac{\partial(\alpha_g \rho_g)}{\partial t} + \nabla \cdot (\alpha_g \rho_g \boldsymbol{U_g}) = 0 \\ \dfrac{\partial(\alpha_s \rho_s)}{\partial t} + \nabla \cdot (\alpha_s \rho_s \boldsymbol{U_s}) = 0 \end{cases} \tag{B.1}$$

$$\begin{cases} \dfrac{\partial(\alpha_g \rho_g \boldsymbol{U_g})}{\partial t} + \nabla \cdot (\alpha_g \rho_g \boldsymbol{U_g U_g}) = -\alpha_g \nabla p + \nabla \cdot \boldsymbol{T_g} + \alpha_g \rho_g \boldsymbol{g} + \beta(\boldsymbol{u_g} - \boldsymbol{u_s}) \\ \dfrac{\partial(\alpha_s \rho_s \boldsymbol{U_s})}{\partial t} + \nabla \cdot (\alpha_s \rho_s \boldsymbol{U_s U_s}) = -\alpha_s \nabla p - \nabla p_s + \nabla \cdot \boldsymbol{T_s} + \alpha_s \rho_s \boldsymbol{g} + \beta(\boldsymbol{u_g} - \boldsymbol{u_s}) \end{cases} \tag{B.2}$$

$$\frac{\partial(\alpha_g \rho_g y_i)}{\partial t} + \nabla \cdot (\alpha_g \rho_g y_i \boldsymbol{U_g} - \alpha_g \rho_g D_{lg} \nabla y_i) = 0 \tag{B.3}$$

The set of equation B.1 represents the continuity equations for gas and solid phases. Momentum equations of gas and solid phases are displayed by equation B.2 with the shear-strain tensor for the solid phase, $\boldsymbol{T_s}$, and solid pressure, p_s, being solved by Kinetic Granular Theory [105]. The last equation B.3, is the species transport equation of the gas phase which include the liquid part, y_i, coming from the FCC Injectors in form of a mixing of gas and atomized liquid.

B.1.2 Numerical model and flow conditions

Normally this kind of simulation, such as FCC riser, as explained before in the theoretical part, involves different physics which makes the simulation cumbersome even by using supercomputers. To avoid any unnecessary complications and delay in the results, a 2D case was modeled. This above approach along with the equations B.1, B.2, and B.3 were then used in the following 2D geometrical configuration:

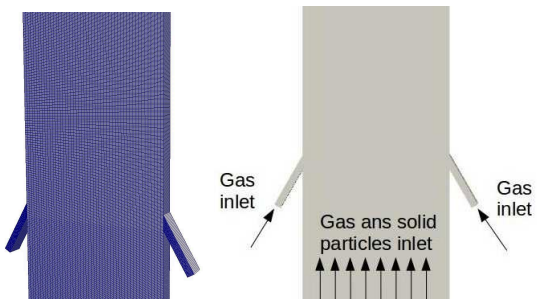

Figure B.1: Riser geometry, boundary conditions and mesh.

The length of the domain about two (2) meters with 0.186 meters of diameter, as well as the fluid and flow properties as used in previous experimental setup [248]. The fluid and flow properties are shown in the table B.1 below. It is to be noted that the solid volume fraction in this case is quite high, $\mathbf{0.25}$, as encountered in many FCC applications.

Table B.1: Summary of fluid and flow properties

Particle diameter	d_p, [m]	6.5e-05
Particle density	ρ_p, [kg/m^3]	1310
Gas density at inlet	ρ_g, [kg/m^3]	1.225
Gas viscosity at inlet	μ_g, [Pa.s]	1.782e-05
Solid volume fraction at inlet	$\alpha_{s,inlet}$	0.25
Superficial gas velocity at the bottom	U_g, [m/s]	3.28

The simulation is run with laminar flow based on the assumptions that the solid volume fraction is high enough to dampen any velocity fluctuation. In the validation test case, both gases coming from the bottom of the riser and the feed spray are air with the same properties. The first part of the FCC Riser simulation process consists of validating the model to which

only air will be used, and then later on a modification to the OpenFOAM® 's original solver is scheduled, for the final part of the thesis, to include the atomized liquid coming from the FCC injectors and see the hypothetical spray-solid-gas behavior inside the FCC Riser. Therefore, the gas-solid results are presented in the following section.

B.1.3 Results and discussion

Results show below the solid volume fraction inside the FCC Riser which is an indicator of the solid particles distribution inside the riser. Firstly, an introductory part of the validation test case has been accomplished so far, which only air and solid particles coming from the bottom of the riser. The next part is underway and will include the air from the injectors. Secondly, once the validation part is finished, as stated previously, the feed liquid jet will be included and a full applicability of the equations B.1, B.2, and B.3 will be made.

Figure B.2 exposes high accumulation of solid particles colored in brown, and light accumulation colored in blue. An agglomerate of solid particles seems to be formed from time to time specially until its weight is balanced with the gravity. Therefore, agglomerates are formed between air-solid pockets. Upcoming results, for next year, are expected to dampened liquid atomization from the FCC Injectors, according to the experimental findings [247].

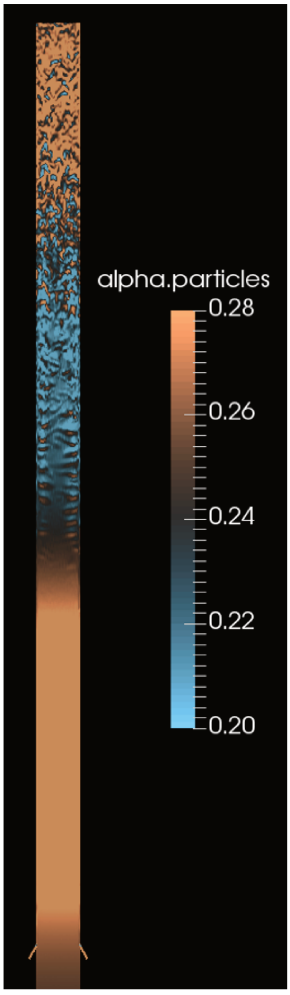

Figure B.2: Solid volume fraction inside the FCC Riser.

B.2 Static Mixer numerical test case

With regard to the static mixer, this type of injector is more in line to which was made in chapter 3. Indeed, due to the low Reynolds and Weber number, it was solved by using 100 % Interface Capturing Approach (ICM). The reason is based on the high viscosity flow inside the injector, which makes low Reynolds and Weber number. It is to be recalled, that these simulation was not in the objectives of the thesis, and the numerical simulation is far from conclusive. However, it was interesting from the industrial point of view, since served as a small answer to $VINCI\ Technologies$ request. Additionally, it was an especial case, in which $ELSA$ approach is not suitable at all.

A static mixer or motionless mixer is a device inserted into a pipe with the objective of manipulating fluid streams to divide, recombine, accelerate/decelerate, spread, swirl or form layers as they pass through the mixer [249]. Since there are no moving parts, the production and manufacture costs are low as well as the pressure drop and maintenance. Normally the energy for the mixing is available in the form of pressure. Hence, pressure drop often serves as a basis for selecting the appropriate static mixer. There are several types of static mixers depending on the particular application. Just to name a few, they vary from typical designs consisting of plates, baffles or helical elements to geometric grids positioned at precise angles to direct flow and increase turbulence.

Normally for liquid-liquid mixing, for example, the measure of uniformity or mixedness most often used is the radial variation coefficient (CoV). Imagine two individual streams, Part A and Part B, entering a static mixer in equal amounts: each component occupies two distinct areas as viewed from the cross-section of the pipe. As the materials move through each mixer element, the areas occupied by each component become more and more intermingled. The proportion of Part A and Part B stays the same at all times but each component becomes more evenly distributed throughout the pipe's cross-section [249].

When it comes about the sizing, in many cases, the diameter of the static mixer is the same size as the process pipeline. The number of elements depends on the degree of mixing required which can be estimated based on flow rate, viscosity, density and percentage of the most minor component. Increasing the number of elements improves mixing efficiency but also leads to a higher pressure loss. Experimentally speaking, high viscosity fluids with low flow rate require cost-prohibitive helical elements not suitable for pipelines that are limited in space.

The heart of a static mixer is the fixed, geometrically shaped elements that mix the product flowing through them with the help of kinetic energy only. Whereas low-viscosity media are normally mixed by flow induced convection and vortex formation (Re > 2300), under laminar flow conditions homogenization has to be achieved by actively separating and recombining the media (i.e. by turning it over), selective radial displacement and shear forces [250]. In many cases, the type and number of mixer elements are chosen so as to affect the best mixing possible without exceeding a maximum allowable pressure drop.

B.2.1 Model description

Generally, static mixers are utilized either for blending or dispersion liquid in gas or gas in liquid. From the turbulent scale point of view, there are also laminar and turbulent flow regimes. Therefore the need to define the regimes based on fluid and flow properties. Figure B.3 shows the Static Mixer boundary conditions where oil and liquid are mixed after the vertical white line, and the vertical-planar baffles are highlighted in the figure.
The table B.2 presents a fluid properties summary and the static mixer dimensions. Hence, several flow properties can be calculated, such as, Reynolds number, viscosity ratio, Weber number, capillary number, among others.
This last term, capillary number, is used of the dispersion of droplets as a function of the viscosity ratio, and is defined as the ratio of the Weber number to the Reynolds number. It

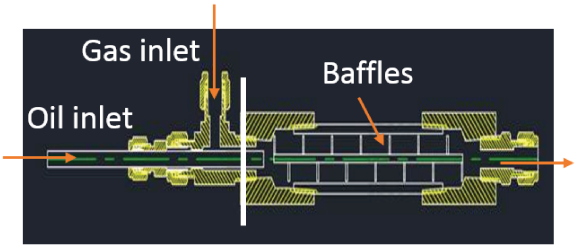

Figure B.3: Static Mixer boundary conditions.

Table B.2: Summary of fluid and flow properties for the Static Mixer

Gas fluid	H_2
Gas inlet diameter	1/4"
Gas viscosity	0.013 cp
Gas density	11.6 kg/m^3
Gas inlet flow rate	6000 Nl/h
Liquid fluid	N-Dodecane
Liquid inlet diameter	3/8"
Liquid viscosity	100 cp
Liquid density	1200 kg/m^3
Liquid flow rate	3 kg/h
Outlet diameter	3/8"

can be seen as the ratio of the "destructive" viscous forces responsible for the rupture of the secondary phase over the "protective" surface tension forces opposing the deformation [24].

Reynolds numbers based on the properties of the table B.2 for the oil and hydrogen are one (1) and two thousand (2000), respectively, which makes the flow completely laminar. Therefore, the dense flow atomization model used before in equation A.1, can not be used in this case. A new strategy must be adopted. A first attempt is to eliminate from the equations the diffusion term which depends mainly from the turbulent velocity fluctuations. By doing so, only the convective and sharpening term should be used, and this is why `interFoam` solver in OpenFOAM® is chosen (only $\boldsymbol{ICM}$ term in the equation 2.8, in chapter 2). A deeper understanding of liquid-gas dispersion in laminar flow can be obtained from the capillary number and viscosity ratio (dispersed viscosity / continuous viscosity). Figure B.4 shows that at lower viscosity ratios, less than $\mathbf{0.1}$, in a simple shear field, very high stresses must be generated in order to break a bubble or a drop. With viscosity ratios above $\mathbf{3.0}$, steady simple shear flows cannot generate stresses high enough to lead to break-up. Nevertheless, results from figure B.4 were obtained using stable conditions which is not case for industrial applications. Therefore, this figure B.4 should be used as a guidance only and not as decisive design parameter.

B.2.2 Validation

Before proceeding with numerical simulation of the static mixer, a validation step is required to ensure the suitability of the proposed model. Figure B.5 shows the boundary conditions with liquid and gas inlets as well as the helical elements. Fluid, turbulent flow properties, and helical elements dimensions were taken from a previous research article [251].
First results are displayed in figure B.6 where flow streamlines can be seen with direction from left (inlet) to right (outlet) colored by velocity. Since pipe diameter and mass flow rate remain constant all over the length, the velocity before and after helical elements will be the one prescribed at the inlet, exhibited on the figure B.6 in light brown colors. Therefore, an

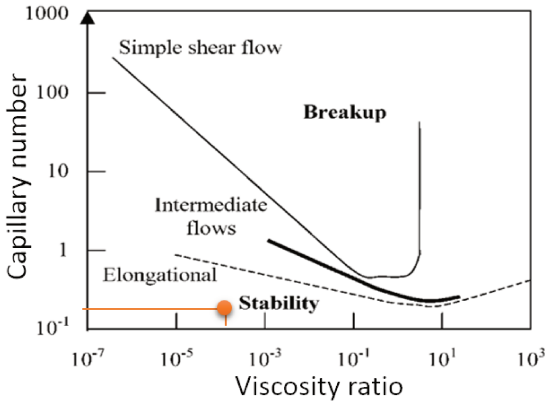

Figure B.4: Flow properties [24].

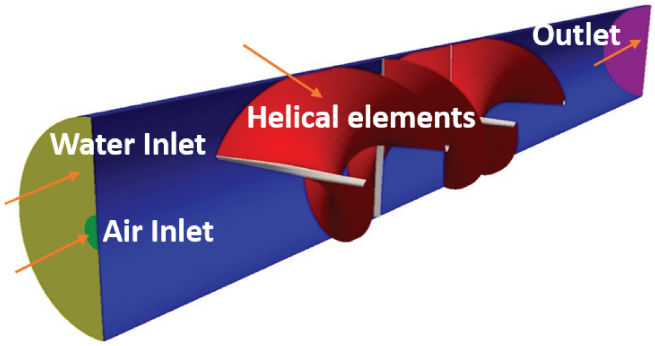

Figure B.5: Helical static mixer boundary conditions.

increased velocity is only due to the helical elements who swirl the flow. Moreover, this flow acceleration is followed by an enhanced turbulent mixing which is in fact the helical elements purpose. Further results to compare with experimental data is being held at the present time.

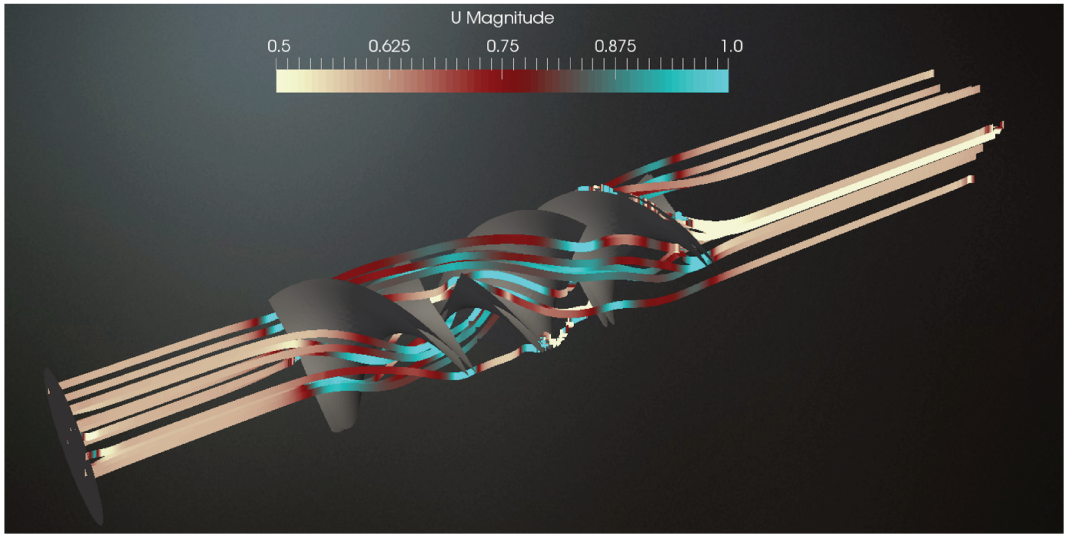

Figure B.6: Flow streamlines colored by velocity.

B.2.3 Static Mixer modeling

The same procedure applied for the FCC Injector was used here. From the boundary conditions and properties given in figure B.3 and table B.2, respectively, a numerical geometry was made in OpenFOAM® to only take into account the fluid part, as shown in figure B.7.

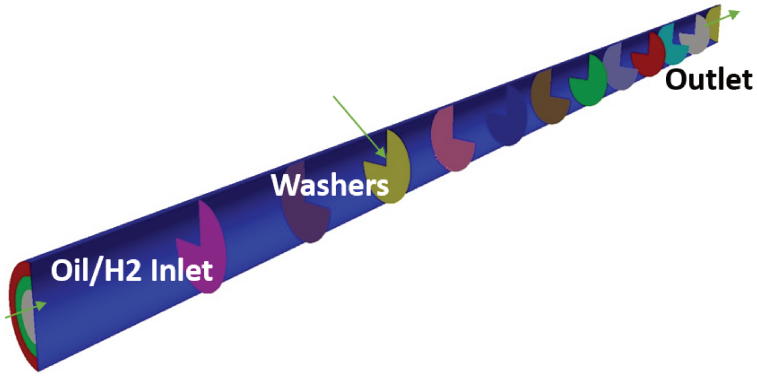

Figure B.7: Geometrical model of the static mixer.

The equations employed are the momentum, and sigma equations 2.9 already explained, and not shown here. The only modification made was to the liquid volume fraction equation which is exactly as the solver in OpenFOAM® namely `interFoam`. Equation B.4 is recalled here, with only the interface capturing method (ICM) to ensure the immiscibility of the phases.

$$\frac{\partial \alpha_l}{\partial t} + \nabla \cdot (\boldsymbol{U} \alpha_l) + \underbrace{\nabla \cdot \boldsymbol{C}_\alpha \boldsymbol{U}_r \alpha_l (1-\alpha_l)}_{ICM} = 0 \tag{B.4}$$

B.2.4 Results and discussion

There are two questions to answer: (1) mixing quality at the exit of the static mixer and (2) what happens inside of the static mixer that enhances or dampens the mixing in order to focus on the future improvements. Figure B.8 displays on the left the oil volume fraction. At the entrance, bottom of the figure, there are the oil at the center and the gas in the outer annulus. Firstly, the liquid length core is broken up due to the gas entrainment, the video which is not shown here, displays pulsating regime next to the inlet, the liquid core gets constructed and

broken up successively. Mainly due to high oil viscosity and high gas momentum compared to the oil momentum at the inlet. Secondly, oil tends to stick a the walls, meanwhile gas tends to flow in the center, this is mainly based on the density difference. While doing the swirl, the heaviest fluid tend to go to the outer part of pipe driven by centrifugal forces, and on the other hand, the lighter fluid remains in the center pipe stream. This behavior will produce high pressure drops since the high viscosity oil will be frictioning at the walls.

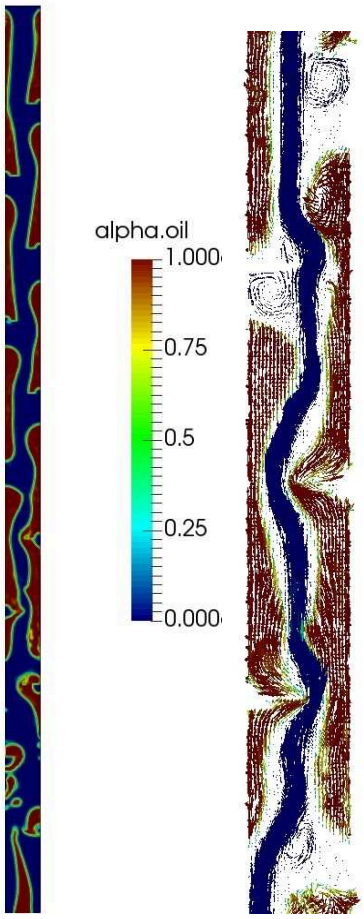

Figure B.8: Oil volume fraction distribution within static mixer (left). Zoomed up flow streamlines between four (4) baffles colored by oil volume fraction (right).

In figure B.8 on the right, a zoomed up view between 4 baffles is indicated. Red vectors represent the oil which presents proximity with the walls, and blue vectors are the gas with predominant flow tendency within pipe center. There are also, as expected, vortexes developed in baffles vicinity. These vortexes might help detaching the oil from the walls, however to do so, more baffles are needed and then the pressure drops will be increased.

Bibliography

[1] A. Vallet and R. Borghi, "Modelisation eulerienne de l'atomisation d'un jet liquide," *Comptes Rendus de l'Academie des Sciences - Series IIB - Mechanics-Physics-Astronomy*, vol. 327, no. 10, pp. 1015 – 1020, 1999.

[2] A. Vallet, A. A. Burluka, and R. Borghi, "Development of a eulerian model for the atomization of a liquid jet," *Atomization and Sprays*, vol. 11, no. 6, 2001.

[3] J. Lasheras, E. Villermaux, and E. Hopfinger, "Break-up and atomization of a round water jet by a high-speed annular air jet," *Journal of Fluid Mechanics*, vol. 357, pp. 351–379, 1998.

[4] M. Pilch and C. Erdman, "Use of breakup time data and velocity history data to predict the maximum size of stable fragments for acceleration-induced breakup of a liquid drop," *International journal of multiphase flow*, vol. 13, no. 6, pp. 741–757, 1987.

[5] "Engine Combustion Network," https://ecn.sandia.gov/.

[6] K. Lounnaci, S. Idlahcen, D. Sedarsky, C. Roze, J.-B. Blaisot, and F.-X. Demoulin, "Image processing techniques for velocity, interface complexity, and droplet production measurement in the near-nozzle region of a diesel spray," *Atomization and Sprays*, vol. 25, no. 9, 2015.

[7] N. Hecht, "Simulation aux grandes échelles des écoulements liquide-gaz : application á l'atomisation," Ph.D. dissertation, University of Rouen, 2014.

[8] J. Mora, R. Bolado, and J. Prince, "Design of hollow cone nozzles for gas oil injection process," in *Proceedings of the World Congress on Engineering*, vol. 2. Citeseer, 2008.

[9] R. Sadeghbeigi, *Fluid catalytic cracking handbook: an expert guide to the practical operation, design, and optimization of FCC units*. Elsevier, 2012.

[10] A. A. Avidan, "Fluid catalytic cracking," in *Circulating fluidized beds*. Springer, 1997, pp. 466–488.

[11] E. process management, "Turbine bypass condenser dump applications," 2002.

[12] S. systems. (2016) New steammax nozzles and injectors help petrochemical producer increase efficiency-result in 15-day payback period. [Online]. Available: https://www.spray.com/literature_pdfs/CS228_SteamMax_Nozzles_%20Injectors_Increase_Efficiency_for_Petrochem_Producer.pdf

[13] C. T. Crowe, *Multiphase flow handbook*. CRC press, 2005, vol. 59.

[14] P. Marmottant and E. Villermaux, "On spray formation," *Journal of fluid mechanics*, vol. 498, pp. 73–111, 2004.

[15] E. Fernandes, M. Heitor, and V. Sivadas, "Towards controlled liquid atomization," in *Center for Innovation Technology and Policy Research, 10th International Symposium on Applications of Laser Techniques to Fluid Mechanics, Lisbon*, 2000.

[16] J. Anez, A. Ahmed, S. Puggelli, J. Reveillon, J. C. Brändle de Motta, and F.-X. Demoulin, "Subgrid liquid flux and interface modelling for les of atomization," in *Ilass Europe. 28th european conference on Liquid Atomization and Spray Systems*. Editorial Universitat Politècnica de València, 2017, pp. 385–393.

[17] D. Stepowski and O. Werquin, "Measurement of the liquid volume fraction and its statistical distribution in the near development field of a spray," *Atomization and Sprays*, vol. 14, no. 3, 2004.

[18] F. Dabonneville, "Development of a multi-approach and multi-scale numerical method applied to atomization," Ph.D. dissertation, Normandie Université, 2018.

[19] Y. Addad, U. Gaitonde, D. Laurence, and S. Rolfo, "Optimal unstructured meshing for large eddy simulations," in *Quality and reliability of large-eddy simulations*. Springer, 2008, pp. 93–103.

[20] A. Umemura and J. Shinjo, "Detailed sgs atomization model and its implementation to two-phase flow les," *Combustion and Flame*, 2018.

[21] R. Lebas, P.-A. Beau, G. Blokkeel, and F.-X. Demoulin, "Elsa model for atomization: To benefit of the eulerian and lagrangian descriptions of the liquid phase," in *ASME 2006 2nd Joint US-European Fluids Engineering Summer Meeting Collocated With the 14th International Conference on Nuclear Engineering*. American Society of Mechanical Engineers, 2006, pp. 565–572.

[22] B. F. Nozzle, "Inc.,(2005). bete spray dryer manual."

[23] R. E. Bedaw and W. F. Walker, "Atomizing spray nozzle for mixing a liquid with a gas," Aug. 31 1993, uS Patent 5,240,183.

[24] L. Fradette, H.-Z. Li, L. Choplin, and P. Tanguy, "Gas/liquid dispersions with a smx static mixer in the laminar regime," *Chemical engineering science*, vol. 61, no. 11, pp. 3506–3518, 2006.

[25] A. Gupta and D. S. Rao, "Effect of feed atomization on fcc performance: simulation of entire unit," *Chemical Engineering Science*, vol. 58, no. 20, pp. 4567–4579, 2003.

[26] A. Murcia, "Numerous changes mark fcc technology advance," *Oil and Gas Journal;(United States)*, vol. 90, no. 20, 1992.

[27] C. I. Pinheiro, J. L. Fernandes, L. Domingues, A. J. Chambel, I. Graca, N. M. Oliveira, H. S. Cerqueira, and F. R. Ribeiro, "Fluid catalytic cracking (fcc) process modeling, simulation, and control," *Industrial & engineering chemistry research*, vol. 51, no. 1, pp. 1–29, 2011.

[28] G. Wang, C. Xu, and J. Gao, "Study of cracking fcc naphtha in a secondary riser of the fcc unit for maximum propylene production," *Fuel Processing Technology*, vol. 89, no. 9, pp. 864–873, 2008.

[29] V. Westergaard and J. A. Fife, "Flue gas cooling," in *Proceedings of 1964 ASME Incinerator Conference*, 1964.

[30] S. V. Nayak, S. L. Joshi, and V. V. Ranade, "Modeling of vaporization and cracking of liquid oil injected in a gas–solid riser," *Chemical Engineering Science*, vol. 60, no. 22, pp. 6049–6066, 2005.

[31] A. Gupta and D. S. Rao, "Model for the performance of a fluid catalytic cracking (fcc) riser reactor: effect of feed atomization," *Chemical Engineering Science*, vol. 56, no. 15, pp. 4489–4503, 2001.

[32] L. Wolschlag and K. Couch, "Uop fcc innovations developed using sophisticated engineering tools," 2011.

[33] R. Lebas, T. Menard, P.-A. Beau, A. Berlemont, and F.-X. Demoulin, "Numerical simulation of primary break-up and atomization: Dns and modelling study," *International Journal of Multiphase Flow*, vol. 35, no. 3, pp. 247–260, 2009.

[34] T. Ménard, S. Tanguy, and A. Berlemont, "Coupling level set/vof/ghost fluid methods: Validation and application to 3d simulation of the primary break-up of a liquid jet," *International Journal of Multiphase Flow*, vol. 33, no. 5, pp. 510–524, 2007.

[35] J. Shinjo and A. Umemura, "Simulation of liquid jet primary breakup: Dynamics of ligament and droplet formation," *International Journal of Multiphase Flow*, vol. 36, no. 7, pp. 513 – 532, 2010.

[36] S. Shinjo and A. Umemura, "Surface instability and primary atomization characteristics of straight liquid jet sprays," *International Journal of Multiphase Flow*, vol. 37, no. 10, pp. 1294–1304, 2011.

[37] M. Ghiji, L. Goldsworthy, P. Brandner, V. Garaniya, and P. Hield, "Numerical and experimental investigation of early stage diesel sprays," *Fuel*, vol. 175, pp. 274–286, 2016.

[38] K. E. Wardle and H. G. Weller, "Hybrid multiphase cfd solver for coupled dispersed/segregated flows in liquid-liquid extraction," *International Journal of Chemical Engineering*, vol. 2013, 2013.

[39] L. Zhou, J. Xia, J. Shinjo, A. Cairns, L. Cruff, and H. Blaxill, "Towards high-fidelity multi-scale simulation of spray atomization," *Energy Procedia*, vol. 66, pp. 309–312, 2015.

[40] C. E. Brennen, *Fundamentals of multiphase flow*. Cambridge university press, 2005.

[41] S. B. Pope, "Pdf methods for turbulent reactive flows," *Progress in energy and combustion science*, vol. 11, no. 2, pp. 119–192, 1985.

[42] O. Simonin, E. Deutsch, and J. Minier, "Eulerian prediction of the fluid/particle correlated motion in turbulent two-phase flows," *Applied Scientific Research*, vol. 51, no. 1-2, pp. 275–283, 1993.

[43] S. O. Unverdi and G. Tryggvason, "A front-tracking method for viscous, incompressible, multi-fluid flows," *Journal of computational physics*, vol. 100, no. 1, pp. 25–37, 1992.

[44] D. Gueyffier, J. Li, A. Nadim, R. Scardovelli, and S. Zaleski, "Volume-of-fluid interface tracking with smoothed surface stress methods for three-dimensional flows," *Journal of Computational physics*, vol. 152, no. 2, pp. 423–456, 1999.

[45] M. Sussman, P. Smereka, and S. Osher, "A level set approach for computing solutions to incompressible two-phase flow," *Journal of Computational physics*, vol. 114, no. 1, pp. 146–159, 1994.

[46] S. Osher and J. A. Sethian, "Fronts propagating with curvature-dependent speed: algorithms based on hamilton-jacobi formulations," *Journal of computational physics*, vol. 79, no. 1, pp. 12–49, 1988.

[47] R. P. Fedkiw, T. Aslam, B. Merriman, and S. Osher, "A non-oscillatory eulerian approach to interfaces in multimaterial flows (the ghost fluid method)," *Journal of computational physics*, vol. 152, no. 2, pp. 457–492, 1999.

[48] M. Kang, R. P. Fedkiw, and X.-D. Liu, "A boundary condition capturing method for multiphase incompressible flow," *Journal of Scientific Computing*, vol. 15, no. 3, pp. 323–360, 2000.

[49] S. Tanguy and A. Berlemont, "Application of a level set method for simulation of droplet collisions," *International journal of multiphase flow*, vol. 31, no. 9, pp. 1015–1035, 2005.

[50] P.-A. Beau, M. Funk, R. Lebas, and F.-X. Demoulin, "Applying quasi-multiphase model to simulate atomization processes in diesel engines: Modeling of the slip velocity," SAE Technical Paper, Tech. Rep., 2005.

[51] M. Sussman and E. G. Puckett, "A coupled level set and volume-of-fluid method for computing 3d and axisymmetric incompressible two-phase flows," *Journal of computational physics*, vol. 162, no. 2, pp. 301–337, 2000.

[52] R. Lebas, T. Menard, P. Beau, A. Berlemont, and F. Demoulin, "Numerical simulation of primary break-up and atomization: DNS and modelling study," *International Journal of Multiphase Flow*, vol. 35, no. 3, pp. 247 – 260, 2009.

[53] Corrosionpedia. (2016) Corrosionpedia. [Online]. Available: https://www.corrosionpedia.com/definition/120/atomization

[54] D. Zuzio, J.-L. Estivalezes, P. Villedieu, and G. Blanchard, "Numerical simulation of primary and secondary atomization," *Comptes Rendus Mécanique*, vol. 341, no. 1-2, pp. 15–25, 2013.

[55] J. C. Beale and R. D. Reitz, "Modeling spray atomization with the kelvin-helmholtz/rayleigh-taylor hybrid model," *Atomization and sprays*, vol. 9, no. 6, 1999.

[56] N. D'Angelo, "Kelvin-helmholtz instability in a fully ionized plasma in a magnetic field," *The Physics of Fluids*, vol. 8, no. 9, pp. 1748–1750, 1965.

[57] E. Villermaux, H. Rehab, and E. Hopfinger, "Breakup regimes and self-sustained pulsations in coaxial jets," *Meccanica*, vol. 29, no. 4, pp. 393–401, 1994.

[58] H. Chaves, C. Kirmse, and F. Obermeier, "Velocity measurements of dense diesel fuel sprays in dense air," *Atomization and sprays*, vol. 14, no. 6, 2004.

[59] M. Linne, M. Paciaroni, T. Hall, and T. Parker, "Ballistic imaging of the near field in a diesel spray," *Experiments in fluids*, vol. 40, no. 6, pp. 836–846, 2006.

[60] W. Cai, C. F. Powell, Y. Yue, S. Narayanan, J. Wang, M. W. Tate, M. J. Renzi, A. Ercan, E. Fontes, and S. M. Gruner, "Quantitative analysis of highly transient fuel sprays by time-resolved x-radiography," *Applied Physics Letters*, vol. 83, no. 8, pp. 1671–1673, 2003.

[61] A. L. Kastengren, C. F. Powell, Y. Wang, K.-S. Im, and J. Wang, "X-ray radiography measurements of diesel spray structure at engine-like ambient density," *Atomization and Sprays*, vol. 19, no. 11, 2009.

[62] L. M. Pickett, J. Manin, A. Kastengren, and C. Powell, "Comparison of near-field structure and growth of a diesel spray using light-based optical microscopy and x-ray radiography," *SAE International Journal of Engines*, vol. 7, no. 2014-01-1412, pp. 1044–1053, 2014.

[63] J. Chaves, W. Falicoff, Y. Sun, and B. Parkyn, "Simple optics that produce constant illuminance on a distant target," in *Nonimaging Optics and Efficient Illumination Systems*, vol. 5529. International Society for Optics and Photonics, 2004, pp. 166–176.

[64] M. Raffel, C. E. Willert, J. Kompenhans *et al.*, *Particle image velocimetry: a practical guide*. Springer Science & Business Media, 2007.

[65] A. H. Lefebvre and V. G. McDonell, *Atomization and sprays*. CRC press, 2017.

[66] P. Beak and D. B. Reitz, "Dipole-stabilized carbanions: Novel and useful intermediates," *Chemical Reviews*, vol. 78, no. 3, pp. 275–316, 1978.

[67] A. L. Kastengren, F. Z. Tilocco, C. F. Powell, J. Manin, L. M. Pickett, R. Payri, T. Bazyn *et al.*, "Engine combustion network (ecn): measurements of nozzle geometry and hydraulic behavior," *Atom. Sprays*, vol. 22, no. 12, pp. 1011–1052, 2012.

[68] J. Qian and C. Law, "Regimes of coalescence and separation in droplet collision," *Journal of Fluid Mechanics*, vol. 331, pp. 59–80, 1997.

[69] Y. Jiang, A. Umemura, and C. Law, "An experimental investigation on the collision behaviour of hydrocarbon droplets," *Journal of Fluid Mechanics*, vol. 234, pp. 171–190, 1992.

[70] F. A. Williams, "Spray combustion and atomization," *Physics of Fluids*, vol. 1, no. 6, pp. 541–545, 1958. [Online]. Available: http://scitation.aip.org/content/aip/journal/pof1/1/6/10.1063/1.1724379

[71] G. Bird, *Molecular gas dynamics and the direct simulation of gas flows*. Oxford University Press, 1994.

[72] F. Laurent and M. Massot, "Multi-fluid modelling of laminar polydisperse spray flames: origin, assumptions and comparison of sectional and sampling methods," *Combustion Theory and Modelling*, vol. 5, no. 4, pp. 537–572, 2001.

[73] F. Laurent, A. Sibra, and F. Doisneau, "Two-size moment Eulerian multi-fluid model: a flexible and realizable high-fidelity description of polydisperse moderately dense evaporating sprays," Jun. 2015. [Online]. Available: https://hal.archives-ouvertes.fr/hal-01169730

[74] C. Yuan, F. Laurent, and R. Fox, "An extended quadrature method of moments for population balance equations," *Journal of Aerosol Science*, vol. 51, pp. 1 – 23, 2012.

[75] S. L. P. Donald A. Drew, *Theory of Multicomponent Fluids*. Springer-Verlag New York, 1999.

[76] G. Blokkeel, B. Barbeau, and R. Borghi, "A 3d eulerian model to improve the primary breakup of atomizing jet," SAE Technical Paper, Tech. Rep., 2003.

[77] J. Chesnel, J. Reveillon, T. Menard, and F.-X. Demoulin, "Large eddy simulation of liquid jet atomization," *Atomization and Sprays*, vol. 21, no. 9, 2011.

[78] A. Andreini, C. Bianchini, S. Puggelli, and F. Demoulin, "Development of a turbulent liquid flux model for eulerian-eulerian multiphase flow simulations," *International Journal of Multiphase Flow*, vol. 81, pp. 88 – 103, 2016.

[79] Hirt, C.W.;Nichols, B.D., "Volume of Fluid (VOF) Method for the Dynamics of Free Boundaries," vol. 39, pp. 201–225.

[80] D. Kothe, W. Rider, S. Mosso, J. Brock, and J. Hochstein, "Volume tracking of interfaces having surface tension in two and three dimensions," in *34th Aerospace Sciences Meeting and Exhibit*, 1996, p. 859.

[81] W. F. Noh and P. Woodward, "Slic (simple line interface calculation)," in *Proceedings of the fifth international conference on numerical methods in fluid dynamics June 28–July 2, 1976 Twente University, Enschede*. Springer, 1976, pp. 330–340.

[82] D. B. Kothe and W. J. Rider, "Comments on modeling interfacial flows with volume-of-fluid methods," *submitted for publication*, 1995.

[83] O. Ubbink, "Numerical prediction of two fluid systems with sharp interfaces," 1997.

[84] X.-S. Tian, H. Zhao, H.-F. Liu, W.-F. Li, and J.-L. Xu, "Three-dimensional large eddy simulation of round liquid jet primary breakup in coaxial gas flow using the vof method," *Fuel Processing Technology*, vol. 131, pp. 396–402, 2015.

[85] M. Ghiji, L. Goldsworthy, V. Garaniya, P. Brandner, and P. Hield, "Cfd modelling of primary atomisation of diesel spray," in *19th Australasian fluid mechanics conference*, 2014, pp. 1–4.

[86] D. Fuster, A. Bagué, T. Boeck, L. Le Moyne, A. Leboissetier, S. Popinet, P. Ray, R. Scardovelli, and S. Zaleski, "Simulation of primary atomization with an octree adaptive mesh refinement and vof method," *International Journal of Multiphase Flow*, vol. 35, no. 6, pp. 550–565, 2009.

[87] G. Tomar, D. Fuster, S. Zaleski, and S. Popinet, "Multiscale simulations of primary atomization," *Computers & Fluids*, vol. 39, no. 10, pp. 1864–1874, 2010.

[88] A. N. Kolmogorov, "The local structure of turbulence in incompressible viscous fluid for very large reynolds numbers," in *Dokl. Akad. Nauk SSSR*, vol. 30, no. 4, 1941, pp. 299–303.

[89] B. Duret, J. Reveillon, T. Menard, and F. Demoulin, "Improving primary atomization modeling through dns of two-phase flows," *International Journal of Multiphase Flow*, vol. 55, pp. 130–137, 2013.

[90] S. B. Pope, "Turbulent flows," 2001.

[91] M. Lesieur, *Turbulence in fluids*. Springer Science & Business Media, 2012, vol. 40.

[92] W. Ling, J. Chung, T. Troutt, and C. Crowe, "Direct numerical simulation of a three-dimensional temporal mixing layer with particle dispersion," *Journal of Fluid Mechanics*, vol. 358, pp. 61–85, 1998.

[93] J. K. Eaton and J. Fessler, "Preferential concentration of particles by turbulence," *International Journal of Multiphase Flow*, vol. 20, pp. 169–209, 1994.

[94] C. Crowe, T. Troutt, and J. Chung, "Numerical models for two-phase turbulent flows," *Annual Review of Fluid Mechanics*, vol. 28, no. 1, pp. 11–43, 1996.

[95] P. Fevrier, "Etude numérique des effets de concentration préférentielle et de corrélation spatiale entre vitesses de particules solides en turbulence homogene isotrope stationnaire," Ph.D. dissertation, Toulouse, INPT, 2000.

[96] S. Elghobashi, "On predicting particle-laden turbulent flows," *Applied scientific research*, vol. 52, no. 4, pp. 309–329, 1994.

[97] A. Kaufmann, O. Simonin, and T. Poinsot, "Direct numerical simulation of particle-laden homogeneous isotropic turbulent flows using a two-fluid model formulation," in *5th Int. Conf. on Multiphase Flow, Yokohama, Japan*, 2004, p. 101.

[98] O. Desjardins, V. Moureau, and H. Pitsch, "An accurate conservative level set/ghost fluid method for simulating turbulent atomization," *Journal of Computational Physics*, vol. 227, no. 18, pp. 8395–8416, 2008.

[99] D. E. H. Chawki *et al.*, "Atomization modeling of liquid jets using an eulerian-eulerian model and a surface density approach," Ph.D. dissertation, Aix-Marseille, 2013.

[100] V. Srinivasan, A. J. Salazar, and K. Saito, "Numerical investigation on the disintegration of round turbulent liquid jets using les/vof techniques," *Atomization and Sprays*, vol. 18, no. 7, 2008.

[101] M. Herrmann, "A parallel eulerian interface tracking/lagrangian point particle multi-scale coupling procedure," *Journal of Computational Physics*, vol. 229, no. 3, pp. 745–759, 2010.

[102] F. Xiao, "Large eddy simulation of liquid jet primary breakup," Ph.D. dissertation, © F. Xiao, 2012.

[103] F. Xiao, M. Dianat, and J. J. McGuirk, "Les of turbulent liquid jet primary breakup in turbulent coaxial air flow," *International Journal of Multiphase Flow*, vol. 60, pp. 103–118, 2014.

[104] H. Weller, "A new approach to vof-based interface capturing methods for incompressible and compressible flow," *OpenCFD Ltd., Report TR/HGW/04*, 2008.

[105] H. Rusche, "Computational fluid dynamics of dispersed two-phase flows at high phase fractions," Ph.D. dissertation, Imperial College London (University of London), 2003.

[106] E. Berberović, N. P. van Hinsberg, S. Jakirlić, I. V. Roisman, and C. Tropea, "Drop impact onto a liquid layer of finite thickness: Dynamics of the cavity evolution," *Physical Review E*, vol. 79, no. 3, p. 036306, 2009.

[107] S. M. Damián, "An extended mixture model for the simultaneous treatment of short and long scale interfaces," *Dissertationsschrift, Universidad Nacional del Litoral, Argentinien. Krepper, E., Lucas, D., Frank, T., Prasser, H.-M., & Zwart, PJ (2008). The inhomogeneous MUSIG model for the simulation of polydispersed flows. Nuclear Engineering and Design*, vol. 238, no. 7, pp. 1690–1702, 2013.

[108] O. Simonin, "Statistical and continuum modelling of turbulent reactive particulate flows," *Lecture Series 1996-02, Von Karman Institute for Fluid Dynamics*, 2000.

[109] Chesnel, "Simulation aux grandes echelles de l'atomisation, application Ãă l'injection automobile," Ph.D. dissertation, University of Rouen, 2010.

[110] H. K. Versteeg and W. Malalasekera, *An introduction to computational fluid dynamics: the finite volume method*. Pearson Education, 2007.

[111] P. Sagaut, *Large eddy simulation for incompressible flows: an introduction*. Springer Science & Business Media, 2006.

[112] J. Smagorinsky, "General circulation experiments with the primitive equations: I. the basic experiment," *Monthly weather review*, vol. 91, no. 3, pp. 99–164, 1963.

[113] F. Nicoud and F. Ducros, "Subgrid-scale stress modelling based on the square of the velocity gradient tensor," *Flow, turbulence and Combustion*, vol. 62, no. 3, pp. 183–200, 1999.

[114] F. Ducros, F. Nicoud, and T. Poinsot, "Wall-adapting local eddy-viscosity models for simulations in complex geometries," pp. 293–299, 1998.

[115] C. W. Hirt and B. D. Nichols, "Volume of fluid (vof) method for the dynamics of free boundaries," *Journal of computational physics*, vol. 39, no. 1, pp. 201–225, 1981.

[116] F.-X. Demoulin, P.-A. Beau, G. Blokkeel, A. Mura, and R. Borghi, "A new model for turbulent flows with large density fluctuations: Application to liquid atomization," *Atomization and Sprays*, vol. 17, no. 4, 2007.

[117] J. Desantes, J. Garcia-Oliver, J. Pastor, A. Pandal, B. Naud, K. Matusik, D. Duke, A. Kastengren, C. Powell, and D. Schmidt, "Modelling and validation of near-field Diesel spray CFD simulations based on the σ-Y model." Universitat Politecnica Valencia, Sep. 2017. [Online]. Available: http://ocs.editorial.upv.es/index.php/ILASS/ILASS2017/paper/view/4715

[118] D. Lee and R. Spencer, "Photomicrographic studies of fuel sprays. naca tech," Note 454, Washington, Tech. Rep., 1933.

[119] R. E. Phinney, "The breakup of a turbulent liquid jet in a gaseous atmosphere," *Journal of Fluid Mechanics*, vol. 60, no. 04, pp. 689–701, 1973.

[120] J. W. Hoyt and J. Taylor, "Waves on water jets," *Journal of Fluid Mechanics*, vol. 83, no. 01, pp. 119–127, 1977.

[121] D. Ervine and H. Falvey, "Behaviour of turbulent water jets in the atmosphere and in plunge pools." *Proceedings of the Institution of Civil engineers*, vol. 83, no. 1, pp. 295–314, 1987.

[122] G. Faeth, L.-P. Hsiang, and P.-K. Wu, "Structure and breakup properties of sprays," *International Journal of Multiphase Flow*, vol. 21, pp. 99–127, 1995.

[123] H. Jasak, "Error analysis and estimation for finite volume method with applications to fluid flow," 1996.

[124] F. Demoulin, P. Beau, G. Blokkeel, A. Mura, and R. Borghi, "A new model for turbulent flows with large large density fluctuations: application to liquid atomization," *Atomization and Sprays*, vol. 17, no. 4, pp. 315–345, 2007.

[125] Q. Xue, M. Battistoni, C. Powell, D. Longman, S. Quan, E. Pomraning, P. Senecal, D. Schmidt, and S. Som, "An eulerian cfd model and x-ray radiography for coupled nozzle flow and spray in internal combustion engines," *International Journal of Multiphase Flow*, vol. 70, pp. 77–88, 2015.

[126] S. B. Pope, "Ten questions concerning the large-eddy simulation of turbulent flows," *New journal of Physics*, vol. 6, no. 1, p. 35, 2004.

[127] J. Fröhlich, C. P. Mellen, W. Rodi, L. Temmerman, and M. A. Leschziner, "Highly resolved large-eddy simulation of separated flow in a channel with streamwise periodic constrictions," *Journal of Fluid Mechanics*, vol. 526, pp. 19–66, 2005.

[128] H. Werner and H. Wengle, "8th symp. turbulent shear flows," *Munich, Germany*, vol. 155, 1991.

[129] F. Denner, D. R. van der Heul, G. T. Oud, M. M. Villar, A. da Silveira Neto, and B. G. van Wachem, "Comparative study of mass-conserving interface capturing frameworks for two-phase flows with surface tension," *International Journal of Multiphase Flow*, vol. 61, pp. 37–47, 2014.

[130] A. Ferrari, M. Magnini, and J. R. Thome, "A flexible coupled level set and volume of fluid (flexclv) method to simulate microscale two-phase flow in non-uniform and unstructured meshes," *International Journal of Multiphase Flow*, vol. 91, pp. 276–295, 2017.

[131] J. Roenby, H. Bredmose, and H. Jasak, "A computational method for sharp interface advection," *Royal Society Open Science*, vol. 3, no. 11, p. 160405, 2016.

[132] F. Raees, D. Van der Heul, and C. Vuik, "Evaluation of the interface-capturing algorithm of OpenFOAM for the simulation of incompressible immiscible two-phase flow," Delft University of Technology, Faculty of Electrical Engineering, Mathematics and Computer Science, Delft Institute of Applied Mathematics, Tech. Rep., 2011.

[133] F.-X. Demoulin, J. Reveillon, B. Duret, Z. Bouali, P. Desjonqueres, and T. Menard, "Toward using direct numerical simulation to improve primary break-up modeling," *Atomization and Sprays*, vol. 23, no. 11, 2013.

[134] E. De Villiers, A. Gosman, and H. Weller, "Large eddy simulation of primary diesel spray atomization," SAE Technical Paper, Tech. Rep., 2004.

[135] A. Leboissetier, "Simulation numérique directe de l'atomisation primaire d'un jet liquide à haute vitesse," Ph.D. dissertation, Paris 6, 2002.

[136] J. Desantes, J. Garcia-Oliver, J. Pastor, A. Pandal, E. Baldwin, and D. Schmidt, "Coupled/decoupled spray simulation comparison of the ecn spray a condition with the σ-y eulerian atomization model," *International Journal of Multiphase Flow*, vol. 80, pp. 89–99, 2016.

[137] J. M. Garcia-Oliver, J. M. Pastor, A. Pandal, N. Trask, E. Baldwin, and D. P. Schmidt, "Diesel spray cfd simulations based on the σ-y eulerian atomization model," *Atomization and Sprays*, vol. 23, no. 1, 2013.

[138] A. Kastengren, F. Tilocco, D. Duke, C. Powell, S. Moon, and X. Zhang, "Time-resolved x-ray radiography of diesel injectors from the engine combustion network," *ICLASS Paper*, no. 1369, 2012.

[139] L.-M. Malbec, J. Egúsquiza, G. Bruneaux, and M. Meijer, "Characterization of a set of ecn spray a injectors: nozzle to nozzle variations and effect on spray characteristics," *SAE International Journal of Engines*, vol. 6, no. 2013-24-0037, pp. 1642–1660, 2013.

[140] J. Matheis and S. Hickel, "Multi-component vapor-liquid equilibrium model for les and application to ecn spray a," *arXiv preprint arXiv:1609.08533*, 2016.

[141] E. Knudsen, E. Doran, V. Mittal, J. Meng, and W. Spurlock, "Compressible eulerian needle-to-target large eddy simulations of a diesel fuel injector," *Proceedings of the Combustion Institute*, vol. 36, no. 2, pp. 2459–2466, 2017.

[142] G. Lacaze, A. Misdariis, A. Ruiz, and J. C. Oefelein, "Analysis of high-pressure diesel fuel injection processes using les with real-fluid thermodynamics and transport," *Proceedings of the Combustion Institute*, vol. 35, no. 2, pp. 1603–1611, 2015.

[143] "Engine Combustion Network | Near-nozzle mixture derived from x-ray radiography." [Online]. Available: https://ecn.sandia.gov/rad675/

[144] R. Payri, B. Tormos, J. Gimeno, and G. Bracho, "The potential of large eddy simulation (les) code for the modeling of flow in diesel injectors," *Mathematical and Computer Modelling*, vol. 52, no. 7-8, pp. 1151–1160, 2010.

[145] N. Kornev, H. Kröger, J. Turnow, and E. Hassel, "Synthesis of artificial turbulent fields with prescribed second-order statistics using the random-spot method," in *PAMM: Proceedings in Applied Mathematics and Mechanics*, vol. 7, no. 1. Wiley Online Library, 2007, pp. 2 100 047–2 100 048.

[146] N. Kornev, H. Kröger, and E. Hassel, "Synthesis of homogeneous anisotropic turbulent fields with prescribed second-order statistics by the random spots method," *Communications in Numerical Methods in Engineering*, vol. 24, no. 10, pp. 875–877, 2008.

[147] A. Vallet and R. Borghi, "Modelisation eulerienne de l'atomisation d'un jet liquide," *Comptes Rendus de l'Académie des Sciences-Series IIB-Mechanics-Physics-Astronomy*, vol. 327, no. 10, pp. 1015–1020, 1999.

[148] X. Pialat, O. Simonin, and P. Villedieu, "A hybrid eulerian–lagrangian method to simulate the dispersed phase in turbulent gas-particle flows," *International journal of multiphase flow*, vol. 33, no. 7, pp. 766–788, 2007.

[149] A. Umemura, "Turbulent atomization subgrid model for two-phase flow large eddy simulation (theoretical development)," *Combustion and Flame*, vol. 165, pp. 154–176, 2016.

[150] W. A. Sirignano, *Fluid dynamics and transport of droplets and sprays*. Cambridge university press, 1999.

[151] Z. Han, S. Parrish, P. V. Farrell, and R. D. Reitz, "Modeling atomization processes of pressure-swirl hollow-cone fuel sprays," *Atomization and sprays*, vol. 7, no. 6, 1997.

[152] L. Allocca, G. Bella, A. De Vita, and L. Di Angelo, "Experimental validation of a gdi spray model," SAE Technical Paper, Tech. Rep., 2002.

[153] P. Senecal, D. P. Schmidt, I. Nouar, C. J. Rutland, R. D. Reitz, and M. Corradini, "Modeling high-speed viscous liquid sheet atomization," *International Journal of Multiphase Flow*, vol. 25, no. 6-7, pp. 1073–1097, 1999.

[154] D. P. Schmidt, I. Nouar, P. Senecal, C. Rutland, J. Martin, R. D. Reitz, and J. A. Hoffman, "Pressure-swirl atomization in the near field," SAE Technical Paper, Tech. Rep., 1999.

[155] R. REITZ *et al.*, "Modeling atomization processes in high-pressure vaporizing sprays," *Atomisation and Spray Technology*, vol. 3, no. 4, pp. 309–337, 1987.

[156] P. J. O'Rourke and A. A. Amsden, "The tab method for numerical calculation of spray droplet breakup," SAE Technical Paper, Tech. Rep., 1987.

[157] G. Blokkeel, F. Demoulin, and R. Borghi, "Modeling of two-phase flows: An eulerian model for diesel injection," in *Thermo-and Fluid Dynamic Processes in Diesel Engines 2*. Springer, 2004, pp. 87–105.

[158] R. Canu, C. Dumouchel, B. Duret, M. Essadki, M. Massot, T. Ménard, S. Puggelli, J. Reveillon, and F.-X. Demoulin, "Where does the drop size distribution come from?" in *Ilass Europe. 28th european conference on Liquid Atomization and Spray Systems*. Editorial Universitat Politècnica de València, 2017, pp. 605–612.

[159] J. Reveillon and L. Vervisch, "Spray vaporization in nonpremixed turbulent combustion modeling: a single droplet model," *Combustion and flame*, vol. 121, no. 1-2, pp. 75–90, 2000.

[160] R. Cao and S. B. Pope, "Numerical integration of stochastic differential equations: weak second-order mid-point scheme for application in the composition pdf method," *Journal of Computational Physics*, vol. 185, no. 1, pp. 194–212, 2003.

[161] M. Gorokhovski, "The stochastic lagrangian model of drop breakup in the computation of liquid sprays," *Atomization and Sprays*, vol. 11, no. 5, 2001.

[162] S. Apte, M. Gorokhovski, and P. Moin, "Les of atomizing spray with stochastic modeling of secondary breakup," *International Journal of Multiphase Flow*, vol. 29, no. 9, pp. 1503–1522, 2003.

[163] M. Gorokhovski and V. Saveliev, "Analyses of kolmogorovâĂŹs model of breakup and its application into lagrangian computation of liquid sprays under air-blast atomization," *Physics of Fluids*, vol. 15, no. 1, pp. 184–192, 2003.

[164] M. Gorokhovski and M. Herrmann, "Modeling primary atomization," *Annu. Rev. Fluid Mech.*, vol. 40, pp. 343–366, 2008.

[165] R. Reddy and R. Banerjee, "Direct simulations of liquid sheet break-up in planar gas blast atomization," *Atomization and Sprays*, 2017.

[166] W. H. DeHaan and W. H. Finlay, "In vitro monodisperse aerosol deposition in a mouth and throat with six different inhalation devices," *Journal of Aerosol Medicine*, vol. 14, no. 3, pp. 361–367, 2001.

[167] M. R. Maxey and J. J. Riley, "Equation of motion for a small rigid sphere in a nonuniform flow," *The Physics of Fluids*, vol. 26, no. 4, pp. 883–889, 1983.

[168] C.-M. Ho and P. Huerre, "Perturbed free shear layers," *Annual review of fluid mechanics*, vol. 16, no. 1, pp. 365–422, 1984.

[169] S. Menon, C. Stone, V. Sankaran, and B. Sekar, "Large-eddy simulations of combustion in gas turbine combustors," in *38th Aerospace Sciences Meeting and Exhibit*, 2000, p. 960.

[170] J. Pozorski and J.-P. Minier, "On the lagrangian turbulent dispersion models based on the langevin equation," *International Journal of Multiphase Flow*, vol. 24, no. 6, pp. 913–945, 1998.

[171] G. E. Box and G. M. Jenkins, *Time series analysis: forecasting and control, revised ed*. Holden-Day, 1976.

[172] S. Pope, "Lagrangian pdf methods for turbulent flows," *Annual review of fluid mechanics*, vol. 26, no. 1, pp. 23–63, 1994.

[173] W. T. Coffey and Y. P. Kalmykov, *The Langevin equation: with applications to stochastic problems in physics, chemistry and electrical engineering*. World Scientific, 2004.

[174] O. U. Guide, "The openfoam foundation," 2011.

[175] C. Hespel, J.-B. Blaisot, M. Gazon, and G. Godard, "Laser correlation velocimetry performance in diesel applications: spatial selectivity and velocity sensitivity," *Experiments in fluids*, vol. 53, no. 1, pp. 245–264, 2012.

[176] S. Idlahcen, L. Méès, C. Rozé, T. Girasole, and J.-B. Blaisot, "Time gate, optical layout, and wavelength effects on ballistic imaging," *JOSA A*, vol. 26, no. 9, pp. 1995–2004, 2009.

[177] E. El-Hannouny, S. Gupta, C. Powell, S. Cheong, R. Sekar, and J. Wang, "Time resolved x-ray measurements of diesel sprays at elevated ambient pressure." Argonne National Lab.(ANL), Argonne, IL (United States), Tech. Rep., 2005.

[178] F. X. Tanner, K. A. Feigl, S. A. Ciatti, C. F. Powell, S.-K. Cheong, J. Liu, and J.-C. Wang, "Structure of high-velocity dense sprays in the near-nozzle region," *Atomization and Sprays*, vol. 16, no. 5, 2006.

[179] Z. Liu and R. Adrian, "Simultaneous imaging of the velocity fields of two phases," 1993.

[180] K. Kiger, "Scanning piv technique to resolve dispersed two-phase flow," in *Third international conference on multiphase flow*, 1998, pp. 8–12.

[181] G. Vaudor, "Atomisation assistée par un cisaillement de l'écoulement gazeux. développement et validation," Ph.D. dissertation, Rouen, 2015.

[182] A. Fluent *et al.*, "Theory guide," *Ansys Inc*, 2015.

[183] M. Klein, A. Sadiki, and J. Janicka, "A digital filter based generation of inflow data for spatially developing direct numerical or large eddy simulations," *Journal of computational Physics*, vol. 186, no. 2, pp. 652–665, 2003.

[184] Y. Pei, M. J. Davis, L. M. Pickett, and S. Som, "Engine combustion network (ecn): Global sensitivity analysis of spray a for different combustion vessels," *Combustion and Flame*, vol. 162, no. 6, pp. 2337–2347, 2015.

[185] J. R. Grace and H. Bi, "Introduction to circulating fluidized beds," in *Circulating fluidized beds*. Springer, 1997, pp. 1–20.

[186] K. Theologos and N. Markatos, "Advanced modeling of fluid catalytic cracking riser-type reactors," *AIChE Journal*, vol. 39, no. 6, pp. 1007–1017, 1993.

[187] H. Ali, S. Rohani, and J. Corriou, "Modelling and control of a riser type fluid catalytic cracking (fcc) unit," *Chemical Engineering Research and Design*, vol. 75, no. 4, pp. 401–412, 1997.

[188] J. S. Buchanan, "Analysis of heating and vaporization of feed droplets in fluidized catalytic cracking risers," *Industrial and Engineering Chemistry Research;(United States)*, vol. 33, no. 12, 1994.

[189] R. K. Gupta, V. Kumar, and V. Srivastava, "Modeling of fluid catalytic cracking riser reactor: a review," *International Journal of Chemical Reactor Engineering*, vol. 8, no. 1, 2010.

[190] R. Quintana-Solórzano, J. Thybaut, P. Galtier, and G. Marin, "Single-event microkinetics for coke formation during the catalytic cracking of (cyclo) alkane/1-octene mixtures," *Catalysis Today*, vol. 127, no. 1, pp. 17–30, 2007.

[191] M. Ahsan, "Prediction of gasoline yield in a fluid catalytic cracking (fcc) riser using k-epsilon turbulence and 4-lump kinetic models: A computational fluid dynamics (cfd) approach," *Journal of King Saud University-Engineering Sciences*, vol. 27, no. 2, pp. 130–136, 2015.

[192] J. Gan, H. Zhao, A. S. Berrouk, C. Yang, and H. Shan, "Numerical simulation of hydrodynamics and cracking reactions in the feed mixing zone of a multiregime gas–solid riser reactor," *Industrial & Engineering Chemistry Research*, vol. 50, no. 20, pp. 11 511–11 520, 2011.

[193] R. Patel, D. Wang, C. Zhu, and T. C. Ho, "Effect of injection zone cracking on fluid catalytic cracking," *AIChE Journal*, vol. 59, no. 4, pp. 1226–1235, 2013.

[194] T. T. Nguyen, S. Mitra, V. Pareek, J. Joshi, and G. Evans, "Comparison of vaporization models for feed droplet in fluid catalytic cracking risers," *Chemical Engineering Research and Design*, vol. 101, pp. 82–97, 2015.

[195] Q. Huang and J. Li, "Experiment and numerical studies on the atomization of a swirl feed nozzle," *Journal of Industrial and Intelligent Information Vol*, vol. 4, no. 1, 2016.

[196] K. Theologos, A. Lygeros, and N. Markatos, "Feedstock atomization effects on fcc riser reactors selectivity," *Chemical Engineering Science*, vol. 54, no. 22, pp. 5617–5625, 1999.

[197] CINES. (2017) Centre informatique national de l'enseignement superieur. [Online]. Available: https://www.cines.fr/en/

[198] TGCC. (2017) Centre de calcul du cea. [Online]. Available: http://www-hpc.cea.fr/index-en.htm

[199] IDRIS. (2017) institut du developpement et des ressources en informatique scientifique. [Online]. Available: http://www.idris.fr/

[200] CRIHAN. (2017) centre regional informatique et d'applications numeriques de normandie. [Online]. Available: http://www.crihan.fr/

[201] OpenFOAM. (2017) The openfoam foundation. [Online]. Available: https://openfoam.org/

[202] GNU. (2017) general public license. [Online]. Available: https://www.gnu.org/licenses/gpl-3.0.en.html

[203] SALOME. (2017) The open source integration platform for numerical simulations. [Online]. Available: http://www.salome-platform.org/

[204] F. Grisch, A. Boukhalfa, G. Cabot, B. Renou, and A. Vandel, "Coria aeronautical combustion facilities and associated optical diagnostics," *AerospaceLab*, no. 11, pp. 13–pages, 2016.

[205] cfMesh. (2017) Free meshing tool. [Online]. Available: http://cfmesh.com/

[206] S. Patankar, *Numerical heat transfer and fluid flow*. CRC press, 1980.

[207] ECN. (2017) Engine combustion network. [Online]. Available: https://ecn.sandia.gov/

[208] M. Instruments, "A basic guide to particle characterization," *Malvern Instrument Limited, UK. Retreived from http://www. atascientific. com. au/publications/wp-content/uploads/2012/07/MRK1806-01-basic-guide-to-particle-characterisation. pdf*, 2012.

[209] J. Homitz, D. M. Sykes, W. F. O'brien, U. Vandsburger, and S. LePERA, "Premixing injector for gas turbine engines," Jan. 18 2011, uS Patent 7,870,736.

[210] T. Gradinger, A. Inauen, R. Bombach, B. Käppeli, W. Hubschmid, and K. Boulouchos, "Liquid-fuel/air premixing in gas turbine combustors: experiment and numerical simulation," *Combustion and Flame*, vol. 124, no. 3, pp. 422–443, 2001.

[211] J. Chin, N. K. Rizk, M. K. Razdan, and A. W. Marshall, "Fuel premixing module for gas turbine engine combustor," Nov. 29 2005, uS Patent 6,968,692.

[212] S. Gövert, D. Mira, J. B. Kok, M. Vázquez, and G. Houzeaux, "The effect of partial premixing and heat loss on the reacting flow field prediction of a swirl stabilized gas turbine model combustor," *Flow, turbulence and combustion*, vol. 100, no. 2, pp. 503–534, 2018.

[213] G. Grant, J. Brenton, and D. Drysdale, "Fire suppression by water sprays," *Progress in energy and combustion science*, vol. 26, no. 2, pp. 79–130, 2000.

[214] J. L. Bryan, *Fire suppression and detection systems*. Prentice Hall, 1993.

[215] V. Babrauskas, *Ignition handbook*. Fire science publishers: Issaquah, WA, 2003, vol. 318.

[216] S. Martorano, "Spray nozzles selections for water spray systems: Options and applications explained," *International Fire Protection*, vol. 41, pp. 30–33, 2010.

[217] F. P. Incropera, D. P. Dewitt, T. Bergman, and A. Lavine, "Fundamentals of mass and heat transfer," *Australia: John Wiley and Sons*, 2002.

[218] Z. Yan, R. Zhao, F. Duan, T. N. Wong, K. C. Toh, K. F. Choo, P. K. Chan, and Y. S. Chua, "Spray cooling," in *Two Phase Flow, Phase Change and Numerical Modeling*. InTech, 2011.

[219] M. Pais, L. Chow, and E. Mahefkey, "Surface roughness and its effects on the heat transfer mechanism in spray cooling," *Journal of Heat Transfer*, vol. 114, no. 1, pp. 211–219, 1992.

[220] Y. Bar-Cohen, "BiomimeticsâĂŤusing nature to inspire human innovation," *Bioinspiration & biomimetics*, vol. 1, no. 1, p. P1, 2006.

[221] A. Ashwood and D. Bharathan, "Hybrid cooling systems for low-temperature geothermal power production," 2011.

[222] J. C. Kloppers and D. G. KroĬLger, "Cooling tower performance evaluation: Merkel, poppe, and e-ntu methods of analysis," *Journal of Engineering for Gas Turbines and Power*, vol. 127, no. 1, pp. 1–7, 2005.

[223] A. Alkhedhair, I. Jahn, H. Gurgenci, Z. Guan, and S. He, "Parametric study on spray cooling system for optimising nozzle design with pre-cooling application in natural draft dry cooling towers," *International Journal of Thermal Sciences*, vol. 104, pp. 448–460, 2016.

[224] J. Yang, L. Chow, and M. Pais, "Nucleate boiling heat transfer in spray cooling," *Journal of Heat Transfer*, vol. 118, no. 3, pp. 668–671, 1996.

[225] J. Yao, K. Tanaka, A. Kawahara, and M. Sadatomi, "Design procedure and performance evaluation of a flat-jet twin-fluid atomizer by siphoning liquid," *IACSIT International Journal of Engineering and Technology*, vol. 7, no. 5, 2015.

[226] S. Nonnenmacher and M. Piesche, "Design of hollow cone pressure swirl nozzles to atomize newtonian fluids," *Chemical Engineering Science*, vol. 55, no. 19, pp. 4339–4348, 2000.

[227] J. C. Thompson and J. P. Rothstein, "The atomization of viscoelastic fluids in flat-fan and hollow-cone spray nozzles," *Journal of Non-Newtonian Fluid Mechanics*, vol. 147, no. 1-2, pp. 11–22, 2007.

[228] G. Ferreira, J. A. García, F. Barreras, A. Lozano, and E. Lincheta, "Design optimization of twin-fluid atomizers with an internal mixing chamber for heavy fuel oils," *Fuel processing technology*, vol. 90, no. 2, pp. 270–278, 2009.

[229] J. García, A. Lozano, J. Alconchel, E. Calvo, F. Barreras, and J. Santolaya, "Atomization of glycerin with a twin-fluid swirl nozzle," *International Journal of Multiphase Flow*, vol. 92, pp. 150–160, 2017.

[230] C. Dumouchel and J.-B. Blaisot, "Laser-diffraction measurement of nonspherical drop sprays," *Atomization and Sprays*, vol. 24, no. 3, 2014.

[231] T. Sikanen, J. Vaari, S. Hostikka, and A. Paajanen, "Modeling and simulation of high pressure water mist systems," *Fire Technology*, vol. 50, no. 3, pp. 483–504, 2014.

[232] S. C. Kim and H. S. Ryou, "An experimental and numerical study on fire suppression using a water mist in an enclosure," *Building and Environment*, vol. 38, no. 11, pp. 1309–1316, 2003.

[233] B. Yao, B. Cong, J. Qin, and W. Chow, "Experimental study of suppressing poly (methyl methacrylate) fires using water mists," *Fire Safety Journal*, vol. 47, pp. 32–39, 2012.

[234] L. Yinshui, J. Zhuo, W. Dan, and L. Xiaohui, "Experimental research on the water mist fire suppression performance in an enclosed space by changing the characteristics of nozzles," *Experimental Thermal and Fluid Science*, vol. 52, pp. 174–181, 2014.

[235] F. Ura, N. Kawabata, and F. Tanaka, "Characteristics of smoke extraction by natural ventilation during a fire in a shallow urban road tunnel with roof openings," *Fire Safety Journal*, vol. 67, pp. 96–106, 2014.

[236] H. I. Mahmud, K. A. Moinuddin, and G. R. Thorpe, "Experimental and numerical study of high-pressure water-mist nozzle sprays," *Fire Safety Journal*, vol. 81, pp. 109–117, 2016.

[237] M. Sadafi, I. Jahn, and K. Hooman, "Cooling performance of solid containing water for spray assisted dry cooling towers," *Energy Conversion and Management*, vol. 91, pp. 158–167, 2015.

[238] M. Sadafi, S. G. Ruiz, M. R. Vetrano, I. Jahn, J. van Beeck, J. Buchlin, and K. Hooman, "An investigation on spray cooling using saline water with experimental verification," *Energy conversion and management*, vol. 108, pp. 336–347, 2016.

[239] M. Sadafi, I. Jahn, and K. Hooman, "Nozzle arrangement effect on cooling performance of saline water spray cooling," *Applied Thermal Engineering*, vol. 105, pp. 1061–1066, 2016.

[240] F. Pereira, C. Ataide, and M. Barrozo, "Cfd approach using a discrete phase model for annular flow analysis," *Latin American applied research*, vol. 40, no. 1, pp. 53–60, 2010.

[241] M. Battistoni, G. M. Magnotti, C. L. Genzale, M. Arienti, K. E. Matusik, D. J. Duke, J. Giraldo, J. Ilavsky, A. L. Kastengren, C. F. Powell *et al.*, "Experimental and computational investigation of subcritical near-nozzle spray structure and primary atomization in the engine combustion network spray d," SAE Technical Paper, Tech. Rep., 2018.

[242] F. Piscaglia, F. Giussani, A. Montorfano, J. Hélie, and S. Aithal, "A multiphase dynamic-vof solver to model primary jet atomization and cavitation inside high-pressure fuel injectors in openfoam," *Acta Astronautica*, 2018.

[243] C. Beringer, J. Bothell, T. Morgan, D. Li, T. Heindel, A. Aliseda, N. Machicoane, and A. Kastengren, "High-speed x-ray flow visualization of a liquid jet," *Bulletin of the American Physical Society*, 2018.

[244] O. Simonin, "Statistical and continuum modelling of turbulent reactive particulate flows," *Lecture series*, vol. 6, 2000.

[245] T. Baker, M. Negri, and V. Bertola, "Atomization of high-viscosity and non-newtonian fluids by premixing," *Atomization and Sprays*, vol. 28, no. 5, 2018.

[246] S. Gehrke and K.-E. Wirth, "Liquid feed injection in a high-density riser," *Chemical engineering & technology*, vol. 31, no. 11, pp. 1701–1705, 2008.

[247] S. Bruhns and J. Werther, "An investigation of the mechanism of liquid injection into fluidized beds," *AIChE Journal*, vol. 51, no. 3, pp. 766–775, Mar. 2005. [Online]. Available: http://onlinelibrary.wiley.com/doi/10.1002/aic.10336/abstract

[248] S. Chen, Y. Fan, Z. Yan, W. Wang, and C. Lu, "CFD simulation of gas-solid two-phase flow and mixing in a FCC riser with feedstock injection," *Powder Technology*, vol. 287, no. Supplement C, pp. 29–42, Jan. 2016. [Online]. Available: http://www.sciencedirect.com/science/article/pii/S0032591015300553

[249] C. Ross and S. C. Company, "Static mixer designs and applications," *White paper from Ross and Son Company*, pp. 1–10, 2017. [Online]. Available: https://www.mixers.com/whitepapers/staticmixer_designs.pdf

[250] M. B. D. Alain Georg, "Once they get going, static mixers and mixer/heat exchangers assure extremely efficient processes," *PROCESS ENGINEERING*, pp. 1–2, 2008. [Online]. Available: http://www.fluitec.ch/download.php?f=61b6d1cc8b9f7ea1afadfb2b934d3177

[251] F. Zidouni, E. Krepper, R. Rzehak, S. Rabha, M. Schubert, and U. Hampel, "Simulation of gas–liquid flow in a helical static mixer," *Chemical Engineering Science*, vol. 137, pp. 476–486, 2015.